

A Thesis Submitted for the Degree of PhD at the University of Warwick

Permanent WRAP URL:

<http://wrap.warwick.ac.uk/177022>

Copyright and reuse:

This thesis is made available online and is protected by original copyright.

Please scroll down to view the document itself.

Please refer to the repository record for this item for information to help you to cite it.

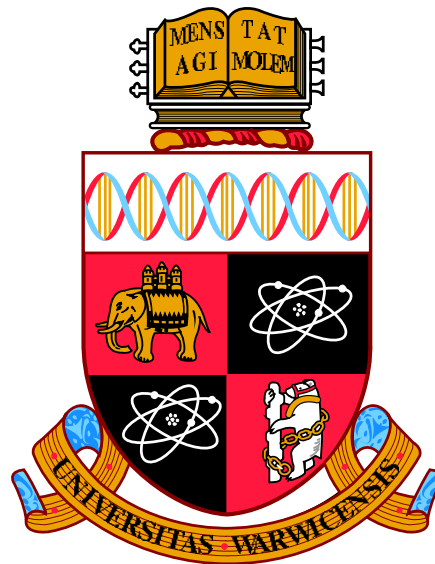
Our policy information is available from the repository home page.

For more information, please contact the WRAP Team at: wrap@warwick.ac.uk

Engineering of the Manufacture of Air-Sensitive Cathode Electrodes for Sodium Ion Batteries

by

Samuel Roberts



A thesis submitted to The University of Warwick
for the degree of
DOCTOR OF PHILOSOPHY

WMG
University of Warwick
June 2022

Contents

1	Introduction	1
1.1	Objective of the PhD	3
1.2	Layout of the Thesis	3
1.3	Impact of the PhD	4
2	Literature Review	6
2.1	Introduction	6
2.1.1	Sodium-ion Battery Operating Concepts	7
2.2	Exploration of Sodium ion Cathode Materials	14
2.2.1	Sodium Cathode Materials	14
2.2.2	Motivation for Layered O3 Oxides	19
2.2.3	Current Problems with Layered O3 Oxides	20
2.2.4	Summary and Conclusions	26
2.3	Manufacture of Sodium Ion Cathode Electrodes	27
2.3.1	Role of the Electrode Structure	27
2.3.2	Electrode Manufacture	30
2.3.3	Characterisation of Electrode Slurries	41
2.3.4	Summary and Conclusions	45
3	Experimental Methods	47
3.1	Electrode Material Manufacture and Analysis	47
3.1.1	NaNMST Synthesis	47
3.1.2	Material Analysis	48
3.1.3	Additional Processing	49
3.2	Electrode Slurry Manufacture and Analysis	49
3.2.1	Rheology	50
3.3	Electrode Manufacture and Analysis	50
3.3.1	Adhesion Testing	51
3.3.2	Four Point Probe	52
3.3.3	XPS	53
3.3.4	Electrochemistry	53
4	Mechanisms of Gelation in Electrode Slurries for High Nickel Content Sodium Ion Battery Cathode Materials	57
4.1	Introduction	57
4.1.1	PVDF (Binder) Stability	58
4.1.2	NMP (Solvent) Stability	59

4.1.3	Carbon Black Stability	60
4.1.4	Layered O3 Oxide	61
4.2	Aims and Objectives	61
4.3	Experimental Setup	62
4.4	Results	63
4.4.1	Active Material Characterisation	63
4.4.2	Electrode Slurry Characterisation	66
4.4.3	Electrode Characterisation	77
4.4.4	Electrochemical Characterisation	79
4.5	Discussion	80
4.6	Conclusions	83
5	Technique Development for the Analysis of Gelation in Electrode Slurries	85
5.1	Introduction	85
5.1.1	Rheological Analysis for Electrode Slurries	86
5.1.2	Practical Shear Rates	88
5.1.3	Oscillatory Rheology	90
5.1.4	Experimental Models	91
5.2	Aims and Objectives	96
5.3	Methods and Materials	97
5.3.1	Rotational Rheology	97
5.3.2	Oscillatory Rheology	98
5.3.3	Maxwell Model	99
5.4	Results and Discussion	99
5.4.1	Rotational Rheology	100
5.4.2	Oscillatory Rheology	107
5.4.3	Maxwell Model	114
5.5	Discussion	119
5.6	Conclusions	120
6	Stabilising Additives for High Nickel Content Cathode Electrode Slurries	123
6.1	Introduction	123
6.2	Aims and Objectives	129
6.3	Materials and Methods	130
6.4	Results and Discussion	131
6.4.1	Stabilisation of the Electrode Inks	131
6.4.2	Effect of the Stabilising Additives on the Electrodes	150
6.4.3	Effect of the Stabilising Additives on the Electrochemical Performance	156
6.4.4	Summary	164
6.5	Conclusions	166
7	Sacrificial Stabilising Additives for High Nickel Content Cathode Materials	169
7.1	Introduction	169

7.2	Aims and Objectives	171
7.3	Experimental Setup	172
7.4	Results and Discussion	173
	7.4.1 Stabilisation of the Electrode Slurries	174
	7.4.2 Effect on the Electrode Properties	186
	7.4.3 Effect on the Electrochemical Performance	192
	7.4.4 Summary	199
7.5	Conclusions	199
8	Conclusions and Future Work	202
8.1	Future Work	205
A	FTIR Peak Fitting Procedure	207
B	Rotational Rheology	212
B.1	Shear ramp with rest intervals	212
B.2	Constant shear rate with shear ramps	213
	References	214

List of Figures

2.1	General charging process in a Na-ion battery.	11
2.2	Naming System and Structure of Layered TMO.	17
2.3	Photograph of Gelled Electrode Slurry (taken by author).	25
2.4	Comparison between an idealised electrode structure and a poorly prepared electrode.	28
2.5	Manufacture of Electrode Slurries, Electrodes, and Cells.	31
2.6	Flory Huggins Model - 2D Representation	33
3.1	Diagram of the Adhesion Testing Setup using the Malvern Panalytical Pro ⁺ rheometer.	52
4.1	Hydrolysis reaction of NMP, forming 4-(methylamino) butanoic acid. .	59
4.2	Ex-situ aging spectra of the carbon-coated active material over 360 minutes and b) Comparisons of the spectra with Na ₂ CO ₃ , NiCO ₃ , NaOH, and the NaNMST sample at time 0 and 360 minutes.	65
4.3	SEM image of the as synthesised NaNMST material a) Primary particles, b) agglomerates, c) SEM image of the as synthesised NaNMST material after exposure for 3 days, (d) EDS layered spectrum and individual elements, labelled by their elemental chemical.	65
4.4	Comparison between a pristine electrode slurry (a) and the gelled sample (b and c).	66
4.5	a) Storage and Loss Moduli, and b) Phase Angle for the Aging Electrode Slurry.	68
4.6	2 Mode Maxwell Model (sometimes referred to as a Burgers Model). .	69
4.7	Primary and secondary mode relaxation times fitted from the Maxwell Model.	71
4.8	Ex-situ FTIR Spectra of the Electrode Slurry.	72
4.9	FTIR Spectra comparisons of the electrode slurry, NMP, PVDF, and 8 % PVDF in NMP solution.	73
4.10	Fitted Ex-situ FTIR Spectra of the Aging Electrode Slurry between 1525 cm ⁻¹ and 1750 cm ⁻¹ fitted for spectra at 0, 10, 20, and 30 minutes. . .	75
4.11	Fitted Ex-situ FTIR Spectra of the Aging Electrode Slurry between 1525 cm ⁻¹ and 1750 cm ⁻¹ fitted for spectra at 60, 90, 120, 240, and 360 minutes.	76
4.12	F1s X-ray Photo-emission Spectroscopy of the as-coated Electrode . .	78
4.13	Dehydrofluorination of PVDF.	78

4.14	a) Half-cell capacity curves for the 1st and 5th cycles for the electrode coated 0 minutes after mixing. b) Half-cell capacity vs cycle number for electrodes coated at 0, 20, and 40 minutes after mixing.	79
4.15	Dehydrofluorination of PVDF and subsequent crosslinking. Crosslinks between PVDF chains have been highlighted in red	81
4.16	Primary mode relaxation time, showing the 3 proposed stages of gel development.	82
5.1	Velocity profile and shear in a doctor blade coater.	89
5.2	Generalised Maxwell Model.	92
5.3	Proposed Expanded Maxwell Model.	93
5.4	2 Mode Maxwell Model (sometimes referred to as a Burgers Model).	94
5.5	Constant Shear Rate of 100 s^{-1} over time.	100
5.6	Flow Curve and Time vs Apparent Viscosity curves for shear rates of 10 s^{-1} and 40 s^{-1}	103
5.7	Areas of exposure in cup and bob geometry.	104
5.8	Flow Curve and Time vs Apparent Viscosity curves for shear rates of 10 s^{-1} and 40 s^{-1}	105
5.9	Initial amplitude sweep, showing the LVER and chosen amplitudes.	108
5.10	Oscillatory rheology time sweep.	109
5.11	Amplitude sweep on gelled electrode slurry.	111
5.12	Gelled electrode slurry sample.	112
5.13	Frequency sweeps taken at 0, 15, 30, 45, 60, and 75 minutes.	113
5.14	Primary mode relaxation time, showing the 3 proposed stages of gel development.	115
5.15	Storage and loss moduli recorded 0 minutes and 90 minutes after mixing, fitted to Maxwell models with 1, 2, and 3 modes.	116
5.16	R-squared values for the fitted Maxwell models containing 1, 2, and 3 modes.	117
6.1	Acid additive chemical structures.	124
6.2	Simplified ionic micelle formation due to the charged heads on the acid additives.	127
6.3	Micelle shape factors.	128
6.4	Fourier transform infrared spectra for the reference electrode slurry and all the electrode slurries containing 2.0 wt% of the acid additives.	133
6.5	Storage and Loss Modulus for the reference electrode slurry and all the electrode slurries containing 2.0 wt% of the acid additives.	137
6.6	Approximated disassociated acid dimensions - dimensions were calculated using Chem3D, PerkinElmer.	141
6.7	Phase Angle for the reference electrode slurry and all the electrode slurries containing 2.0 wt% of the acid additives.	145
6.8	Maxwell Mode - Primary and Secondary Relaxation Times for the reference electrode slurry and all the electrode slurries containing 2.0 wt% of acid additives.	149

6.9	Adhesion strength for electrodes made from the reference electrode slurry and all the electrode slurries containing 2.0 wt% of the acid additives. Electrode slurries were coated immediately after mixing was completed.	152
6.10	Comparison adhesion strength for electrodes made from the reference electrode slurry and all the electrode slurries containing 2.0 wt% of the acid additives. Bars show coatings made from electrode slurries coated immediately after, and 40 minutes after mixing was completed.	153
6.11	Comparison electrode conductivity for electrodes made from the reference electrode slurry and all the electrode slurries containing 2.0 wt% of the acid additives.	155
6.12	Cycling capacity vs cycle number for electrodes made from the reference electrode slurry and all the electrode slurries containing 2.0 wt% of the acid additives.	156
6.13	Electrochemical Impedance Spectroscopy for electrodes made from the reference electrode slurry and all the electrode slurries containing 2.0 wt% of the acid additives.	159
6.14	Equivalent circuit used for the electrochemical impedance spectroscopy.	160
6.15	Cathode solid electrolyte interphase layer resistance fitted from the electrochemical impedance spectroscopy in figure 6.13 after the formation cycle and after 10 cycles.	162
6.16	Charge transfer resistance fitted from the electrochemical impedance spectroscopy in figure 6.13 after the formation cycle and after 10 cycles.	163
7.1	Acid additive chemical structures.	170
7.2	Dissolution of sodium acid salts in NMP.	174
7.3	Storage and Loss Modulus for the reference electrode slurry and all the electrode slurries containing the active material milled with 2.0 wt% of the sodium salts.	176
7.4	Phase angle changes for the reference electrode slurry and all the electrode slurries containing the active material milled with 2.0 wt% of the sodium salts.	180
7.5	Maxwell Mode - Primary and Secondary Relaxation Times for the reference electrode slurry and all the electrode slurries containing the active material milled with 2.0 wt% of the sodium salts.	185
7.6	Adhesion strength for electrodes made from the reference electrode slurry and all the electrode slurries containing the active material milled with 2.0 wt% of the sodium salts. Electrode slurries were coated immediately after mixing was completed.	187
7.7	Comparison adhesion strength for electrodes made from the reference electrode slurry and all the electrode slurries containing the active material milled with 2.0 wt% of the sodium salts. Bars show coatings made from electrode slurries coated immediately after, and 40 minutes after mixing was completed.	189

7.8	Comparison electrode conductivity for electrodes made from the reference electrode slurry and all the electrode slurries containing the active material milled with 2.0 wt% of the sodium salts. The inset graph shows conductivities between 0 and 400 Sm^{-1} , for a clearer comparison between all electrodes, other than those containing sodium stearate.	190
7.9	Cycling capacity vs cycle number for electrodes made from the reference electrode slurry and all the electrode slurries containing the active material milled with 2.0 wt% of the sodium salts. The shaded areas denote the standard deviations of the measurements.	193
7.10	Electrochemical Impedance Spectroscopy for the reference electrodes and electrode containing the sacrificial additives. Performed after the formation (first cycle) and after the tenth cycle.	195
7.11	Cathode solid electrolyte interphase layer resistance and charge transfer resistance - fitted from the electrochemical impedance spectroscopy in Figure 7.10 after the formation cycle and after 10 cycles. Samples have been incremented along the x-axis for clearer distinction between them.	196
A.1	FTIR Peak Fitting with No Baseline	209
A.2	FTIR Peak Fitting - Cubic Spline Baseline	209
A.3	FTIR Peak Fitting - Convex Hull Baseline	210
A.4	FTIR Peak Fitting - Linear Baseline with additional edge points	210
A.5	FTIR Peak Fitting - Straight, Linear Baseline	211
B.1	Shear ramp with rest intervals.	212
B.2	Constant shear rate with shear ramps.	213

List of Tables

2.1	Literature Sodium-Ion Cathode Materials and Slurry Compositions. . . .	18
2.2	Hansen Solubility Parameters.	35
5.1	Calculated Shear Rates for the Lab Doctor Blade Coater.	89
5.2	Akaike Weights (w_i) for the electrode slurry relaxation times fitted to 1, 2, and 3 Modes.	118
5.3	Summary of Rheological Methods Tested.	120
6.1	Properties of acid additives used in this study.	125
6.2	pK_a Values of the acid additives used in this study.	125
6.3	FTIR functional groups of acid additives.	135
6.4	Approximated micelle critical packing parameters (from Figure 6.6) and predicted structures.	142
6.5	Summary of storage and loss values, phase angle values and the loss factor (G'/G'') after 40 minutes and 90 minutes.	147
6.6	Summary of effects to the electrode slurry and electrodes due to the acid additives.	165
7.1	Summary of storage and loss values, phase angle values and the loss factor (G'/G'') after 40 minutes and 90 minutes.	183
7.2	Summary of effects to the electrode slurry and electrodes due to the sacrificial additives.	200

List of Equations

2.1	Conversion between electrode potential and Gibbs free energy	7
2.2	Sodium standard electrode potential	8
2.3	Lithium standard electrode potential	8
2.4	Nernst equation	8
2.5	Sodium TMO Half Equation	9
2.6	Sodium Hard Carbon Half Equation	9
2.7	Sodium Hard Carbon Full Cell Intercalation	9
2.8	Expanded Nernst equation (including reactant and product activities) . .	9
2.9	Cell Overpotential	12
2.10	Butler-Volmer Equation	12
2.11	Faraday's Law of Electrolysis	13
2.12	Active Material Theoretical Capacity	13
2.13	Electrode Theoretical Capacity	13
2.14	Specific Energy	14
2.15	Gibbs Free Energy	34
2.16	Boltzmann Equation	34
2.17	Hildebrand Equation	35
2.18	Equilibrium Phase Behaviour In Colloids	38
2.19	Stokes Law Drag Force	40
2.20	Calculation of Shear Stress	41
2.21	Calculation of Apparent Viscosity	41
2.22	Calculation of Complex Modulus	42
2.23	Calculation of the Storage Modulus	42
2.24	Calculation of the Loss Modulus	42
3.1	Tap Density	48
3.2	Active Mass	54
3.3	Theoretical Coating Density at 0 % Porosity	54
3.4	Electrode Volume	54
3.5	Electrode True Density	55
3.6	Electrode Porosity	55
4.1	Maxwell Model Relaxation Time	70
4.2	Generalised Maxwell Mode - Storage Modulus, G'	70
4.3	Generalised Maxwell Mode - Loss Modulus, G''	70
4.4	Formation of NaF	77
5.1	Shear Rate	88
5.2	Strain	90
5.3	Maxwell Model Relaxation Time	94
5.4	Akaike Information Criterion	95

5.5	Corrected Akaike Information Criterion	95
5.6	Akaike rescaling and weighting	95
5.7	Akaike Weights	96
5.8	Maxwell Mode - Storage Modulus, G'	99
5.9	Maxwell Mode - Loss Modulus, G''	99
6.1	Micelle Critical Packing Parameter	129

Nomenclature

E^ϕ	Standard Electrode Potential
AIC _c	Corrected Akaike Information Criterion
w _i	Akaike Weights
AB	Acetylene Black
AIC	Akaike Information Criterion
BCD	Battery Capacity Determination
CPE	Constant Phase Element
EIS	Electrochemical Impedance Spectroscopy
KB	Ketjen Black
NaNMST	$\text{NaNi}_{1/2}\text{Mn}_{1/2}\text{Sn}_{1/8}\text{Ti}_{1/8}\text{O}_2$
NLLS	Non-Linear Least Squares
NMC	LiMO_2 , where M is a combination of Nickel Manganese Cobalt in varying quantities
OCV	Open Circuit Voltage
RLCs	Residual Lithium Compounds - such as LiOH and Li_2CO_3
SoC	State of Charge
TM	Transition Metal
TMO	Transition Metal Oxides

Acknowledgements

My PhD journey has been fraught with obstacles, including a global pandemic, the moving of my main supervisor and research group to a different university, years of glovebox problems and failings, and many lab shutdowns. Completing this journey would not have been possible without all those who have helped and supported me along with way.

I would like to begin by thanking my supervisor Prof. Emma Kendrick for giving me the opportunity to embark on this journey and, who, despite moving to a different university, has continued to provide me with her expertise and guidance throughout my PhD. I'd like to extend my gratitude to my supervisor, Prof. Mark Simmons, who has provided a different outlook and expertise. To Dr Simon Leigh, for his help and support at the start of my PhD. I would finally like to thank my supervisor Dr. Claire Dancer, who has stepped in as my primary supervisor at Warwick and has greatly supported me, providing encouragement and reassurance.

I would also like to thank all those part of (and formerly of) the Energy Materials Group, particularly Dr. David Burnett, Dr. Dominika Gastol, Dr. Lin Chen, Dr. Scott Gorman, Dr. Carl Reynolds, and Dr. Tanveerkhan Pathan for their teachings, guidance, assistance, and expertise throughout my PhD. I would like to extend a special thanks to Dr. Brij Kishore for his incredible generosity, assistance, and friendship throughout my PhD journey.

Thank you to all my colleagues in the Energy Innovation Centre, especially to my fellow PhD peers of Keiron Noble-Vickrage, Matthew Lloyd, Craig Jenkins, Evé Wheeler Jones, Mike Jolley, Ben Silvester, and Sanghamitra Moharana. We have gone through so much together, and the support and friendship of you all has made this adventure all the more enjoyable.

Thank you to all my friends, particularly Zac Coe, and Aaron Byrne, for their understanding and encouragement during my PhD work, and the temporary distractions when times have been hard. Thank you to Edzafirah Eddie, for her love and support over the final chapters of my PhD journey.

Finally, a special thanks to my family for all the love and care they have given me throughout my life. To my brother for his love and friendship through my PhD. To my dad, who has helped and advised me through this journey and to my mum, who has supported me massively, especially in the last months of my PhD after my funding had ended, when I have needed it the most.

Declaration

This thesis is submitted to the University of Warwick in support of my application for the degree of Doctor of Philosophy. It has been composed by myself and has not been submitted in any previous application for any degree or to any other high education institute or university.

The work presented (including data generated and data analysis) was carried out by the author except in the cases outlined below:

- i) X-ray Photoemission Spectroscopy (XPS) measurements were carried out by Dr Marc Walker, Department of Physics

Abstract

The demand for energy storage devices is ever-growing, especially due to the electrification of transport and increased use of clean but intermittent energy. Sodium-ion batteries are a prospective sustainable alternative to ubiquitous lithium-ion batteries due to the abundance of sodium, and their cobalt-free cathodes. High nickel O3-type oxides show promising energy densities; however, their incorporation into composite electrode slurries containing NMP and PVDF causes a time dependency in the rheological properties, which leads to inhomogeneous coatings being produced. This work aims to assess and engineer the manufacture of electrode slurries containing these high nickel O3-type oxides by understanding the mechanisms behind the time dependent rheological changes, developing tools capable of studying electrode slurries that exhibit changes to their rheological properties over time, and by formulating electrode slurries that have a stable coating window using additives into the slurry mix.

To understand the reasons behind the time dependant rheological changes in the slurry, first a combination of SEM, EDS, and FTIR was used to investigate how the O3-oxide surface changes with exposure to air, demonstrating formation of NaOH on the active material. From the presence of XPS peaks due to NaF it was established that the subsequent gelation of the slurry was initiated by the NaOH, causing dehydrofluorination and crosslinking of PVDF. The electrode slurry gelation, investigated using the novel rheological technique developed for this research, demonstrated three stages likely limited by the concentration of saturated structures.

Secondly, to monitor and map rheological changes with time, a novel oscillatory rheological characterisation method, utilising multiple rapid frequency sweeps and a subsequent fitting to a 2 mode Maxwell model, was developed for this application. Evolution of this technique proceeded through characterisation trials, initially utilising and incrementally adapting rotational rheological methods and, subsequently, advancing through a range of oscillatory methods.

Finally, to stabilise the rheological changes of the slurry, two sets of additives were investigated. The first set, a collection of organic acids, assumed to inhibit the formation of NaOH, were incorporated into the electrode slurries during mixing. Additives of acetic acid and maleic acid led the electrode slurry stabilisation, hypothesised due to the formation of inverse micelles. The final set of additives, which were sodium salts of the first, aimed to increase the electrochemical performance, while maintaining the stabilisation to the electrode slurries. These were assumed to be sacrificially coated onto the active materials using a facile ball milling technique.

The most successful additive was sodium maleate, due to a suppression of the electrode slurry gelation with simultaneous enhancement of the electrochemical performance. These methods and tools developed for sodium ion could also be relevant for other battery types.

Chapter 1

Introduction

With the ever increasing global energy consumption, [1, 2] there has become an urgent demand for energy storage devices. [2–4] Rechargeable alkali batteries, in particular, lithium ion batteries (LIBs), are commonly used in portable electronic devices, such as phones and laptops, and, more recently, electric vehicles [5, 6]. They have dominated the battery industry since their conception in the early 1970s [7–9]. Whilst these LIBs are ubiquitously recognised as a panacea for energy storage, having high voltage, long cycle life, and a high specific energy, [10, 11] their high cost [12] and the reliance upon critical materials such as graphite, cobalt, and lithium, [13] have caused alternatives to be sought. [14]

Sodium-ion batteries (NIBs) are appealing alternatives to LIBs due to their higher natural abundance over lithium, and potential for lower cost cells. [2, 15, 16] This potential for lower cost cells comes from the lower cost of sodium materials [2] and the reduced restrictions of cell materials. For sodium ion batteries, aluminium can be used as a current collector for both the anode and the cathode. In comparison, lithium has an alloying tendency with aluminium at voltages less than 0.3 V vs Li/Li⁺, meaning that aluminium cannot be used as the anode-side current collector. [17, 18] Instead another metal has to be used, such as copper – resulting in a higher cost and weight of the cells (copper has a density of 8.96 g cm⁻³, whereas aluminium has a density of 2.70 g cm⁻³) [2, 16, 18] - a

study by Vaalma *et al.*, 2018, established that, on average, a reduction of 3.0% of the total battery cost could be achieved by this material exchange. [19]

As an emerging technology, NIBs have a large range of suitable cathode materials available, including transition metal oxides, polyanionic, prussian blue analogues, and organic cathodes. [2, 15, 20–29] A important group among these suitable materials are transition metal oxides (TMOs), [30] with the general formula Na_xMO_2 ($0 < x \leq 1$, and M refers to a combination of transition metals). TMOs can be categorised further, into P2, P3, O2, O3, based on the coordination of sodium and the stacking pattern (investigated further in Chapter 2). Out of these, O3 oxides have the highest sodium content, relating to higher potential capacities, which gives them commercial potential as sodium cathode materials. [30–32]

The sodium cathode material used in this study, $\text{NaNi}_{1/2}\text{Mn}_{1/4}\text{Sn}_{1/8}\text{Ti}_{1/8}\text{O}_2$, is a promising NIB material with a high volumetric energy density and low cost, as reported in a full cell arrangement. [14] However, for this material and many other layered O3 oxide materials, especially those with a high nickel content, significant processing challenges exist. These active materials experience both surface and bulk phase reactions when exposed to air, [33] resulting in the formation of sodium residues such as Na_2CO_3 [34] or NaOH . [35] Furthermore, exposure to air of electrode slurries containing these layered O3 oxide materials, along with n-methyl-2-pyrrolidone (NMP) and poly(vinylidene fluoride) (PVDF) causes them to gel, [36, 37] which renders the slurries uncoatable and therefore unusable. As a result, careful cathode slurry preparation is required.

Therefore, the objective of this work is to improve and investigate the manufacturing method of NIBs, in particular, the manufacture of a span of sodium ion cathode materials that cause a gelling of the electrode slurry, leading to an uncoatable electrode slurry and an unusable batch of material.

1.1 Objective of the PhD

The specific objectives of this research are the:

- Elucidation and examination of the specific gelation mechanism that occurs in sodium ion layered O₃ oxide electrode slurries.
- Development of a non-destructive, non-interfering analysis technique to assess the gelation and measured rheological properties of rechargeable battery electrode slurries.
- Investigation of the prevention or reduction of this gelation mechanism.
- Exploration of the improvement to the electrochemical performance of the active material, while maintaining the stability of electrode slurry.

1.2 Layout of the Thesis

The subsequent layout of this thesis is as follows.

Chapter 2 explores existing literature and begins by introducing and establishing the core concepts in the operation of sodium ion batteries. The examination of existing literature is then split between an investigation of sodium ion cathode materials and the manufacture of sodium ion cathode electrodes. Part 1, the exploration of sodium ion cathode materials, covers the main classes of sodium cathode active materials, the rationale behind the chosen active material, and the problems associated with this material. Part 2, the manufacture of sodium ion cathode electrodes, examines the key electrode properties and structures, the characterisation of electrode slurries, and the processes involved in electrode manufacture.

Detailed descriptions of the experimental procedures and methods, along with the experimental apparatus and equipment, and material specifics can be found in Chapter 3.

Chapter 4 is the first of four results chapters, each focusing on one of the PhD objectives. Here, the elucidation of the specific gelation mechanism that occurs in sodium ion layered O₃ oxide electrode slurries is explored.

Chapter 5 establishes the rheological method used to characterise the structure development of the electrode slurries in this PhD, and explores the development of this analysis method.

The investigation of the first set of additives used to stabilise the electrode slurry gelation can be found in Chapter 6. The inclusion of these additives into the electrodes was via the mixing process of the electrode slurries.

The final results chapter, the investigation of the second set of additives can be found in Chapter 7. These additives were milled with the active material to form sacrificial coatings on the active materials.

Finally, Chapter 8 summarises the work demonstrated in this thesis, presents the key findings, and gives recommendations for future work.

1.3 Impact of the PhD

Two review papers have arisen from the literature exploration of this PhD, with the second containing experimental research on the reactions of PVDF with different bases:

- **Roberts, S. and Kendrick, E. (2018)** The re-emergence of sodium ion batteries: Testing, processing, and manufacturability, *Nanotechnology, Science and Applications*, 11. doi:10.2147/NSA.S146365. [14]
- **Marshall, J. E., Zhenova, A., Roberts, S., Petchey, T., Zhu, P., Dancer, C.E.J., McElroy, C.R., Kendrick, E., Goodship, V. (2021)** On the solubility and stability of polyvinylidene fluoride, *Polymers*, 13(9), pp. 1–31. doi:10.3390/polym13091354. [37]

Furthermore, an experimental paper based on the first and second results chapters (Chapters 4 and 5), has been published in the Journal of Colloids and Interface Science:

- **Roberts, S., Chen, L., Kishore, B., Dancer, C.E.J., Simmons, M.J.H., Kendrick, E. (2022)** Mechanism of gelation in high nickel content cathode slurries for sodium-ion batteries, *Journal of Colloid and Interface Science*, 627, pp. 427-437. doi:10.1016/j.jcis.2022.07.033. [38]

Additional experimental papers based on the results from Chapters 6 and 7 are planned.

Chapter 2

Literature Review

2.1 Introduction

As established in Chapter 1, the literature review for this PhD research has been split into three main sections. Firstly, there is an introduction into the core operating concepts of sodium ion batteries. This section establishes the fundamental theories and concepts involved in the operation of sodium ion batteries, along with the processes involved and the key comparative measures.

Secondly there is the exploration of the sodium ion cathode materials, which investigates the main classes of sodium cathode active materials, the rationale behind the chosen active material, and the problems associated with this material. This section serves as identifying the main research gap in sodium layered O3 literature.

One of the main problems established in the first part of this literature review (Section 2.2) drastically affects the manufacture of sodium layered O3 electrode slurries and electrodes. Therefore the final part of the literature review covers the manufacture of sodium ion cathode electrodes, beginning by establishing the key electrode properties and demonstrating the importance of a rigorous electrode slurry mixing stage. Subsequently, there is an investigation into the formation of electrode slurries, an exploration into specific failure mechanisms in these slurries, and a characterisation of

electrode slurries. Finally, the processes involved in manufacture of electrodes are established, with potential problems originating from the electrode slurry mixing stage being detailed.

2.1.1 Sodium-ion Battery Operating Concepts

Introduction of the core concepts in the operation of sodium ion batteries are useful for understanding the motivation behind research decisions and to establish the range of comparative measures.

2.1.1.1 Nernstian Electrochemical Thermodynamics

One of the downside of NIBs is the operating voltage. NIBs operate at a lower voltage than LIBs, [39] which can be demonstrated by their standard electrode potentials, E^ϕ .

The standard electrode potential is defined as a measure of the potential for a reaction to occur at an electrode when all substances involved are in their standard states (2nd Law of Thermodynamics). It is always relative to a reference electrode - a single electrode potential cannot be measured by itself and can only be measured in comparison to another electrode, such as a reference electrode, commonly a standard hydrogen electrode. [40,41] It is synonymous with Gibbs free energy (ΔG) and can be converted using Equation (1st Law of Thermodynamics) 2.1

$$E^\phi = -\frac{\Delta G}{nF} \quad (2.1)$$

where n is the number of charge carriers transferred and F is the Faraday constant equal to approximately $9.6485 \times 10^4 \text{ Cmol}^{-1}$. This equation can similarly be used to convert the electrode potential from Equation 2.4, E , to Gibbs free energy.

For NIBs the associated half equation for the sodium reference electrode (sometimes referred to as Na/Na⁺) is given by Equation 2.2, and comes to a value of -2.71 V, relative

to the standard hydrogen electrode. [42, 43]



(*aq* indicates a species in solution, and *s* indicates a solid material)

For lithium ion batteries, this reference electrode (Li/Li⁺) has a half equation given by Equation 2.3, and comes to a value of -3.04 V, relative to the standard hydrogen electrode. [42, 43]



As Li/Li⁺ has the more negative standard electrode potential when compared to Na/Na⁺, lithium ion cells will have a high voltage. [39] This can be further expressed by use of the Nernst equation (Equation 2.4).

The Nernst equation (Equation 2.4) [40, 41] is a valuable tool in electrochemistry and provides a link between the chemical equilibrium and electrical potentials.

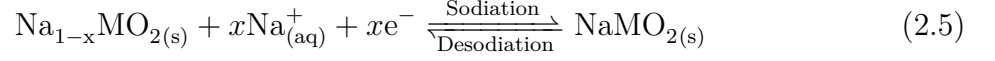
$$E = E^\phi - \frac{RT}{nF} \ln Q \quad (2.4)$$

where R is the universal gas constant equal to approximately $8.3145 \text{ JK}^{-1}\text{mol}^{-1}$, T is the temperature in Kelvin, and Q is referred to as the reaction quotient for the cell reaction [40]. This reaction quotient is a sum of the activities of the products and reactants - an expansion of the Nernst equation including the activities of the products and reactants can be found in Equation 2.8.

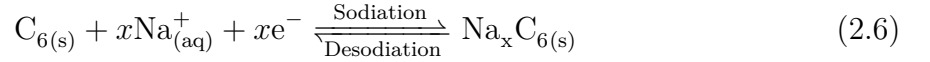
In a full cell configuration, the electrode potential, E^ϕ , of the whole cell is the difference between the standard electrode potentials of the cathode and the anode (providing they have the same reference electrode). Similarly, the electrochemical reaction equation for

the full cell can be formed from combining the half equations of the anode and cathode, such as demonstrated by the example below.

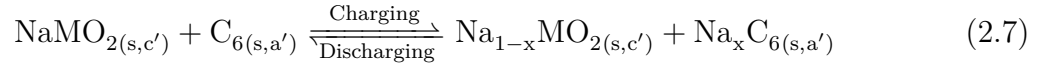
The general half equation for a sodium TMO cathode material is given by Equation 2.5:



where M represents the transition metals. And for a sodium hard carbon anode material, the half equation is given by Equation 2.6:



By combining equations 2.5 and 2.6 the full cell equation can be formed: [44]



Reactants and products have been marked with a' denoting the anode, and c' denoting the cathode.

The equilibrium between the chemical and electrical potentials in this full cell configuration can be described using an expanded version of the Nernst equation, which includes the activities of the reactants and products (Equation 2.8). [45]

$$E = E^\phi - \frac{RT}{nF} \ln \frac{[Na_{1-x}MO_{2(s,c')}][Na_xC_{6(s,a')}]}{[NaMO_{2(s,c')}][C_{6(s,a')}] \quad (2.8)$$

Square brackets, $[\]$, represent the activities of the counterpart. As a note, activities are brought to the power of the stoichiometric coefficients - in the example given, the

stoichiometries are 1. [45] As the cell is charged, there is a transfer of sodium from the cathode to the anode relating to greater values of $[\text{Na}_x\text{C}_{6(\text{s},\text{a}')}]$ and $[\text{Na}_{1-x}\text{MO}_{2(\text{s},\text{c}')}]$. Computing Equation 2.8, will give a negative value of E , and a positive Gibbs free energy (Equation 2.1). Hence the reaction is non-spontaneous and requires the input of energy - charging the cell.

In the reverse process, sodium is transferred from the anode back to the cathode - larger values of $[\text{NaMO}_{2(\text{s},\text{c}')}]$ and $[\text{C}_{6(\text{s},\text{a}')}]$. Therefore, E will be positive and the Gibbs free energy will be negative. Hence the reaction is spontaneous, and the stored energy is released. This transfer of sodium is via the reversible process known as intercalation, which occurs at both the cathode and the anode. An exploration of this mechanism can be found in Section 2.1.1.2, and Figure 2.1. In general, as demonstrated, the thermodynamics in these rechargeable alkali metal cells is dictated by the cell potential, driving the individual half cell reactions occurring at the anode and cathode.

2.1.1.2 Intercalation

Intercalation is one of the fundamental mechanisms that occurs in alkali metal batteries and it is the mechanism that enables the storage of energy.

Intercalation involves an “intercalant” species undergoing a reversible insertion into the structure of a “host”, commonly a crystalline-like lattice [48], without drastically changing the structure of the “host”. During the intercalation process, as demonstrated by Figure 2.1, there is a transfer of ions across the cell, through the electrolyte and separator, while electrons are transferred through any connected devices. Typically, the intercalating ion inserts more readily into the cathode structure than the anode and problems more commonly arise at the anode side. [48–56]

Due to the larger ionic radius of sodium over lithium, intercalation and de-intercalation into sodium ion electrodes show slower kinetics, especially at high current densities. [57] However, ultimately the intercalation chemistry is very similar for sodium and lithium ion batteries, and so similar materials can be used for each. [58]

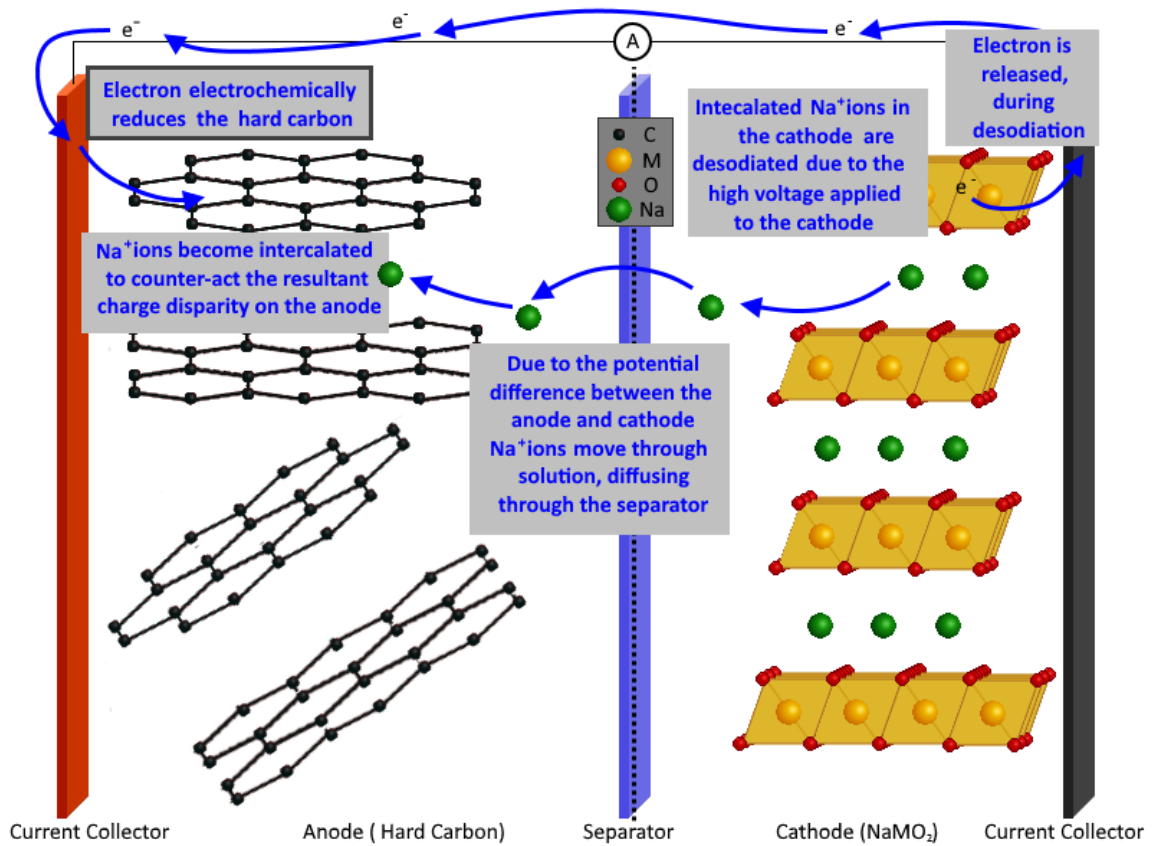


Figure 2.1: General charging process in a Na-ion battery. [Adapted] [46,47].

2.1.1.3 Butler-Volmer Kinetics

A thermodynamic equilibrium is reached when the cell is not under a current load (not charged or discharged). The voltage this cell is at is known as the open circuit voltage (OCV).

Measurement of the OCV is useful for ensuring reproducible results. By measuring the OCV before cycling and allowing the cell to reach a thermodynamic equilibrium (plateau in an OCV vs time plot), cell conditions that would alter the electrochemical behaviour, such as the penetration of the electrolyte into the electrodes, can be ensured. [59]

The overpotential, η , is a difference between the nominal potential, E , and the equilibrium potential, E_{eq} , as shown in Equation 2.9. The equilibrium potential is the OCV ($E_{eq} = \text{OCV}$).

$$\eta = E - E_{\text{eq}} \quad (2.9)$$

This overpotential drives the return of any perturbations from the equilibrium potential, [60] and the resulting current can be described by the Butler-Volmer equation. [61]

$$j = j_0 \left[e^{\frac{-\alpha_c n F \eta}{RT}} - e^{\frac{\alpha_a n F \eta}{RT}} \right] \quad (2.10)$$

where j is the electrode current density, j_0 is the exchange current density, and α_c and α_a are the charge transfer coefficients between the electrode and the electrolyte at the cathode and anode, respectively. [61]

The Butler-Volmer equation can be further used to calculate the current density during the cell charge and discharge. It is evident, from Equation 2.10, that the current density across the electrodes is heavily influenced by the charge transfer coefficients. As the charge transfer resistances change during cell cycling, such as due to the formation of the SEI layer (see Chapter 2), the localised current density, and therefore the kinetics, in the cell will change. Electrode kinetics are influenced by the electric conductivity and the ionic conductivity through the electrode. [62] Therefore, in general, the kinetics in the cell are dictated and influenced by the current applied.

2.1.1.4 Fundamental Battery Properties

One of the main measures for the characterisation and comparison of electrode materials is the specific capacity. Primarily measured in mAh/g, the capacity of an electrode is a measure of the duration of continuously discharge (or charge) at a given current. For example, for an electrode that has a capacity of 2.5 mAh, discharging at 2.5 mA will last 1 hour. [63]

The theoretical specific capacity of an electrode is calculated using Faraday's Law of Electrolysis (Equation 2.11), which states that for 1 mole of reactants, where n moles of electrons are released, the amount of electrical charge, q , can be calculated using Equation 2.11 (n is often referred to as the number of charge carriers). [63]

$$q = nF \quad (2.11)$$

where F is Faraday's constant, equal to 2.6801×10^4 mAh/mol (9.6485×10^4 C mol⁻¹/3.6).

The specific theoretical capacity of the active material, q_{AM} , is usually given by a gravimetric basis and so the specific electrical charge, q , needs to be divided by the molecular weight of the active material (Equation 2.12). [63]

$$q_{AM} = \frac{nF}{M} \quad (2.12)$$

where M is the molecular weight of the active material, in g/mol. For the theoretical capacity of an electrode q_E , as they are made up of an active material, a binder, and a conductive additive (as demonstrated in Chapter 2), Equation 2.13 is required. [63]

$$q_E = q_{AM} \cdot x_{AM} \quad (2.13)$$

where x_{AM} is the fraction of the active material in the electrode.

Measurements of specific energy (also referred to as the energy density of a cell) are similarly useful points of comparison. Calculations of the specific energy of a cell can be made using Equation 2.14:

$$\text{Specific energy} = V_n \cdot q_E \quad (2.14)$$

where V_n is the nominal voltage of the cell. This nominal cell voltage refers to the average voltage the cell is at during cycling, and is affected by the positions of the charge transfer plateaus. Typically values of specific energy are given in Wh/kg. [14]

For practical applications, such as for electric vehicles, where space or weight is limited, cell properties are often compared on a volumetric basis or a gravimetric basis, and so the value calculated using Equation 2.14 may require additional processing, such as by division of the cell density.

2.2 Exploration of Sodium ion Cathode Materials

2.2.1 Sodium Cathode Materials

2.2.1.1 Polyanionic Compounds

Polyanionic compounds refer to the class of materials that contain multiple anion moieties; the negatively charged part of the material is made up of multiple elements. These structures include phosphates, fluorophosphates, pyrophosphates, as well as NASICON structures [64]. For LIBs, an example of a polyanionic compound is the ever popular LFP, or LiFePO_4 . This has an olivine structure with the phosphorous occupying tetrahedral sites and the iron (or in the general olivine form, the transition metal) forming an octahedral environment [65, 66]. It is well known for its excellent cycling stability as some iron ions can occupy the lithium ion gaps to maintain charge neutrality and preserve the structure of the material during intercalation and de-intercalation [67–69].

The NASICON structure – sodium (**Na**) super ionic **con**ductor – refers to a family of materials with the general structure of $\text{Na}_x\text{B}_y(\text{PO}_4)_3$. There are some exceptions such as $\text{Na}_2\text{Fe}_2(\text{SO}_4)_3$ or $\text{Na}_2\text{MnP}_2\text{O}_7$ that are still classed as a NASICON material due to the similarities of the structures. [70] Since the theoretical capacity is proportional to the

number of potential charge carriers and inversely proportional to the molecular weight of the cathode material (as established in Chapter 1), NASICON materials, with their large polyanionic group tend to have low capacities when just one charge carrier is utilised. In many NASICON structures, however the number of sodium ions can be two or three, resulting in a higher capacity. This can complicate the electrochemistry and create several charge transfer plateaus [26,70]. NASICON structures have been used as both cathode [26] and anode materials [26], as well as for an electrolyte material [71,72].

2.2.1.2 Prussian Blue Analogues

Prussian blue (PB) battery materials [28,29,73,74] are based on the paint colour Prussian blue. The typical structure of PB is $\text{Fe}[\text{Fe}(\text{CN})_6]$, where CN is bonded by a triple bond. In this structure, iron can be coordinated by either the carbon or the nitrogen and, as such, results in two separate and reversible redox pairs. PB materials are extremely attractive as battery materials as these two redox pairs fall within the electrochemically stable window of water. For most lithium and sodium materials, the electrochemical region is either too high, leading to the electrochemically breakdown of water, or use of water is unsuitable for the cathode or anode material. [74]

2.2.1.3 Organic Cathodes

Organic materials have potential as cathode materials as they have a flexible molecular structure which allows fast kinetics during the intercalation of sodium ions as the ion insertion causes little special hindrance. However, they tend to have poor conductivity, resulting in poor electrochemical performance and are, overall, poorly understood as an electrode material [70]. Specific examples of organic cathodes include DSR, Disodium Rhodizonate Salt ($\text{C}_6\text{O}_6\text{Na}_2$) [75] or the mixed NASICON and organic (SiO_4) cathode structure of $\text{Na}_{3.1}\text{V}_2(\text{PO}_4)_{2.9}(\text{SiO}_4)_{0.1}$ [76]. Wang *et al.*, 2020, studied varying effects of SiO_4 content in the mixed structure – between $0.05 < x < 0.15$, where $\text{Na}_{3+x}\text{V}_2(\text{PO}_4)_{3-x}(\text{SiO}_4)_x$, and established that substitution of SiO_4 enhanced the

electrochemical performance of the NASICON material. [76]

2.2.1.4 Sodium Transition Metal Oxides

Layered transition metal oxides, or TMOs, refer to a class of cathode material with a general formula of Na_xMO_2 , where x is typically between 0.5 and 1 (however some studies have been carried out on sodium rich transition metal oxides - $x > 1$, [77] and other have been performed on extremely sodium deficient transition metal oxides - $x < 0.5$ [72, 78]. M refers to a mixture of transition metals, chosen for its role in stabilising the structure, improvements to the cycling stability, and improvements to the overall electrochemical performance. Due to the nature of these intercalating materials, M should have an overall oxidation state that will balance the x^+ from the sodium and the 4^- from the oxygen. Additionally, as the sodium is intercalated in and out of material the redox couple of the transition metals should be able to reflect this change [79]. Studies have also been performed on TMOs with an altered anion structure that will allow for an increased or decreased overall oxidation state of the transition metal group, M , i.e. additions of fluorine to the structure. [80] Some examples of these TMO structures can be found in table 2.1. These Na_xMO_2 transition metal oxides have a layered structure that allows for easy intercalation of sodium ions. Layers are made up of edge-sharing octahedral MO_6 with sodium ions in-between these MO_6 sheets. Conventionally, most Na_xMO_2 (for $x \leq 1$) fall into two groups, P2 and O3-type sodium metal oxides. The environment of the sodium ions dictates the naming of the compound; in a sodium deficient structure ($x < 1$) the sodium ions are in a prismatic (P) arrangement with oxygen and where $x = 1$, the sodium ions are in an octahedral (O) arrangement. The number associated with these structures refers to the layer stacking of the oxygen; 2 refers to ABBAABBA... and 3 refers to an ABCABC... arrangement [78, 79, 81, 82]. This can be clearly seen in Figure 2.2.

During cycling, P2 materials tend to be good at maintaining their structure and, hence, do not experience much structural change during intercalation and de-intercalation.

The stability largely depends on the average oxidation state of transition metals, M . For most P2 materials, the oxidation state of M is around 3.3^+ (higher than the 3^+ for O3 structures) and allows for a stable structure across the majority of the cycling range – for a sodium content between 0.3-0.7 [78].

In comparison, the O3 structures are stable where x is 1 (no sodium has been removed from the structure), due to the balance from the oxidation state of the mixture of transition metal oxides (3^+), but when sodium is removed from the structure, $x < 1$, the structure will transform to a P3 phase due to a deficiency of sodium in the structure, which can cause low kinetics [78, 83].

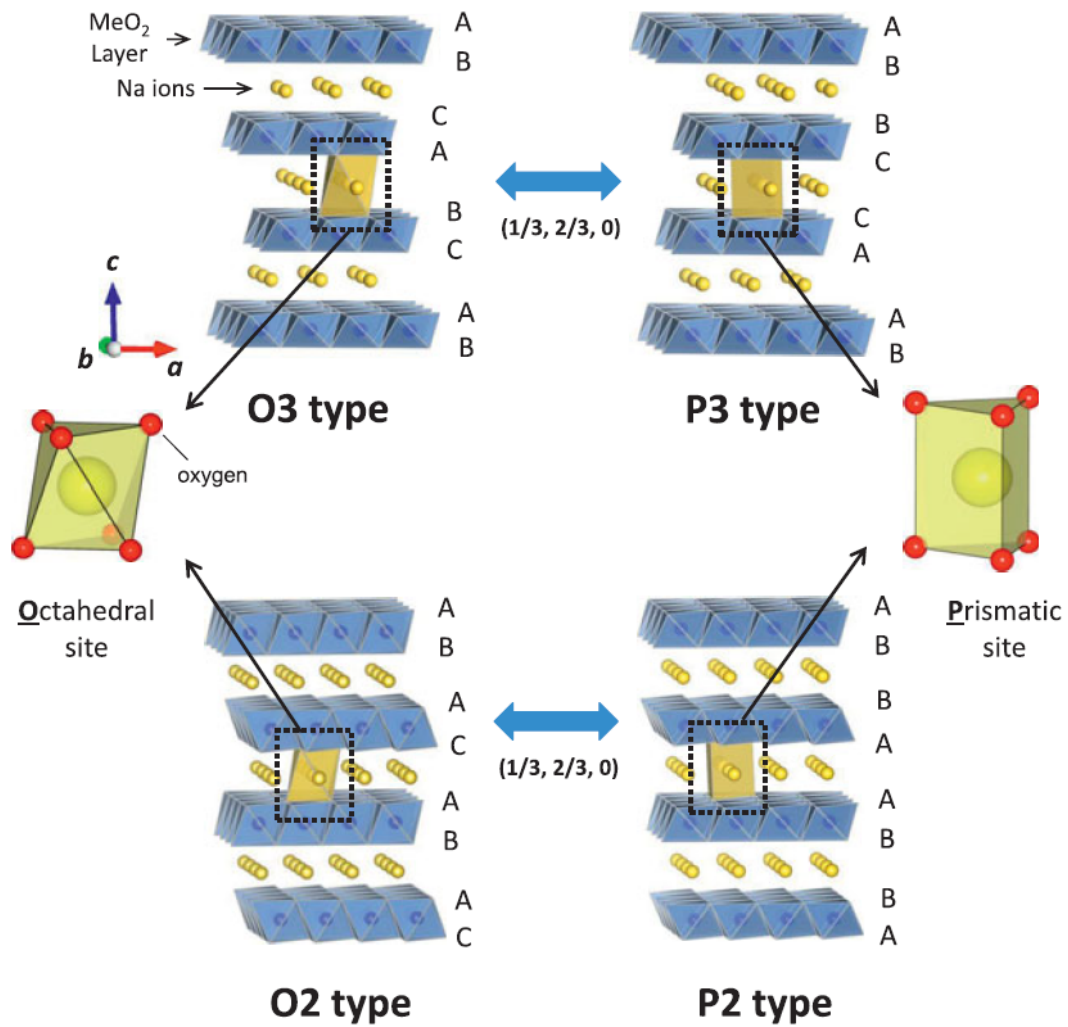


Figure 2.2: Naming System and Structure of Layered TMOs [81].

Table 2.1: Literature Sodium-Ion Cathode Materials and Slurry Compositions.

Author(s) and Year	Active Material Structure	Active Material - wt%, of solids	Conductive Additive(s) - wt%, of solids	Binder(s) [wt%, of solids]	Solvent	Capacity (mAh/g) [Retention]	Cycles
Aragon <i>et al.</i> , 2017 [20]	TMOs - P-Type	$\text{Na}_{2/3}\text{Fe}_{1/3}\text{Mn}_{2/3}\text{O}_2$ - 80	Carbon Black - 10	PVDF - 10	NMP	130 [42.3%]	40
Abouimrane <i>et al.</i> , 2012 [21]		$\text{Na}_{0.75}\text{Mn}_{0.7}\text{Ni}_{0.23}\text{O}_2$ - 80	Super P- 10	PVDF - 10	NMP	101 [90.1%]	50
Martinez. ¹ <i>et al.</i> , 2017 [84]		$\text{Na}_{0.67}[\text{Fe}_{0.5}\text{Mn}_{0.5}]\text{O}_2$ - 75	Carbon Black - 15	PVDF - 10	NMP	50 [98%]	40
Wu <i>et al.</i> , 2016 [85]		$\text{Na}_{0.46}\text{Ni}_{0.22}\text{Co}_{0.11}\text{Mn}_{0.66}\text{O}_2$ - 85	Conductive C - 10	PVDF - 5	NMP	106 [80.3%]	200
Hasa <i>et al.</i> , 2015 [22]		$\text{Na}_{0.6}\text{Ni}_{0.22}\text{Fe}_{0.11}\text{Mn}_{0.66}\text{O}_2$ - 80	Super P - 10	PVDF - 10	NMP	168 [84%]	10
Zhao <i>et al.</i> , 2020 [86]		$\text{Na}_{2/3}\text{Ni}_{1/3}\text{Mn}_{2/3}\text{O}_2$ - 80	Acetylene Black - 10	PVDF - 10	-	83 [97.5%]	10
Zheng <i>et al.</i> , 2017 [10]	TMOs - O-Type	$\text{Na}[\text{Cu}_{1/9}\text{Ni}_{2/9}\text{Fe}_{1/3}\text{Mn}_{1/3}]\text{O}_2$ 70	Super P - 20	PVDF - 10	NMP	260 [19.2%]	100
Wang <i>et al.</i> , 2021 [87]		$\text{NaLi}_{1/3}\text{Mn}_{2/3}\text{O}_2$ - 76	Super P - 20	PTFE - 4	-	190 [94.7%]	40
Yeon <i>et al.</i> , 2020		$\text{Na}[\text{Ni}_{0.5}\text{Mn}_{0.5}]\text{O}_2$ - 85	Carbon Black - 10	PVDF - 5	NMP	147.5 [75.5%]	100
Wang <i>et al.</i> , 2016 [15]		$\text{NaNi}_{0.5}\text{Mn}_{0.3}\text{Ti}_{0.2}\text{O}_2$ - 80	Acetylene Black - 10	PVDF - 10	NMP	138 [95%]	50
Kouthaman <i>et al.</i> , 2020 [23]		$\text{NaFe}_{0.45}\text{Co}_{0.45}\text{Ti}_{0.1}\text{O}_2$ - 80	Super P - 10	PVDF -10	NMP	142 [70.4%]	50
Moez <i>et al.</i> , 2020 [24]		$\text{NaFe}_{0.5}\text{Ni}_{0.5}\text{O}_2$ - 70	Carbon Black - 20	PVDF - 10	-	137 [86%]	50
Zhou <i>et al.</i> , 2020 [88]		$\text{NaMn}_{1/3}\text{Fe}_{1/3}\text{Ni}_{1/3}\text{O}_2$ - 80	Super P - 10	PVDF - 10	NMP	131 [21%]	150
Hwang <i>et al.</i> , 2017 [34]		$\text{Na}[\text{Ni}_{0.6}\text{Co}_{0.2}\text{Mn}_{0.2}]\text{O}_2$ - 85	Super P - 10	PVDF - 5	-	151 [75%]	300
Demirel <i>et al.</i> , 2015 [25]	TMO	$\text{Na}_{0.44}\text{MnO}_2$ - 80	Acetylene Black - 10	PVDF - 10	NMP	105 [50%]	60
Jian <i>et al.</i> , 2012 [26]	NASICON	$\text{Na}_3\text{V}_2(\text{PO}_4)_3$ - 70	Acetylene Black - 20	PVDF - 10	NMP	98.6 [99%]	10
Wang <i>et al.</i> , 2020	MPO ²	$\text{Na}_{3.1}\text{V}_2(\text{PO}_4)_{2.9}(\text{SiO}_4)_{0.1}$ - 70	Acetylene Black - 20	CMC - 10	Water	106.5 [98%]	500
Wang <i>et al.</i> , 2016 [75]	Organic	DSR ³ ($\text{C}_6\text{O}_6\text{Na}_2$) - 70	Super P - 20	CMC - 10	Water	264.7 [55.7%]	100
Tang <i>et al.</i> , 2019 [27]		$\text{Na}_2\text{AQ}26\text{DS}^4$ - 60	Ketjen, CNTs - 20, 10	PAN ⁵ - 10	-	137 [86.8%]	300
Liu <i>et al.</i> , 2017 [28]	PBAs	$\text{Na}_2\text{FeFe}(\text{CN})_6$ - 70	Conductive C - 20	Alginate -10	Water	107 [74 %]	500
Ye <i>et al.</i> , 2016 [29]		$\text{Na}_2\text{FeFe}(\text{CN})_6$ - 70	Super P - 20	PVDF - 10	NMP	103 [70.9 %]	400

¹ - Martinez de Ilarduya² - Mixed Polyanionic and Organic³ - Disodium rhodizonate⁴ - Polyanionic Anthraquinone⁵ - Polyacrylonitrile Copolymer

This class of TMOs can be characterised as having a two dimensional layered structure, however, TMOs can form other two dimensional structures, as well as three dimensional structures. Some structures can be formed that are extremely deficient in sodium or completely sodium free that have an open structure that allows for sodium insertion and removal, and is therefore suitable for intercalation and electrochemical cycling [78]. Research into these materials can be beneficial as it enables sodium electrochemical compounds where synthesis is impossible if they contain sodium.

Table 2.1 shows literature examples of sodium ion cathode materials. Some of the most widely researched cathode materials include TMOs, polyanionic, prussian blue analogues, and organic cathodes.

2.2.2 Motivation for Layered O3 Oxides

As evident in table 2.1, layered O3 oxides have several benefits over some of the other sodium ion cathode materials, especially in terms of the electrochemical performance [58].

Examining the capacities exhibited by the layered O3 oxides across different publications, the lowest is 131 mAh/g for $\text{NaMn}_{1/3}\text{Fe}_{1/3}\text{Ni}_{1/3}\text{O}_2$, and the average of the capacities is higher than that of other materials, giving these materials the potential to rival lithium cathode materials in capacity stored. However, by observation of table 2.1 it can be similarly noted that, while there is a lot of variation in the capacity retention over a number of cycles, typically the O3 oxides have a lower capacity retention than P-type materials due to a poorer cycling stability. Further benefits of layered O3 oxides are their facile synthesis [81] and their ease of doping [82].

Furthermore, sodium layered O3 oxides share many structural similarities to some of the popularly lithium ion cathode materials. These similarities have suggested the notion of a "drop-in" technology, with researchers transferring their extensive knowledge from lithium ion cathodes to sodium ion cathodes. [14] Additionally, as stated in Chapter 1, the sodium cathode material used in this study, $\text{NaNi}_{1/2}\text{Mn}_{1/4}\text{Sn}_{1/8}\text{Ti}_{1/8}\text{O}_2$, in a full cell arrangement, has been compared other promising sodium full cells and has been shown

to have the highest volumetric and gravimetric energy densities. [14]

Ultimately, this makes these sodium layered O3 oxides potential as commercial battery materials but a challenge to work with and research into these materials can be extremely beneficial to the industry.

2.2.3 Current Problems with Layered O3 Oxides

Exploration into the literature of sodium layered O3 oxides has identified two main gaps, regarding research into the issues of these materials. The cycling stability and electrochemical performance of different layered O3 oxides cathode materials for sodium ion batteries has been extensively studied. [10,88]

However, there have been very few studies made on the stability of these materials in air, and even fewer studies have been made on the stabilities of these materials in electrode slurries. For analogous lithium materials, some studies have explored the material storage and stability in air.

Therefore, this section will begin by exploring the current knowledge contributions regarding the stability of these materials in air. It will continue by examining the viability of comparing these sodium layered O3 materials to lithium analogues. Finally, an investigation into the current research regarding stability of analogous lithium materials will be made.

2.2.3.1 Instability in Air

2.2.3.1.1 Sodium Ion Cathode Materials

Layered O3 oxide materials, in general, are unstable in air and degrade upon exposure [14]. However, particularly for sodium layered O3 cathode materials, there has not been much evidence of research into the degradation mechanisms.

Few studies, especially experimental papers, can be found in literature. One review paper by Hwang *et al.*, 2017, demonstrated that one of the major challenges is the formation of NaOH and Na₂CO₃ on the surface of active cathode materials [64].

However, comparisons with other review papers demonstrates inconsistencies regarding the formation of sodium residues, with some sources suggesting that Na_2CO_3 [34, 89] forms and others suggesting NaOH . [35, 90]

Hwang *et al.*, 2017, further states that this is of a particular challenge in (pre)sodiated cathode materials - the increase in sodium content of the cathode materials increases the reactivity of the material [64]. However, as stated, this was written in a review paper and, experimentally, little has been done to demonstrate this.

2.2.3.1.2 Analogies to High Nickel Content Lithium Cathode Materials

In comparison, *some* research into the degradation of high nickel content lithium ion cathode materials has been performed. This is useful for this research into sodium transition metal (TM) layered oxides as there has been demonstrated similarities between high nickel content lithium TM oxides, particularly NMC811 ($\text{LiNi}_{0.8}\text{Mn}_{0.1}\text{Co}_{0.1}\text{O}_2$) and, to some extent NMC 622 ($\text{LiNi}_{0.6}\text{Mn}_{0.2}\text{Co}_{0.2}\text{O}_2$), with sodium layered O3 oxides [14, 91].

Due to structural similarities, it is possible that the O3 layered oxides of lithium and sodium cathode materials can be compared [58, 91, 92], and insights can be transferred to these sodium materials. Structurally, these materials are very similar - octahedrally (O) arranged sodium ions and the layer stacking of these materials (3) denotes that a layered O3 oxide material have an octahedral coordinated sodium with 3 stacking layers, which is the same structure as present in lithium 811 NMC materials [78, 79, 81, 82].

Furthermore, studies have been made directly comparing the structures and chemical similarities between sodium and lithium oxides. A review by Nayak *et al.*, 2018, directly compared lithium and sodium ion battery materials [91]. A primary point of comparison of layered oxides used was LiCoO_2 and NaCoO_2 , which both have similar structures. However, there are some differences between the materials, namely, the different redox potentials and cycling evolutions. For the lithium cathodes the material mostly maintains an O3 structure during cycling, whereas the sodium cathodes transition from an O3

structure to a P3 structure [91].

A similar comparison was made by De La Llave *et al.*, 2016, wherein the materials under comparison were $\text{LiMn}_{0.5}\text{Ni}_{0.5}\text{O}_2$ and $\text{NaMn}_{0.5}\text{Ni}_{0.5}\text{O}_2$. De La Llave *et al.*, 2016, concluded that the sodium material undergoes a transition during cycling from O3 to P3 (and back), whereas the lithium material does not. The conclusion of the authors was that the larger size of the sodium ion puts strain on the host material [92]. De La Llave *et al.*, 2016, additionally suggested that these materials shared similar surface phenomena, although this statement was not really expanded on [92].

While the shared chemical properties of lithium and sodium themselves suggests a comparison between these two [91], these differences demonstrate that care should be taken when comparing material properties.

2.2.3.1.3 Insights from Analogous Lithium Cathode Materials

As stated, due to the material similarities between sodium TM layered oxides and high nickel content lithium TM oxides, it is possible to translate some of the conclusions drawn from studies on similar lithium based materials.

A study by Jung *et al.*, 2018, examined the effect of ambient storage on lithium NMC 811. For ambient storage of 1 year the active material was found to develop a new surface composed of mostly a nickel carbonate and lesser quantities of nickel hydroxide, to a thickness of 10 nm. The quantities of these surface species was calculated using gas chromatography to quantify the amount of carbon dioxide released when the ambiently stored lithium NMC 811 was reacted with hydrochloric acid. While these changes were detected on lithium NMC 811, they did not occur when lithium NMC 111 was exposed to similar conditions [93]. Notably, the drastic increase in nickel between the NMC 811 and the NMC 111, causes the surface reactivity to increase, and enables surface reactions between air and the NMC 811 to occur. At higher storage temperatures these surface reactions are able to occur for NMC materials with less nickel - NMC 622 ($\text{LiNi}_{0.6}\text{Mn}_{0.2}\text{Co}_{0.2}\text{O}_2$) [94], and NMC 532 ($\text{LiNi}_{0.5}\text{Mn}_{0.3}\text{Co}_{0.2}\text{O}_2$) [95] - and similar

surface reactions have been documented for higher temperature storage of LiNiO_2 . In literature, these reacted compounds, that form on the surface on these materials have been collectively referred to as "Residual Lithium Compounds", or RLCs (although most of the literature RLCs are lithium hydroxides and lithium carbonates, rather than nickel based compounds).

The reactions of H_2O and CO_2 were similarly investigated by Su *et al.*, 2020. In the study by Su *et al.*, 2020, lithium NMC 811 was stored in a controlled airflow reactor for 24 hours, with varying gases passed over it, including dry CO_2 , wet CO_2 , and wet inert gas. It was found that for the material stored in wet CO_2 the quantities of RLCs increased greatly, whereas for the materials stored in the other two environments the quantities of RLCs increased "finitely" [96]. The conclusion by Su *et al.*, 2020, was that both H_2O and CO_2 are crucial to the formation of RLCs. However, purely based on the results presented it seems likely that this is not the only conclusion that can be reached; Su *et al.*, 2020, did not examine the quantities of RLCs at different times and the creation of RLCs in these different environments could be rate limited [96].

These results are contradicted by the study performed by Zou *et al.*, 2020. In their investigation, lithium NMC 811 was tested with air, N_2 , O_2 , CO_2 , and water vapour. It was found that water vapour readily reacts with the surface of the NMC, forming LiOH . Whereas exposure of N_2 , O_2 , and CO_2 do not react with the surface of the NMC. However, air exposure was found to form LiOH and Li_2CO_3 upon the surface (all after 30 minutes). Furthermore, after water vapour was exposed to the surface, pre-forming the LiOH , this could react with CO_2 in as little as 10 minutes, forming Li_2CO_3 [97]. This is a clear contradiction to the findings of Su *et al.*, 2020; Zou *et al.*, 2020, found that NMC 811 was able could react with water to form LiOH , whereas Su *et al.*, 2020, found the opposite [96, 97]. Another interesting finding by Zou *et al.*, 2020, was the formation route of LiOH . By use of in situ ETEM, it was found that LiOH forms via a two-step reaction. Firstly the lithium ions diffuse to the surface of the material, which is followed by a surface reaction with H_2O that forms the LiOH [97].

Further investigation of these RLCs have been performed by Busa *et al.*, 2020 [98]. In their research, Busa *et al.*, 2020, discovered similar findings to these previous studies [93, 96, 97]; Li_2CO_3 and LiOH could build up on the surface on lithium NMC 811 upon exposure to ambient conditions. Additionally, electrochemical investigation of the as synthesised and the exposed material was compared, showing a significantly poorer cycling performed for the exposed material. Furthermore, differential capacity plots highlighted a large decline in the performance, as well as a shift towards lower voltages for the first large capacity transfer of the material [98]. As comparison, long-term general cycling of NMC 811 has been characterised in detail, such as by Li *et al.*, 2020 [99].

Ultimately, while research on analogous lithium cathodes, has demonstrated the formation of LiOH and Li_2CO_3 , contradictions lie between these studies and the exact surface reactions are difficult to define. Therefore, experimental research into this literature gap of air sensitivity of sodium layered oxides will likely be beneficial to analogous lithium cathodes.

2.2.3.2 Gelation of the Electrode Slurry

These layered O3 instabilities in ambient conditions are not limited to the material phase and can affect the electrode slurries and electrode formation. During the manufacture of these sodium ion layered O3 cathode materials (and high nickel content lithium metal oxides), electrode slurries containing NMP and PVDF can gel, a phenomenon that has been historically poorly researched. The physical effect of this gelation can be clearly seen in Figure 2.3. This electrode slurry gelation has been observed at a lab scale and for industrial scale mixing and coating. It is this gelation mechanism and reactions of the electrode slurries in ambient conditions that has very little documented research, especially for layered O3 sodium ion cathode materials. No experimental research was found in this direct area, however, a few mechanisms have been suggested in review papers and patents.

In a patent by Paulsen *et al.*, 2009, a gelation mechanism was suggested wherein the

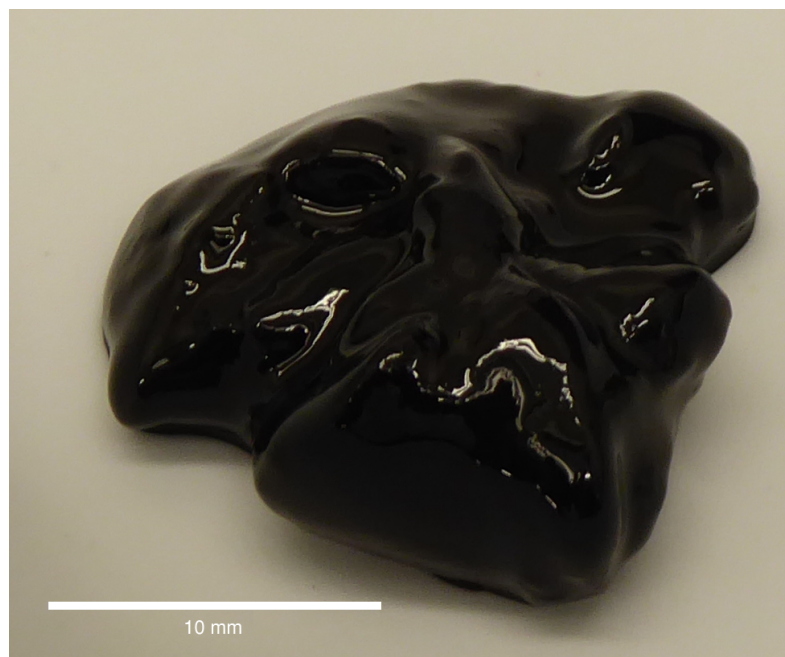


Figure 2.3: Photograph of Gelled Electrode Slurry (taken by author).

deterioration of the electrode slurries was said to be caused by the polymerisation of the NMP-PVDF slurry [100]. However, there was no experimental evidence to support this and there was no indication of the mechanism of this suggested polymerisation. Furthermore, it seems unlikely that PVDF, or any other vinyl fluoride polymers, (or any polymers for that matter) are able to re-polymerise with NMP. A co-polymerisation reaction is more likely, however, a review of PVDF literature suggests that this is not possible, as in their existing forms, neither PVDF or NMP has any C=C double bonds for polymerisation or co-polymerisation to occur from [100].

An alternate degradation and gelation mechanism was suggested by a review from Teichert *et al.*, 2020, but very little experimental research has been done to investigate or confirm this mechanism, and there have not been any such studies performed on sodium cathode materials. This suggested mechanism involved the dehydrofluorination of PVDF followed by a subsequent cross-linking of neighbouring chains, causing the gelation of the electrode slurry. [101]

A review by Seong *et al.*, 2020, further highlighted the lack of research in this area and proposed the same gelation mechanism as Teichert *et al.*, 2020. [101,102] The review

by Seong *et al.*, 2020, suggested two alternative mechanisms that have been researched in other industries. The first mechanism for this gelation is that of a colloidal glass or gel based on the high solids content of conductive carbon and active material in the electrode slurries [102] (see Section 2.3.2.2.1). The other degradation route that was suggested by Seong *et al.*, 2020, was the depolymerisation of PVDF, which was similarly investigated by Loginova *et al.*, 1983 (albeit the aim of the research by Loginova *et al.*, 1983, was not for batteries [103]). In the suggested depolymerisation of PVDF, the transformed PVDF loses its normative adhesive properties and instead is able to adhere to active material particles, enabling the sedimentation of these heavier particles and collapsing the colloidal suspension. [102, 103]

2.2.4 Summary and Conclusions

Firstly, as clearly demonstrated, there is a lack of conclusive evidence and research into the specific gelation mechanism of high nickel content layered lithium ion cathode materials, and even less research into the mechanism of the similar sodium ion layered O₃ oxides. Research into this mechanism would be highly beneficial to the industry (as suggested by Seong *et al.*, 2020 [102]), not only for sodium ion layered O₃ oxides but, due to the structural and material similarities, this research would be beneficial to lithium ion layered O₃ oxides.

Secondly, as a direct result of this first point, there have been no investigations into the direct countering of this gelation mechanism; whether it can be prevented and stopped, and what would be the effect of this stabilisation on the electrochemical performance on these materials.

2.3 Manufacture of Sodium Ion Cathode Electrodes

2.3.1 Role of the Electrode Structure

The structure of an electrode plays a vital role in its electrochemical performance. [104] Micro and nanostructures within the electrodes can influence the kinetics and electrochemical properties within a cell. [105, 106] An ideal electrode needs to be homogeneous, comprised of an even and well distributed pore network, and be interlinked by a conductive carbon network. An ideal structure, comprising of these key properties can be found detailed in Figure 2.4.

Transport across an electrode can be characterised between electrical transport and ionic transport, with these properties and resistances ultimately controlling the kinetics in the cell. [62, 107, 108] Current flows through the path of least-resistance, which may mean transitions are made between the ionic and electrical transport modes. [62]

As introduced by Equation 2.10, the charge transport coefficients, determined by localised resistances, dictate the current densities through an electrode. In a poor electrode structure, channels of high localised current densities can form due to high relative differences in resistances, leading to unfavourable defects, such as dendrite growth. These properties significantly impact the battery performance. [108]

2.3.1.1 Electrical Transport

Electrical transport throughout an electrode is characterised by the conductivity of an electrode. It dictates the path and ease of electron transport during the intercalation process. [62] Sufficient electrical transport, due to good electrical pathways, have been demonstrated to enhance the reaction rate at an active material surface. [109] A conductive additive is required to create an electrically conductive network across the electrodes, [104, 110] and decrease the internal resistance of electrodes. This is required to aid in the transport of electrons across the electrode, in particular for cathode systems, which

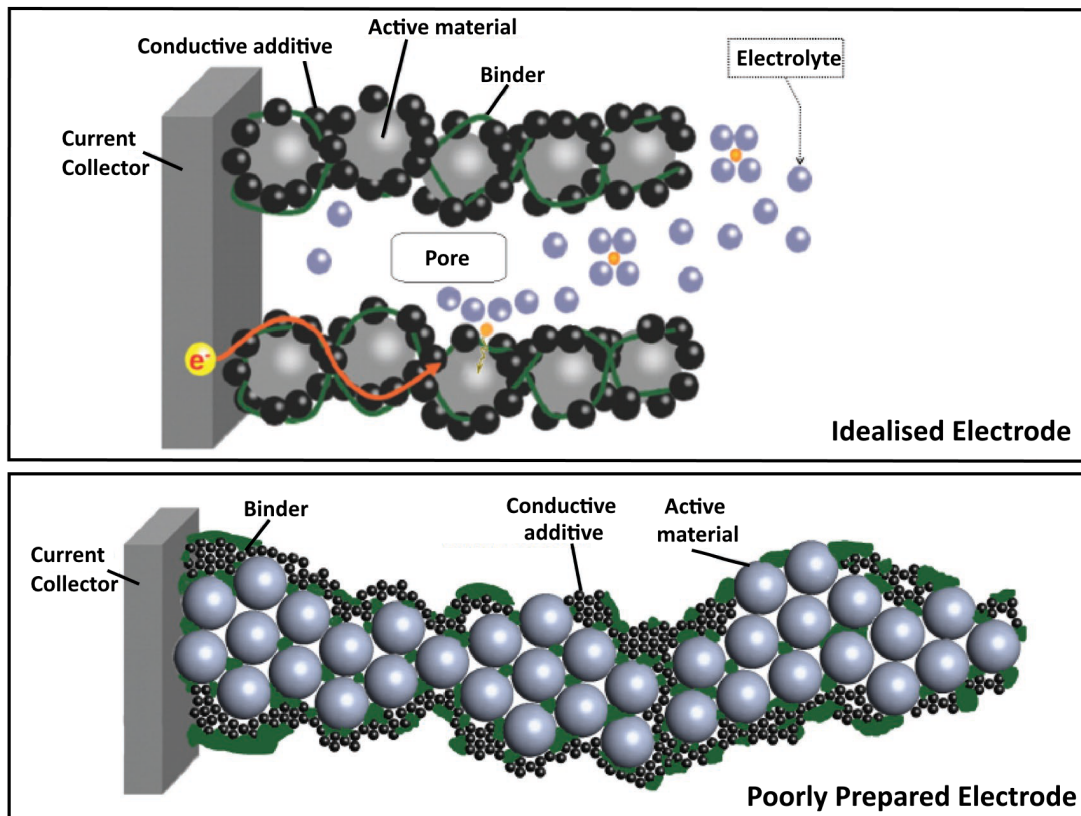


Figure 2.4: Comparison between an idealised electrode structure and a poorly prepared electrode - Adapted from Kraytsberg *et al.*, 2016 [104].

tend not to be as electrically conductive. [109] The physical interconnections between the active material and conductive additive is important. Low binder amounts can decrease the electrode conductivity due to reduced physical contact with the active material and conductive nanoparticles. [111]

2.3.1.2 Ionic Transport

Ionic transport primary dictates the diffusion of ions in the liquid phase, the electrolyte, distributed throughout the pores of the electrode. The classification of the ion diffusion within a cell is important for cell comparisons, and for alterations and improvements with one such drive being to shorten the diffusion path of the intercalating ion, demonstrated by favourable kinetics. [112–115]

Diffusion can be characterised by the porosity, pore size, and tortuosity of the electrode with additional classifications obtained from an estimation of the active surface area of

the electrode. [116] These parameters primarily influence the transport of ions across an electrode. [108]

Computation studies calculating the tortuosity and porosity of an electrode from cross-sectional SEM images have demonstrated to be able to predict the ion transport over an electrode, further highlighting the relationship between the electrode structure and its transport properties. [117]

2.3.1.3 SEI/CEI Formation

The solid-electrolyte interface, SEI layer (sometimes referred to as the cathode-electrolyte interface, CEI, specifically for cathodes) is formed in all alkali metal cells and occurs when a cell is charged and discharged, hence, related to the first cycle capacity losses of a cell. [8, 12] However, further SEI formation will, undoubtedly occur at other points in the life of a cell and, indeed, across a cell's lifetime. [118–120] The SEI can have both positive and negative effects on cells and so its formation should be carefully considered. An ideal SEI, as proposed by Peled, should be: insoluble and homogeneous; a good electronic insulator and is able to protect the electrode while still allowing cation transport [12].

Formation of an SEI layer changes the localised charge transfer coefficients, as introduced in Equation 2.10. While the formation of an SEI layer can improve the charge transfer coefficients, [121] it is important for the SEI to be a homogeneous layer. [9] Otherwise, spots of high localised current densities can form, leading to unfavourable defects, such as dendrite growth. Formation of a homogeneous SEI layer can be promoted due to a homogeneous electrode surface, [122, 123] influenced by the coating, drying, and calendaring processes.

It has been demonstrated that the SEI layer is made up of many compounds, and is dependent on the environment within the battery, such as electrolyte composition, and electrode compositions. [124] The SEI is formed by precipitation via the decomposition of the electrolyte solvents, or the decomposition of co-intercalated ions [125]. For example, when using a conventional electrolyte, containing carbonate solvents and PF_6 based salts,

the SEI layer may contain alkyl-carbonates, polymeric carbonates, and fluorides. [125] In cell cycling the intercalating ions can irreversibly react, forming products that will add to the SEI layer [126]. In many cases, where organic compounds are used in the electrolyte, which is standard in industry, the SEI will contain solid organics [55, 114, 120].

It is thought that the SEI can be responsible for: electrode passivation [55, 114, 125, 126], reducing of cell capacity [114], increasing in the charge-discharge polarisation [114], increasing the conductivity of an electrode [114], preventing degradation and buffering the decomposition of the electrode through side reactions [55, 126].

Careful consideration of these properties and property changes is useful when analysing electrochemical performances of cells, and for the development of optimised electrodes.

2.3.1.4 Electrode Adhesion

The adhesion of an electrode can be similarly effected by its structure. Poor distribution of components in an electrode, such as less binder near the current collector, can related to reduced electrode adhesion. [127] Poorly optimised, and overly high, drying rates are known to have a impact on the adhesion of electrodes due to the affect on the binder distribution. [128] Adhesion strength has been shown to be promoted by roughing or etching the current collector surface during coating. [129]

Ultimately, the coating adhesion strength is an important property in electrodes as it can influence the electrochemical handling during cell construction and affect the life of an electrode during cycling. [130]

2.3.2 Electrode Manufacture

Electrodes are formed through a multistep process that begins with manufacture of an electrode slurry (or electrode ink). Figure 2.5 demonstrates the typical processing route of an alkali metal ion battery: electrode slurries are mixed (stages 1, 2, 3), the slurry is coated upon a current collector (4, with some possible methods of coating demonstrated), coatings are dried (5), calendered (6), and vacuum dried ensuring

maximum solvent removal (7), the electrodes are made into cells (8), cells undergo a formation and conditioning stage (9), and the completed cells are formed (10).

Constructing the electrodes in this manner means that their thickness can be carefully controlled so that particular specific capacities can be realised for high power or energy applications.

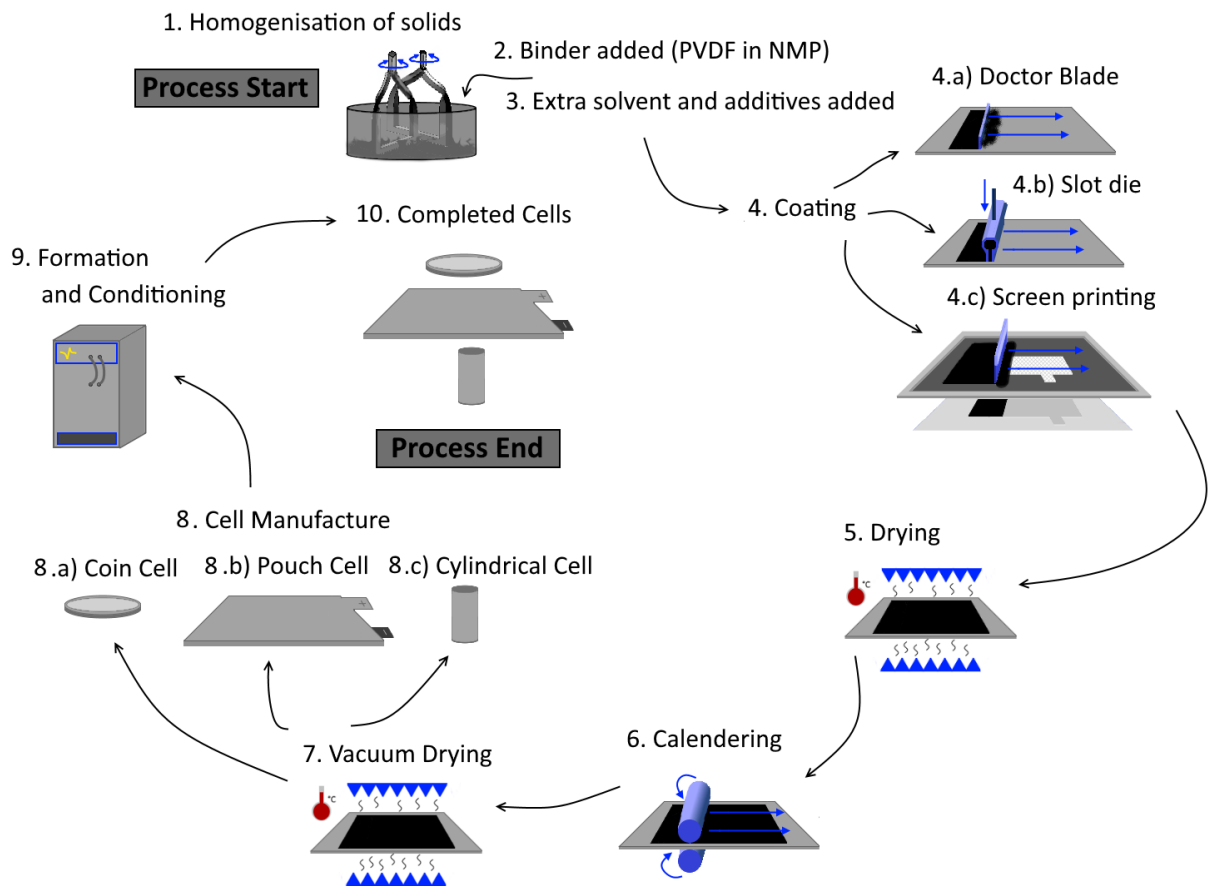


Figure 2.5: Manufacture of Electrode Slurries, Electrodes, and Cells.

2.3.2.1 Electrode Slurry Formation

Electrode slurries are comprised of an active material, a conductive additive, a binder, and a solvent (as demonstrated in Table 2.1).

These electrode slurries are, in essence, colloidal suspensions; particles of active

material and conductive additives are suspended in the continuous phase of a binder (a polymer) dissolved in a solvent. Rheologically, these electrode slurries behave as viscoelastic materials, with the colloidal suspension producing both visco, liquid like, and elastic, solid liquid, behaviours.

Therefore, to develop a greater understanding of the electrode manufacturing process, it is important to consider the processes mechanisms and, hence, the physical structure of the complex fluids used in slurry cast manufacturing.

2.3.2.1.1 Continuous Phase

The continuous phase, in the case of electrode slurries, is the solvated polymer. This binder material makes up 5 - 10 wt% of the electrode slurry solids (as shown in Table 2.1) These binder materials tend to be high molecular weight polymers, which can make their dissolution difficult.

Polyvinylidene fluoride (PVDF), one of the most prevalent binders for sodium ion cathodes (as evident in Table 2.1), is particularly difficult to dissolve due to its polarity. In battery applications, the main solvent used to dissolve it is N-methyl-2-pyrrolidone (NMP). [36]

The difficulties regarding the dissolution of high molecular weight polymers has been explored by Billmeyer *et al.*, 1984. [131] For most compounds, including low molecular weight polymers, solvation happens very quickly, dissolution occurs and the solution is formed. However, for polymers, especially the high molecular weight polymers, where chains are tightly coiled and entangled due to the intra and intermolecular forces, an initial step of loosening and unravelling is first required. This step, as noted by Billmeyer, 1984, is known as the swelling of the polymer; chains and segments of the polymer turn from being “aggregated”, in their tightly coiled and entangled states, to “solvated”, where they are loosened and less entangled, however the chains and segments are still group. The second step is the dissolution of the polymer chains, where solvated molecules are dispersed and the solution is formed. [131]

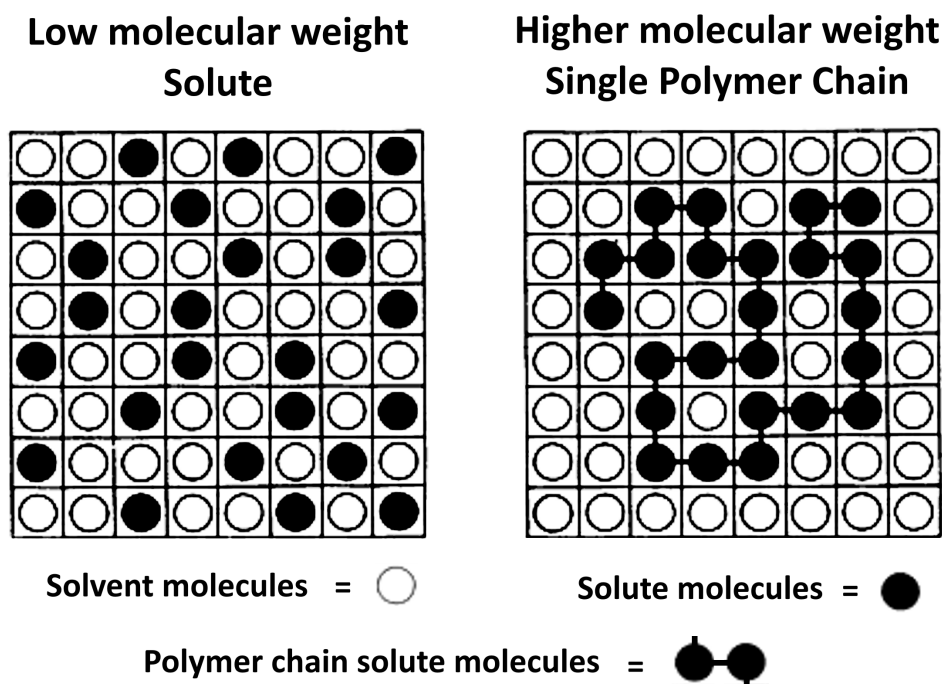


Figure 2.6: Flory Huggins Model - 2D Representation (Adapted from Adeyinka *et al.*, 2014 [132]).

This process of swelling and dissolution is heavily dependent on the strengths of polymer-polymer interactions and the polymer-solvent interactions. The comparisons of these strengths will also dictate whether the polymer will actually dissolve. If the polymer-solvent interaction is stronger, solvent molecules are able to adsorb onto polymer chains, loosening and detangling the chains. These solvent molecules help to force chains apart and swell the coiled polymers. Mixing has no effect on this swelling process as it is entirely dictated by the polymer-solvent interactions. Once the entire polymer chain is solvated and the swelling state has completed, the fully solvated polymer with solvent molecule within the coil forms an ellipsoid shape, known as the hydrodynamic volume and, the dissolution of the polymers can begin [131].

From a thermodynamics point of view, the determination of a polymer's solubility can be realised by the Gibbs free energy (ΔG) and the solubility parameters.

The Gibbs free energy can be calculated using Equation 2.15:

$$\Delta G = \Delta H - T\Delta S \quad (2.15)$$

where ΔH is the change in the enthalpy of mixing, T is the overall absolute temperature of the solvent and solute, and ΔS is the change in entropy of mixing. Dissolution will only occur if ΔG is negative. In general, as entropy tends to increase for particles when they are in solution than when they are in a solid state, due to the more chaotic arrangement, ΔS will likely be positive. Similarly, by the nature of absolute temperature, T will be positive and so the overall term will be positive. However, for polymers in solution, ΔS is significantly smaller than for individual particles in solution. A simplified model was developed separately by Flory and Huggins [133, 134] that demonstrated the differences between ΔS for particles and for polymers, and encompasses the Boltzmann equation:

$$\Delta S = k \ln W \quad (2.16)$$

where W is the number of possible arrangements in the lattice and k is the Boltzmann constant.

Assuming there is no overlap of molecules on any particular site, there is far fewer possible arrangements for the polymer in the lattice, rather than separate particles – for the same number of particles as “segments”, as can be seen from Figure 2.6. Relatively speaking, this means ΔS will be small.

Therefore, from Equation 2.15, for ΔG to be negative, ΔH must be smaller than $T\Delta S$. Small values of ΔH arise from specific interactions, such as hydrogen bonding, between the polymer and solvent molecules. Larger values of ΔH describe situations where there are no such interactions between the polymer and solvent and, as such, can be determined by the Hildebrand Equation (Equation 2.17): [135]

$$\Delta H = \phi_s \phi_p (\delta_s - \delta_p)^2 \quad (2.17)$$

where ϕ_s and ϕ_p are the volume fractions of the solvent and the polymer, and δ_s and δ_p are known as the solubility parameters for the solvent and polymer [136,137].

Data tables, specifically for Hansen Solubility Parameters, split these solubility parameters for the solvent or the polymer (δ_s or δ_p) into a Dispersion parameter (δ_D), a Polar parameter (δ_P), and a Hydrogen Bonding parameter (δ_H). [135]

Based on Equation 2.17, the small values of ΔH will result from similar values of polymer and solvent solubility parameter, or higher value for the polymer than the solvent.

Table 2.2 shows the Hansen solubility parameters for NMP, water, and PVDF. It is evident that for the dispersion solubility parameter, both, NMP and water have similar values to PVDF. For the polar solubility parameter, while the values of NMP and PVDF are similar, water has a much higher value. Finally, for hydrogen bonding solubility parameter, it is clear that PVDF have similar values, but water has a much greater value.

Between these Hansen solubility parameters, presented in Table 2.2, and Equation 2.17, NMP is far more suitable as a solvent for PVDF than water, and will more likely result in a negative Gibbs free energy.

Furthermore, it is evident that any changes to the chemical structure of PVDF or NMP, will change their solubility parameters, and affect the dissolution.

Table 2.2: Hansen Solubility Parameters.

	Dispersion, δ_D	Polar, δ_P	Hydrogen Bonding, δ_H	Reference
NMP	18.0	12.3	7.2	[37,135]
Water ^a	15.5 - 18.1 ^b	12.9 - 20.4	15.5 - 42.3	[135]
PVDF	17.0	12.1	10.2	[135]

^aValues of solubility parameters for water tend not be particularly accurate as its behaviour often depends on its local environment. [135]

^bWater has a range of Hansen Solubility Parameters between derivations based on the vaporisation of water and those calculated using SPHERE software. [135]

Ultimately, the dissolution of high molecular weight polymers (which includes most binder materials in electrode slurries) is a slow process and requires specific solvents to dissolve them. Additionally, for the manufacture of electrode slurries, the solids content of the binder solution is maximised, thereby allowing for more rheological control during the mixing stage - additional solvent can be easily added to reduce the viscosity. This further increases the time required for binder dissolution. Often, the PVDF binder is pre-dissolved in the NMP as this process takes significantly more time than the electrode slurry mixing.

2.3.2.1.2 Discrete Phase

Colloidal suspensions, as stated, consist of a continuous and a discrete phase. In the case of an electrode slurries, the discrete phase covers the active material and any conductive additives. It encompasses any particles that do not dissolve into the solution, and that are instead suspended in the solution. On a gravimetric basis, the discrete phase comprises of 40 - 50 wt% [125] of an electrode slurry, which corresponds to a volumetric basis of approximately 20 - 30 vol%. [138] The active material makes up the bulk of the solids in an electrode slurry, with quantities typically ranging from 70 - 90 wt% of the total solids (as evident in Table 2.1). Often for cathode materials, a conductive additive is the next greatest constituent, between 5 - 20 wt% of the total solids. Carbon black is the commonly chosen as the conductive additive for electrode slurries, with several different varieties available:

- Super P and C carbon blacks [13, 139–144]
- Ketjen black (KB) [109, 140, 145–147]
- Acetylene black (AB) [3, 109, 145, 147–150]

However, the differences in the electrochemical performance due to the choice of carbon black seem to be marginal. [109] A study by Takamura *et al.*, 2000, investigated the effects of varying amounts KB and AB on the charge and discharge efficiencies of electrodes

manufactured in the same manner. It was established that the quantity of conductive additive plays a significantly larger part in the electrochemical performance than the specific additive. [109]

Most conductive additives tend to have a much lower bulk density than particle density. [151] Due to these high surface areas and electrostatic forces, many conductive additives easily flocculate [152] and require additional energy to break up.

The mixing of the discrete phase with the continuous phase, forming the electrode slurries, has been researched, with different mixing sequences [127, 153, 154], mixing parameters [130, 153–155] or mixers tested. [127, 155, 156]

As illustrated by Sawhney *et al.*, 2022, specific sequences and parameters need to be optimised for a new material, especially for new sodium ion battery materials. [155] Similarly, as demonstrated in Table 2.1, there is a large range of formulation options for these electrode slurries that need to be optimised on a materials basis.

While the different options for electrode slurry formulations and mixing parameters have been widely investigated, there has been little investigation into the different failure mechanisms of these electrode slurries. Therefore, failure mechanisms of colloidal systems has been investigated.

2.3.2.2 Failure Mechanisms and Jamming Effects

These failure mechanisms, and poor mixing of electrode slurries, will effect the properties of the electrodes. Some failure mechanisms of colloidal suspensions can be referred to as jamming effects, whereby the inability for the suspension to flow and behave conventionally can be due to a jamming of one of the phases.

2.3.2.2.1 Colloidal Glasses

In colloids, the “glassy” state is a system wherein the spatial arrangement of molecules and particles is frozen in structural disorder. There are a few routes by which this can occur, however, they mostly involve the discrete part of the suspension, and are different

to the concept of glass transition in polymers.

2.3.2.2.2 Glass Transition due to Crowding

The glass transition due to crowding follows Bernal's hard-sphere glass transition model from the 1960s. The concept is that the flow of the polymeric solution is frozen due to the crowding of hard molecules, such that any movement of particles is blocked by adjacent particles caging it in place. Each adjacent particle is also caged by its neighbours and hence movement is prevented.

The theory modelling states that this glass transition purely depends on the volume fraction, and due to assuming perfect hard spheres of particles, the equation for calculating the equilibrium phase behaviour is fairly simple.

$$\phi = \frac{4}{3}\pi R^3(N/V) \quad (2.18)$$

where R is the radius of the hard spheres, N is the number of spheres, and V is the volume. From experimental calculations of Pusey and van Meegen, in the late 1980s [157, 158], the system is said to be a fluid up to values of ϕ , the equilibrium phase behaviour = 0.494. This is the lowest free-energy state where particles are still able to freely move. Between $\phi = 0.494$ and $\phi = 0.545$, both fluid and crystal exist. Between $\phi = 0.545$ and $\phi = 0.74$, the system is said to be crystalline and, finally, above $\phi = 0.74$ the colloidal system defaults to close packing.

2.3.2.2.3 Glass Transition due to Depletion

The concept of this glass transition is due to the creation of depletion zones around particles. These depletion zones can be generated via a few methods. [159] It is extremely common in colloidal systems for particles to have an interaction range that is less than their diameter, with low values of attraction, so typically, any energy input from mixing or the Brownian movement of the particles, in short timescales, will likely have a higher

strength that the particle-particle attraction and prevent agglomerations. However, in a colloidal system with a non-adsorbing polymer (such as in the case in the electrode slurries), collisions between particles and polymers, perhaps caused by Brownian motion, as well as the interactions between them, can create an area devoid of polymers around the particles, a depletion zone.

These depletion zones cause particles to pull neighbouring particles towards them by use of a net osmotic force and, providing this osmotic force is stronger than particle-polymer interactions, the system will act as a glass, and the system will jam [159].

2.3.2.2.4 Glass Transition due to Particle-Particle Interactions

As mentioned before, while it is ubiquitous in colloids for the particle-particle interaction range to be less than the diameter of the particles, it is not uncommon for larger range interactions, as well as higher strength interactions. Van der Waals forces between particles, based on the distance, can affect whether particles are attracted or repulsed from one another.

Higher strength interactions involve the electrostatic interactions between particles. Particles in the dispersed phase can carry electric charges on their surfaces, which can be attractive or repulsive, and will cause electric double layers to surround these particles. In electrode slurries, especially the cathode slurries, active materials are commonly negatively charged enabling the conductive additives, as well as positive ions, to act as counter-ions. Immediate contact with the particle forms the Stern layer, which is composed of oppositely charged ions, close to the surface of these particles. Past the Stern layer is the diffuse layer that contains a ‘cloud’ of charged particles and ions, with the part of the ‘cloud’ that moves with the particle known as the slipping plane. At each of these layers, different potentials exist: the surface potential, the stern potential, and the zeta potential (the potential at the slipping plane), and force between particles at their instantaneous distance is controlled by the strengths of these potentials.

Ultimately, regardless of the origin of these forces, Van der Waals or electric double

layer, an attractive force will cause particles to aggregate and repulsive forces can cause a caging effect such as demonstrated in section 2.3.2.2.2 [160, 161].

2.3.2.2.5 Gels

Gelation in colloidal system involves the “jamming” of polymers, typically the continuous phase. It is realised by the formation of a giant macromolecule that percolates through the entire solution. This can be a result of neighbouring chains forming crosslinks between one another, until sufficient interconnection is reached and the macromolecule is large enough to move as one. Similar results of polymer gelation can be as a result of high conversions in step-growth polymerisations. The formation of this macromolecule results in an abrupt increase in viscosity and a transition to an elastic response to deformation, over a viscous response. At the specific gel point, the value of $\tan \delta$, the ratio between the loss (the viscous component of a viscoelastic material) and the storage moduli (the elastic component), becomes independent of the frequency used in an experimental test [162].

2.3.2.2.6 Sedimentation

A fairly common phenomenon in colloidal suspensions is the gravitation settling of particles, especially for particles of greater than 100 nm [161]. It is possible for smaller particles in high viscosity fluids where the gravitation force is less than the drag force, as calculated by a derivation of Stoke’s Law [161].

$$F_g = (\rho_p - \rho_f)g\frac{4}{3}\pi R^3 \quad (2.19)$$

Settling and sedimentation of particles can also be effected by the attractive and repulsive forces in the colloidal suspension, and it is possible that the forces exerted by smaller particles on larger particles can slow down their settling [161].

Ultimately, these failure mechanisms can cause issues during electrode coating, or can result in poor electrode coatings. Therefore, the identification of these failure mechanisms

within an electrode slurry is important for facile and effective coating.

2.3.3 Characterisation of Electrode Slurries

Electrode slurries are complex rheological fluids with high solids content (these can be higher than 50 wt%) [125]. These slurries are difficult to characterise. Large particles or agglomerations can give false readings, due to, both, the narrow gaps obstructions in rheometers, or from the settling of solid particles [163].

The main methods used to characterise electrode slurries are rheological techniques, split between inline and offline, [127], with offline rheology being more commonly employed. [127] These offline rheological techniques can be further characterised between rotational rheology and oscillatory rheology. An introduction into these techniques will be examined in this chapter, with a more detailed exploration found in Chapter 5.

Rotational rheology examines the apparent viscosity of material through measurements of shear force at given shear rates, as demonstrated by Equation 2.20:

$$\tau = \frac{F}{A} \quad (2.20)$$

where τ is the shear stress, F is the measured shear force, and A is the area of shear. For a rheometer this is set by the geometry used. The apparent viscosity, η , is then calculated through use of Equation 2.21:

$$\eta = \frac{\tau}{\dot{\gamma}} \quad (2.21)$$

where $\dot{\gamma}$ is the shear rate.

Rotational rheological measurements are a commonly used method in the characterisation of electrode slurries. [110, 164–167] Offline rotational rheology measurements are generally taken at shear rates relating to the coating instrument, and,

if the viscosity is low enough, it is assumed that an electrode coating can be made. [127] However, use of rotational rheology can sometimes be inadequate in its characterisation of electrode slurries, as explored in Chapter 5, and some of the electrode slurry jamming processes, explored in Section 2.3.2.2, cannot be properly identified. Therefore, oscillatory rheology techniques are used that can infer additional information about the electrode slurry structure.

Oscillatory rheology measures the viscoelasticity of a material. It demonstrates that fluids can be categorised by examination of the complex modulus (G), comprised of the storage (G') and loss (G'') moduli, which are measured by the phase shift (δ) between the shear strain (γ) response of an applied shear stress (τ). The relationships between these values can be found in Equations 2.22, 2.23, and 2.24. [168–170]

$$G = \frac{\tau}{\gamma} = G' + iG'' \quad (2.22)$$

$$G' = G \cos(\delta) \quad (2.23)$$

$$G'' = G \sin(\delta) \quad (2.24)$$

The storage and loss moduli are indicative of the elastic response of the fluid and viscous response of the fluid, respectively; a material that is entirely elastic (a solid) will exhibit no phase shift (0°) between shear stress and shear strain, $G' \gg G''$, and a material that is entirely viscous (a fluid) will exhibit a 90° phase shift, $G'' \gg G'$. [168–170] Ultimately, the characterisation of an electrode slurry is an important step in the electrode manufacturing process, [127] and will therefore, be a key point of investigation in this PhD.

2.3.3.1 Electrode Coating

The process of electrode coating has been extensively optimised (both experimentally and theoretically) [165, 171], for existing coating methods [36, 110, 126, 152, 156, 165, 171–175], but more coating and printing methods are being explored, such as spray coating [172, 176, 177], ink jet [172], or 3D printing [178, 179].

The most common methods of coating are: slot-die [156, 165, 171, 180–182], and doctor blade [177, 180, 183–187], with roll-to-roll coating [165, 180, 185] (used in reel-to-reel coating [185]) used for larger scale applications.

In general, these methods of coating share the same general process: an electrode slurry is applied to a current collector via some pump or slot, or manually. The coat is then “spread” by movement of the coating blade (or slot) onto the current collector. A variable gap is the primary contributor to the thickness of the electrode coating, with the solvent quantity in the electrode slurry acting as a further control. [165, 186, 188, 189] Different coating methods have been established to cover differing ranges of shear rate, [127] which can enable the use of different electrode slurry viscosities. However, despite the choice of coating method, a poorly mixed electrode slurry will still result in poor quality electrodes, such as those demonstrated in Section 2.3.1, Figure 2.4.

One such example is due to the poor packing of conductive additive particles. The low bulk density of these materials can allow the incorporation of air into the electrode slurry, causing large voids during electrode coating, rendering the electrode useless. [151] Careful mixing and, in some cases, degassing is required to remove these voids from the electrode slurry. [190] Other can arise due to a lack of sufficient energy or time inputted during the mixing stage, resulting in discrete phase agglomerates remaining in the electrode slurry. Schmitt *et al.*, 2013, examined the origins of different types of electrode coating defects. [165] It was established that striped defects can arise from the presence of agglomerates larger than the coating gap in the electrode slurry during coating. [165]

Furthermore, particularly for large scale coating operations, the electrode slurry jamming mechanisms identified in Section 2.3.2.2 can cause unstable flow, creating

undulations or ribbing defects in coating. [165]

2.3.3.2 Electrode Drying

The drying of the coated electrode slurry is similarly important in the process of electrode formation [181]. Susarla *et al.*, 2018, studied the effect of solvent removal during electrode drying for NMP based electrode slurries. During the study, it was concluded that, for a 150 μm electrode, initial solvent removal is very rapid. After the first 30 seconds of drying, mass transfer limitations dominate and the drying rate decreases. Numerically, for drying temperatures of 75 – 95°C, 90% of solvent removal occurs within the first half of drying and removal of the final 10 % takes the same amount of time [181]. Jaiser *et al.*, 2016, highlighted the significance of electrode drying for the mechanical properties of the electrodes. The study demonstrated that over the course of the drying process, the adhesive force of the electrode evolves; capillary forces and solvent removal promote a migration of binder to a film on the surface of the electrode. As top-down consolidation of the film occurs, a concentration gradient of the binder in the electrode forms. At this point it is vitally important to allow enough time to ensure that the distribution of binder equilibrates throughout the electrode [191].

Ultimately, electrode drying can be split into two drying regimes, heat transfer limited, which contributes to the first 90 % of solvent removal, and mass transfer limited, the final 10 % of solvent removal [181]. The high drying rate of the first regime has the potential to form cracks, or stress related defects, in the electrodes [181], which can hinder the electrochemical performance. The secondary, mass transfer limited regime can result in poor distribution of binder in the electrodes [191], which hinders the electrochemical and mechanical performance. However, while the drying stage is able to alter the structure of the electrode [181,191], it is unable to rectify the detrimental effects of a poorly mixed electrode slurry.

2.3.3.3 Electrode Calendering

Electrode calendering is similarly considered an important step in the production of lithium or sodium ion batteries [186, 192, 193]. Zheng *et al.*, 2012, studied the effects of calendering upon a $\text{LiN}_{1/3}\text{Co}_{1/3}\text{Mn}_{1/3}\text{O}_2$ based cathode. It was concluded that calendering improves the particle-to-particle contact and adhesion within an electrode. However, the porosity and specific surface area of the electrode are both reduced, which increases the tortuosity [186]. Calendering has been proven to increase the volumetric energy density of the material. It decreases the distance between neighbouring active-material particles via the compression of inactive-material composites – the active material particles do not deform with calendering [186].

Contradictory to Zheng *et al.*, 2012, Haselrieder *et al.*, 2013, concluded that, especially for anodes, active material particle deformation occurs, and increases proportionally with compression rate. Furthermore, calendering decrease the surface roughness via the closing of surface-open pores of the electrode [194]. In combination, the closing of surface-open pores and the deformation of active materials, significantly reduces the specific capacity of the electrode [194]. However, Haselrieder *et al.*, 2013, and Zheng *et al.*, 2012, both conclude that over-calendering decreases the specific capacity due to a closing of pores [186, 194]. Other studies have similarly analysed the calendering process, which concur with the findings of Haselrieder *et al.*, 2013 and Zheng *et al.*, 2012 [139–141, 186, 195].

2.3.4 Summary and Conclusions

This exploration of literature has demonstrated that the rheology and homogeneity of the electrode slurries, as well as the coating and subsequent processing of the electrodes, has a significant influence on the final electrochemical performance of the cell. Therefore, any inhomogeneity, or failings in the electrode slurry will have a considerable impact. Thus, for facile and repeatable processing, it is important that these failings be characterised and investigated.

Similarly, as explored in Section 2.2, electrode slurries containing sodium ion layered O₃ oxides, such as those investigated in this thesis, have been shown to gel. Therefore, the elucidation and countering of this gelation, shown to have a serious impact on the electrode manufacture, will form the basis for this research.

Chapter 3

Experimental Methods

The chapter outlines the materials and experimental methods used throughout this PhD research. Experimental methods and materials that are specific to individual chapters have been detailed therein.

3.1 Electrode Material Manufacture and Analysis

3.1.1 NaNMST Synthesis

$\text{NaNi}_{1/2}\text{Mn}_{1/2}\text{Sn}_{1/8}\text{Ti}_{1/8}\text{O}_2$ (Na-NMST) was synthesised by a solid-state method. Stoichiometric quantities (to produce 100 g of product) of Na_2CO_3 , $\text{Ni}(\text{NO}_3)_2 \cdot 6\text{H}_2\text{O}$, MnCO_3 , SnO_2 , and TiO_2 , (all sourced from Alfa) were ball milled using a Glen Creston roller mill in a 1000 mL HDPE Azlon roller pot, with 100 g of 5 mm zirconia balls and 100 g of 10 mm. Due to the volatility of sodium during the solid-state synthesis, an extra 5 wt% of Na_2CO_3 was added.

The powders were wet milled with isopropanol. Over the first day of milling, 250 mL of isopropanol was added and the pressure inside the pot was released every *ca.* 30-60 minutes. Afterwards an extra 200 mL of IPA was added to account for the volatility of the IPA and the pot was milled for more than 48 hours to ensure complete homogeneity. The IPA was removed and condensed under vacuum at approximately 50°C. This dried

precursor material was fired at 900°C for 24 hours. The resulting as-synthesised Na-NMST was transferred into an argon filled glove box at 200°C.

3.1.2 Material Analysis

The synthesis of the Na-NMST material was verified using a Malvern PANalytical AERIS X-ray Diffractometer. The Na-NMST material was first loaded onto the sample holder inside a glovebox to minimise the air exposure before the measurement was obtained. XRD measurements and analysis were performed by a colleague at the University of Birmingham, who is familiar with this technique.

The tap density of the material was determined using a standard method [196]. The active material was placed in a graduated cylindrical vessel and tapped until the volume no longer reduced. The volume was then measured using the graduated cylindrical vessel and the sample weight was determined using a balance. The tap density can then be calculated as a normal density, such as with Equation 3.1:

$$\rho_{tap} = \frac{m_{material}}{V_{tap}} \quad (3.1)$$

3.1.2.1 SEM/EDS

Scanning Electron Microscope (SEM) characterisation of the powder was performed using a Zeiss SUPRA 55-VP with elemental analysis performed using an Oxford Instruments energy-dispersive X-ray (EDX) spectrometer. SEM and EDS analysis were achieved using an acceleration voltage (EHT) of 5 kV and 15 kV, respectively. SEM images and quantitative elemental analysis were obtained on the as-synthesised material and on material that had been exposed to lab air for *ca.* 72 hours. To ease the material transport, the material was exposed to lab air after it had been pre-placed on SEM stubs.

3.1.2.2 FTIR

Powders were chemically characterised using a Bruker Vertex 70v Fourier Transform Infrared spectrometer (FTIR) with a diamond attenuated total reflectance accessory. Measurements were taken every 10 minutes whilst the material was situated on the diamond and exposed to lab air. Exactly the same method was employed for slurry samples. Slurry samples were situated on the diamond and exposed to lab air with measurements taken every 10 minutes. The slurry samples were transported to the FTIR spectrometer in sealed vessels following their mixing in the dry room. For all the measurements, data was recorded from 4500 to 100 cm^{-1} , using 16 scans at a resolution of 4 cm^{-1} , with appropriate background measurements taken for each spectrum.

3.1.3 Additional Processing

In order to homogenise the particle size, the active material was milled in a Retsch PM100 Planetary Ball Mill. One third of the total conductive carbon black (IMERYS, Super C65) was added to coat the particles and to aid in the conductive properties of the electrode. 45 g of 5 mm, and 15 g of 10 mm zirconia balls were added to the 50 mL mill pot. The powders were milled at 300 rpm for 45 minutes, with a reversal of direction every 15 minutes.

3.2 Electrode Slurry Manufacture and Analysis

Electrode slurries were formed by mixing the carbon coated Na-NMST with the remaining conductive carbon black, and an 8 wt% PVDF (polyvinylidene fluoride) (Solvey 5130) binder in NMP (N-methyl-2-pyrrolidone) solution in a ratio of 89:6:5 by weight. This changed to 89-X:6:5:X, in the cases where an additive was added. X represents the ratio of the additive and was between 0.5-2. The cathode ink was mixed in sealed pots in a Thinky ARE-250 Planetary Mixer, situated in a Munters dry room with a maximum dew point of - 40°C. Materials were measured out under a recirculator hood (also situated in

a dry room) or in an argon filled glove box.

There were 3 stages of mixing: initially the active material and the extra NMP, measured to give a final solids content of 40 wt%, followed by the addition of carbon black, and, finally, the PVDF solution. Each mixing stage lasted 5 minutes with a speed of 1300 rpm. For situations where additives were employed, each additive was mixed with NMP, prior to the start of this mixing route.

3.2.1 Rheology

Physical measurements of the slurry rheology were obtained using a Malvern (now Netzsch) Panalytical Pro⁺ rheometer. Frequency sweeps were performed, from 0.1 Hz to 100 Hz at an amplitude of 0.1 %, which resides in the linear viscoelastic region (LVER). A minimum of three repeats per sample was used to confirm the measurements. A second amplitude of 0.02 % (which also resides in the LVER) was used, where possible, to further validate the measurements for many of the samples, however due to the lab time restrictions, this was only performed for certain sample sets. A constant pre-shear of 10 s⁻¹ for 30 seconds was performed at the start of measurements to eliminate any time dependence in the samples and ensure consistency between results. The frequency sweeps were performed every 5 minutes on the electrode slurry, between 40 mm roughened parallel plates. A solvent trap containing deionised water and a Peltier-plate set to 25°C was used to maintain the temperature and humidity over the course of all rheological measurements.

3.3 Electrode Manufacture and Analysis

Electrodes were formed by coating the electrode slurry onto an aluminium substrate using a doctor blade set at 150 µm, aiming for a loading of 60-80 gsm. They were then dried on a hotplate at 80°C for 40 minutes, followed by overnight in a vacuum oven at 120°C. For additional characterisation of the slurry exposure, three different coatings were made

from the electrode slurries, one on the just-mixed slurry (i.e. immediately after mixing), one was coated 20 minutes after mixing and 40 minutes after mixing (at which point the slurry gelation was noticeable). All coating was performed inside a recirculator hood situated in a dry room.

3.3.1 Adhesion Testing

The adhesive strength of the electrodes was tested using Malvern (now Netzsch) Panalytical Pro⁺ rheometer, in force measurement mode, via a 180° peel test. The setup of these adhesion testing measurements can be seen in Figure 3.1. This method was developed by a colleague at the University of Birmingham and can be found detailed in the study by Zhang *et al*, 2022. [197]

The electrode coatings were cut to strips with the same width as the double-sided tape (Ultratape - Double-Sided Tape 19 mm x 33 m). The electrode coatings were stuck to the rheometer bottom plate, coating side down, using the same double-sided tape and curved upwards, denoted as “a” in Figure 3.1. An additional piece of tape was attached to the end of the coating (“b” in Figure 3.1), and then attached to the top rheometer plate (“c”).

For consistency, the rheometer was always zeroed, and the top of the tape (“c”) was attached to the top plate, when it was at a height of 20 mm. The top plate was then raised at a speed of 10 mm/s to 186 mm. The coating and the tape were pulled apart vertically, with a 180° angle between them. Adhesion measurements require clean removal of coating from the current collector. In experiments where bottom layers of the electrode coating remain on the current collector, these are measurements of cohesion, not adhesion, and the experiment required repeating. Final adhesion values were calculated using 3 samples from each sample set. Errors were taken as the standard deviation between these measurements.

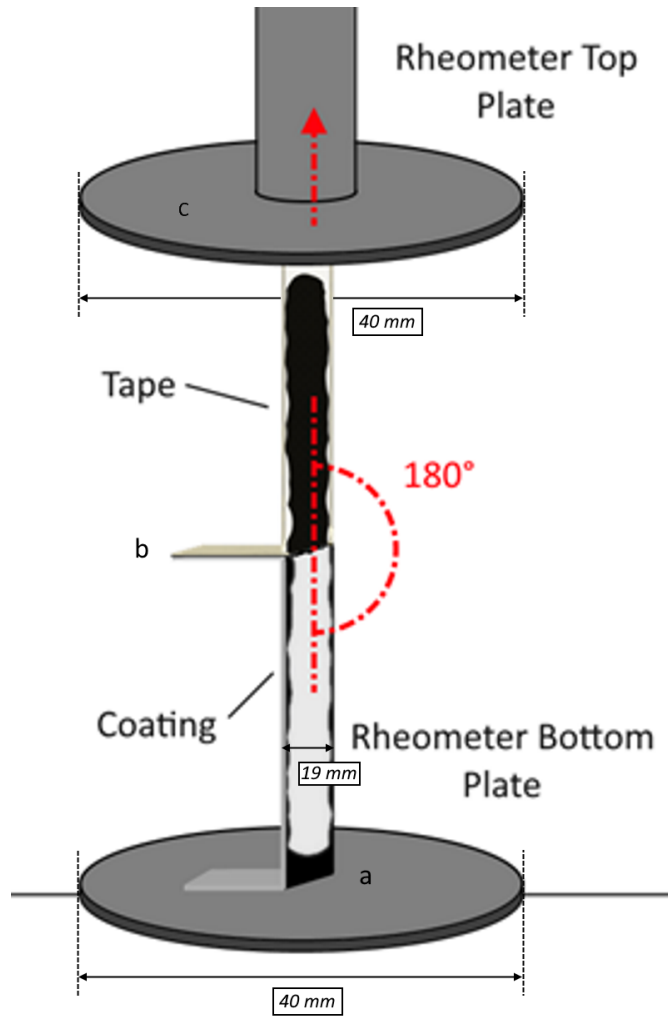


Figure 3.1: Diagram of the Adhesion Testing Setup using the Malvern Panalytical Pro⁺ rheometer.

3.3.2 Four Point Probe

The conductivity of the electrodes was measured using a Ossila Four-Point Probe. Ideally, conductivity measurements should be performed on samples that have been coated (or placed) onto a non-conductive substrate. However, due to the time limitations caused by the COVID-19 pandemic, electrodes that had been coated onto aluminium foil were used. This was deemed acceptable, as measurements were to be used on a comparative basis and all samples were coated onto aluminium that had been cut from the same roll. Electrodes were cut into a circular geometry with a diameter of 14.8 mm. The thickness

of the electrodes was measured (using the same method as detailed in the Section 3.3.4.1) before hand and entered into the software to allow for a thickness correction calculation.

For each additive (or sample set), the conductivity of three different electrodes were examined cut from different points across multiple coatings. Each electrode then received 25 measurement repeats from the Ossila Four-Point Probe, with a target current of 1 mA and a maximum voltage of 4.5 V. Averages and standard deviations were then calculated from these three sets of 25 measurements to form a single average and standard deviation.

3.3.3 XPS

X-ray photoelectron spectroscopy (XPS) data on the as-manufactured electrodes was acquired using a Kratos Axis Ultra DLD spectrometer. Samples were transferred to the spectrometer using an airless transfer unit with an argon atmosphere. The surfaces of the samples were found to charge slightly under the X-ray beam during the experiments and to compensate for this, the surfaces were flooded with a beam of low-energy electrons during data acquisition. This in turn required subsequent re-referencing of the data, using the graphitic component of the C1s region at 284.3 eV as the reference point. The data were analysed with the CasaXPS software package, using Shirley backgrounds, mixed Gaussian–Lorentzian (Voigt) line shapes, and asymmetry parameters where appropriate.

3.3.4 Electrochemistry

3.3.4.1 Electrode Measurements

The electrodes were weighed out using a Sartorius SE2 ultra-micro balance, which allows measurements to a precision of 0.1 μg . The sample stage includes a draft shield and cover for high accuracy measurements. A stack of 3 foils were measured at the same time and averaged for later calculation of active mass. Calculation of active mass (m_A) was done using Equation 3.2, where m_{TE} is the total electrode mass, m_F is the averaged foil mass, and f_A is the fraction of active material in the electrode (in this case between 0.89 and

0.87).

$$m_A = (m_{TE} - m_F) \cdot f_A \quad (3.2)$$

The electrode thickness was measured using a Mitutoyo ABS Digital Depth Gauge, mounted on a Mitutoyo Gauge Stand with Hardened Steel Anvil for measurement stability. For each measurement, the spindle was carefully and slowly lowered onto the electrode surface, so as to not depress the electrode and cause false readings. To allow for variations across the electrode surface, 3 thickness were taken at different points and then averaged.

An approximation of the electrode porosity was calculated by first calculating a theoretical coating density at 0 % porosity. This was achieved by using a weighted average method, as seen in Equation 3.3, where ρ_x is the density of component x, f_x is the mass fraction of component x, and x represents the component in the slurry. Each solid component is included in the equation. The electrodes are vacuum dried, so all the NMP is evaporated off. Material densities were obtained from suppliers data sheets, PVDF – 1.78 g/cm³ [198]

$$\rho_0 = \frac{(\rho_A \cdot f_A) + (\rho_{C65} \cdot f_{C65}) + (\rho_{PVDF} \cdot f_{PVDF})}{(f_A + f_{C65} + f_{PVDF})} \quad (3.3)$$

The true density of the electrode (ρ_E) was calculated by dividing the electrode mass ($m_{TE} - m_F$) by the volume of the electrode (V_E), as seen in Equation 3.5. The calculation of the volume of the electrode can be seen in Equation 3.4, where t_{TE} is the thickness of the whole electrode (including foil), t_F is the thickness of the foil, and d_E is the diameter of the electrode, in this case 14.8 mm.

$$V_E = (t_{TE} + t_F) \cdot \frac{\pi \cdot d_E^2}{4} \quad (3.4)$$

$$\rho_E = \frac{m_T E - m_F}{V_E} \quad (3.5)$$

The approximation of the electrode porosity (φ_E) can then be calculated using Equation 3.6, which will give the value as a fraction. Electrode porosity is usually expressed as a percentage, so this value needs to be multiplied by 100.

$$\varphi_E = \frac{1}{\rho_E} - \frac{1}{\rho_0} \quad (3.6)$$

3.3.4.2 Cell Construction

Half-cells were assembled in an argon filled glovebox, using sodium metal as the counter (and reference) electrodes, Celgard 2325 and glass fibre (GF/A, Whatman) discs, both cut to 16 mm as dual separators, and the cathode electrodes cut to 14.8 mm.

The GF/A separator was placed next to the electrode, and the Celgard 2325 next to the metallic sodium to reduce dendrite growth. 70 μ L of 1M NaPF₆ in EC:DEC (1:1 V/V) with FEC additive (5.3 wt% FEC) (Fluorochem) was used as the electrolyte. Cells were made into CR2032 coin cells.

3.3.4.3 General Cycling

Cells were held at their open circuit voltage (OCV) for 24 hours directly after assembly to allow for complete electrolyte saturation in the cell. This was used for all electrochemical tests – general cycling, and EIS measurements.

For standard cycling, cells were subjected to an initial formation cycle with a low current of 10 mA/g for first cycle. A “Battery Capacity Determination” (BCD) step was then performed, allowing a C-rate to be used. All subsequent cycles were performed a rate of C/10. Cells were charged between 2.0 V and 4.2 V, with measurements recorded

every 35 mV or every 30 seconds.

3.3.4.4 Electrochemical Impedance Spectroscopy (EIS)

EIS measurements were performed on half cells that had undergone the same formation cycles as the “General Cycling”. Each EIS measurement was taken at 50 % “State of Charge” (SoC). A BCD step was performed after formation, which would allow a C-rate to be determined – based upon a rated capacity obtained at 10 mA/g, a rate of 1C means the cell would charge to 100 % SoC in 1 hour, a rate of 0.5C means the cell would take 2 hours to fully charge. After the BCD, a 50 % SoC could be achieved by charging at C/10 for only 5 hours.

EIS measurements were taken between a frequency range of 10 kHz to 10 mHz, with 3 measurements taken per frequency and then averaged. EIS data has been fitted with the software package, Z-view, using Non-Linear Least Squares (NLLS). The equivalent circuit, and the motivation behind using it, has been detailed in Chapter 6. Fittings have a maximum chi-squared value of 1×10^{-4} .

Chapter 4

Mechanisms of Gelation in Electrode Slurries for High Nickel Content Sodium Ion Battery Cathode Materials

4.1 Introduction

As established, many layered O₃ oxide materials, especially those with a high nickel content, undergo both surface and bulk phase transformations when exposed to air, [33] resulting in the formation of sodium residues such as Na₂CO₃ [34] or NaOH. [35] As a note, there are inconsistencies in the literature regarding the formation of sodium residues with some sources suggesting Na₂CO₃ [34, 89] and others suggesting NaOH. [35, 90] Additionally, exposure to air of electrode slurries containing these layered O₃ oxide materials, along with NMP and PVDF causes them to gel, [36, 37] which renders the slurries uncoatable and therefore unusable. As a result, careful cathode slurry preparation is required.

The elucidation of the gelation mechanism has been approached in a methodical

manner. Firstly, an in-depth literature review of the stability of the electrode slurry components has been performed, with a particular focus on chemical stabilities of these components. Secondly, a detailed analysis of the physical and chemical changes of the electrode materials over time has been made. Subsequently, the electrode slurry, as a whole, has been investigated, with observations made into the time dependent alterations of the structural and chemical properties. Finally, the effect that these electrode slurry alterations have upon the electrochemical properties of these materials has been explored.

4.1.1 PVDF (Binder) Stability

PVDF, like other vinyl fluorides, is well known for its chemical stability [199] and high hydrophobicity [200]. PVDF has been shown to be largely unreactive to acids [200, 201], which is beneficial for sodium ion batteries as HF can form due to reactions of the electrolyte salts (NaPF_6) [34, 202].

However, alkaline degradation of PVDF with hydroxides has been widely explored in literature [203–206]. A hydroxyl group can prompt a dehydrofluorination reaction, causing a removal of HF from the PVDF structure [203–206]. This dehydrofluorination reaction causes conjugated double bonds to form between neighbouring carbon atoms that are then able to react with adjacent polymer chains, creating crosslinks. [199].

Xiao *et al.*, 2014, detailed a colour change of PVDF membranes from white to brown and then black during a treatment by a 15 wt% NaOH solution (initially colourless). However, to note, this observation is unlikely to be of use in the analysis of electrode slurries as, due to the presence of carbon black, immediately after mixing, the slurries are black or dark brown in colour and opaque. An important finding by Xiao *et al.*, 2014 was, despite the usual inactivity of the C=C bond in infrared spectroscopy, a low absorbance intensity at 1600 cm^{-1} was found in dehydrofluorinated PVDF (after 22 hrs of NaOH treatment) [206]. Similarly, an earlier examination of the surface modification of PVDF by alkaline treatment performed by Ross *et al.*, 2000, established a growth in intensity of

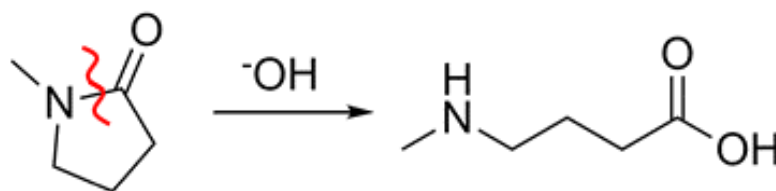


Figure 4.1: Hydrolysis reaction of NMP, forming 4-(methylamino) butanoic acid.

this 1600 cm^{-1} C=C bond in infrared spectroscopy. Over a 254 hour period this peak at 1600 cm^{-1} steadily increased, with initial observations appearing at 48 hours (although it is unclear as to whether this was the first measurement after 0 hours, or whether this was the first time that this peak appeared) [207].

Due to the suggested formations of basic sodium residuals (Na_2CO_3 [34] or NaOH [35]) due to reactions of sodium layered O3 oxide with air, it is possible that this alkaline degradation of PVDF may play a role in the gelation of these electrode slurries.

4.1.2 NMP (Solvent) Stability

NMP, as discussed in chapter 2, is chosen due to its ability to dissolve PVDF. NMP, itself, has excellent thermal and chemical stability [208]. It is well known as a co-solvent, due to its complete miscibility with water and many other solvents [208–210]. However, its affinity to water causes a hygroscopicity and it has been shown to degrade under aqueous alkaline conditions. A study by Ou *et al.*, 2017, detailed a hydrolysis reaction that occurs between NMP and a hydroxyl group. [209, 211, 212]. During the hydrolysis of NMP, a ring opening reaction occurs, and the lactam structure of NMP splits between the N and the C=O, forming 4-(methylamino) butanoic acid, as shown in Figure 4.1.

It has been established that the degradation of NMP causes the colourless liquid to change to a yellow – yellow/orange colour. [209] An investigation by Uno *et al.*, 1968, examined the colour reactions of different structural amines. It was found that for aliphatic amines, primary and secondary amines had a yellow colour, while tertiary amines were colourless. For aromatic amines, primary amines produce a reddish brown

colour and secondary amines form a green colour. NMP is a tertiary aliphatic amine which, after a ring-opening reaction, transforms into a secondary aliphatic amines, hence the colour change [213].

NMP has also been suggested to degrade under sonication [214]. A study by Yau *et al.*, 2015, established that for dispersions of single walled carbon nanotubes in NMP, after sonication, contained small particulates. [214]. Yau *et al.*, 2015, concluded that NMP degrades under sonication.

While sonication has not been used to disperse the electrode slurries in this study, the phenomena of this particulate formation is important to consider, especially when high energy mixers may be used for the formation of electrode slurries [214]. Similarly, with the potential presence of hydroxyls, due to the reactions of sodium layered O3 oxides with air, the hydrolysis of NMP should be considered in the investigation of the electrode slurry gelation.

4.1.3 Carbon Black Stability

Carbon blacks (CB) have been established as having high chemical stabilities. [215,216] However, residuals, due to the high surface areas of CBs, are able to absorb onto the surfaces of CBs. [215]

A study by Kim *et al.*, 2007, compared the surface characteristics of CB materials that had undergone an acid treatment, a base treatment, or a neutral treatment, which consisted of a washing stage and a vacuum drying stage. Using FTIR analysis, it was established, in the untreated materials, that several functional groups, including hydroxyl, carboxyl, and ether groups could be identified in the surface species. [215] Base treated CBs show increased intensities in the hydroxyl peak. Neutrally treated carbon blacks demonstrated the lowest quantities of surface species. [215]

Ultimately, while the study by Kim *et al.*, 2007, demonstrates that CBs are able to surface absorb functional groups, they have chemical resistances to acids and bases. [215] Furthermore, as the vacuum drying of CBs (the neutrally treated CB) is the most effective

at removing surface residuals, any CBs used in this PhD have been vacuum dried for more than 24 hrs and stored in a sealed container inside glove-box prior to their use.

4.1.4 Layered O3 Oxide

For the final electrode slurry component, the active material, existing studies regarding its stability have been explored in Chapter 2. As established these materials undergo surface and bulk phase transformations when exposed to air. However, there are inconsistencies in the literature regarding the formation and nature of surface species. Therefore, a further investigation into the stability of the $\text{NaNi}_{1/2}\text{Mn}_{1/4}\text{Ti}_{1/8}\text{Sn}_{1/8}\text{O}_2$ active material in air is made in this chapter.

This chapter describes the investigation of the gelation of electrode slurries containing the cathode material, $\text{NaNi}_{1/2}\text{Mn}_{1/4}\text{Ti}_{1/8}\text{Sn}_{1/8}\text{O}_2$, firstly through the analysis of the active material in air, secondly, the analysis of the electrode slurry, and finally, the study of the electrodes. This study and results are believed to be transferable to other sodium cathode materials of a similar structure, as well as high (greater than 60 %) nickel content layered materials for lithium ion cathodes - a comparison between high nickel content lithium layered cathodes and high nickel content sodium layered cathodes was made in Chapter 2.

4.2 Aims and Objectives

The overall focus of this PhD research, as established in Chapter 1.1, is the investigation and stabilisation of the sodium ion cathode slurries of high nickel content layered O3 materials. The first stage of this process is the elucidation of the gelation mechanism through the following objectives:

- Establish the reactions of the active material in air and examine the surface species that form as a result.

- Investigate any chemical changes in the electrode slurry over the course of slurry gelation.
- Observe how the measured rheological properties of the electrode slurry change.
- Establish a nominal processing window of these electrode slurries after which coating becomes unfeasible.
- Determine the effect that electrode slurry gelation has upon the electrochemical properties of these materials.

4.3 Experimental Setup

General methods used in this research can be found in Chapter 3. Experimental methods specific to this chapter include XPS, and specific cell cycling parameters.

X-ray photoelectron spectroscopy (XPS) data on the as-manufactured electrodes was acquired using a Kratos Axis Ultra DLD spectrometer. Samples were transferred to the spectrometer using an airless transfer unit with an argon atmosphere. The surfaces of the samples were found to charge slightly under the X-ray beam during the experiments and to compensate for this, the surfaces were flooded with a beam of low-energy electrons during data acquisition. This in turn required subsequent re-referencing of the data, using the graphitic component of the C1s region at 284.3 eV as the reference point. The data was analysed with the CasaXPS software package, using Shirley backgrounds and mixed Gaussian–Lorentzian (Voigt) line shapes and asymmetry parameters where appropriate.

Electrodes had an average thickness of 50.3 μm ($\pm 4.3 \mu\text{m}$) and an average loading of 77.2 gsm ($\pm 7.95 \%$). They were not calendared, and the porosity of the electrodes was estimated to be 15 % ($\pm 2.5 \%$). Cells were subjected to an initial formation cycle with a lower current of 10 mA/g for first cycle, and 15 mA/g for all subsequent cycles.

4.4 Results

The elucidation and investigation of the gelation mechanism in these high nickel content sodium cathode electrode slurries will be explored in the following manner:

1. The changes to the active material as it reacts with air will be explored through the use of FTIR analysis, and SEM/EDS analysis.
2. The effect on the stability of the electrode slurries will be chemically explored through the use of FTIR, and, mechanically, through the use of oscillatory rheology and fitting to a Maxwell model. The analysis will be split between the measured storage and loss modulus and the phase angles from the oscillatory rheology. This data will be fitted to a Maxwell model, in order to extract the relaxation time of the electrode slurries. The development of these oscillatory rheology techniques and analysis can be found in Chapter 5
3. Further chemical analysis will be established through the use of XPS analysis on the formed electrodes.
4. Finally, electrochemical measurements will investigate the changes to the electrochemical properties of electrodes that have been coated at various times after mixing - exploring the effects of slurry gelation.

4.4.1 Active Material Characterisation

To understand the evolution of the active material in air, the active material powder was examined by measuring FTIR spectra every 30 minutes for 360 minutes. The resultant aging FTIR spectra shown in Figure 4.2a illustrates the chemical changes to the powder sample as it is exposed to air.

The very broad peak at the high frequencies, between 2500 cm^{-1} and 3500 cm^{-1} , in Figure 4.2a, is indicative of H-bonds, from OH stretching in, both, hydroxyl groups and

absorbed surface water molecules. [217] At 2350 cm^{-1} there is an asymmetrical double peak which is typical of CO_2 . [218] Interestingly, there does not appear to be much change to the intensity over time, suggesting that the absorbed CO_2 is at saturation, or it is being used up in a reaction, such as in the formation of a carbonate (any adsorbed CO_2 consumed is likely immediately replaced from the air).

The peaks between 1423 cm^{-1} and 669 cm^{-1} are more difficult to assign to a compound as both carbonates and hydroxides share these regions. Carbonates show a stretching at 1425 cm^{-1} , typically asymmetrical [219] and hydroxides can show an OH bending at around 1420 cm^{-1} . [220] A comparison of these peaks with pure carbonate (Na_2CO_3 [221] and NiCO_3 [222]) and hydroxide compounds (NaOH [222]) is shown in Figure 4.2b. The three highlighted regions in Figure 4.2b demonstrate the shared peaks, with the bands at 1423 cm^{-1} and 879 cm^{-1} being the most observable.

It is clear that NiCO_3 is not being formed. There is no overlap with the peak at 820 cm^{-1} , despite sharing the peak at 1434 cm^{-1} . From the broad region of OH stretching between 2500 cm^{-1} and 3500 cm^{-1} , as well as peaks at 1422 cm^{-1} , 879 cm^{-1} and 701 cm^{-1} , it is likely that NaOH or Na_2CO_3 is present (Figure 4.2b). The spectrum for NaOH shares the very broad region of OH stretching between 2500 cm^{-1} and 3500 cm^{-1} , as well as peaks at 1422 cm^{-1} , 879 cm^{-1} , and 701 cm^{-1} . Na_2CO_3 similarly shares peaks at 1429 cm^{-1} and at 878 cm^{-1} .

Further analysis with SEM and EDX (Figure 4.3) shows platelet-like particles existing both singly and as agglomerates. Primary particles were found to be approximately $750\text{ nm} \times 350\text{ nm} \times 150\text{ nm}$ in size (as seen in Figure 4.3a) with agglomerates being far larger, as seen in Figure 4.3b. After approximately 500 mg of the active material powder was mounted onto a SEM stub and exposed to the air in an open vial for 3 days, acicular (or needle-like) particles could be seen to emanate from the particle agglomerates (Figure 4.3b).

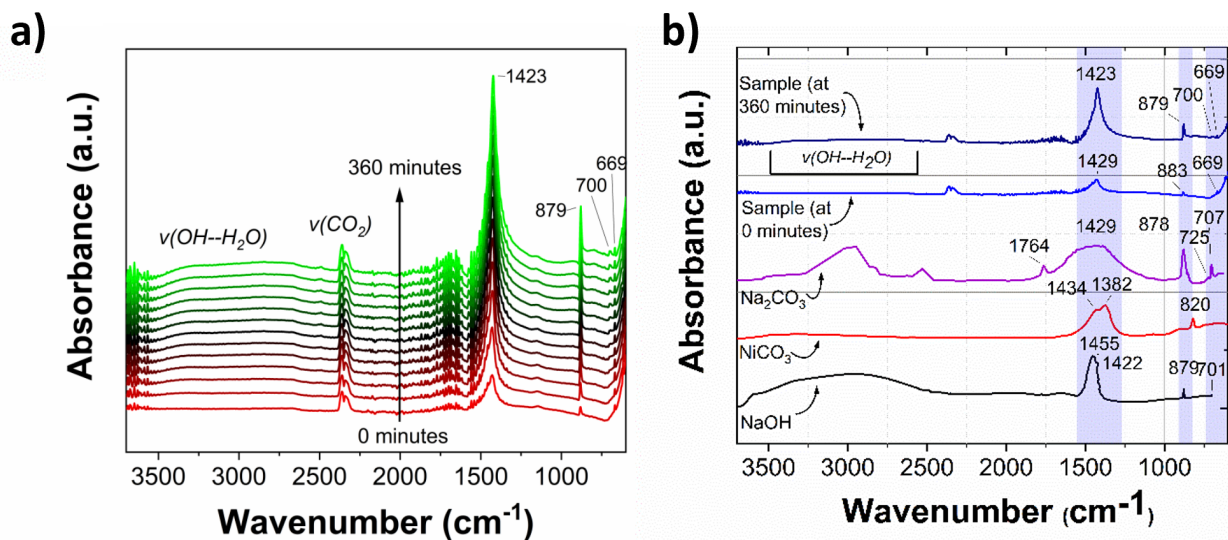


Figure 4.2: Ex-situ aging spectra of the carbon-coated active material over 360 minutes and b) Comparisons of the spectra with Na_2CO_3 [221], NiCO_3 [222], NaOH [222] and the NaNMST sample at time 0 and 360 minutes.

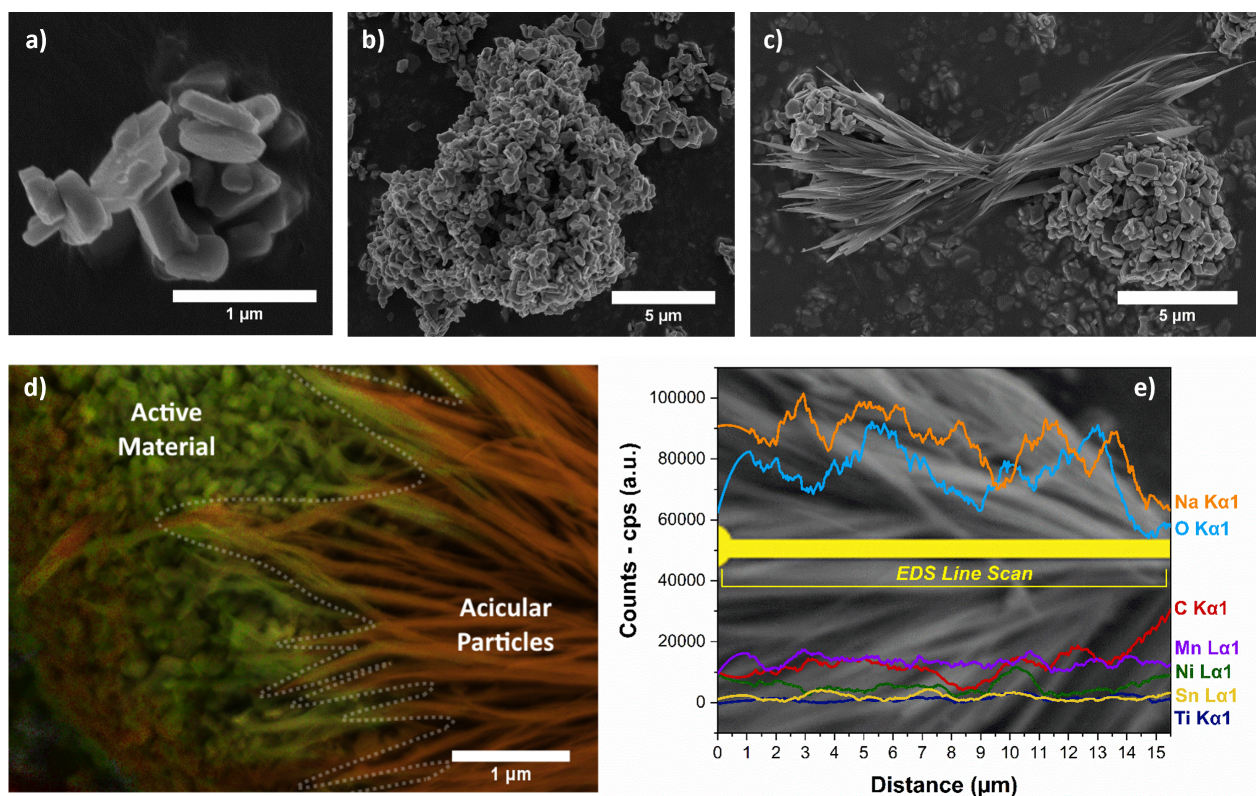


Figure 4.3: SEM image of the as synthesised NaNMST material a) Primary particles, b) agglomerates, c) SEM image of the as synthesised NaNMST material after exposure for 3 days, (d) EDS layered spectrum and individual elements, labelled by their elemental chemical.

EDS was used to further analyse the composition of the crystals formed as shown in Figure 4.3d. Based on the elemental line scan (Figure 4.3e), it is observed that the acicular particles contain sodium and oxygen in a 1:1 ratio, with lower levels of the transition metals and carbon. This indicates that these acicular particles are NaOH, supporting the results of the FTIR analysis, and rules out the presence of Na₂CO₃. Na₂CO₃ would show as a ratio of 2:1 sodium to carbon, or 2:3 sodium to oxygen.

4.4.2 Electrode Slurry Characterisation

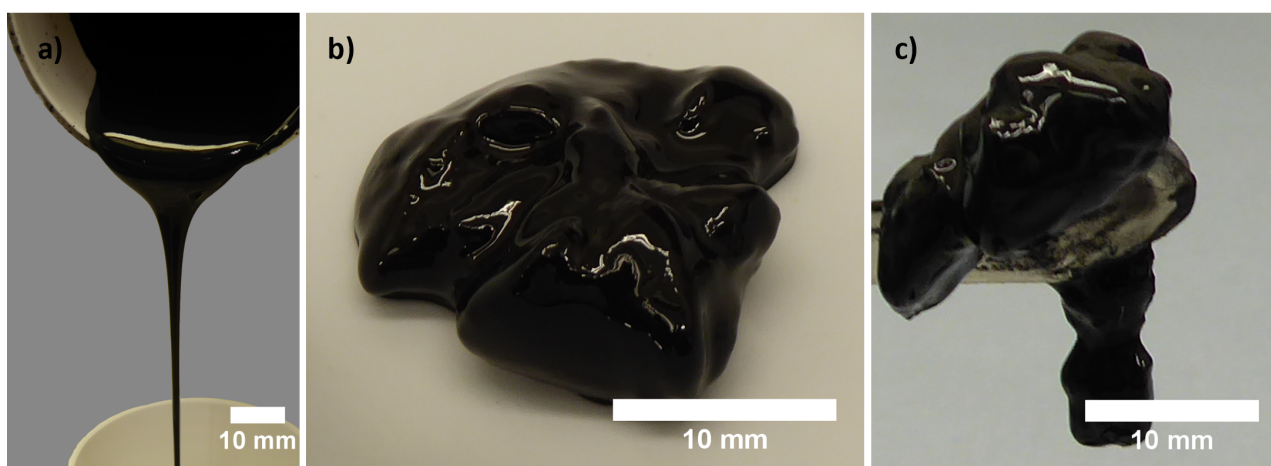


Figure 4.4: Comparison between a pristine electrode slurry (a) and the gelled sample (b and c).

Figure 4.4 shows the effects upon the electrode slurry once gelation has occurred, and highlights the physical issues for coatability. Initially, just after the electrode slurry has been mixed, it can flow very easily and freely (Figure 4.4a). Once the electrode slurry has reached a gel-like state (Figure 4.4b and c) it becomes impossible to coat homogeneously and reliably. If a physical gel is forming, this can be broken up with increased shear or additional solvent, however if a chemical gel forms this is typically irreversible. The point at which the ink or slurry becomes uncoatable is poorly defined, and this is often done qualitatively in the laboratory through observation. In manufacturing this is often determined through defect observations in the coatings and adhesion properties after or during coating. [127, 223–225] In this work, the gelation had a very significant effect upon

the measured rheological properties. To predict the coatibility from the rheological data would save significant time and cost for electrode development.

There is a wide processing window for viscosity, however with the increase in viscosity, a change in the viscoelastic properties can also be observed. However, there are several challenges in the measurement of these changes. The high solids fraction of electrode slurries (usually more than 40 wt%) brings a risk of confinement jamming, forming a physical gel. Computational calculations and experimental measurements have shown that this can begin to occur at a solids volume fraction of 54.5 v %. [226]

These properties have been studied further to monitor the onset of different physical and chemical changes in the slurry.

4.4.2.1 Ex-situ Rheology studies of the Electrode Slurry

Oscillatory rheology was performed to determine the nature of the gelation and to analyse the degree of gelation of the electrode material. Figure 4.5a shows the storage, G' , and loss, G'' , moduli for the aging electrode slurry. It can be seen that both G' and G'' increase over the course of the aging measurements, with a larger increase observed for G' , consistent with the notion of a gelling slurry. Furthermore, as the aging increases, both the rigidity and strength of the electrode slurry gels increase. [227–229]

As demonstrated, there are no studies investigating changes to the storage and loss moduli in electrode slurries. However, studies of gels in different industries can establish the applications of G' and G'' to gel properties. The research on laryngeal mucus by Peters *et al.*, 2021, demonstrated that absolute values of G' and G'' relate to the rigidity of the gel. [228] Additionally, a study by Wildmoser *et al.*, 2004, exploring the quality aspects of ice cream using oscillatory rheology, determined that absolute values of G' describe material rigidity. [227] Similar conclusions were made by Ahmad *et al.*, 2015, which examined the formation of gels in gellan and dextran blends. [229] The study established that the ratio and difference between G' and G'' , including the phase angle, demonstrates the strength of the gel formed. [170, 228–230]

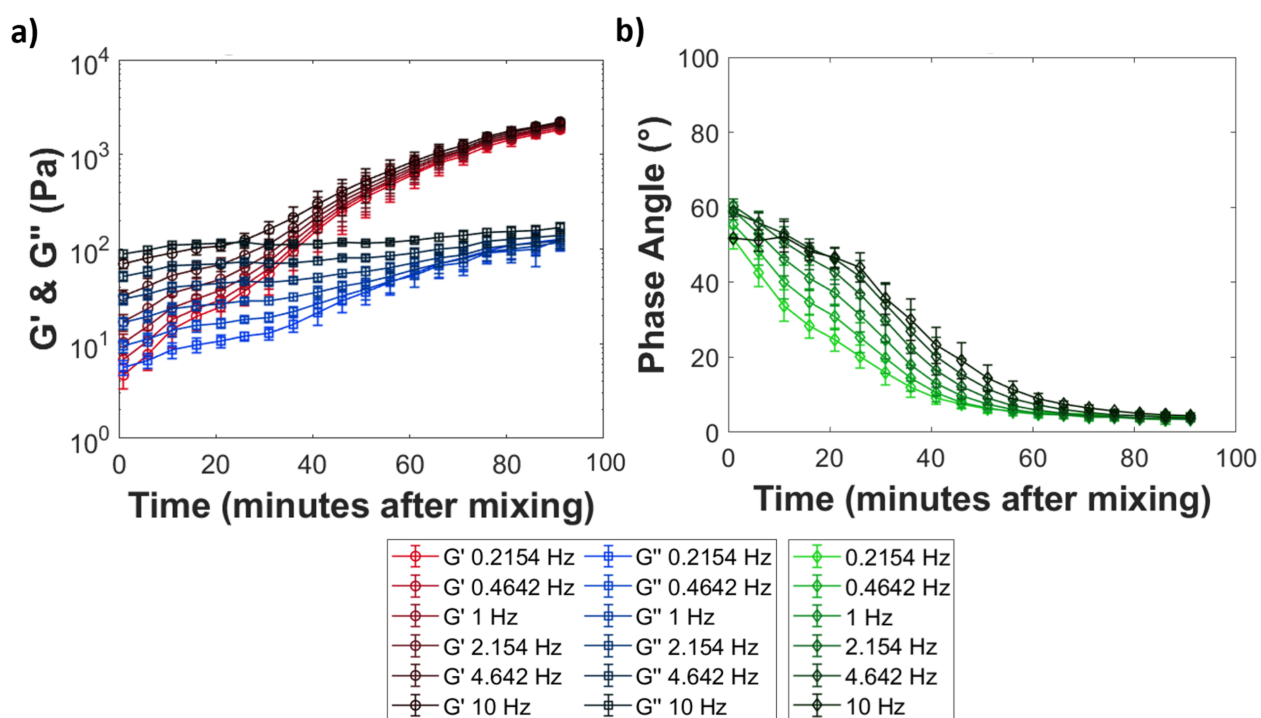


Figure 4.5: a) Storage and Loss Moduli, and b) Phase Angle for the Aging Electrode Slurry.

G' and G'' both demonstrate a convergence of measurements obtained at different frequencies towards the end of the rheological measurements. The convergence is a strong indication of a gel point, GP. [231] As this point of convergence occurs where the viscoelasticity no longer depends on observation time, it is clear that this is not the formation of a physical gel (such as a colloidal glass) but rather a reaction is occurring to form a chemical gel.

There are several classical rheological indicators of a gel, with the convergence of G' and G'' in time at different frequencies being previously mentioned. Another rheology indicator of a gel is the crossover point of G' and G'' , which occurs almost immediately, although this seems to be more of a suggestion of a gel. [232] Due to the fact that '0 minutes' refers to the start of the rheological measurements not the point at which the slurry is mixed (and it does not take into account the transfer time of less than 5 minutes), it seems logical that there is gelation occurring during the mixing of the electrode slurry.

The changes in the phase angle, Figure 4.5b, illustrates the balance between the

viscous and elastic forces. Initially, the phase angle is at 40° with slight differences depending on the frequency (or observation time). This indicates a system with a slight dominance towards the storage modulus and the elastic behaviour. This phase angle decreases as the electrode slurry aging progresses, until 65-70 minutes into the experiment where the convergence occurs, and the phase angle reaches $1-2^\circ$. At this point the gel is realised, and elastic behaviour is almost fully dominant. By the end of the rheological measurements, the physical manifestation of the gel had reached a point where it was completely uncoatable, with properties as shown in the photograph in Figure 4.5b.

4.4.2.2 Maxwell Model and Electrode Slurry Relaxation Time

To further analyse these rheological properties and determine the coatability of the gel, the data was fitted to a 2 mode Maxwell model using the Reptate software package. [233] The Maxwell Model [233,234] postulates that oscillatory data can be fitted using a model incorporating single or multiple modes, each comprised of an elastic, Hookean spring element (E) and a viscous, Newtonian Fluid, dashpot element (η) in series. Multiple modes can be used in parallel to increase the parameters of fitting and improve the quality of fit, however it is recommended to only use one mode per decade of data as shown in Figure 4.6. [233]

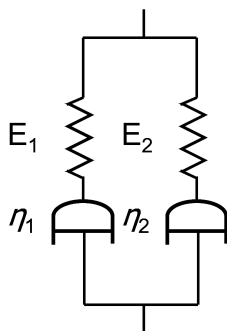


Figure 4.6: 2 Mode Maxwell Model (sometimes referred to as a Burgers Model).

A key property from this model is the relaxation time, τ , which is the ratio between the viscous element and the elastic element, as shown in Equation 4.1.

$$\tau = \eta/E \quad (4.1)$$

This is a theoretical property where times much shorter than the relaxation time will behave as a solid (spring), and times longer than the relaxation time will behave as a fluid (dashpot). As stress is equal across a mode and strain is the summed, a rearrangement and differentiation of Hooke's Law and a rearrangement of the Newtonian law of viscosity allows the following equations (Equations 4.2 and 4.3) to be written:

$$G_a' = E_a(\omega\tau_a)^2/(1 + \omega\tau_a)^2 \quad (4.2)$$

$$G_a'' = E_a(\omega\tau_a)/(1 + \omega\tau_a)^2 \quad (4.3)$$

where a denotes the mode and ω is the angular frequency of the oscillation.

From Figure 4.7, it can be seen that the primary relaxation time slowly increases for the first 30 minutes. During this time, the secondary relaxation time is relatively unchanged and upon deformation the electrode slurry will still revert to viscous behaviour relatively quickly. Then, the primary relaxation time rapidly increases indicating that the gelation is rapidly progressing. After 45 minutes, which is suggested as the maximum processing window of this electrode slurry, the rate of primary relaxation time increase drops. The gel structure is formed, with a macromolecule of connected chains throughout the electrode slurry. After this point, the interconnections between chains strengthen slowly and the gel strength increases.

In terms of the secondary relaxation time, values are much lower, and only change slowly over the period of gelation. The secondary relaxation times denotes the behaviour of the electrode slurry over very short time scales. Below approximately 0.2 s,

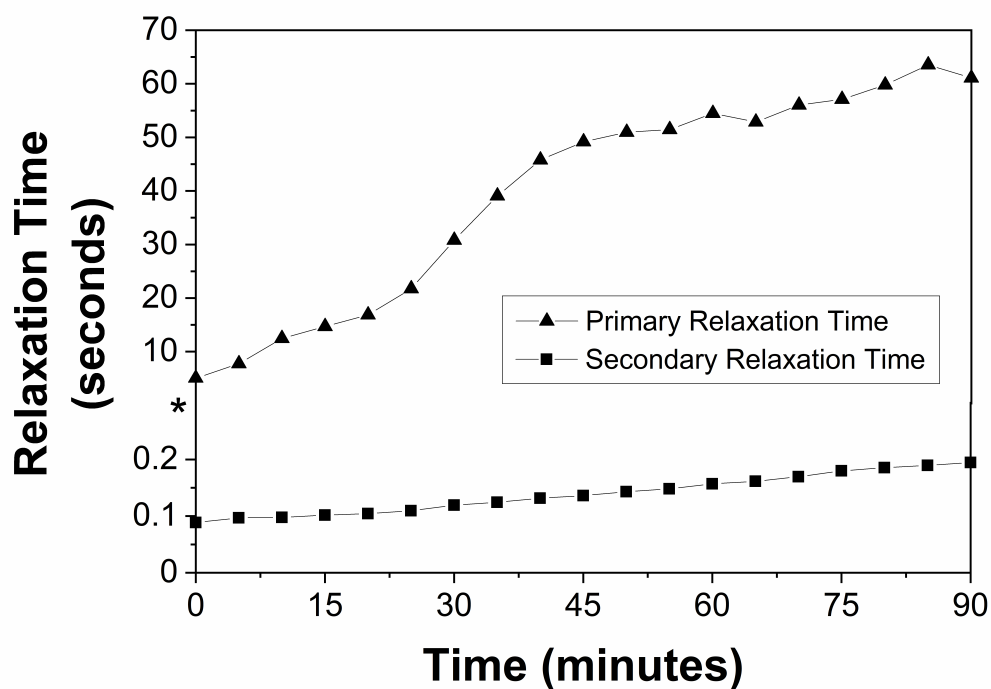


Figure 4.7: Primary and secondary mode relaxation times fitted from the Maxwell Model.

the secondary relaxation time signifies that the electrode slurries exhibit a strong elastic response, similar to that of a yield stress in a Herschel-Bulkley fluid. Above this secondary relaxation time, the strong elasticity of the electrode slurry partially relaxes, and the primary Maxwell mode elastic response dominates. It is only above the primary relaxation time that the electrode slurry will act fully viscous and flow.

4.4.2.3 Ex-situ Fourier-transform Infrared Spectroscopy

Ex-situ FTIR analysis has been used to analyse the chemical changes during gelation. The main groups relating to water, hydroxide, NMP, PVDF and carbonates are discussed, as shown in Figure 4.8. Separate spectra of the individual compounds for comparison can be found in Figure 4.9.

The ex-situ FTIR spectra of the electrode slurry are shown in Figure 4.8. The medium-intensity broad peak at 3442 cm^{-1} , indicative of an OH stretching vibration, can be contributed to surface absorbed water in the electrode slurry and from hydrogen bonding

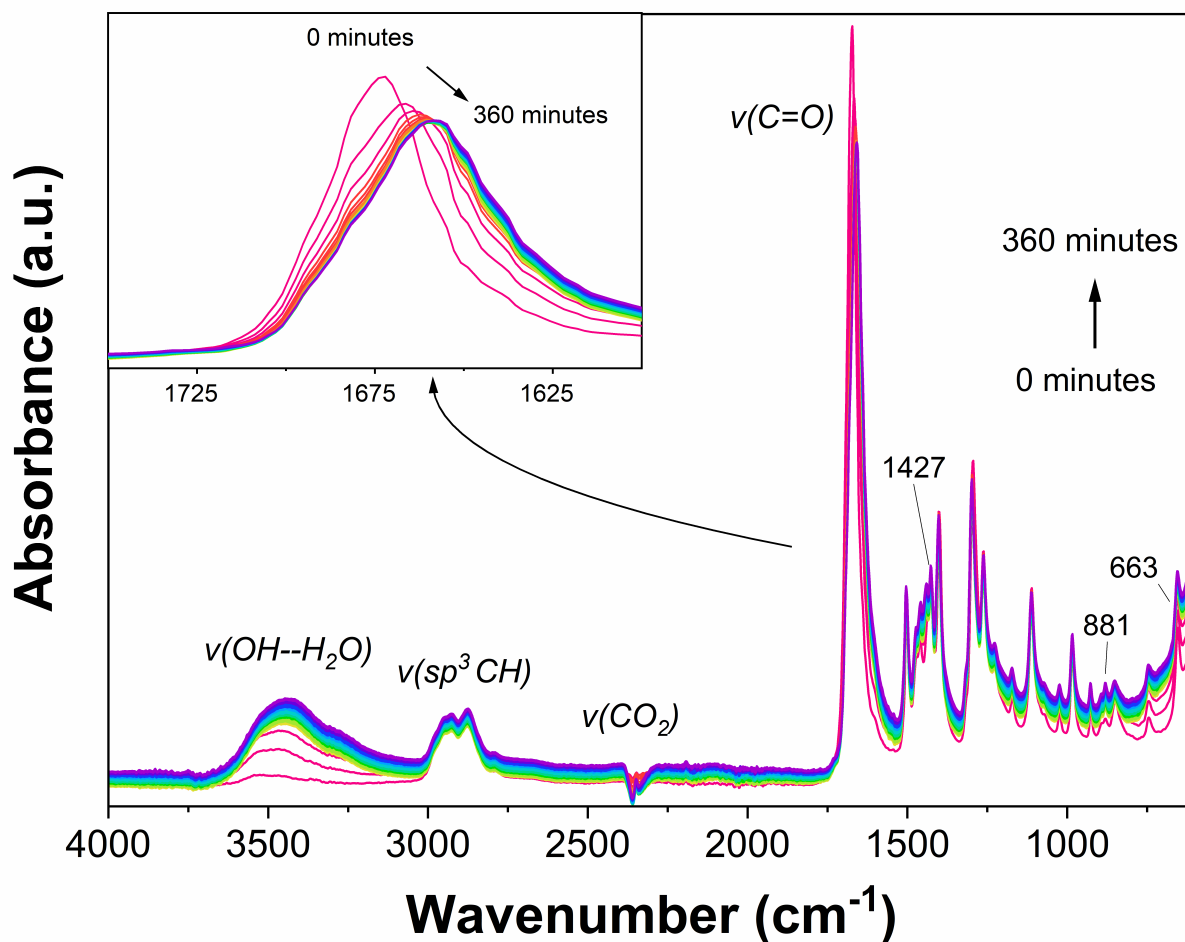


Figure 4.8: Ex-situ FTIR Spectra of the Electrode Slurry.

throughout the slurry. The increase in the intensity of this peak over time demonstrates that more water is being absorbed as the aging progresses and the amount of hydrogen bonding is similarly increasing. During the course of the ex-situ measurements, the OH stretching peak also experiences a broadening, which is consistent with the increased effects of hydrogen bonding.

There is a slight bump at 3300 cm^{-1} , suggestive of a very weak shoulder peak. This peak could be attributed to the OH stretching of metal hydroxides, such as the designation as discussed for the powder FTIR, in Figure 4.2.

The bands located at 3014 cm^{-1} and 2953 cm^{-1} can be assigned to the CH_2 asymmetric and symmetric vibration in NMP. [235] The peak at 2875 cm^{-1} can be attributed the CH

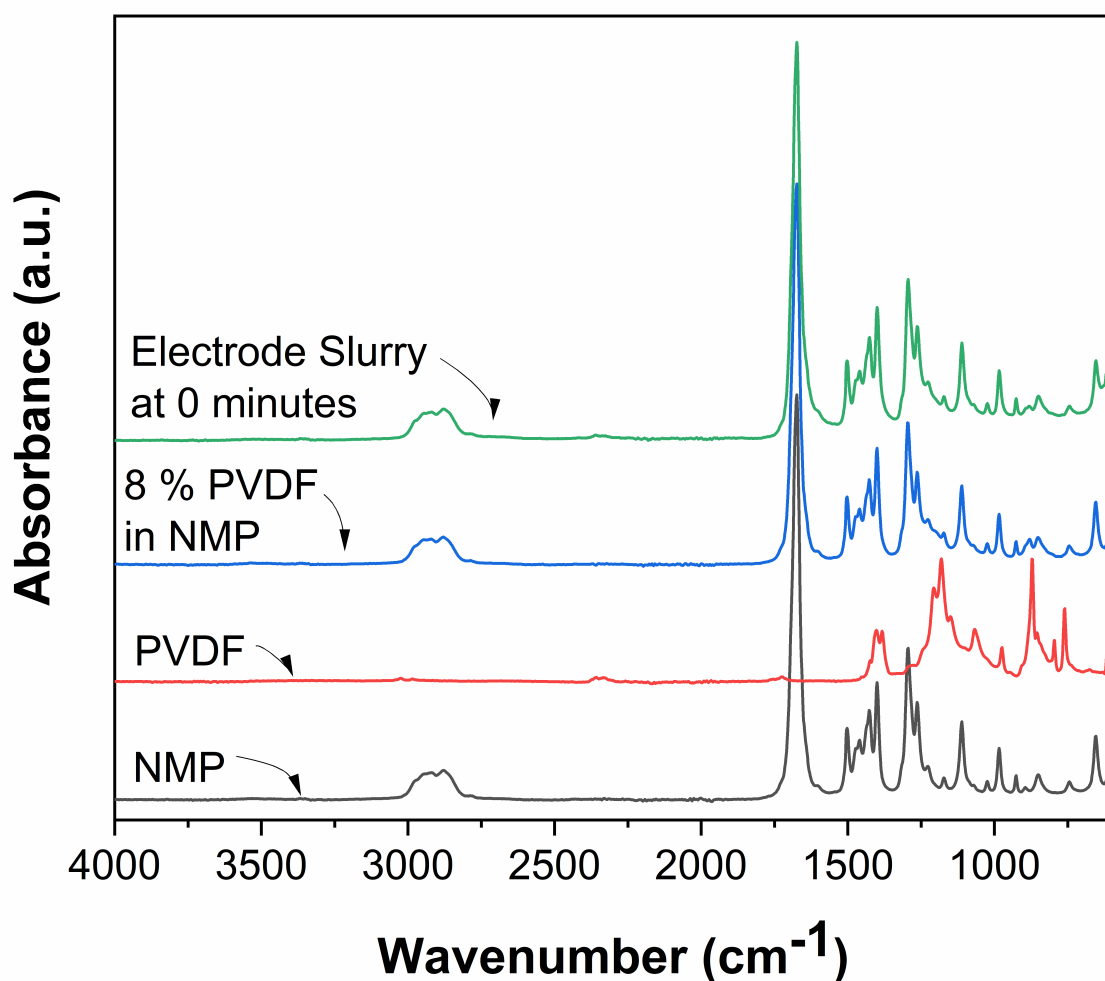


Figure 4.9: FTIR Spectra comparisons of the electrode slurry, NMP, PVDF, and 8 % PVDF in NMP solution.

stretching in sp^3 hybridised carbons, likely belonging to those in the NMP. 2792 cm^{-1} shows a weak peak that could be assigned to the CH stretching in sp^3 hybridised carbon in NMP. The CH_2 bonds in PVDF would similarly show at these points, however, due to the quantities of NMP and PVDF in the electrode slurries, the contributions due to PVDF would be far smaller.

In Figure 4.8 there are two peaks at 2361 and 2341 cm^{-1} which can be easily assigned to asymmetrical peaks due to CO_2 . [218]

The highest intensity peak belongs to C=O stretching peak. γ -lactams, such as NMP,

typically exhibit a stretching at 1750-1700 cm^{-1} . [221] However, the effect of the methyl group on the nitrogen, over a single hydrogen, causes a greater resonance effect that causes the C=O stretching to shift to lower wavenumbers - 1670 cm^{-1} , resulting in a wavenumber that is as expected for NMP.

The remaining peaks that have been highlighted, at 1427 cm^{-1} , 881 cm^{-1} , 663 cm^{-1} , are the positions denoting NaOH from the powder FTIR (Figure 4.2). Across all these spectra, from 0 – 360 minutes (Figure 4.2), it is very difficult to assign these to NaOH. There is a lot of overlap in these positions with those peaks of NMP (as seen in Figure 4.9). However, a lack of NaOH could suggest that it is being used in a reaction (similar to the lack of changes in the intensity of the CO_2 for the active materials, discussed in Section 4.4.1).

There are many peaks being obscured by the high intensity C=O stretching, and so the peaks under this region have been fitted (Figure 4.10). The data shown in Figure 8 is for scans between 0 and 30 minutes. Fitted data for the later scans can be found in Figure 4.11. The fitted peaks under this region include: a growing peak at 1617 cm^{-1} , a peak that shifts from 1647 cm^{-1} to 1637 cm^{-1} , a large peak at 1665 cm^{-1} , a second growing peak at 1681 cm^{-1} and a final peak at 1691 cm^{-1} .

The main peak can be assigned to the C=O bond in the NMP, initially at 1673 cm^{-1} and it shifts to lower wavenumbers over time, 1663 cm^{-1} at 30 minutes. This shift is likely due to hydrogen bonding occurring as water is absorbed into the electrode slurry. Additionally, there is a slight broadening of this peak due to the absorbance of water creating a larger number of environments for this functional group.

Secondly, the broad, low intensity peak, initially at 1617 cm^{-1} , can be assigned to conjugated C=C stretching, as has been previously assigned to alkaline treated PVDF in literature. [205–207] As the aging progresses, there appears to be a very slight shift in this peak, along with a slight increase in the intensity, suggesting that there is an increase in the number of these C=C structures within the PVDF as time progresses.

Finally, the peak initially lying at 1648 cm^{-1} can also be assigned to non-conjugated

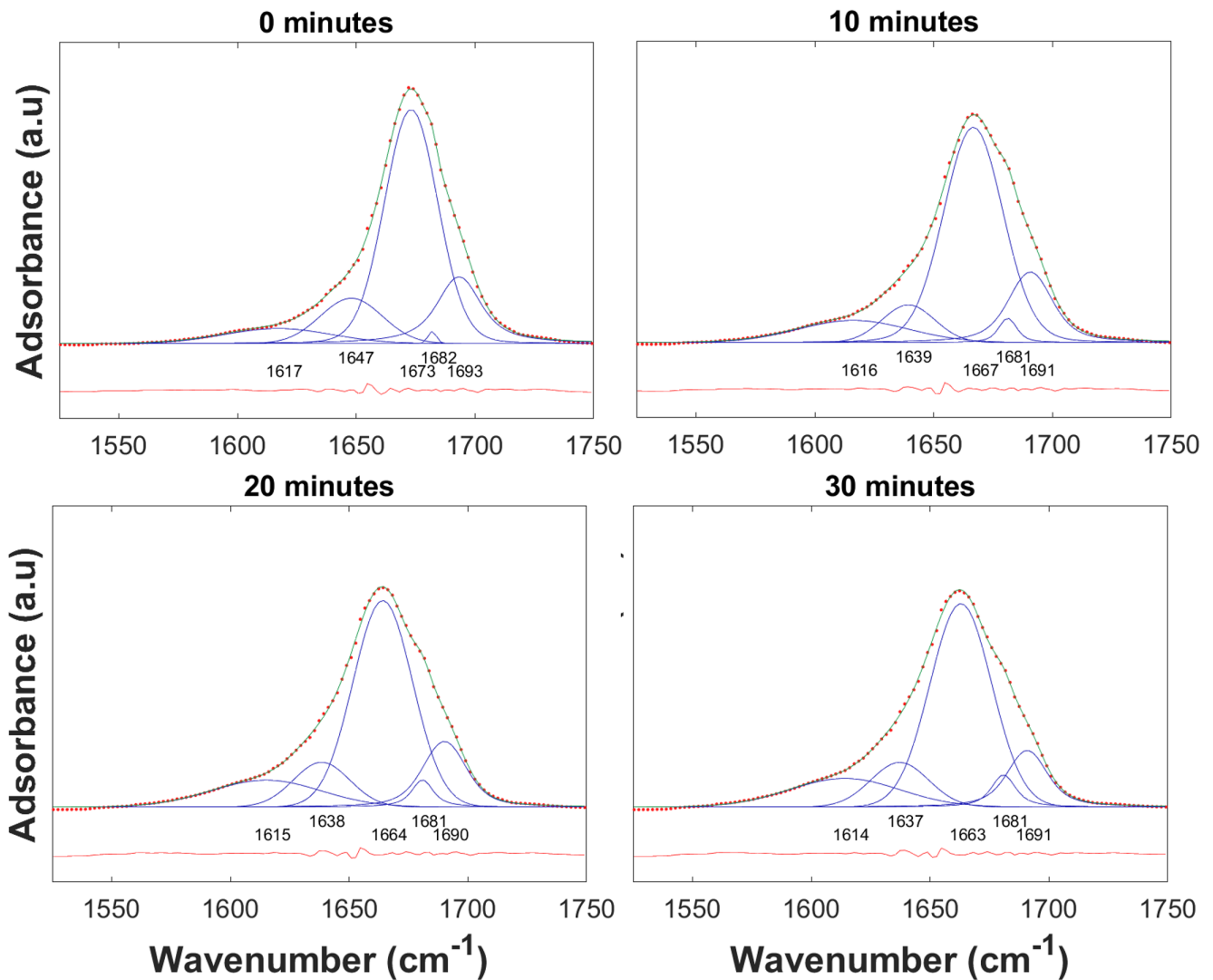


Figure 4.10: Fitted Ex-situ FTIR Spectra of the Aging Electrode Slurry between 1525 cm^{-1} and 1750 cm^{-1} fitted for spectra at 0, 10, 20, and 30 minutes.

C=C structures. [205,236] As the electrode slurry ages, there appears to be a slight shift in this peak, likely due to the effects of hydrogen bonding. There is very little overall change in the intensity of this peak, suggesting that while there may be incremental changes to the amount of non-conjugated C=C structures in the electrode slurry, the overall quantity remains constant, i.e. the rates of production and loss of C=C are equal. Curiously, by comparison of the changes to these two peaks, the quantity of conjugated C=C structures increases while the quantity of non-conjugated C=C structures remains near constant. It can be inferred that the degree of conjugation in the PVDF structure is slowly increasing as the dehydrofluorination reaction progresses. The peak at 1682 cm^{-1} ,

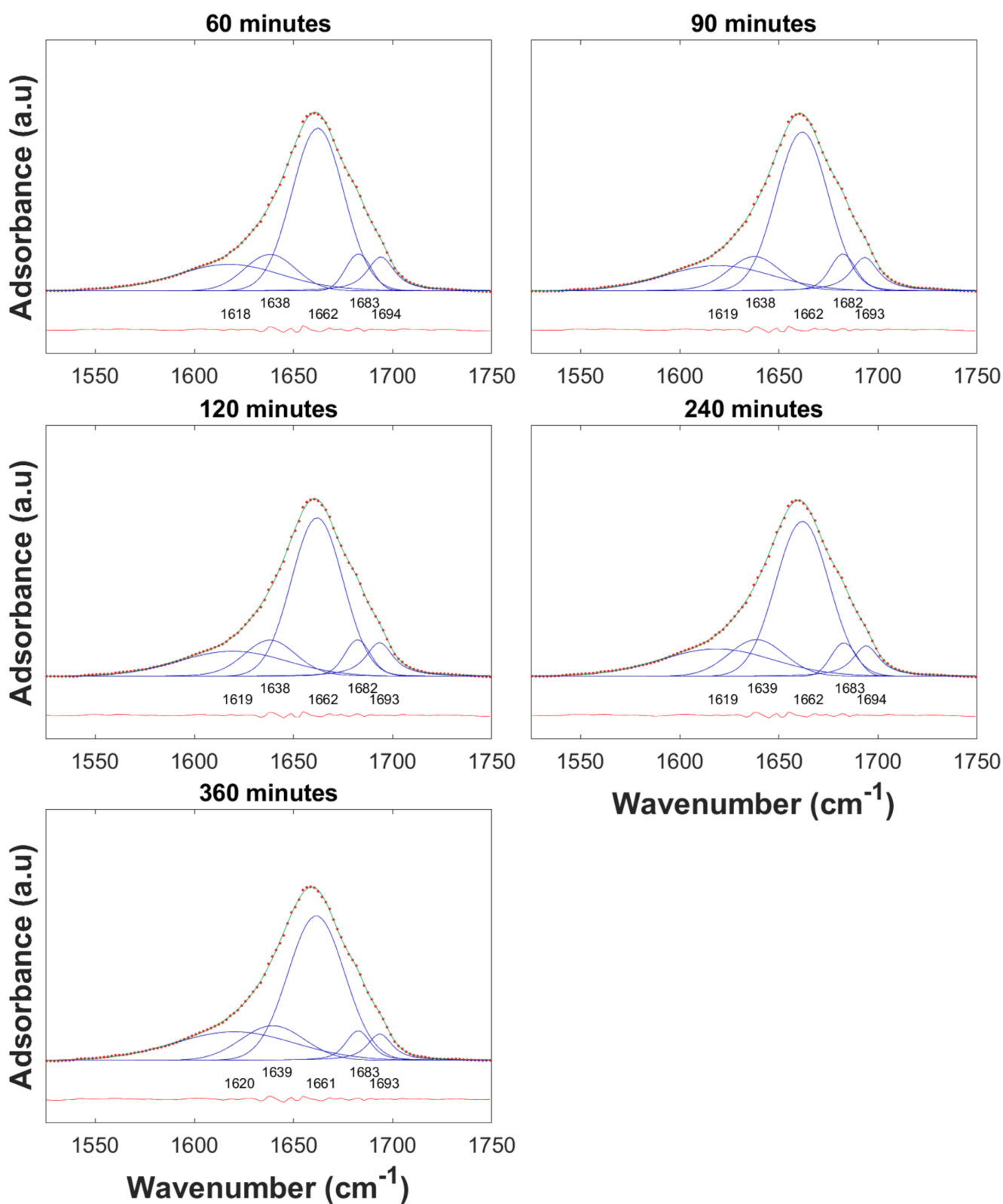


Figure 4.11: Fitted Ex-situ FTIR Spectra of the Aging Electrode Slurry between 1525 cm^{-1} and 1750 cm^{-1} fitted for spectra at 60, 90, 120, 240, and 360 minutes.

later at 1681 cm^{-1} , indicates a second C=O stretching occurs, additional to the C=O stretching of NMP. NMP has been previously reported to degrade under basic conditions, causing a ring opening reaction to occur, forming 4-(methylamino) butanoic acid. [209] As the electrode aging progresses, this initially sharp low intensity peak grows in intensity, consistent with a formation of 4-(methylamino) butanoic acid.

Overall, due to the presence of the C=C structures, both conjugated and non-conjugated, evident in the fitted FTIR data, it is most likely that a dehydrofluorination reaction is occurring, creating these structures.

4.4.3 Electrode Characterisation

4.4.3.1 X-ray Photoelectron Spectroscopy - XPS

For further chemical analysis, the coated and dried electrodes were analysed using XPS. These electrodes (for XPS analysis) were coated immediately after mixing of the electrode slurry and then allowed to dry for 40 minutes while exposed to air. This allowed the reaction to occur as the electrodes were drying and, hence, the chemical changes to be observed without the gel network percolating the entire electrode slurry, rendering it completely uncoatable.

Figure 4.12 shows the F1s XPS spectra, with three distinct components, two of which relate to the PVDF, while the feature at 684.3 eV can only be assigned to NaF. The presence of NaF is due to an expulsion of HF from the PVDF structure, followed by a reaction with NaOH forming NaF and H₂O, as shown by Figure 4.13 and Equation 4.4.



By comparison of the areas, an elemental quantification can be obtained, and an idea of the degree and progression of the reaction can be noted – 81.3 % for CF₂CH₂, 3.0 % for CF₂CF₂, and 15.7 % for NaF Assuming that all of the expelled HF reacts to form

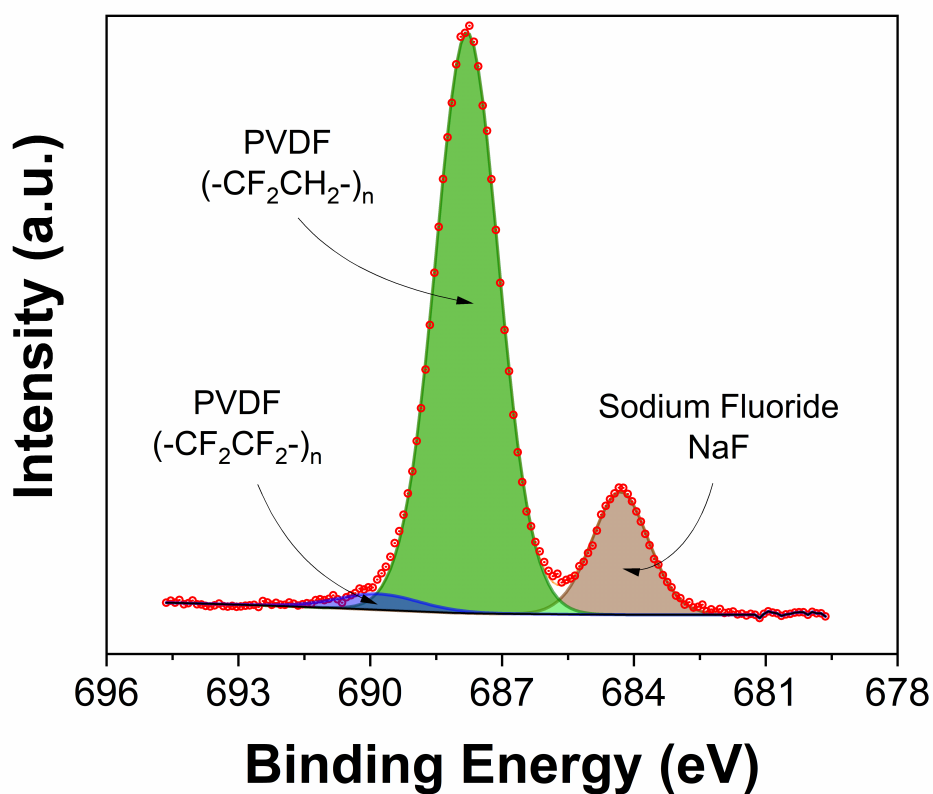


Figure 4.12: F1s X-ray Photo-emission Spectroscopy of the as-coated Electrode

NaF, after the aging reaction has been allowed to progress, 15 % of the fluorine in the PVDF was expelled from the polymer and so 15 % of the gelled PVDF binder contains conjugated or cross-linked structures.

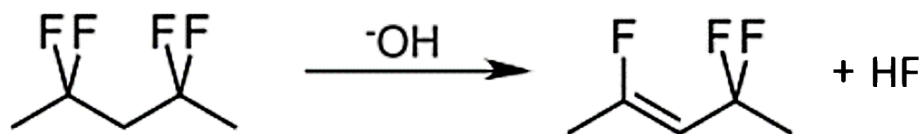


Figure 4.13: Dehydrofluorination of PVDF.

4.4.4 Electrochemical Characterisation

The effect of the electrode slurry aging was further examined using electrochemical analysis. Electrodes were coated at different intervals after the mixing was completed, with electrode coating at 40 minutes being just possible. Beyond this time the electrode slurry was too solid-like to coat.

Figure 4.14a shows the capacity curves for the material in a half cell setup for the first and fifth cycles. It is evident that there is a charge transfer plateau at 2.8 V, which can be clearly seen for the charge and discharge curves in the first cycle.

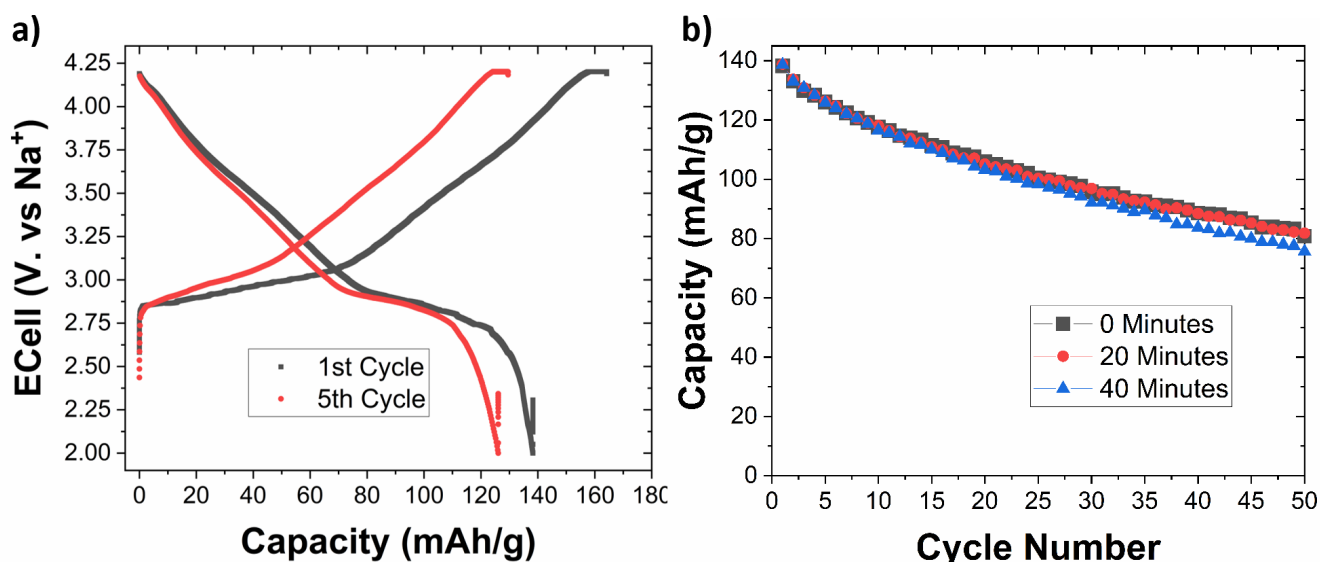


Figure 4.14: a) Half-cell capacity curves for the 1st and 5th cycles for the electrode coated 0 minutes after mixing. b) Half-cell capacity vs cycle number for electrodes coated at 0, 20, and 40 minutes after mixing.

There are, however, notable changes due to the electrode slurry aging, as seen in Figure 4.14b. Over 50 cycles, the capacity of the material reduces from 138 ± 1.5 mAh/g to 81 ± 1.8 mAh/g (averages and standard deviations calculated from no less than 3 cells). The formation of NaOH due to the surface reactions of the active material (Figures 4.2 and 4.3), causes a loss of sodium, the charge carrier, from the active material which leads to a reduction in the capacity of the cells. By coating the electrode slurry 20 minutes after

mixing, there appears to be very little change in the life of the cell; the chemical changes due in the electrode slurry at this point are not enough to affect the life of the electrode. Coating after 40 minutes of mixing means these chemical changes seem to have a more sizeable effect and a steady reduction from 138 ± 1.7 mAh/g to 75 ± 1.8 mAh/g over the 50 cycles is observed.

During electrode cycling, there is a reduction in capacity of the material, as evident in electrodes coated 0 minutes after mixing. This active material is unstable when cycling to 4.2V, regardless of any surface reactions prior to being assembled into a cell. However, as stated, this reduction increases for the electrodes coated 40 minutes after mixing. It seems evident that the formation of NaOH, with a loss of sodium from the active material, causes a structural change that exacerbates the inherent instability of the material when cycling.

4.5 Discussion

The FTIR and XPS results demonstrate that a dehydrofluorination reaction is occurring during the aging of the electrode. This is a base catalysed reaction of PVDF in which a carbon-carbon double bond is formed as a result of the elimination of hydrogen fluoride (HF) units from the polymer, as shown in Figure 4.15, which has been widely reported in PVDF literature. [199, 207, 237, 238] The formation of these C=C structures allows a crosslinking between PVDF chains to occur, creating a gel network throughout the electrode ink.

The presence of a base, NaOH, has been confirmed from FTIR and SEM analysis (Figures 4.2 and 4.3). In similar lithium-ion battery systems, it has been shown that LiOH is evolved first, followed by the formation of Li_2CO_3 . [96] However, the analysis methods used in this study were unable to detect the presence of Na_2CO_3 and it is possible that the carbonate forms over larger timescales than those used in this research. Regardless, as this study has shown that NaOH is responsible for the gelation of the electrode slurries,

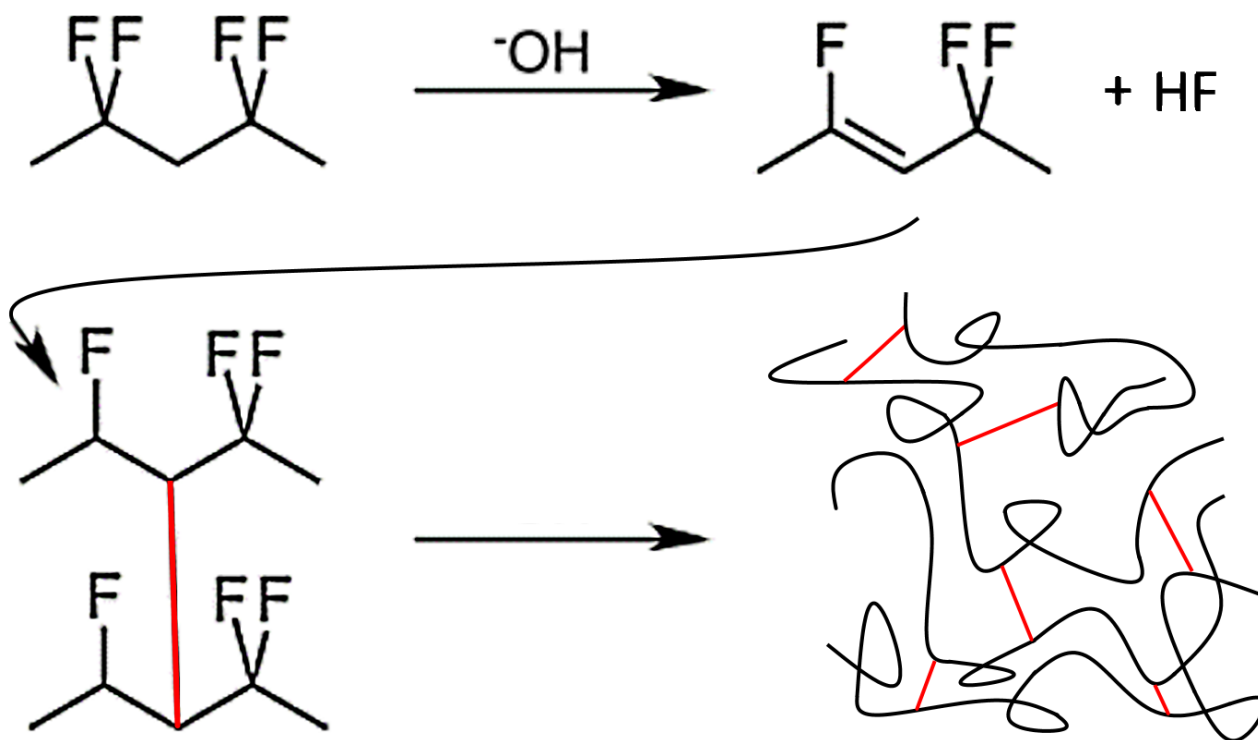


Figure 4.15: Dehydrofluorination of PVDF and subsequent crosslinking. Crosslinks between PVDF chains have been highlighted in red

it is suggested that the formation of LiOH could be the cause of gelation in analogous lithium cathode electrode slurries.

The dehydrofluorination and subsequent crosslinking has been verified through interpretation of the phase angle rheology, Figure 4.5b, where the later trend towards 1-2 % phase angle, coupled with the convergence of moduli at all measured frequencies with observation time depicts a chemical gel, as opposed to a physical gel.

If the assumption that the storage modulus, G' , is directly linked to the gel structure is made (Figure 4.5a), it can be inferred that there are three stages of gel development. These can be observed in the plot of the primary relaxation time as a function of time, as seen in Figure 4.16. The first stage is an initially slow rate, whereby the quantities of base are still increasing to the point of saturation and the dehydrofluorination is occurring, but the crosslinking is still slow. The second stage occurs at a faster rate, whereby the

highest concentration of C=C structures exists, and crosslinking can readily occur. As this reaction progresses, the quantity of C=C structures decreases until, the third stage where the remaining C=C structures are able to crosslink between chains at a slower rate.

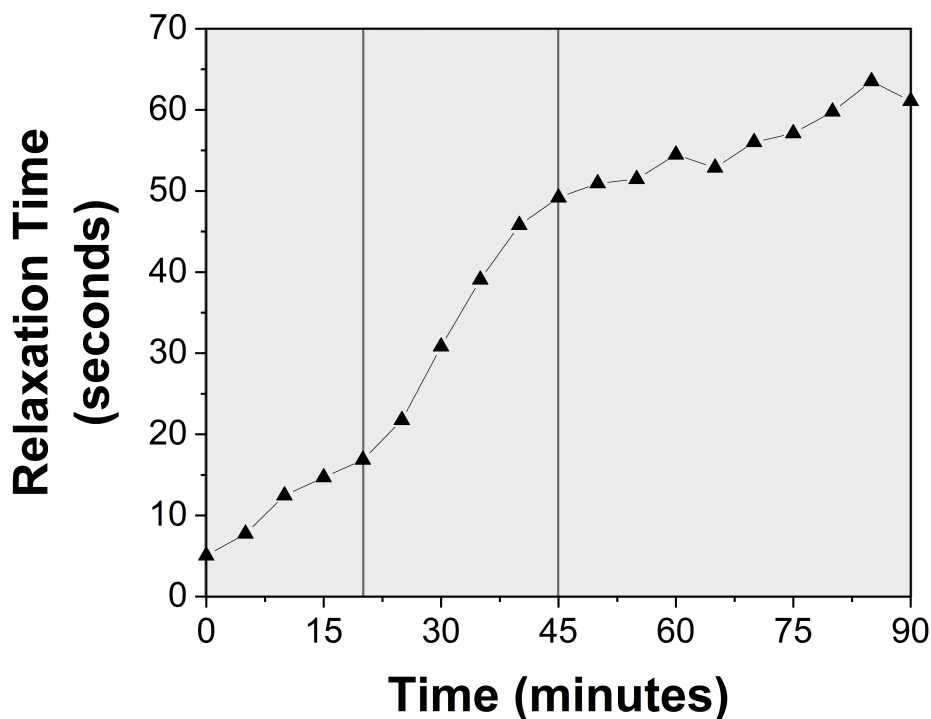


Figure 4.16: Primary mode relaxation time, showing the 3 proposed stages of gel development.

Another observation that is suggested by the FTIR data (Figures 4.8, 4.10, and 4.11) is the hydrolysis and ring opening reaction of NMP, Figure 4.1, which has been detailed in literature. [209,211]

This reaction occurs with a base present and, by examining the FTIR data in Figures 4.8, 4.10, and 4.11, there is a suggestion that this reaction is occurring. However, due to the very low intensities of the peaks, the presence of 4-(methylamino) butanoic acid either cannot be confirmed, or it exists in very small quantities. Thus, it likely does not contribute significantly to the gelation of these electrode slurries.

In terms of the electrochemical behaviour, the loss of sodium from the active material due to a reaction forming NaF has only a small effect on the electrode capacity and

capacity decline during cycling (Figure 4.14). However, it is worth noting that these are half cells, and an excess of sodium ions is present in the system. A greater effect of this sodium loss might be displayed in full cells, and will be explored in future work.

In this system the major challenge with electrode aging remains the gelation and the affect this has on the coatability. Suppression of this gelation would mean this material or analogous materials (for both sodium and lithium ion batteries) may be more freely tested, examined, and optimised. One potential solution to this problem is to coat the surface of these electrode materials with a sacrificial or blocking material to prevent exposure to air and so stop sodium surface species from forming. An alternative may be the use of an additive in these electrode slurries that is able to absorb water or pacify the surface.

4.6 Conclusions

Gelation leading to difficulties in coating PVDF and NMP electrode slurries is widespread and affects many materials, especially high nickel content layered O3 sodium-ion cathode materials. Beginning with the instability of the powder materials, the source of this gelation has been investigated along with its effect on the electrode slurry and subsequent electrodes.

$\text{NaNi}_{1/2}\text{Mn}_{1/4}\text{Ti}_{1/8}\text{Sn}_{1/8}\text{O}_2$, a O3-type layered oxide material, prepared by a solid state method was investigated for its processability and stability in electrode manufacturing. In order to satisfy the first objective, the effects of air on the active material were characterized using FTIR and SEM, and sodium hydroxide was observed over prolonged exposure.

Satisfying the second and third objectives, the stability of the slurries for electrode coating, was further investigated using rheology, FTIR and XPS characterisation. Sodium fluoride was observed through XPS in the electrode slurries after mixing and gelation. This is formed due to the reaction of sodium from the layered oxide with fluorine from the PVDF. It has therefore been established that, chemically, the dehydrofluorination

reaction and subsequent crosslinking are the route cause of the electrode slurry gelation.

From the time dependent rheological studies a three stage structure development in the electrode slurry was observed. First the PVDF is defluorinated, which causes cross-linking of the chains, which in turn causes a non-reversible chemical gelation of the slurry. The three stages of gelation are likely related to the concentrations of C=C bonds. Initially there is the creation of saturated structures, via a dehydrofluorination stage. Secondly there is a crosslinking stage, which results in the highest rate of gelation. Finally, a slow crosslinking stage, whereby the rate of gelation is limited by the low quantity of saturated structures.

Regarding the fourth objective, analysis of the relaxation time establishes a nominal processing window of 20 minutes. 20 minutes after mixing demonstrates a point just before the rapid increase of the electrode slurry relaxation time.

For the final objective, electrochemical testing in sodium-metal anode half-cells with coatings produced 0, 20, and 40 minutes after mixing showed limited initial capacity differences. However, after 50 cycles, an increased capacity decline was observed for electrodes coated after 40 minutes of mixing. Electrodes coated 20 minutes after mixing demonstrated a more consistent capacity decline to those coated immediately after mixing, further reinforcing the nominal processing window of 20 minutes.

In summary the alkalinity of the sodium layered oxide, due to the sodium hydroxide formation, causes defluorination and cross-linking of the PVDF binder material. These cross-linking reactions cause a gelation of the electrode slurries. The increased insulating inorganics (NaF), formed as a result of the liberated HF in the dehydrofluorination, cause increased capacity fade during cycling. Therefore, in order to improve the stability and cycling performance of these highly alkaline oxides, changes in the methodology for mixing and coating are required.

Chapter 5

Technique Development for the Analysis of Gelation in Electrode Slurries

5.1 Introduction

During electrode coating, a poorly mixed electrode slurry with many large agglomerates will result in inhomogeneous electrodes, despite maintaining coating parameters. [239] A poorly mixed or gelled electrode slurry may not even be coatable because it may possess an apparent viscosity which is too high or too low to be processed in the coating equipment. The slurry rheology, which is a function of its microstructure, is therefore critical; surface and bulk rheological properties can dictate coating flow performances. [127] As a simple example, a slurry with a large amount of carbon black agglomerates will exhibit higher apparent viscosities. [239]

Chapter 2 outlined previously the importance of homogeneity in electrode coatings. This can be defined in terms of the thickness, density distribution and particle and material distribution, [240] as any defects in this uniformity can result in a poor rate performance [241] and localised aging of the electrode. [109]

Chapter 4 has demonstrated that sodium cathode electrode slurries undergo a gelation that progresses with time. Should this be detectable by an on- or off-line method upstream of the final coating step, this would enable interventions to be made in the process. This chapter explores the use of rheological measurements in this capacity. An added benefit is that rheological analysis can be used to infer electrode properties before coating has been performed. For example, electrode slurries with elastic properties may demonstrate shear memory, and certain alignments of slurry components can be retained, which can influence the conductivity. [127]

As will be explored in this chapter, the standard rheological measurements initially carried out to analyse electrode slurries were found to be unsuitable for the investigation of this gelation. This chapter presents experimental work carried out to modify and optimise rotational and oscillatory rheology measurements for examination of the gelation process. The results of these measurements are discussed in the light of the expected and possible electrode microstructures formed.

5.1.1 Rheological Analysis for Electrode Slurries

The academic literature describes the rheological analysis of electrode slurries via many different methods. Rotational measurements are useful for understanding the flow behaviour and shear dependant nature of the electrode slurries. [110, 165] Rotational rheology utilising flow curves has been used to compare various slurry processing methods, [110, 164–167] or to analyse the aging of an electrode slurry. [242] Similarly, analysis has been performed to analyse the effect of additives on the electrode slurries [139, 243] or the comparison of different binder systems. [138, 244] These flow curves have also been used to fit the electrode slurries as generalised non-Newtonian fluids, such as a power law fluid. [165]

While the flow curve measurement using rotational rheometers is effective, in many cases, additional measurements, such as oscillatory measurements, have been sought. [138, 139, 166, 167, 243, 244] Oscillatory measurements can differentiate between

the elastic, (G') solid, elements of the electrode slurry and the viscous, (G'') flow, elements. [127,244] By comparing the elastic and viscous elements it is possible to infer the microstructural properties of the slurry, such as the settling behaviour of the particles [244] or the formation of a gel structure. [243]

Despite these methods, a precise determination of the coatability of the electrode slurry is still poorly researched. For other applications, such as ink-jet printers, the relationship between the rheological properties and the printability has been investigated. [245] Woo *et al* (2013), compared the plots of viscosity, and elastic and viscous modulus with the drop formation accuracy of ink dispersions with the higher viscosity inks demonstrating unstable printing performance. Additionally, for the unstable dispersions, the elastic modulus dominated over the frequency range tested. For the normal and stable dispersions, the viscous modulus was significantly higher for the majority of frequencies. [245] However, as discussed by Reynolds *et al.*, 2021, the high weight percentage of solids in electrode slurries causes the elastic and viscous moduli to be similar. Hence, this particular use of coatability testing is unfeasible. [127]

Similarly, understanding coatability using the rotational rheology in the method used by Woo *et al.*, 2013, is also unfeasible. Rotational rheology can be used to calculate a processing range of feasible apparent viscosities for electrode slurries. [127,138] This is typically done by finding the viscosity of the electrode slurry at the lowest shear rate of the coater, where it will suitably flow. [127] The electrode slurries tend to be shear thinning [165] and so higher apparent viscosities can be handled by using higher shear rates on the coater. However, this method does not always solve the problem, and defects and inhomogeneous coats may still occur. [165]

The electrode slurries that are investigated as part of this work change over time, and there is generally a 'coatability window' for which electrode coating is possible, past this point the electrode slurry starts to become a solid and is unpourable. The precise coatability window is difficult to define. Due to this time dependency, standard shear rate rheology measurements do not work, as the electrode slurry has changed in structure

by the time a full sweep has been performed. In this work, the current methods for rheological analysis of the electrode slurries are described, with the time dependency of the slurry structure explored. A methodology has been developed that illustrates the changes in the slurry properties over time, so that a coatability window can be measured

5.1.2 Practical Shear Rates

As discussed, it is important to define and understand the shear rates experienced by the electrode slurry during the coating stage. This is vital for both rheological testing and comparison of electrode coating methods.

When an electrode slurry is deformed, as demonstrated by a velocity profile in a coating device, Figure 5.1, shearing occurs. The severity of the velocity profile determines the shear rate, a steeper velocity gradient will correspond to a higher shear rate, as shown in Figure 5.1. By using infinitesimal layer thickness, local shear rates can be approximated, such as with Equation 5.1. Bulk shear rates can be approximated taking the velocity difference and layer thickness over the whole electrode slurry.

$$\dot{\gamma} = \frac{dv}{dx} \quad (5.1)$$

where $\dot{\gamma}$ is the shear rate, v is the velocity, and x is the separation distance. [127]

It is important to define the shear rates of coating equipment, lab scale and commercial, as due to the different geometries, and speeds, and coating gap size used, the rates can vary greatly. For example, by considering a doctor blade coater, as used throughout the course of this research, such as described in Figure 5.1, the shear rates can be simply approximated. However, a few assumptions are required. Firstly, there is no slip condition – the speed of the slurry in contact with the blade of the coater is equal to the speed of the coater. Similarly, the speed of the slurry in contact with the current collector is equal to zero (for a doctor blade coater the current collector is clipped down and motionless).

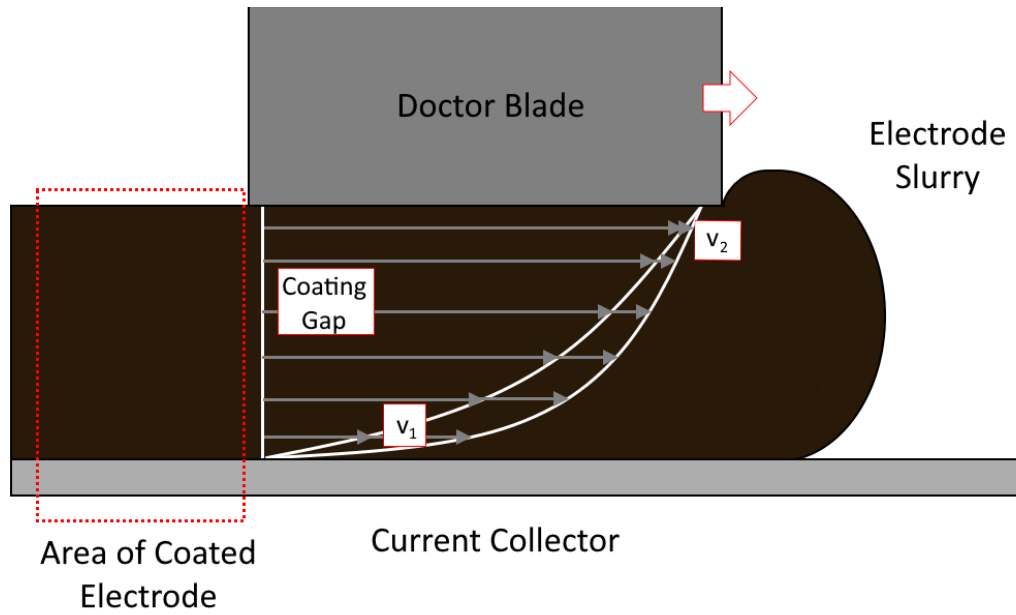


Figure 5.1: Velocity profile and shear in a doctor blade coater.

Table 5.1: Calculated Shear Rates for the Lab Doctor Blade Coater.

Coating Gap (μm)	Shear Rate (s^{-1})
50	167
100	83
150	56
200	42
250	33
300	28
350	24

Additionally, the shear rate of the coater occurs directly below the blade – slurry effects on either side of the coater are not considered.

By using the slowest speed on the doctor blade coater, 0.5 m/min (or 8.33×10^{-3} m/s), the shear rate can be approximated over a range of coating gaps, as seen in Table 5.1.

Clearly, from Table 5.1, it can be noted that there is a large range of possible shear rate and highlights the issue with analysing the rheology of the electrode slurry at a single shear rate.

Similarly, different coaters will have different shear rates. A large-scale electrode coater, such as a reel-to-reel coater, where the current collector is moving in the same

direction as the slurry, has a very small difference in speeds, as shown in Figure 5.1. It will produce shear rates that are much lower. A shear rate of 10 s^{-1} is fairly easy to produce for a reel-to-reel coater – for a doctor blade coater it would require a gap size of more than 1 mm, which is excessively large for this application.

Additionally, the shear rates within a mixer will likely be far higher, creating an even larger range of possible shear rates.

5.1.3 Oscillatory Rheology

Rotational measurements can measure the viscosity of the electrode slurry at specified shear rates, making this method useful for pairing with particular coating instruments.

Oscillatory measurements, on the other hand, differ in a few ways. Where rotational measurements tend to limit shear rate, and measure shear stress, oscillatory measurements have additional variables that can be limited. Measurement frequency, which can be defined as the rate of oscillations, can be thought of as an observation time of measurements. A higher frequency relates to a smaller observation time, whereby there is very little time between deformations and measurements.

The amplitude of measurements is the strain of measurements and can be defined as how much deformation occurs. It can be calculated using the following equation,

$$\text{Strain}(\gamma) = \frac{r}{h}\theta \quad (5.2)$$

where r is the radius of the plates, h is the separation distance between the plates, and θ is the angle of the plate deformation (in radians).

By using oscillations as opposed to rotations, these measurements are able to distinguish between the elastic and viscous contributions to the viscosity.

5.1.4 Experimental Models

Valuable insights into the structure developed during the gelation of the electrode slurry can be gained from experimental models.

5.1.4.1 Polymer Models

Several polymer models were considered for the modelling of these electrode slurries. These included the: Rouse Model, [246, 247] Kremer-Grest Model, [248, 249] Arm Retraction Model, [250] and the more generalised and expandable, Maxwell Model. [250, 251]

Out of the fundamental polymer models, the Rouse Model, which uses beads and harmonic springs to model the polymer chains, [247] and the Kremer-Grest Model, which utilises an entangled tube model, [249] are the simplest of those considered, and do not consider solid particles. The Arm Retraction Model, which explores entangled monomer units, that are retracted and pulled in by larger polymer arms, seems more suitable for these electrode slurries. However, like the Rouse and Kremer-Grest models, this model is specifically tailored to monodisperse systems, where only one molecular weight of polymer is accounted for.

For electrode slurries, especially where PVDF is used, typically a polydisperse polymer is used, that encompasses several molecular weights. Furthermore, the system in these electrode slurries is far more complex, with a polydisperse polymer and solid particles mixed in. It is far more suitable to utilise a generalise and tailorable model that can be fitted to experimental data.

5.1.4.2 Generalised Maxwell Model

The Generalised Maxwell Model can capture the relaxation behaviour of polymers in certain time ranges. [233, 234] It postulates that oscillatory data can be fitted using a model incorporating single or multiple modes, each comprised of an elastic, Hookian

“spring” element (E) and a viscous, Newtonian Fluid “dashpot” element (η) in series. Multiple modes can be used in parallel to increase the parameters of fitting and improve the quality of fit (as shown in Figure 5.2). [233] The initial elastic modulus, E_∞ , is the model’s elastic modulus at $t = \infty$. It is used to predict the model’s behaviour at large timescales. The properties and uses of the Maxwell Model make it, or some variation of it, ideal for this application.

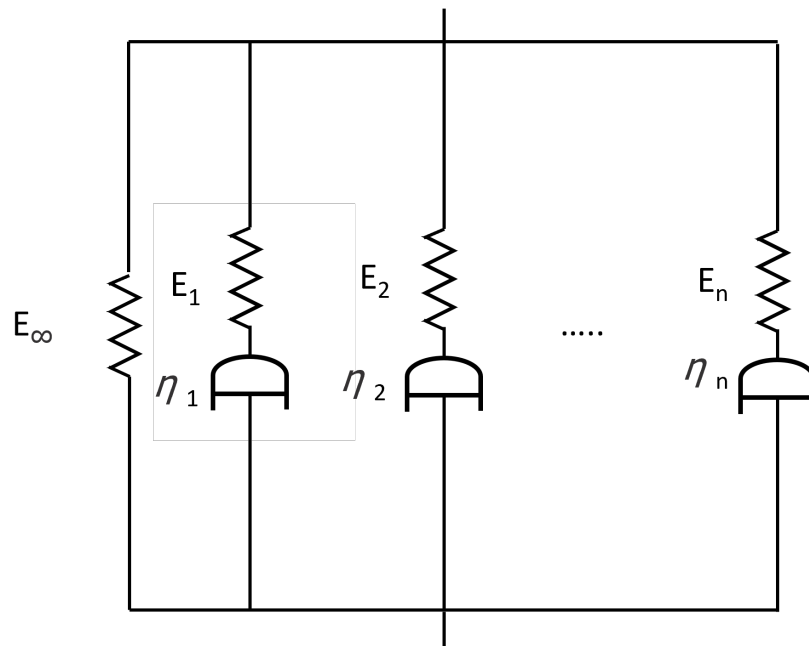


Figure 5.2: Generalised Maxwell Model.

5.1.4.3 Expanded Maxwell Model

An initially proposed use of the Maxwell Model was an expansion and selection of the generalised model. Based on the methodology used in Electrochemical Impedance Spectroscopy (EIS), whereby intrinsic properties and mechanisms of electrochemical cells can be fitting to equivalent circuit models, a similar methodology was hypothesised for this application, as shown in Figure 5.3.

In one iteration of this Expanded Maxwell Model, it is proposed that the elastic element, E_1 , and the viscous element, η_1 , are expanded and fitted to a distribution relating to the polydisperse PVDF. This would be fitted to the molecular weight distribution of

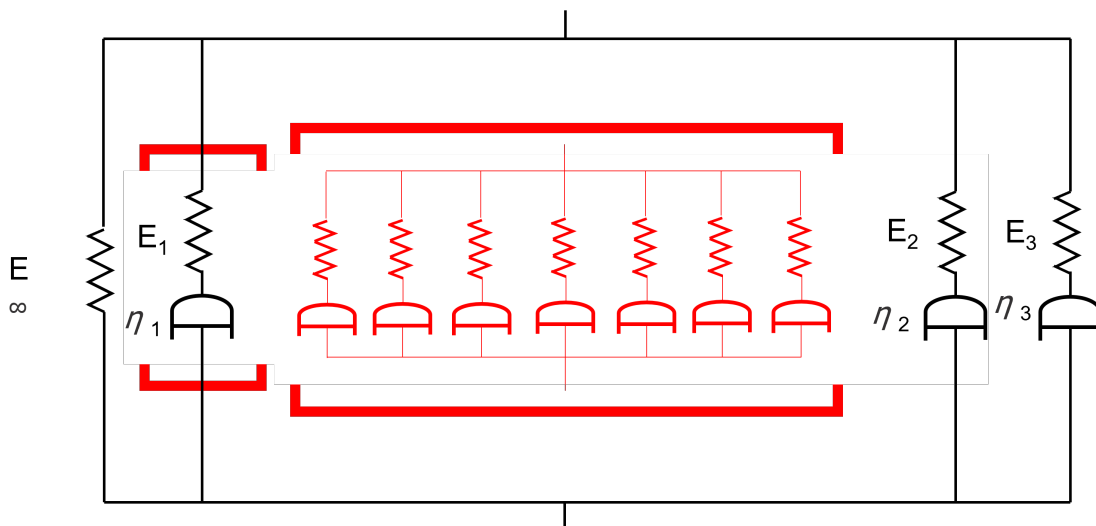


Figure 5.3: Proposed Expanded Maxwell Model.

the polymer binder, and it is assumed that this would remain fixed throughout the data. Secondly, the next set of elements, E_2 and η_2 , would relate to the entanglement of polymer chains and contributions to the solid particles. This would be fitted from initial electrode slurry data (i.e. at $t = 0$ minutes), and would, similarly, be fixed through the rest of the data. The final set of elements, E_3 and η_3 , would be free and fitted to each time set of frequency data. It was thought that this would relate to the gelation of the electrode slurry and the structural development in the electrode slurry could be traced through this element.

Ultimately, however, this proposed model did not make it into practice. Information of the molecular weight distribution is not easily available from the manufacturers, Solvay. Instead, it is merely stated as a distribution being between 1,000,000 and 1,100,000 gmol^{-1} . Furthermore, by fixing certain modes and allowing others to be freely fitted, there is a danger that rheological changes can be attributed incorrectly. For instance, any changes and development to the entanglement of polymer chains would be attributed to the gelation and structural development of the electrode slurry.

5.1.4.4 Reduced Maxwell Model

Ultimately, the Maxwell Model was fitted to fewer modes, such as the one seen in figure 5.4. In this model, the initial elastic modulus, E_∞ , which is used to predict the model's behaviour at large timescales, is removed. This is done as, due to the changing structure, the initial elastic modulus is unable to track the gelation of the electrode and extrapolation to larger timescales would be inaccurate.

An important variable that can be extracted from this model is the relaxation time, which is the ratio between the viscous element and the elastic element.

The relaxation time (τ) can be calculated using Equation 5.3: [233]

$$\tau = \frac{\eta}{E} \quad (5.3)$$

This relaxation time is a theoretical property that states times much shorter than the relaxation time will behave as a solid (spring), and times longer than the relaxation time will behave as a fluid (dashpot).

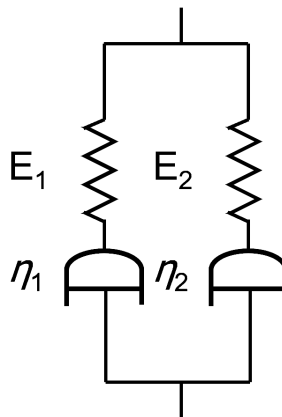


Figure 5.4: 2 Mode Maxwell Model (sometimes referred to as a Burgers Model).

Once the relaxation times have been extracted from the model, they can be plotted against time and the development of the polymer structure can be observed.

5.1.4.5 Akaike Information Criterion

The difficulty with using a Maxwell Model such as this is determination of the number of modes to use. One method to compare the number of modes is by using a statistical method such as Akaike Information Criterion. Akaike Information Criterion (AIC) is a statistical method that can be used to analyse the quality of a fitted model and rank competing models. [252–254] AIC uses a quality of fit, such as residual sum of squares, the number of data points the model has been created from, and the number of parameters in the model. A calculation of the value can be found in Equation 5.4:

$$AIC = n \left[\ln \left(\frac{RSS}{n} \right) \right] + 2k \quad (5.4)$$

where n is the sample size, k is the number of parameters, and RSS is the value of residual sum of squares. [252] For smaller data sets, typically where n/k is less than 40, a second-order bias correction is required, leading to a corrected Akaike Information Criterion (AIC_c). [252–254] Calculation of AIC_c is performed using Equation 5.5:

$$AIC_c = AIC + \frac{2k(k+1)}{n-k-1} \quad (5.5)$$

From Equation 5.5, it can be noted that for very large data sets, where n tends to large numbers, the value of AIC_c approximates to AIC. As the values of AIC (or AIC_c) are mostly arbitrary and completely dependent on sample size and number of parameters, they need to be rescaled based on the minimum AIC, such as Equation 5.6:

$$\Delta_i = AIC_{(c,i)} - AIC_{min} \quad (5.6)$$

where Δ represents the rescaled and weighted value, and i is the index for each model.

By using this equation, the “best” model will have a score value of 0, as it will have the minimum AIC. Complete comparison between models is conveniently done by calculating weighting of their respective scores against one another, such as with Equation 5.7.

$$w_i = \frac{e^{-\frac{\Delta_i}{2}}}{\sum e^{-\frac{\Delta_i}{2}}} \quad (5.7)$$

By using Equation 5.7, the Akaike Weights, w_i , for each model can be calculated where all values sum to 1.

5.2 Aims and Objectives

The aim of the work presented in this chapter was to develop a set of robust and reliable experimental methods to enable rheological characterisation of the gelling electrode slurries. This required the methods to be readily repeatable, non-destructive and non-intrusive, to be able to probe the structural development of the electrode slurry over time, and most importantly, to be able to identify when the electrode slurry becomes uncoatable. It is important to note that, in this case, non-destructive refers to a technique that can continuously obtain reliable measurements over its duration without destroying the gel network and invalidating the results. This was achieved via the following objectives:

- Determination of the apparent viscosity of electrode slurry as it changes over time via rotational rheometry and thus establish the time taken for the gelation of the electrode slurry to finalise.
- Assessment of the coatability of the electrode slurry and identification of when the electrode slurry becomes uncoatable.
- Use of oscillatory rheometry to elucidate any trends and reaction rates in the structural development of the electrode slurry and thus distinguish between a

chemical and physical gel.

5.3 Methods and Materials

Electrode slurries were produced using the standard method, as discussed in Chapter 3. Carbon coated Na-NMST was mixed with the remaining conductive carbon black, and an 8 wt% PVDF (polyvinylidene fluoride) (Solvey 5130) binder in NMP (n-methyl-2-pyrrolidone) solution in a ratio of 89:6:5 by weight. The cathode slurry was mixed in sealed pots in a Thinky ARE-250 Planetary Mixer, situated in a Munters dry room with a maximum dew point of - 40° C. There were three stages of mixing, details of which can be found in Chapter 3.

5.3.1 Rotational Rheology

Rotational rheology measurements were performed using an Anton Paar RheolabQC rheometer, using a CC14 14 mm diameter bob geometry, and an EMB-Z4 measuring cup.

Three different experiments were performed.

1. Constant shear rate time sweep. The slurry was held at a shear rate of 100 s^{-1} with rheological measurements every 6 seconds.
2. Shear ramp with rest intervals. Shear ramp between 0.1 and 1000 s^{-1} performed every 10 minutes, with complete rest between sets of measurements, as shown in Figure B.1.
3. Constant shear rate with shear ramps. Shear ramp between 0.1 and 1000 s^{-1} performed every 60 minutes. Between shear ramps, the slurry was held at a shear rate of 10 s^{-1} with rheological measurements every 30 seconds, as shown in Figure B.2.

5.3.2 Oscillatory Rheology

Oscillatory rheology measurements were obtained using a Malvern Panalytical Pro+ rheometer, equipped with a 40 mm diameter roughened parallel plate geometry to minimise wall slip. A Peltier plate, set to 25°C, and a solvent trap, containing deionised water was used to maintain the temperature and humidity respectively during sample measurement.

An amplitude sweep at a frequency of 1.59 Hz, (10 radians s^{-1}), was performed to determine the linear viscoelastic region (LVER), to ensure the integrity of the sample during gelation. Three different oscillatory measurements were attempted.

1. Oscillatory rheology measurement, analogous to the first experimental setup. A time sweep was carried out at a constant amplitude and frequency within the LVER, (0.2 % in the presented data, at 1.59 Hz). Oscillatory measurements of G' and G'' were taken every 5 minutes.
2. Gelation measurement. The sample was allowed to gel for 90 minutes and then an amplitude sweep was performed on the sample until destruction. The sample was loaded onto the rheometer and a constant pre-shear of $10 s^{-1}$ for 30 seconds was performed. It was then rested for 1 hour, after which an amplitude sweep between 0.1 % and 1000 % at a frequency of 1.59 Hz was applied to the electrode slurry. This amplitude sweep took around 45 minutes to complete.
3. Multiple frequency sweeps from 0.1 Hz to 100 Hz at two different amplitudes, 0.02 % and 0.1 %, both of which reside in the linear viscoelastic region (LVER). A constant pre-shear of $10 s^{-1}$ for 30 seconds was performed at the start of measurements to eliminate any time dependence in the samples and ensure consistency between results. The frequency sweeps were performed every 5 minutes on the electrode slurry.

5.3.3 Maxwell Model

The fitting of a Maxwell model was performed using the Reptate software package. [233] Reptate uses a least-squares fitting procedure on a log basis.

Experimental data can be fitted by first generating equations of G' and G'' for the model. In series, stress remains equal through spring and viscous elements. Strain is calculated as the summation of strains in each element. By using a differentiation of Hooke's Law and Newtonian law of viscosity allows the following equations to be constructed,

$$G'_a = E_a \frac{(\omega\tau_a)^2}{(1 + \omega\tau_a)^2} \quad (5.8)$$

$$G''_a = E_a \frac{(\omega\tau_a)}{(1 + \omega\tau_a)^2} \quad (5.9)$$

where a denotes the mode and ω is the angular frequency of the oscillation.

5.4 Results and Discussion

This results section will be structured in a different manner to the other results chapters. Firstly, there will be an exploration of rotational rheological analysis, covering three different methodologies (outlined in Section 5.3). Secondly, there will be an investigation of the electrode slurries using oscillatory rheology, similarly covering three different techniques. Finally, there will be an examination of model fitting to these electrode slurries.

5.4.1 Rotational Rheology

5.4.1.1 Constant Shear Rate Time Sweep

The first objective of this chapter, the determination of the apparent viscosity of electrode slurry as it changes over time, and thus establishing the time taken for the gelation to finalise, was approached through the use of rotation rheology, widespread in the characterisation of electrode slurries. [115, 127, 139, 164, 174, 255] The most obvious method to do this was through the use of a constant shear rate over time measurement, as seen in Figure 5.5. A constant shear rate of 100 s^{-1} was chosen to mimic the shearing during both coating and mixing.

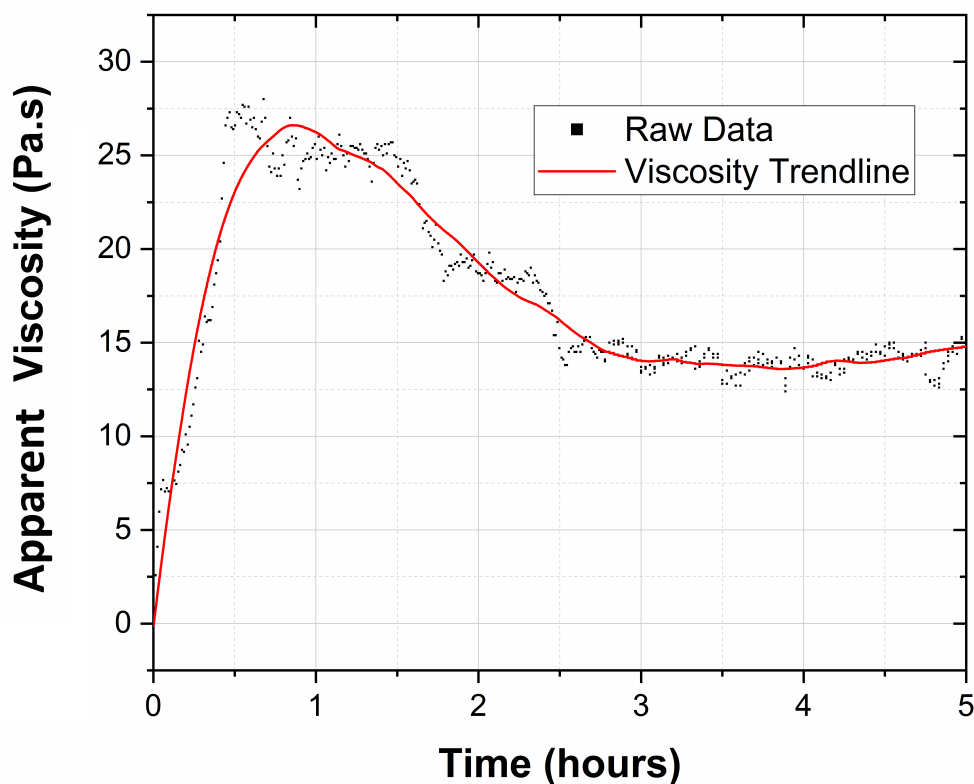


Figure 5.5: Constant Shear Rate of 100 s^{-1} over time.

Figure 5.5 shows the changes to the electrode slurry viscosity over time. 4 key regions can be noted from the measurements. Initially, there is a rapid increase lasting

approximately 45 minutes, where the apparent viscosity rises from 2 Pa.s to around 26 Pa.s, a tenfold increase in apparent viscosity. Secondly, a plateau (or slight decline) lasting approximately 1 hour at around 25 Pa.s. Subsequently there is a steady decline to approximately 15 Pa.s, where the second plateau lasts for the remainder of the measurements.

The initial rapid increase in viscosity is contrary to the thixotropic and shear thinning nature of these electrode slurries [256] and suggests two things. Firstly, it can be inferred that there is a gel or complex structure forming. [256] Secondly, as there is not a further increases in viscosity, it can be suggested that the full extent of the gelation is reached within the first 45 minutes. The decline to the second plateau, at approximately 15 Pa.s, could suggest that there is a collapse in the structure formed, and the constant shearing of the rheometer has caused any gel structures to align and flow more easily past one another.

The present of this secondary plateau might suggest that the electrode slurry is still coatable, due to the drop in the apparent viscosity. Similarly, as it has been demonstrated in Section 5.1.2, the shear rate of a coating device can cover a large range, and by using a coater with a shear rate that is higher than 100 s^{-1} further structure alignment and flow within this electrode slurry seems possible. However, physical evidence of slurry gelation demonstrates that this electrode slurry is no longer coating, reinforcing the notion that it is difficult to determine the coatability, and a different technique is required to fully probe the structure of these electrode slurries.

A further concern is the potential for shear induced gelation. Shear induced gelation has been reported for colloidal dispersions, [257] albeit for different chemicals. In the study by Cabane *et al.*, 1997, a water based colloidal dispersion was able to gel after being experienced to a critical shear rate of 1000 s^{-1} . [257] It was concluded that the constant shear rate time sweep was not appropriate for the testing as it interfered with and, likely, destroyed the gel structure in the electrode slurry. Similarly, it was unable to really probe and investigate the structural development of the gelation or determine

when the electrode slurry was uncoatable .

Therefore, while this method has been able to identify the apparent viscosity of the electrode slurry and demonstrate a gelation time (satisfying the first objective – Section 5.2), the use of a constant shear rate time sweep was deemed unsuitable. It was proposed that rest periods would reduce the risk of a shear induced gelation, and that shear ramps would facilitate further examination of the electrode slurry measured rheological properties.

5.4.1.2 Shear Ramps with Rest Intervals

As examined, while the initial method of constant shear rate was able to demonstrate a gelation time, the employment of shear ramps into the rheological characterisation hoped to further elucidate the structural development in the electrode slurry. The shear rate input over time for this method can be found in Section 5.3, Figure B.1. As Figure 5.5 demonstrates, the second, and final, plateau was reached after 2.5 hours, and so this method utilising multiple shear ramps was performed up to this point.

While flow curves were taken every 10 minutes, the data shown in Figure 5.6, is that of every 20 minutes. Figure 5.6 shows these flow curves, with two apparent viscosity curves at individual shear rates of 10 s^{-1} and 40 s^{-1} plotted to the side. These two shear rates have been highlighted as these relate to a doctor blade shear rate with a nominal gap of $200 \text{ }\mu\text{m}$ (40 s^{-1}) and that of a reel-to-reel coater, to account and allow for large-scale coating operations (10 s^{-1}).

By observing the increases in apparent viscosity at single shear rates, the trends become more evident. For the shear rate of 10 s^{-1} , there is slight increase over 0.75 hours. Subsequently, the apparent viscosity increases from 2.2 to 2.9 Pa.s over around 1.25 hours. After 2 hours there is a slight decline to 2.7 Pa.s. At the shear rate of 40 s^{-1} , there is a very similar story, a slight rise in the viscosity over 0.75 hours, followed by a steady over 1.25 hours. Due to the shear thinning nature of these electrode slurries, this increase is from lower apparent viscosities of 1.28 Pa.s to 1.42 Pa.s. After 2.25 hours

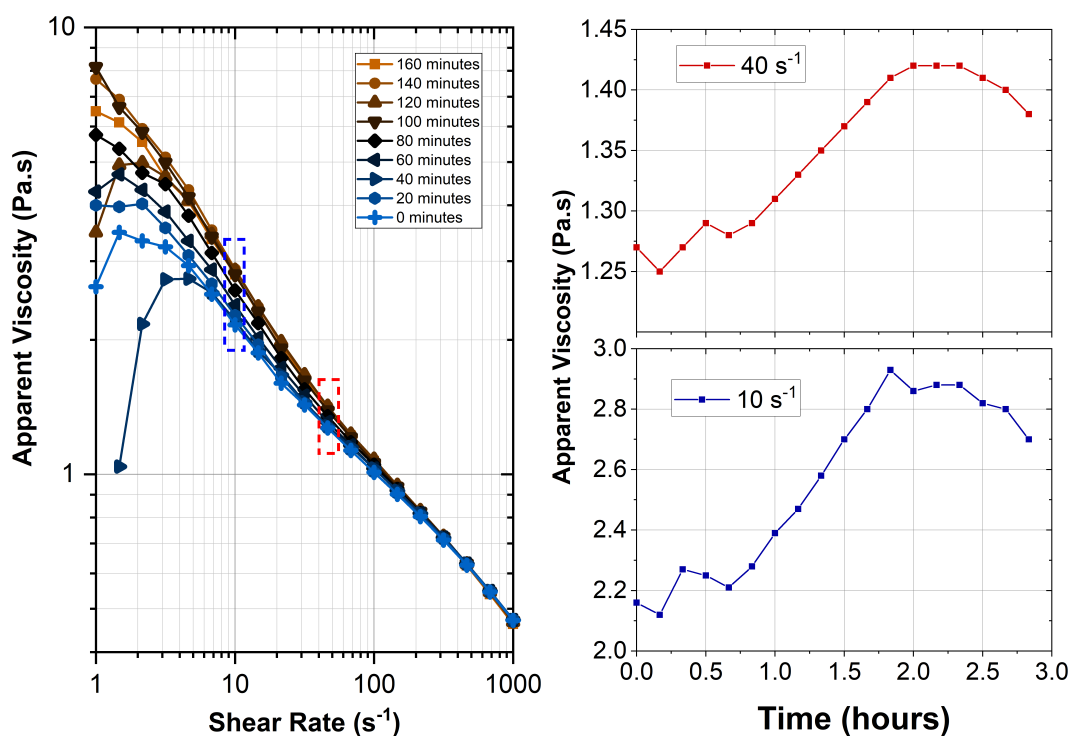


Figure 5.6: Flow Curve and Time vs Apparent Viscosity curves for shear rates of 10 s^{-1} and 40 s^{-1} .

there is a decline to $1.38 \text{ Pa}\cdot\text{s}$. The apparent viscosity remains relative constant over the time period.

These apparent viscosities are very low, especially when compared to the results depicted in Figure 5.5. The increases in apparent viscosity are similarly low and an interpretation of Figure 5.6 alone would suggest that there is no gelation occurring, contrary to Figure 5.5. However, due to the set-up of the shear ramps, where the electrode slurry was sheared for 7 minutes and at rest for 3 minutes, the electrode slurry frequently experiences shears rate up to 1000 s^{-1} . It seems plausible to suggest that, while the electrode slurry is able to gel under a shear rate of 100 s^{-1} , this higher shear rate could disrupt the formation of the gel.

Another possibility is due to the closed viscosity of the cup and bob geometry, as demonstrated in Figure 5.7. In this geometry, only the top surface is exposed to lab air. Therefore, the ratio of the exposed surface area to the unexposed volume is very low. Due

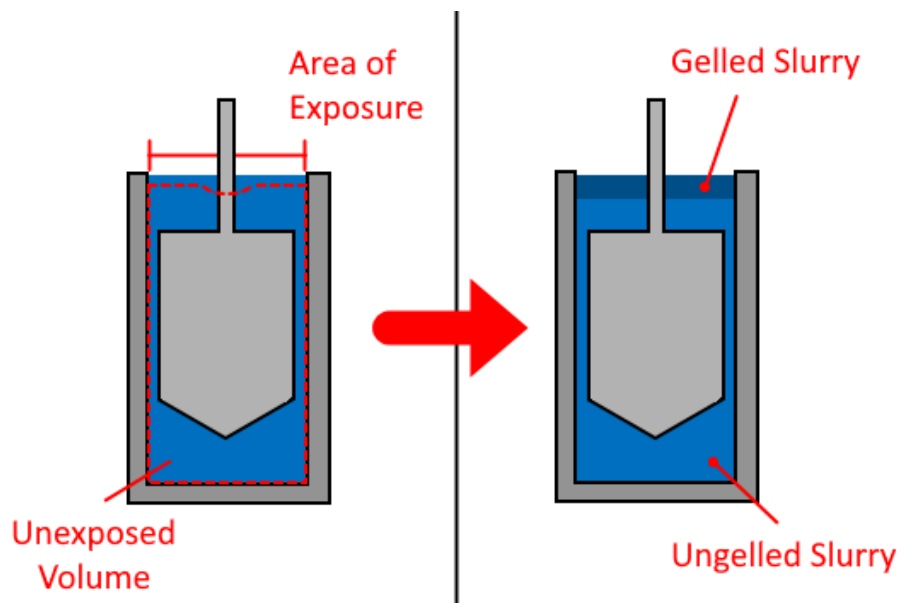


Figure 5.7: Areas of exposure in cup and bob geometry.

to this, changes to the apparent viscosity of the electrode slurry as it gels become less evident in the results. The fluid bulk obscures the effect of the electrode slurry gelation on the apparent viscosity.

Comparing these two techniques, the utilisation of a constant shear rate of 100 s^{-1} has demonstrated a large increase in the apparent viscosity, and the complete rest between shear ramps has displayed very little increase over a similar time period. It can, hence, be suggested that a shear-induced gelation is occurring in this system.

Therefore, based on these conclusions, modifications to this method have been suggested. Firstly, by utilising longer gaps between the shear ramps, a reduction to the effect of the high shear rates disrupting the development of the electrode slurry gel can be expected. Secondly, to investigate the notion of shear induced gelation, between shear ramps the electrode slurry will be subjected to a constant shear rate, which is a lower shear rate of 10 s^{-1} . Finally, rheological analysis will be run for an extended period of time, primarily to establish the final gelation time.

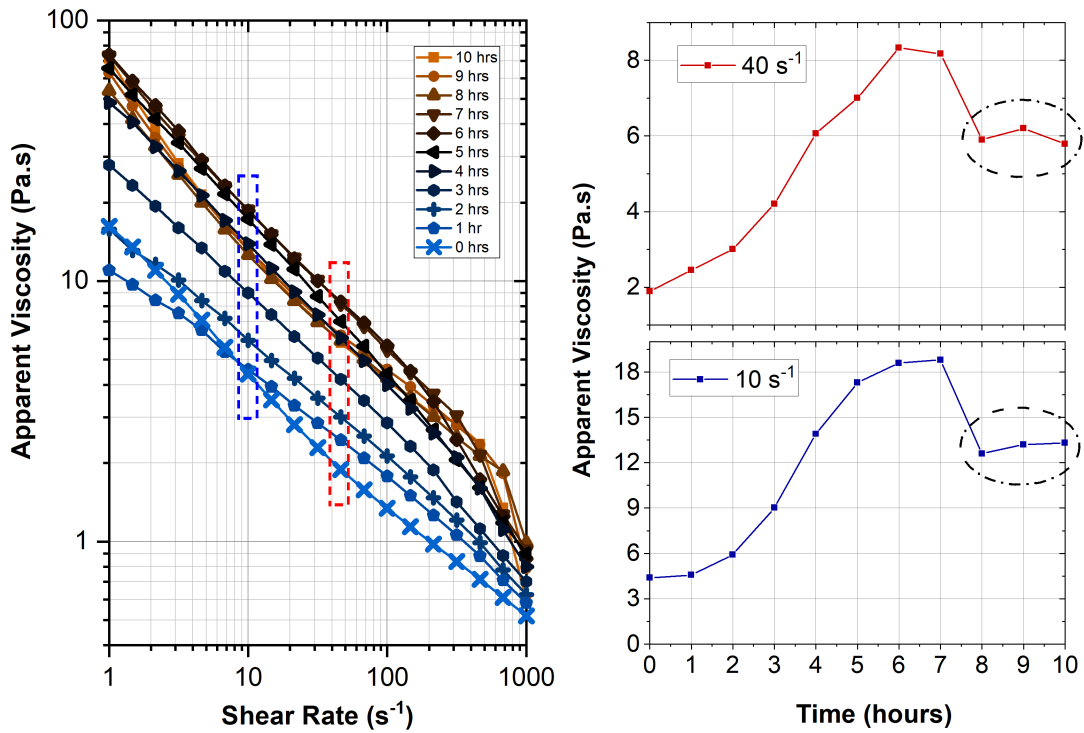


Figure 5.8: Flow Curve and Time vs Apparent Viscosity curves for shear rates of 10 s^{-1} and 40 s^{-1} .

5.4.1.3 Constant Shear Rate with Shear Ramps

Figure 5.8 shows the changes to the flow curves taken every hour, with individual apparent viscosities at 10 s^{-1} and 40 s^{-1} plotted to the side, in the same manner as Figure 5.6. For the majority of shear rates in the flow curve in Figure 5.8, the apparent viscosities are higher for subsequent measurements. However, for shear rates below 10 s^{-1} measurements between 0 and 2 hours show a decreased apparent viscosity for subsequent measurements and it is only after 2 hours that subsequent measurements demonstrate increasing apparent viscosities. It is unclear as to why this occurs, however it could be a result of the shear thinning nature of these electrode slurries [256] - initial measurements, which have lower apparent viscosities may be more susceptible to shear thinning and therefore retain decreased apparent viscosities for subsequent measurements.

For the individual shear rates, the shear rate curve of 10 s^{-1} , shows an initial slow increase between 0 and 2 hours from a viscosity of approximately 4 to 6 Pa.s. Subsequently, lasting 4 hours, there is a far steeper incline, and the apparent viscosity increases from 6 to 18 Pa.s, where a slight plateau, lasting 1 hour, resides. There is then a rapid decline in viscosity, to approximately 12 Pa.s, which remains for the remainder of the measurements, until 10 hours.

For the shear rate of 40 s^{-1} , the pattern is very similar to 10 s^{-1} , albeit with far lower apparent viscosities. There is a slow increase from 2 to 3 Pa.s over 2 hours, after which there is a more rapid increase from 3 to 8 Pa.s over 4 hours. There is a more distinct plateau than the shear rate of 10 s^{-1} , between 6 and 7 hours. There is then another decline, and a plateau from 8 to 10 hours, at an apparent viscosity of 6 Pa.s.

From this measurement it seems evident that the electrode slurry gelation is realised after approximately 5 to 6 hours, with a plateau reached after this point. Similarly, to the constant shear measurement, Figure 5.5, a second lower plateau occurs, albeit at 8 hours.

However, it was noted that at high shear rates a portion of gelled material was expelled from the geometry. This material run off thus invalidated the measurement.

By spreading out the shear ramps, this technique is able to probe slightly more into the gelation development. In fact, the shape of the curve produced by this technique is very similar to those produced by the final method. However, as mentioned, this is not a very robust method. The material run-off, attributed to the cup and bob geometry means the electrode slurry gelation is not properly analysed. Additionally, it can be noted that, due to the large differences between these rotational rheology experiments (Figures 5.5, 5.6, and 5.8), the constant shearing of the electrode slurry interferes with the structure development of the electrode slurry.

Therefore, it is clear that an optimal measurement set up has not been reached and experimentation using oscillatory rheology is suggested.

5.4.2 Oscillatory Rheology

5.4.2.1 Oscillatory Time Sweeps

As stated in Section 5.3, to rule out the effects of measurement shear and deformation on the electrode slurry, an initial amplitude sweep is performed prior to the experimental measurements. Figure 5.9 shows this initial amplitude sweep, performed on the ungelled electrode slurry (an amplitude sweep on the gelled electrode slurry can be seen in Figure 5.11). It is evident that the linear viscoelastic region (LVER) is a long region between 0.01 Pa and 10 Pa, as the rapid drop-off of G' and G'' does not occur until an amplitude of approximately 40 %. 3 amplitude points have been highlighted as potential amplitudes for subsequent oscillatory characterisations. The largest amplitude, 0.2 %, was used for these oscillatory time-sweep measurements. However, due to the slight increase and decrease in G'' from approximately 0.12 to 0.80 Pa, where the values do not remain linear, this amplitude of 0.2 % was only used for these oscillatory time-sweep measurements. Instead, amplitude values of 0.02 and 0.1 % were used.

One standard method for studying the cure or gelation of a fluid is the use of oscillatory time sweeps, [258] where the intersection of G' and G'' , known as the gel point, is measured. Using a constant amplitude and frequency, G' and G'' are recorded over time. [258]

Figure 5.10 shows the changes to G' and G'' over approximately a 14-hour window. Over the first two hours of measurement G' and G'' increase from values of 120 and 17 Pa to 16000 and 2000 Pa, respectively. This is an increase of more than 100-fold. A plateau is reached after these two hours and remains for the remainder of the measurements. The final values of G' and G'' are 1300 and 15000 Pa, respectively, a slight decrease on those at the start of the plateau.

It should be acknowledged that this value of gelation time (approximately 2 hours) is around the same order of magnitude as the very initial rotational rheology measurements (gelation time is approximately 1 hour). However, the analysis of the LVER guarantees that there is no deformation of the electrode slurry sample in this measurement, and

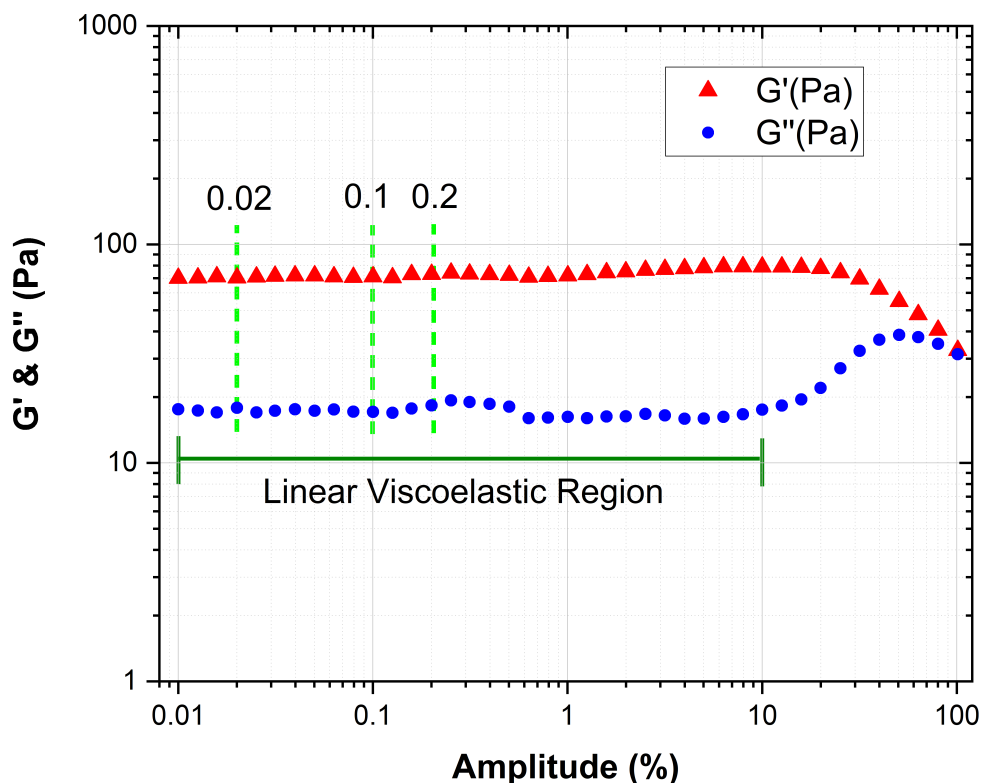


Figure 5.9: Initial amplitude sweep, showing the LVER and chosen amplitudes.

the effect of shear on the electrode slurry can be noted. Therefore, it can be noted that actively shearing the electrode slurry seems to speed up the gelation time and reduce the time of final gelation formation.

Furthermore, due to the fact that G' is higher than G'' for the entirety of the measurements, it is evident that the cross-point of G' and G'' , i.e. the electrode slurry gel point, has been reached and passed, or does not exist for these electrode slurries. It should be noted that these measurements directly follow the amplitude sweep, checking that oscillatory measurements lie in the LVER, so measurements are than 30 minutes after the mixing of the electrode slurry was completed. Therefore, the gel point has occurred in either, the mixing of the electrode, the transportation between the mixing equipment and the rheometer, or during the measurement of the amplitude sweep.

By continuing measurements after the plateau was reached, it ensures that the gel

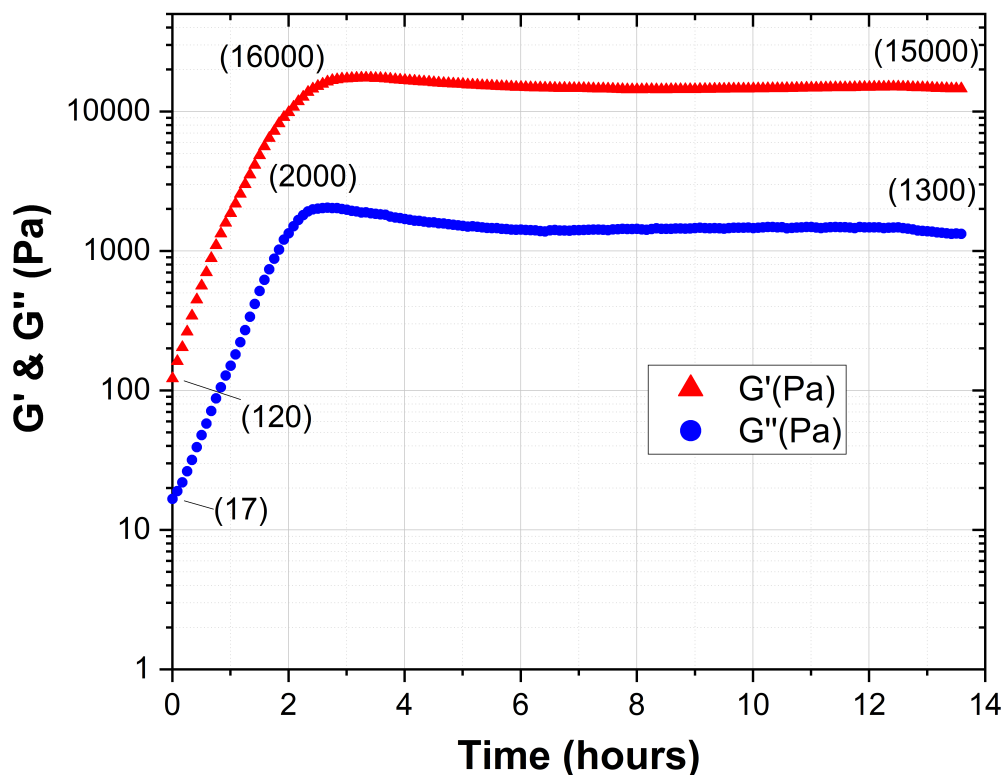


Figure 5.10: Oscillatory rheology time sweep.

does not form as an initial intermediary structure and then continue to develop at a later stage.

Ultimately, due to the length of time of the measurement setup and initial amplitude sweep, this method is unable to probe a gel point time for this electrode slurry. A suggested change is to use the initial amplitude sweep as a standard for all future measurements and use amplitudes within this LVER without performing the same amplitude sweep on every set of measurements. By removing this timely procedure, measurements closer to the gel point can be obtained. It is worth noting that using the same parameters as performed in this test, without performing the amplitude sweep, G' was still higher than G'' at the start of measurements.

Furthermore, this technique of an oscillatory time sweep is unable to distinguish between a physical and chemical gel. However, it is worth noting that due to the relative

magnitudes of both G' and G'' , and the large increases that G' and G'' experience, it seems likely that there is a chemical gel forming. A physical gel, such as a confinement jamming effect would likely have lower values of G' and G'' .

A possible method of distinguishing between a physical and chemical gel is by performing an amplitude sweep when a gel has formed. By ramping up the amplitude, a physical gel is able to flow again. A chemical gel would not flow and instead would be broken apart.

Ultimately, this method runs into some of the same issues as the rotational rheology constant shear rate time sweeps. Namely that only a single frequency and amplitude of deformation are being used in the measurement. It is, therefore, difficult to extrapolate and realise different frequencies and amplitudes. Similarly, this method does not probe into the coatability of the electrode slurries. It would be more beneficial to use a range of amplitudes, or frequencies, or both in measurements.

5.4.2.2 Amplitude Sweeps

Figure 5.11 shows the amplitude sweep of the electrode slurry gel formed after 90 minutes, until destruction. It can be seen that initially there is a very slow increase in G' and G'' between 0.1 and approximately 30 %. This steady incline can be attributed to the continuation of the gel structure within the sample. Furthermore, it is useful in demonstrating the extent of the LVER. It shows that the chosen amplitudes of 0.02 and 0.1 % remain in the LVER after the gel structure has formed.

After the amplitude of 30 %, there is a noisy decline in G' and G'' and then after 120 % there is further decline, along with complete noise and heavily distorted data. As previously mentioned, if this gel formed was a physical gel, increasing the amplitude would show a definitive cross point between G' and G'' . After that cross point, G'' would dominate over G' and the material would easily flow. However, in this case, as seen in Figure 5.11, there is no conclusive cross point. Instead, as the data becomes very noisy and distorted, it suggests that the sample is being ripped apart and fragmented, strongly

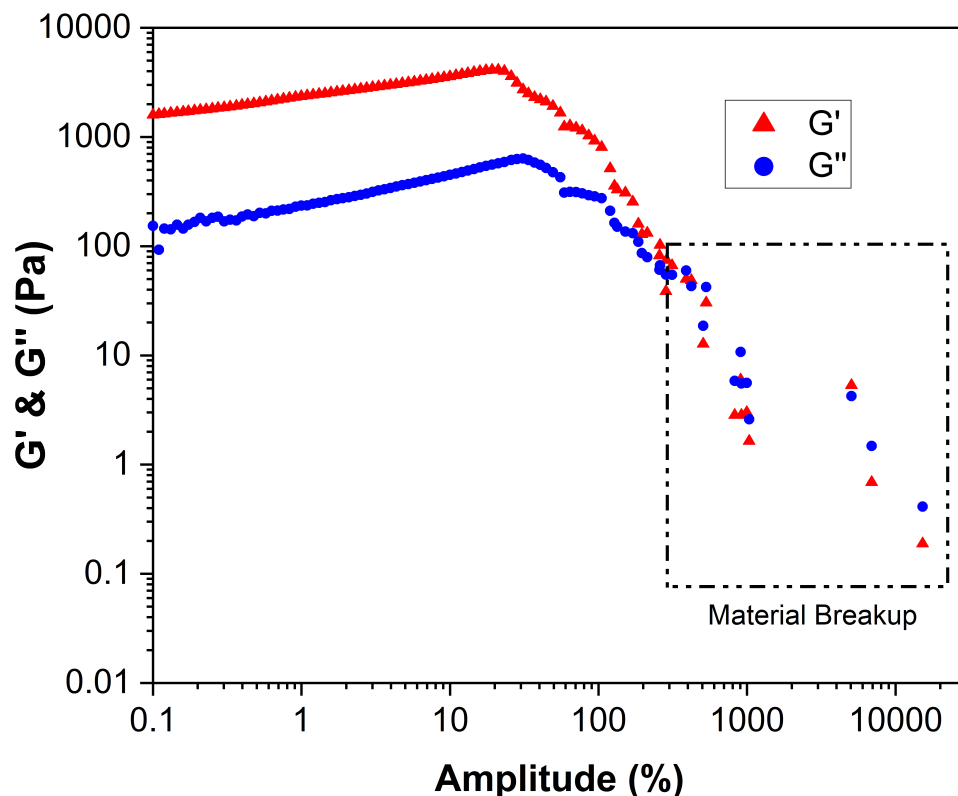


Figure 5.11: Amplitude sweep on gelled electrode slurry.

suggestive of a chemical gel.

While this distinction between a chemical and physical gel is useful, and aids in answering the final objective, these distortions in the data are clearly not useful in determining the coatability of the material or probing the nature of the sample gelation. Furthermore, due to the nature of these amplitude sweeps, samples experience amplitudes of shear that are higher than the linear viscoelastic. This means that this measurement technique is a destructive technique that will interfere with the electrode slurry gelation. Similarly, both oscillatory techniques covered are unable to assess the coatability of the electrode slurry and infer any trends and reaction rates in the structural development of the electrode slurry. Therefore, analysis using the frequency domain, and a non-destructive amplitude is suggested for the analysis of these electrode slurries.

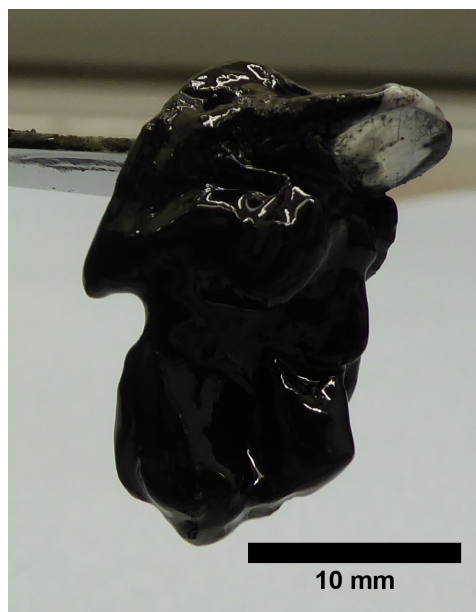


Figure 5.12: Gelled electrode slurry sample.

5.4.2.3 Frequency Sweeps

The examined rheological method involves the taking of multiple frequency sweeps, as seen in Figure 5.13. It was decided that these measurements would be taken over a time of 90 minutes. While the initial oscillation measurements (Figure 5.10) demonstrate that the gelation and structural development continues for approximately two hours, physical observations have shown that the electrode slurry has become completely gelatinous and uncoatable, as seen in Figure 5.12, after far less time.

A collection of frequency sweeps can be seen in Figure 5.13. Data was recorded every 5 minutes for a total of 90 minutes. In the interest of brevity, frequency sweeps every 15 minutes, up to 75 minutes have been shown in Figure 5.13. Detailed analysis of this data can be found in (Chapter 4) and so only the benefits of this method and a summary of the analysis will be, subsequently, explored. By performing these frequency sweeps every 5 minutes, it reduces the risk that the time of measurements are greater than the time of structural development. A further benefit of this experimental setup comes as a result of removing the amplitude sweep at the start of measurements.

In the frequency sweep at 0 minutes, in Figure 5.13, a cross-point between G' and

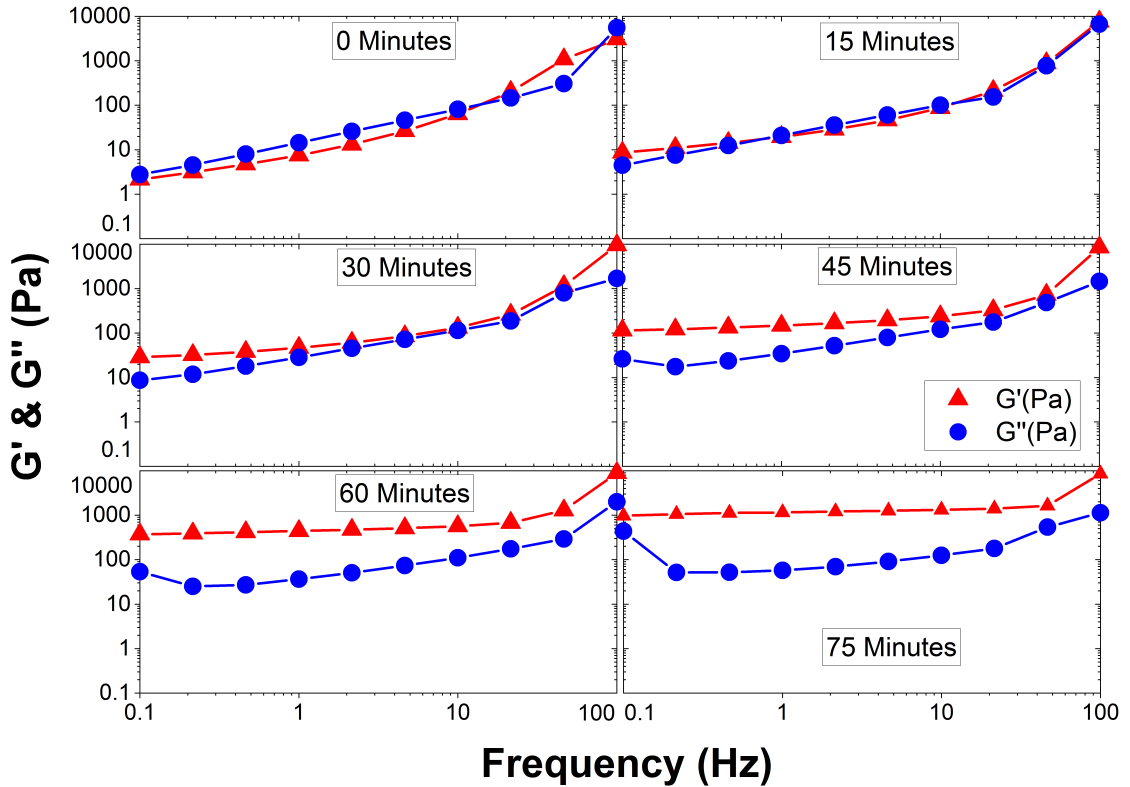


Figure 5.13: Frequency sweeps taken at 0, 15, 30, 45, 60, and 75 minutes.

G'' can be seen at approximately 10 Hz. Before this cross-point, G'' dominates and the electrode slurry behaves like a viscous media, flowing easily. The observation of this cross-point has not been observed in previous experimental methods, and it highlights the benefits of rheological analysis across a range of measurement frequencies.

Additionally, when analysing these frequency sweeps, relating frequency to observation time becomes useful. From Figure 5.13, it can be observed that, until 30 minutes, the values of G' and G'' increase as the frequency increases. At higher frequencies, corresponding to smaller observation times, the strength of the response to deformation increases. Furthermore, as the time progresses, the difference between the elastic and the viscous components increases at higher frequencies. This implies that over small timescales the electrode slurry responds elastically, similar to that of a yield stress material, and over larger timescales, the elasticity in the slurry relaxes, and the

slurry is able to flow viscously. This notion of a relaxation time can be calculated and analysed further through use of a Maxwell model, as explored in Section 5.4.3.

Furthermore, these measurements can be used to determine between a chemical and physical gel. Confinement jamming in this system is identified by a point where G' becomes frequency independent, while G'' remains frequency dependent. [259, 260] Consequently, identification of gel formation is shown at a point where $G' \gg G''$, [261–263] and, both, G' and G'' have a sufficient degree of frequency convergence.

This method is very useful as the results can be processed in different ways with either frequency or time as the x axis domain as can be observed in Figure 5.13 or Figure 4.5, Chapter 4, respectively. Furthermore, the phase angle, which describes the relationship between G' and G'' , can be extracted and plotted against time for different frequencies (as observed in Figure 4.5, Chapter 4).

5.4.3 Maxwell Model

The oscillatory rheological technique of multiple frequency sweeps (Figure 5.13) is very useful as the frequency data reveals structural insights into the progression of the electrode slurry gelation. Furthermore, as stated, this data can be easily fitted to a Maxwell model.

As demonstrated in Chapter 4, by fitting the data to a Maxwell Model and extracting the relaxation times (calculated by the use of Equations 5.3, 5.8, and 5.9), changes to the relaxation behaviour of the electrode slurry over time can be observed. As introduced in Section 5.1.4.4, the observation time is a theoretical property that states that for times much shorter than this relaxation time the electrode slurry will behave as a solid (spring), and for times longer than the relaxation time the electrode slurry will behave as a fluid (dashpot).

These relaxation times can be observed in the plot of the primary relaxation time, as seen in Figure 5.14. A detailed analysis of the fitted relaxation time is explored in Chapter 4, where it is demonstrated that the relaxation time shows 3 stages of gel development.

These three stages of gelation are likely related to the concentrations of C=C bonds.

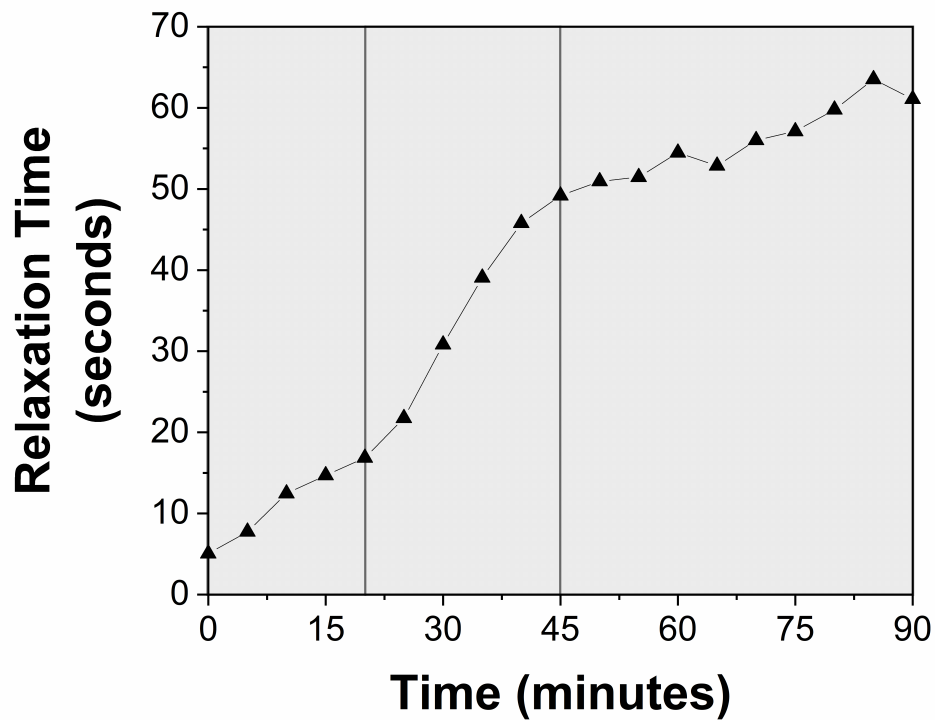


Figure 5.14: Primary mode relaxation time, showing the 3 proposed stages of gel development.

Initially there is the creation of saturated structures, via a dehydrofluorination stage. Secondly there is a crosslinking stage, which results in the highest rate of gelation. Finally, a slow crosslinking stage, whereby the rate of gelation is limited by the low quantity of saturated structures.

As introduced in Section 5.1.4.4, the number of modes in the Maxwell Model can be varied, altering the quality of fitting and proposing new theoretical behaviour. For a 2 mode Maxwell mode, the secondary relaxation time signifies that the electrode slurries exhibit a strong elastic response, similar to that of a yield stress in a Herschel-Bulkley fluid. Additional modes can suggest additional yield points.

While these additional modes can improve the quality of data fit, as shown in Figure 5.15, it is important to analyse these models to avoid over-fitting. It is evident in Figure 5.15 that by using 1 mode the quality of the fit is very poor and should not be considered. Models of 2 or 3 modes produces fits that are much closer to the experimental data. The

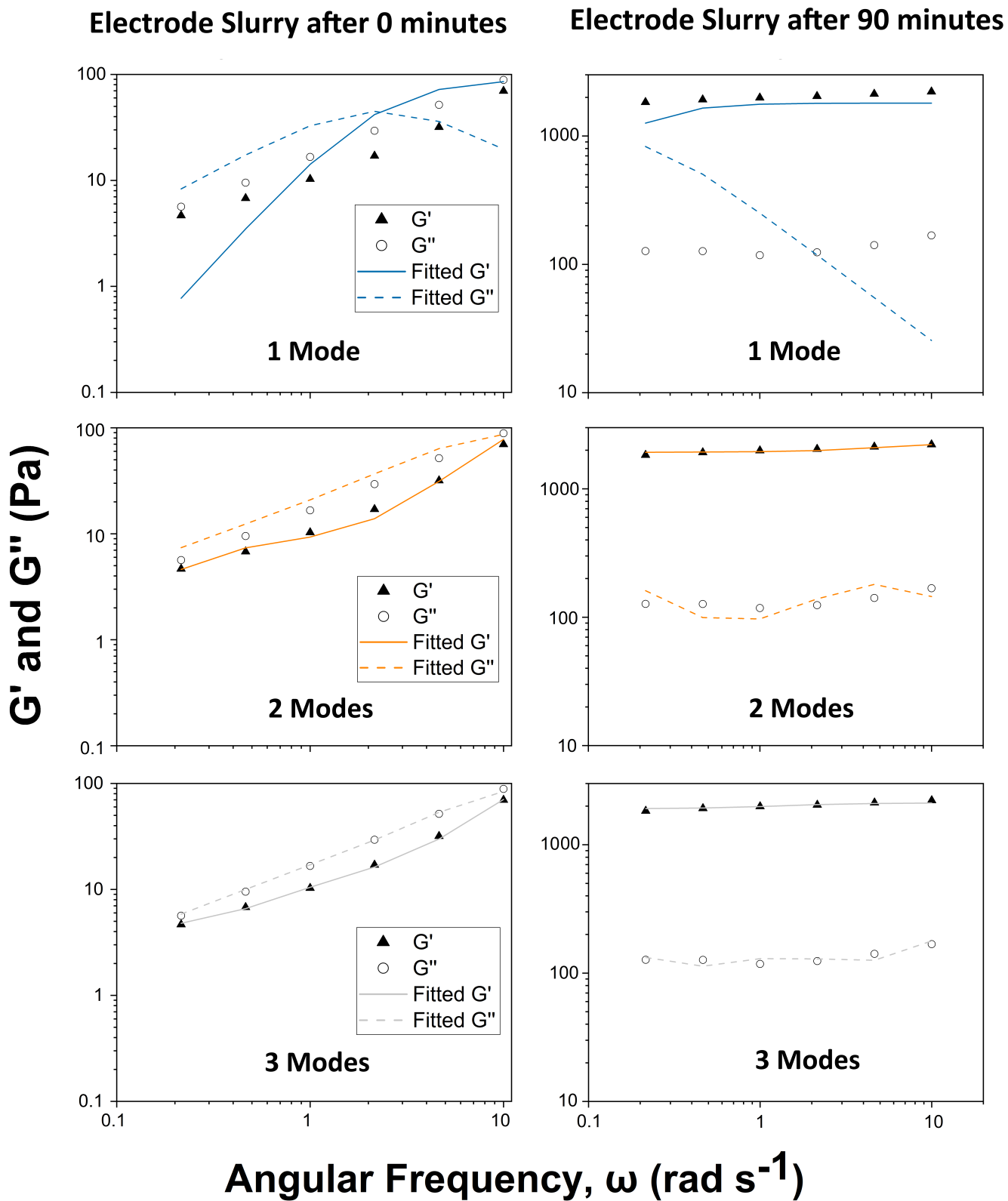


Figure 5.15: Storage and loss moduli recorded 0 minutes and 90 minutes after mixing, fitted to Maxwell models with 1, 2, and 3 modes.

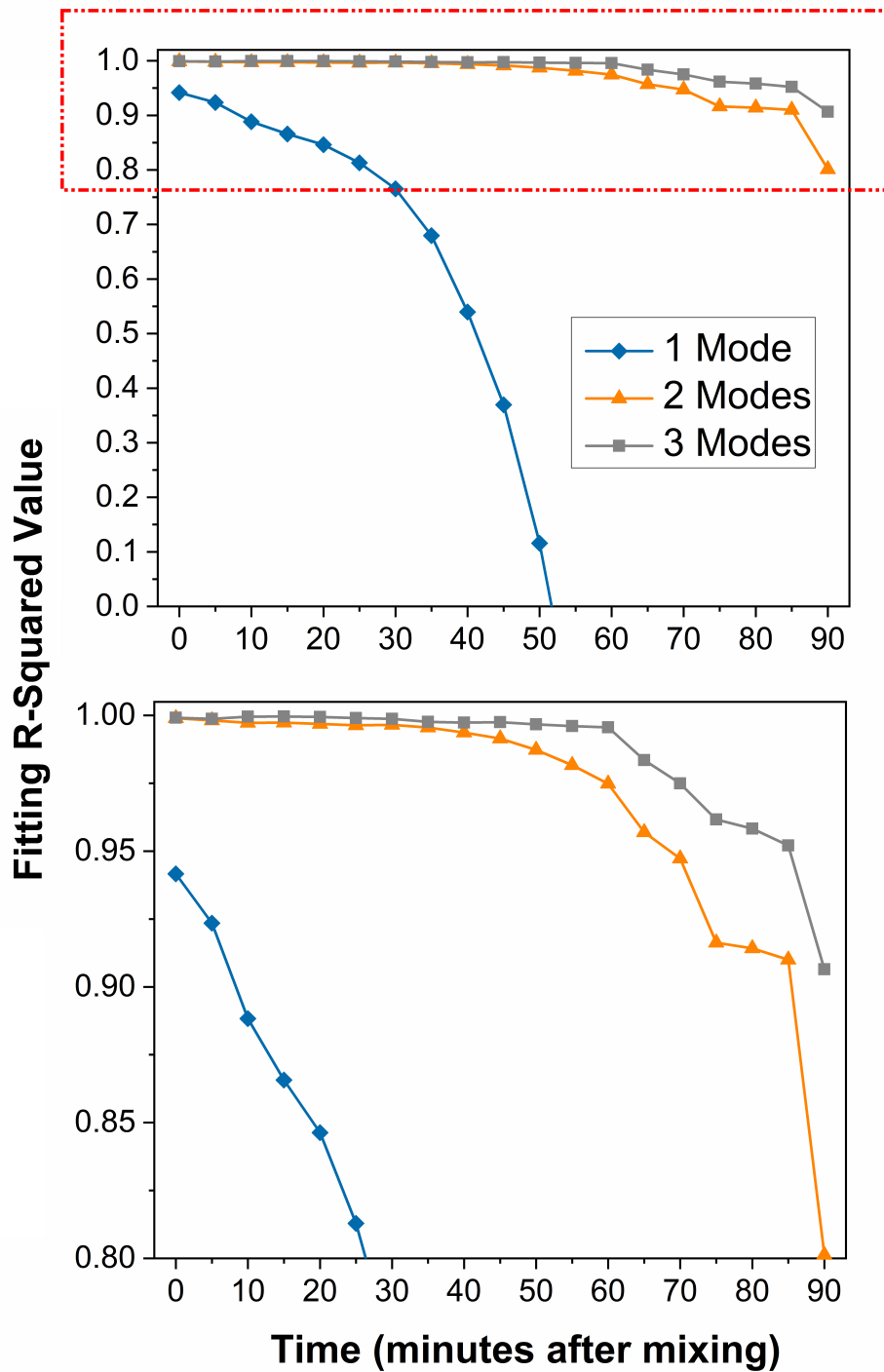


Figure 5.16: R-squared values for the fitted Maxwell models containing 1, 2, and 3 modes.

Table 5.2: Akaike Weights (w_i) for the electrode slurry relaxation times fitted to 1, 2, and 3 Modes.

Time (minutes after mixing)	1 Mode	2 Modes	3 Modes
0	1.81×10^{-13}	5.57×10^{-3}	1.02×10^{-4}
5	1.04×10^{-13}	5.10×10^{-4}	3.30×10^{-5}
10	5.52×10^{-14}	2.47×10^{-4}	8.99×10^{-2}
15	4.36×10^{-14}	6.76×10^{-4}	3.04×10^{-1}
20	3.74×10^{-14}	5.28×10^{-4}	6.74×10^{-2}
25	2.91×10^{-14}	4.94×10^{-4}	7.27×10^{-3}
30	2.12×10^{-14}	1.89×10^{-3}	4.86×10^{-3}
35	1.57×10^{-14}	2.17×10^{-3}	5.80×10^{-4}
40	1.36×10^{-14}	1.99×10^{-3}	2.13×10^{-3}
45	1.35×10^{-14}	2.19×10^{-3}	2.04×10^{-2}
50	1.56×10^{-14}	1.74×10^{-3}	3.26×10^{-2}
55	1.89×10^{-14}	1.66×10^{-3}	1.01×10^{-1}
60	2.16×10^{-14}	1.57×10^{-3}	3.37×10^{-1}
65	2.96×10^{-14}	7.58×10^{-4}	1.45×10^{-3}
70	3.22×10^{-14}	8.09×10^{-4}	4.26×10^{-4}
75	4.03×10^{-14}	5.96×10^{-4}	3.90×10^{-4}
80	4.41×10^{-14}	2.03×10^{-3}	9.29×10^{-4}
85	4.36×10^{-14}	2.80×10^{-3}	7.42×10^{-4}
90	5.77×10^{-14}	3.28×10^{-4}	1.82×10^{-4}
Averages	3.33×10^{-14}	1.11×10^{-3}	3.92×10^{-3}

R-squared values for these models can be seen in Figure 5.16. The quality of the fits using models containing 1, 2 and 3 modes can be further examined in these R-squared values (Figure 5.16). It can be noted that as the electrode slurries ages the quality of the fit decreases, this can be similarly observed in Figure 5.15. Additionally, it can be seen, in Figure 5.16, that fitting to 3 modes gives the highest R-squared values. However, it is still difficult to determine if over-fitting is occurring.

Another method to compared the quality of fit of different models is through the use of AIC. Akaike weights for 3 different models, for each time interval, can be found in Table 5.2. It can be clearly seen that 1 mode fitting is very inappropriate for this application. It produces models with very low Akaike scores, indicating a poor fitting to the experimental data. Between 2 modes and 3 modes, the scores are a lot closer. 3 modes clearly have some time values that have very high quality of fits, such as 10, 15, 20, 55, and 60 minutes. Additionally, the fitting at 60 minutes is the overall best fitting. However, the fitting of 3

modes also demonstrate values with very poor Akaike weights, with some being an order of magnitude lower than 2 modes. In comparison, the fitting of 2 modes has far more even Akaike weights. Literature examples of Maxwell fittings also state that only 1 mode should be used per decade of data. [233] Based on these factors, 2 modes are chosen for all subsequent Maxwell Models.

5.5 Discussion

A summary of the rheological methods explored in this chapter, can be seen in Table 5.3. Each of the aims and objectives established in Section 5.2 have been split into individual objectives *a – f*. The methods have been further characterised by the general method objective of being non-destructive and non-intrusive. Cells marked with 1/2 and a checkmark represent partial satisfaction of the objectives.

As established and made evident in Table 5.3, one of the major issues concerning the rotational rheology studies is the intrusion into the electrode slurry characterisation. Across the methods illustrated by Figures 5.5, 5.6, and 5.8, it has been demonstrate that a shear induced gelation effect is occurring, which makes an objective characterisation of the electrode slurry gelation impossible.

The destruction of the electrode slurry sample has been labelled as a further general differentiating measure between techniques. While the second rotational rheology technique has been labelled as being non-destructive in Table 5.3, this is dependent on the shear rates tested and very high shear rates will likely disrupt and destroy the electrode slurry gel sample, as exhibited in method 3, the constant shear rate with shear ramps.

This table has been useful in the identification of the optimal rheological method for the analysis of electrode slurries.

Table 5.3: Summary of Rheological Methods Tested.

Method		Objectives						General Objectives	
		<i>a</i>	<i>b</i>	<i>c</i>	<i>d</i>	<i>e</i>	<i>f</i>	<i>Non-Destructive</i>	<i>Non-Intrusive</i>
Rotational Rheology	1	✓	✓	1/2✓	1/2✓			1/2✓	
	2							1/2✓	
	3			1/2✓	1/2✓				
Oscillatory Rheology	4		✓					✓	✓
	5						✓		
	6		✓	✓	✓	✓	1/2✓	✓	✓

Rheological Methods - Lines show the split between rotational and oscillatory (Section 5.3)

1	Constant shear rate time sweep
2	Shear ramps with rest intervals
3	Constant shear rate with shear ramps
4	Oscillatory time sweep
5	Amplitude sweep
6	Frequency sweeps

Objectives - Lines show the split between the individual aims and objectives (Section 5.2)

a	Determines Apparent Viscosity
b	Establishes Gelation Time
c	Assesses the coatability
d	Identifies a point of uncoatability
e	Elucidates trends in the structural development
f	Distinguishes between a chemical and physical gel

5.6 Conclusions

The objective of this work was to develop a rheological characterisation method capable of establishing a processing window for the electrode slurry, identifying a point when the electrode slurry becomes uncoatable, and probing the structural developing of the electrode slurry gelation.

This was approached initially through the use of rotational rheological methods, and subsequently using oscillatory methods. The first objective was the determination of the apparent viscosity of electrode slurry as it changes over time via rotational rheometry and thus establish the time taken for the gelation of the electrode slurry to finalise. Utilisation of a constant shear rate time sweep, a gelation time of 45 minutes was established, with an electrode slurry apparent viscosity of 2 Pa.s that increases to 26 Pa.s for the gelled electrode slurry sample.

The second objective, assessing the coatability of the electrode slurry and identifying when the electrode slurry becomes uncoatable, was only partially possible using the constant shear rate time sweep, that has been demonstrated to satisfy objective one, as made evident in Table 5.3. Therefore, two further rotational rheological methods were examined, one consisting of shear ramps with rest intervals and another of a constant shear rate with shear ramps. The method of a constant shear rate with shear ramps was able to partially assess the coatability and identify a point of uncoatability, prompting a progression to oscillatory rheology techniques. Furthermore, comparisons between the three rotational rheology methods establishes a process of shear induced gelation due to these measurements, and demonstrates that these measurements affect the gelation mechanism. Oscillatory measurements began through a characterisation using an oscillatory time sweep, which was able to establish a gelation time but was unable to assess the coatability of the electrode slurry or identify a point of uncoatability. The finalised method of multiple rapid frequency sweeps with subsequent Maxwell model fitting was able to fully satisfy this second objective.

The final objective was to elucidate any trends and reaction rates in the structural development of the electrode slurry and thus distinguish between a chemical and physical gel. It has been demonstrated that the relaxation time, fitted from method of multiple frequency sweeps is able to elucidate trends in the structural development of the electrode slurry. Additionally this method is able to partially distinguish between a chemical and physical gel due to the behaviour of the storage and loss moduli across the

measured frequencies. This method has been suggested as a partial satisfaction to this objective as typically amplitude sweeps are required to distinguish between these gel types. Furthermore, due to the identification of the LVER, it can be established that this developed method was both non-destructive and non-intrusive to the electrode slurry gelation.

Ultimately, the finalised method of the multiple rapid frequency sweeps with subsequent Maxwell model fitting, is able to satisfy the all objectives (aside from the determination of the apparent viscosity, oscillatory rheology instead can establish a complex viscosity).

Chapter 6

Stabilising Additives for High Nickel Content Cathode Electrode Slurries

6.1 Introduction

It has been established in Chapter 4 that the primary gelation mechanism of high nickel content sodium cathode electrode slurries is the dehydrofluorination and cross-linking of PVDF. This gelation process initiates from the formation of NaOH on the surface of the active materials. Therefore, a suitable method to reduce this undesired gelation, is to reduce or eliminate the presence of this NaOH as it is formed.

One possible method is through the addition of acids into the electrode slurry. This has the aim of neutralising the NaOH before the dehydrofluorination of PVDF is able to occur. Additionally, by delaying the addition of PVDF into the electrode slurry mixing process (i.e. through addition of the acid additive at the start of the current electrode slurry mixing process), it allows the NaOH to be neutralised before reaction with PVDF can occur.

Organic acids with carboxylic acid groups were ultimately decided as the class of acid additives to test in the stabilisation of the gelation process. It has been widely reported that polyacrylic acid (PAA) produces greater adhesion strengths than PVDF

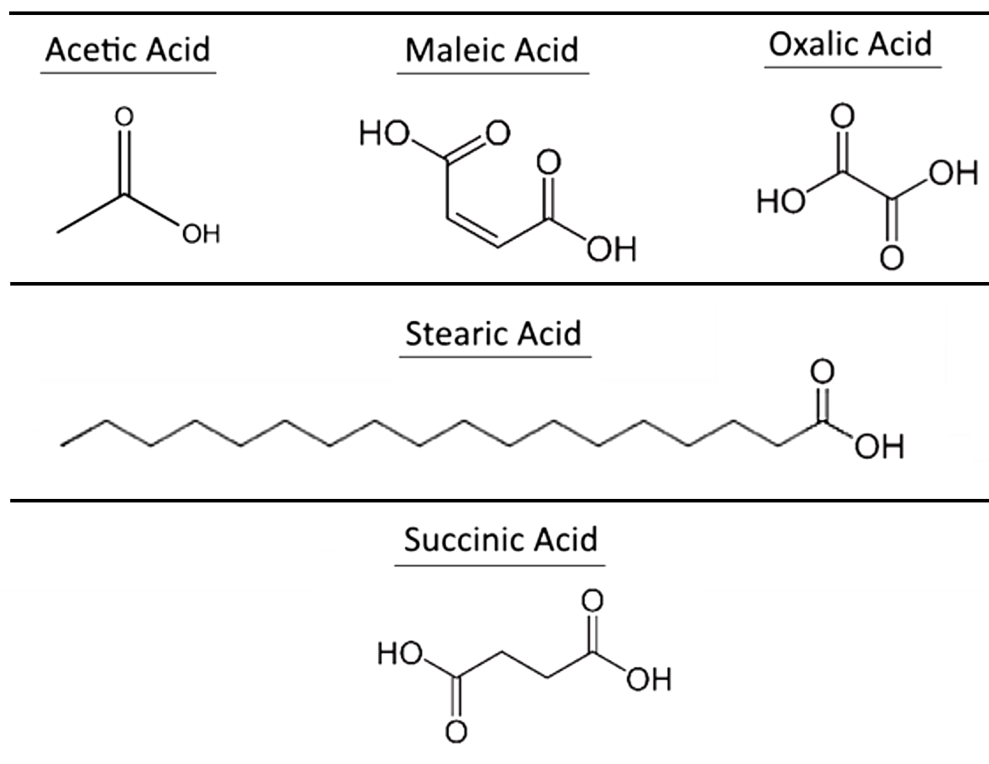


Figure 6.1: Acid additive chemical structures.

[264]. The general assumption is that the carboxylic acid groups play a vital role, through their hydrogen bonding and amorphous nature, in producing this high adhesion strength [64, 264–266].

Carboxylic acid groups have been shown to electrochemically reduce under cycling for silicon anodes in lithium ion batteries [267, 268]. The electrochemical reduction forms carboxylates that act as a protective SEI layer. These carboxylic acid groups favourably reduce over the electrolyte, and the decomposition of the electrolyte can be lessened [267, 268]. Despite the different chemistries (lithium-ion vs sodium-ion batteries), the use of carboxylic acids, over inorganic or other organic acids, could prove beneficial to electrode cycling.

Table 6.1: Properties of acid additives used in this study.

Acid	Carbon Backbone Length	COOH Groups	Molecular Mass	Saturated
<i>Acetic</i>	2	1	60.05	N
<i>Maleic</i>	4	2	116.07	N
<i>Oxalic</i>	2	2	90.03	N
<i>Stearic</i>	18	1	284.48	Y
<i>Succinic</i>	4	2	118.09	N

Table 6.2: pK_a Values of the acid additives used in this study.

Acid	Dissociation Steps		Reference
	1	2	
<i>Acetic</i>	4.76	-	[269]
<i>Maleic</i>	1.92	6.23	[270]
<i>Oxalic</i>	1.23	4.19	[270]
<i>Succinic</i>	4.19	5.48	[270]
<i>Stearic</i>	9.5	-	[271]

5 organic acids, as shown in Figure 6.1, have been chosen because of their varied structures, and different strengths and properties. The 5 chosen acid additives are acetic acid, maleic acid, oxalic acid, stearic acid, and succinic acid.

Acids with a single carboxylic group (acetic and stearic), and those containing two carboxylic groups (also known as dicarboxylic acids) (maleic, oxalic, and succinic) have been chosen to observe the effect of increasing the number of groups. Furthermore, by using acetic acid and stearic acid as additives, a comparison between the chain length of the additive can be considered, see Figure 6.1 (Table 6.1 outlines these properties as well). Similarly, by considering oxalic acid and succinic acid, a comparison of chain length in the dicarboxylic acids can be made. Maleic acid has the same carbon backbone length as succinic, albeit with as an unsaturated structure, containing a carbon-carbon double bond.

The properties of the acids can be seen in Table 6.1. It should be noted that the quantities of acids were added on a weight percentage basis and so electrode slurries containing acetic acid would contain the highest number of moles of additive. However, as some of the acids are dicarboxylic acids, electrode slurries with the additives of oxalic,

maleic, and succinic would actually contain more moles of carboxylic groups. Although, the degree of acid protonation, the pK_a values, should also be considered in evaluating the likely differences between the acids.

The pK_a values, or the strengths, of the acid additives can be found in table 6.2. It is clear that oxalic acid is the strongest acid of the chosen additives, with a primary dissociation pK_a of 1.23. Maleic acid is the next strongest acid with a primary pK_a of 1.92. However, as the secondary pK_a of maleic acid, 6.23, is above that of acetic acid, 4.76, for the same weight of additive, acetic acid may prove to be stronger. Succinic acid, has a primary dissociation pK_a , 4.19, that is equal to the secondary dissociation pK_a of oxalic acid, and so can be considered a weaker acid. Stearic acid, is by far the weakest acid, with a pK_a of 9.5 [269–271].

There are other properties and interactions of these acids that should be noted for this investigation. Oxalic acid has been shown to corrode aluminium and aluminium alloys. This corrosion could etch into the aluminium current collector which could help to improve the contact and adhesion strength of the electrode [272,273].

In some studies, acetic acid has been shown to have a mild corrosive effect on aluminium [274]. However, this corrosion was over a 24 hour period [274], the effect on the aluminium as the electrode slurries dry over a 1 hour period is likely to be minimum. Otherwise, corrosion of aluminium by acetic acid has been shown to require 95 % acetic acid at boiling point [273]. Aluminium, in general, is resistant to organic acids at room temperature, however, higher molecular weight acids, at high temperatures, are able to corrode the aluminium [273]. It is therefore suggested that, due to the low quantity of acid additives, 2 wt%, and the temperatures below 30° (the mixing equipment does heat up over the course of the mixing), it can be assumed that there is little, to no, corrosion of the aluminium current collector by all of the acid additives, bar oxalic acid.

It is worth noting that aluminium is very rapidly attacked by alkalis and readily complexes with hydroxyl ions [273], such as those formed due to the instability of the active material. Once an acid additive has been reacted away, it is possible for the further

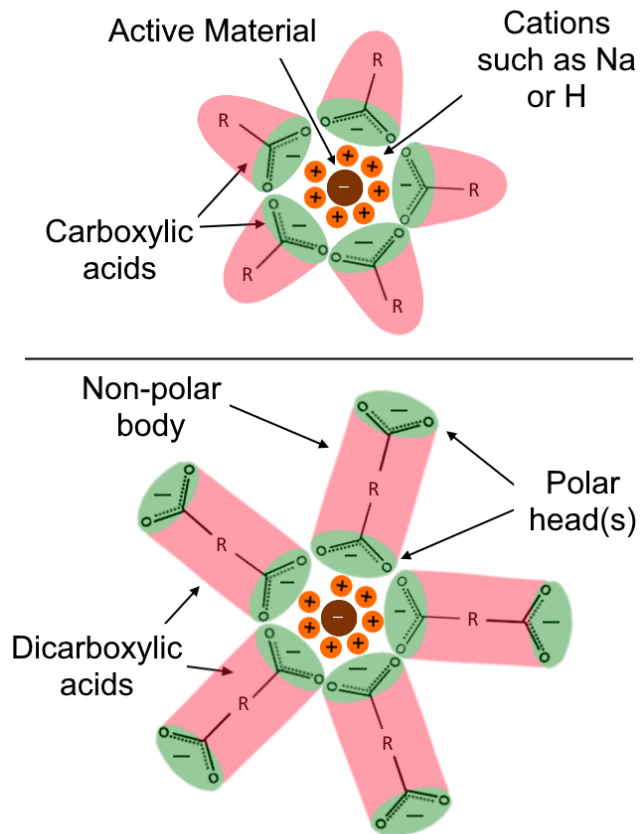


Figure 6.2: Simplified ionic micelle formation due to the charged heads on the acid additives.

production of hydroxides to corrode the aluminium current collector.

Along with these properties, these acids have the potential to colloidally stabilise the electrode slurry. The presence of a disassociating acid in the electrode slurry will increase the concentration of ions and, hence, decrease the thickness of the diffuse part of the electric double layer around carbon and active material particles [275]. This effect has the potential to reduce the extent of colloidal jamming on charged particles in the electrode slurry.

The removal of sodium from the active material, forming NaOH, will create a negative charge across the surface. The disassociation of the carboxylic acid group in the acid additives can create a charged head and, hence, the acid additives have the potential to form ionic micelles (based on charge distributions), as shown in Figure 6.2 [276–279].

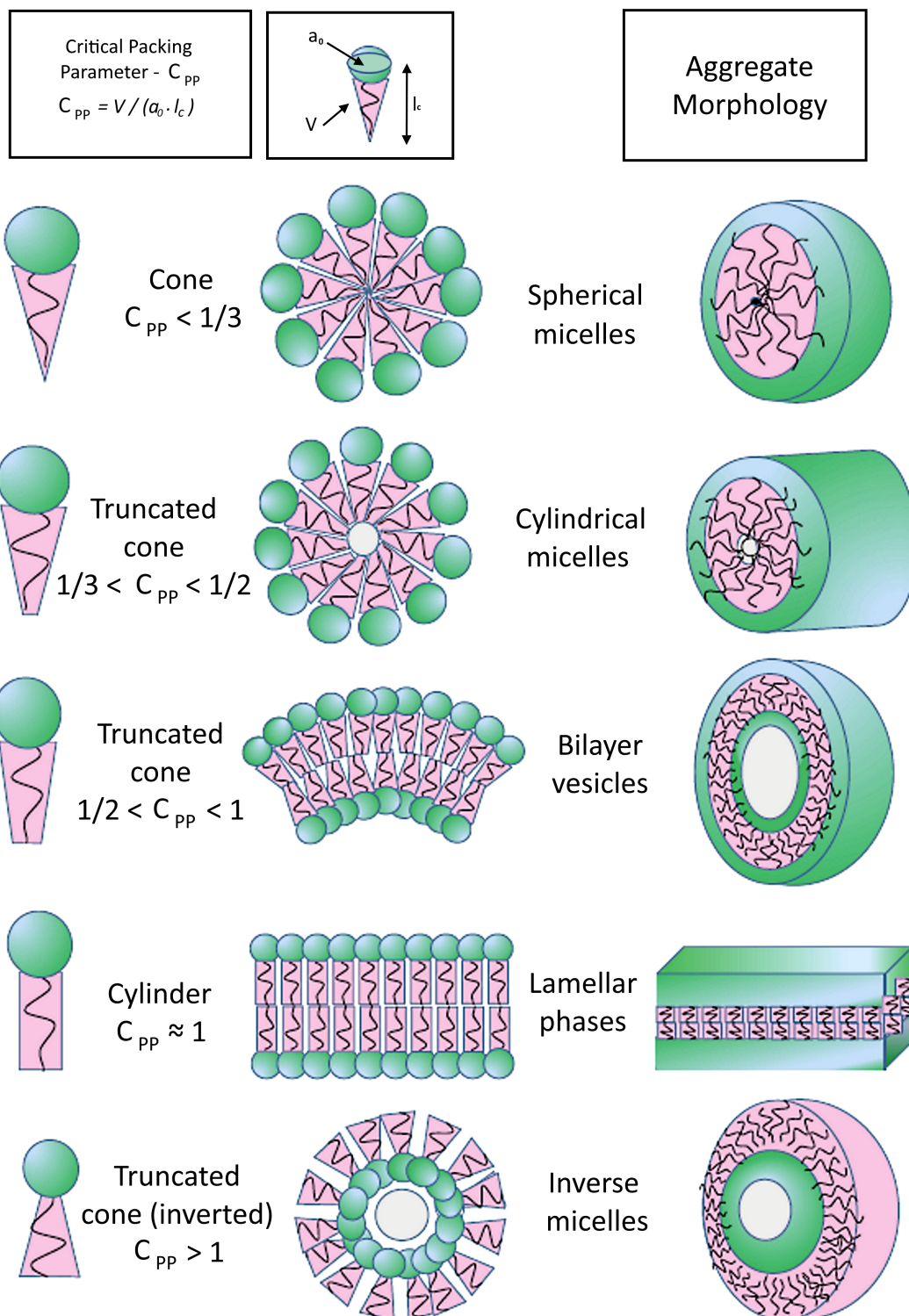


Figure 6.3: Micelle shape factors as explored by Lombardo *et al.*, 2015 [276].

Figure 6.3 shows possible ionic micelle formations. In this application, the green circles that denote the charged ionic head groups, represent a carboxylic group connected to an active material. Therefore, for the micelle configurations of spherical micelles, cylindrical micelles, bilayer vesicles, and lamellar phases the active material will be around the outside of the micelle, and thereby exposed to the atmosphere. For the final structure, inverse micelles, the active material is situated within the aggregate, and therefore shielded from the atmosphere.

As demonstrated in Figure 6.3, calculations of the micelle critical packing parameter, C_{PP} can be used to predict the aggregate morphology, the structure of the micelles that are formed. This critical packing parameter can be calculated by use of Equation 6.1.

$$C_{PP} = \frac{V}{a_0 l_c} \quad (6.1)$$

where V is the effective volume of the charged chains, a_0 is the effective charged head-group surface area, and l_c is the effective chain length. In the case of the additives explored in this chapter, as the charged head-group is a carboxylic group, a_0 will be the same for all monoacids, and doubled for the diacids (assuming both carboxylic groups can be used).

This chapter covers the analysis of the effect of these acid additives (acetic, maleic, oxalic, stearic, and succinic) on the physical and chemical properties of the electrode slurries, through the use of FTIR and rheological analysis. It explores the changes these additives have on the physical properties of the electrodes, through adhesion testing and conductivity measurements, and it explores the changes to the electrochemical properties.

6.2 Aims and Objectives

Through the additions of the aforementioned acid additives, the major goal of the work presented in this chapter was to extend the processing window of high nickel content

sodium cathode electrode slurries. Consequently, to benefit any potential future research studies, it was important to investigate the mechanisms that enabled an extension to this processing window. This was achieved through the following objectives:

- Achieve a stabilisation of the electrode slurry gelation past the 20 minute processing window established for the reference electrode slurry (Chapter 4).
- Observe how the measured rheological properties of the electrode slurry change over this time.
- Assess how the measured rheological properties of the electrode slurry change after this nominal processing window to examine if the processing window can be extended.
- Measure the effect that these stabilising additives have on the properties of the electrodes.

6.3 Materials and Methods

Electrode slurries were produced using an alteration of the standard method, discussed in Chapter 3. Carbon coated Na-NMST ($\text{NaNi}_{1/2}\text{Mn}_{1/4}\text{Sn}_{1/8}\text{Ti}_{1/8}\text{O}_2$) was mixed with the remaining conductive carbon black, an 8 wt% PVDF (polyvinylidene fluoride) (Solvay 5130) binder in NMP (n-methyl-2-pyrrolidone) solution, and an acid additive in a ratio of 87:6:5:2 by weight. The cathode ink was mixed in sealed pots in a Thinky ARE-250 Planetary Mixer, situated in a Munters dry room with a maximum dew point of - 40°C.

Acid additives used were HPLC grade with a purity $\geq 99\%$, acetic acid (Acros Organics), maleic acid (Sigma-Aldrich), oxalic acid (Sigma-Aldrich), stearic acid (VWR Chemicals), and succinic acid (Acros Organics).

There were four stages of mixing, with one additional stage before the normal method outlined in the experimental methods chapter (Chapter 3). Initially, the acid additive and the extra NMP, measured to give a final solids content of 40 wt%, were mixed together.

The nominal mixing time of 5 minutes and speed of 1300 rpm were sufficient for each of the organic acids to dissolve in NMP. The main electrode slurry manufacturing method was then used. 3 separate mixing stages began with the addition of carbon coated active material. This was followed by the addition of carbon black, and, finally, the PVDF solution. Each mixing stage lasted 5 minutes with a speed of 1300 rpm.

All other analysis methods can be found detailed in Chapter 3.

6.4 Results and Discussion

The analysis of these acid additives (Figure 6.1) will be explored in the following manner.

1. The impact of the acid additives on the chemical stability of the electrode slurry will be investigated through the use of FTIR analysis.
2. The effect these acid additives have on the physical stability of the electrode slurries will be explored through the use of oscillatory rheology and the fitting of a Maxwell model. The analysis will be split between the measured storage and loss modulus and the phase angles from the oscillatory rheology, and the fitted relaxation times from the Maxwell models.
3. The changes to the electrode properties will be analysed through the use of adhesion measurements and conductivity measurements.
4. The effects of the acid additives on the electrochemical properties will be measured using cycling analysis and electrochemical impedance spectroscopy evaluations.
5. Finally, a summary table that highlights the most and least optimal additives at each stage of characterisation will be given.

6.4.1 Stabilisation of the Electrode Inks

The effect of the stabilising additives on the electrode slurries was characterised using two methods, a chemical analysis using FTIR and a physical analysis using oscillatory

rheology.

6.4.1.1 Ex-situ FTIR studies of Electrode Slurries

The chemical progression of the electrode slurry was characterised by use of FTIR, as seen in Figure 6.4. The reference electrode slurry, analysed in Chapter 4, has been included in Figure 6.4 for comparison purposes.

In general, the major points of comparison between the spectra can be split between the degree of reaction and the speed of reaction. The degree of reaction can be noted by the growth in the spectra peaks (*i.e.*, the reference electrode slurry has more peak growth than the oxalic acid spectra, therefore the reference electrode slurry has a greater degree of reaction than the oxalic acid electrode slurry). The degree of reaction can also be noted in the inset of each spectra (denoting the C=O stretching), where the shift in the peak shows the extent of reaction. For each inset, the final point of reaction for the reference electrode slurry has been added with a dotted line.

The speed of reaction is a comparison point that can be observed by how close the spectra lines are (similar to contour lines). Closer lines denote a slower reaction speed, and further apart spectra shows a faster reaction.

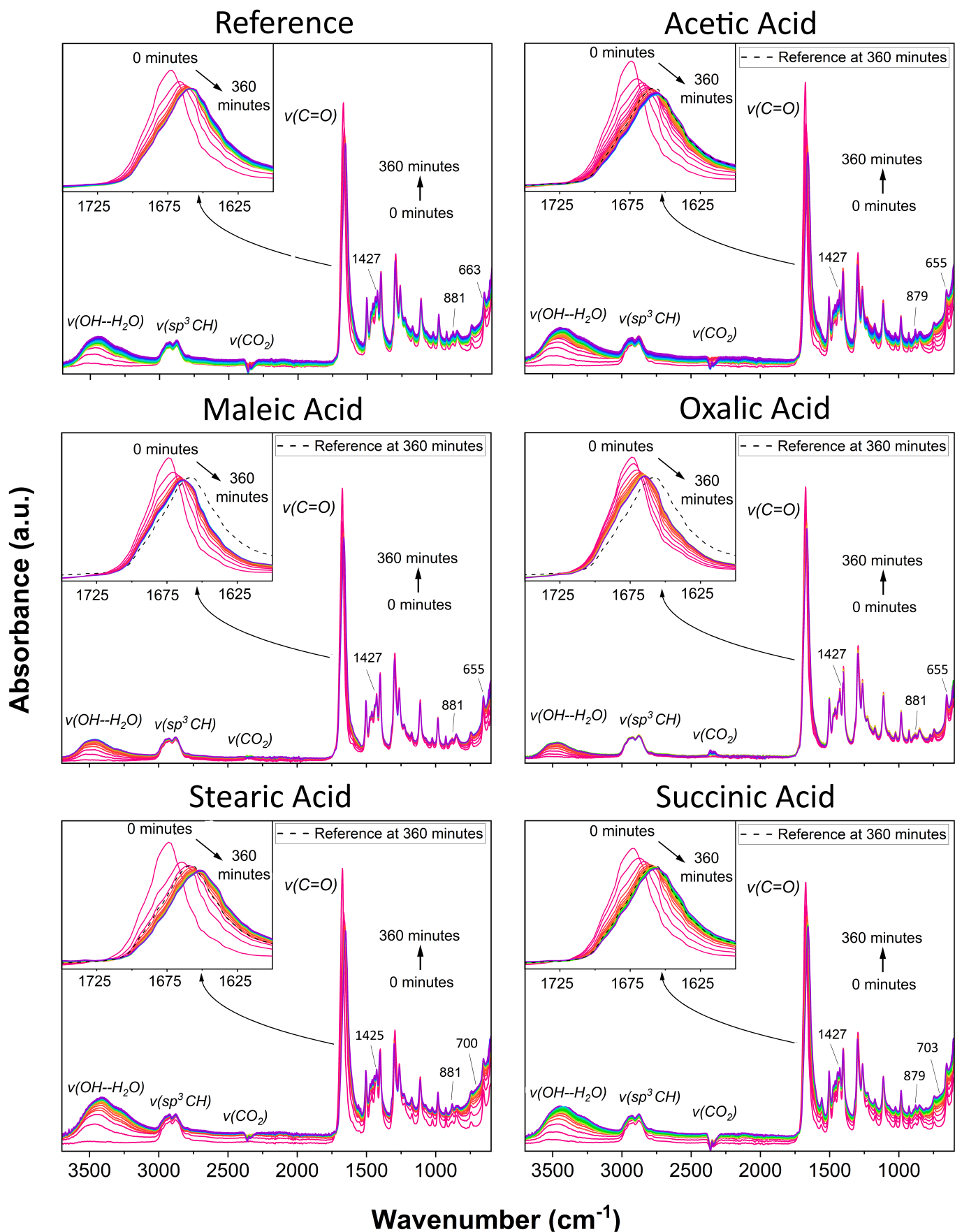


Figure 6.4: Fourier transform infrared spectra for the reference electrode slurry and all the electrode slurries containing 2.0 wt% of the acid additives.

The major functional groups of note have been annotated on Figure 6.4. There is a medium-intensity broad peak with a peak centre at approximately 3500 cm^{-1} , attributable to the OH stretching of surface absorbed water in the electrode slurry, and to hydrogen bonding throughout the electrode slurry.

The weak shoulder peak at approximately 3300 cm^{-1} can be attributed to the OH stretching of metal hydroxides. The progression of this shoulder peak can be used as an indicator of NaOH formed due to the reactions of the active material. As established in Chapter 4, the following peaks, between approximately 3000 cm^{-1} and 2700 cm^{-1} relate to the CH stretching in NMP. Peaks at 3014 cm^{-1} and 2953 cm^{-1} can be assigned to the CH_2 asymmetric and symmetric vibrations in NMP. Peaks at 2875 cm^{-1} and 2792 cm^{-1} can be assigned to the CH stretching in sp^3 hybridised carbons in NMP. The asymmetrical peaks at 2361 and 2341 cm^{-1} can be attributed to the stretching of CO_2 .

The high intensity peak at approximately 1670 cm^{-1} can be attributed to the C=O stretching, primarily in NMP. However, with the addition of 2 wt% of each acid additives into the electrode slurries, the C=O stretching in the carboxylic acid groups would appear in this region. Demonstrated in Chapter 4, the hydrogen bonding and resonance effect in NMP causes the C=O stretching of γ -lactams, typically between 1750 and 1700 cm^{-1} [280], to shift to lower wavenumbers. This effect of hydrogen bonding can similarly shift the wavenumbers, depicted in table 6.3 of the acid additives. Subsequently, as demonstrated in Chapter 4, there is a region of IR peaks belonging to NMP and PVDF. For comparison purposes, the annotated peaks at approximately 1427 , 880 , and 655 (or 700) cm^{-1} are the peaks that are closest to those found in NaOH. However, many of these share an overlap with peaks belonging to NMP and PVDF, hence it is impossible to confirm the present and formation of NaOH in this region of the spectra. Interestingly, in the spectra for the electrode slurries containing stearic acid and succinic acid, there is a weak peak at approximately 700 cm^{-1} that forms over the 360 minute measurement duration. It is possible that this peak can be attributed to NaOH.

Overall, from Figure 6.4, it is clear that comparing the spectra of the reference

Table 6.3: FTIR functional groups of acid additives.

Acetic Acid	Maleic Acid	Oxalic Acid	Stearic Acid	Succinic Acid	Assignment
3400 (s)	3412 (s)	3404 (s)	3505 (w)	3360 (w)	ν OH
2935 (w)	-	-	2963 (w)	3030 (s)	ν CH(CH ₃)
-	-	-	2916 (s)	2932 (s)	ν CH(CH ₂)
-	-	-	2810 (s)	2744 (s)	ν CH(CH ₂)
-	2583 (s)	-	-	-	ν CH(CH)
1770 (w)	1711 (s)	1762 (s)	1710 (s)	1683 (s)	ν C=O
-	-	1742 (w)	-	-	ν C=O
1413 (s)	1456 (s)	1354 (w)	1470 (s)	1414 (s)	β OH
1295 (s)	1430 (s)	-	-	1306 (s)	β OH
-	1253 (s)	1260 (s)	1119 (s)	1196 (s)	ν C-O
-	1206 (s)	-	-	-	ν C-O
[281]	[282, 283]	[280, 284]	[280, 285]	[280, 286]	

electrode slurry to those containing the acid additives shows only very slight changes. The large presence of NMP in the electrode slurries and the small quantity of 2.0 wt% of acid additive is unlikely to cause major differences between the IR spectra, however, over time some changes do appear.

The two main areas of alterations lie at approximately 3400 cm^{-1} , relating to $\nu(\text{OH}--\text{H}_2\text{O})$, the OH stretching of surface absorbed water and hydrogen bonding in the electrode slurry, and at 1675 cm^{-1} , relating to $\nu(\text{C}=\text{O})$, C=O stretching. Coupled with the $\nu(\text{OH}--\text{H}_2\text{O})$ at approximately 3400 cm^{-1} is the weak shoulder peak at approximately 3300 cm^{-1} , which can be used as an indicator of NaOH formed.

As previously outlined, from these areas of alterations, there are two main indicators for the degree of reaction. Namely, the speed of reaction progression, and the degree of reaction progression.

The extent of reaction progression is most evident in the inset of each spectra, in Figure 6.4, relating to the $\nu(\text{C}=\text{O})$. The spectra of the reference electrode slurry after 360 minutes, can be seen indicated by the dotted line. It can be clearly noted that for electrode slurries containing either oxalic acid, or maleic acid, the final spectra contains a C=O peak at a higher wavenumber. For electrode slurries containing additives of acetic acid, stearic acid, or succinic acid, the C=O peak in the final spectra is at a lower

wavenumber.

In Chapter 4, it has been suggested that the ring opening reaction of NMP caused by the reaction with hydroxyl ions can shift and broaden the C=O peak to lower wavenumbers. This ring opening reaction forms 4-(methylamino) butanoic acid. Therefore, the greater the shift in this C=O peak, the larger the quantity of 4-(methylamino) butanoic acid, indicating that more free hydroxyl ions have been able to react with NMP. Additionally this peak can indirectly indicate a greater presence of NaOH in the electrode slurry.

The electrode slurries that resulted in a reduced shift in this C=O peak are namely oxalic acid and maleic acid. Therefore, it can be concluded that the stronger acids cause less free hydroxyl acids and a lower extent of reaction.

Furthermore, the weak shoulder peak at 3300 cm^{-1} , the indicator of NaOH formed, shows smaller magnitudes for the acids with lower pK_a values, oxalic and maleic acid. Similarly, these stronger acids cause a slower shift in the $\nu(\text{C}=\text{O})$ peak and a slower increase in the $\nu(\text{OH}--\text{H}_2\text{O})$ peak. It can thus be concluded that the strength of the acid is the primary contributor to the chemical changes in the electrode slurries.

6.4.1.2 Ex-situ Rheology studies of Electrode Slurries

Discussed in Chapter 5, the results from performing multiple frequency sweeps can be processed and observed in several different ways. It is important to review the different data sets of the storage and loss moduli, the phase angle, and the relaxation time calculated from the Maxwell modelling of this data.

6.4.1.2.1 Storage and Loss Moduli

The storage and loss moduli for electrode slurries containing the acid additives can be found in Figure 6.5. While the results were recorded every 5 minutes over a frequency sweep, as demonstrated in 5, frequency data sets have been separated out and shown over time.

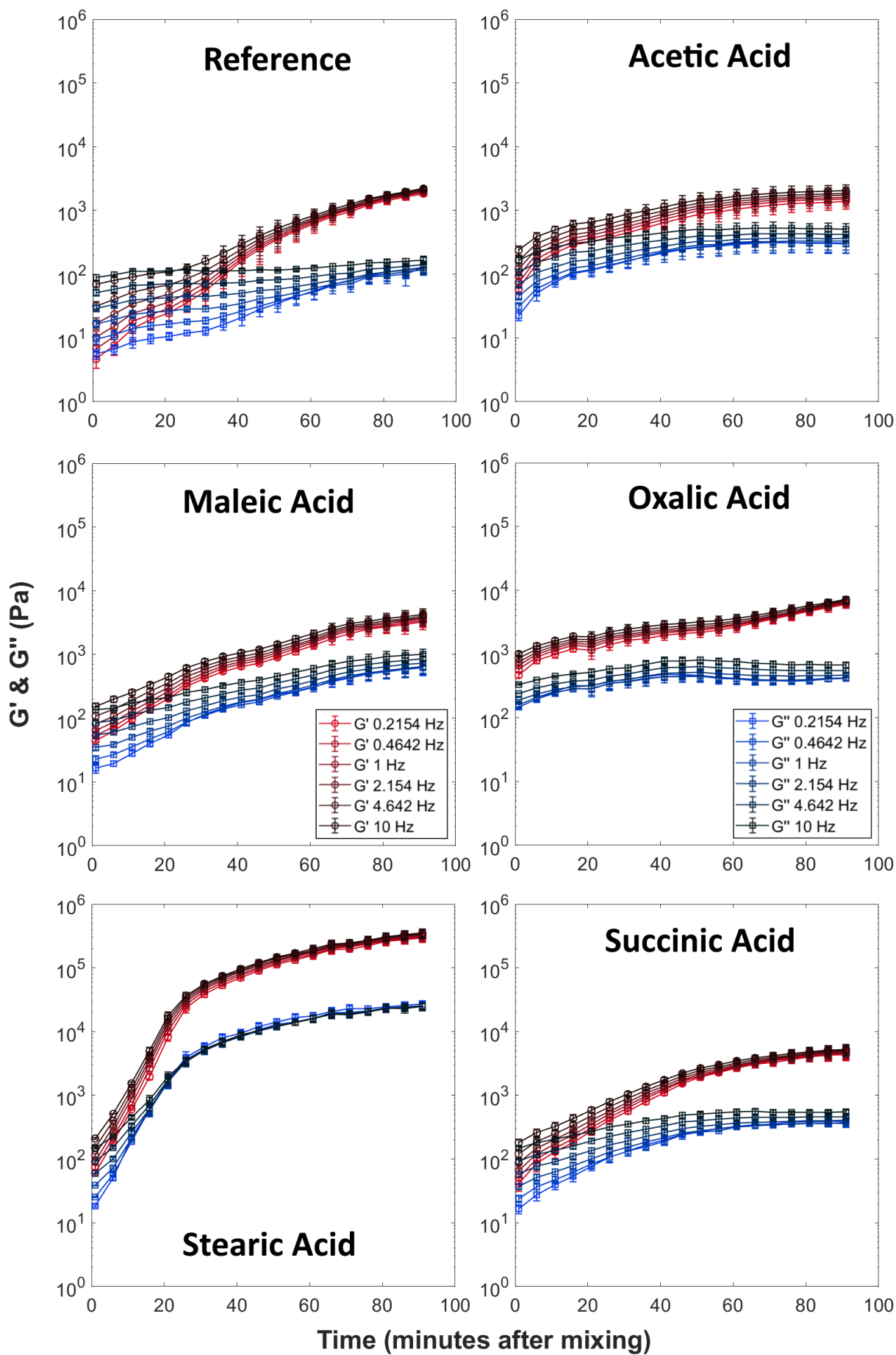


Figure 6.5: Storage and Loss Modulus for the reference electrode slurry and all the electrode slurries containing 2.0 wt% of the acid additives.

For comparison purposes, the reference electrode slurry has been included. Initially, for the reference electrode slurry, the values of G' and G'' are very similar. For the highest frequency of 10 Hz, G' and G'' are approximately 100 Pa and for the lowest frequency of 0.2154 Hz the values of G' and G'' are 10 Pa.

G' increases more rapidly than G'' for all frequencies with a gradual increase for approximately 20 minutes and a more rapid increase until approximately 40 minutes, whereby the rate slows. Finally G' reaches a value of 2000 Pa, a 20 fold increase for the highest frequencies and a 200 fold for the lowest. This massive increase in the storage modulus is consistent with the formation of a chemical gel.

In terms of G'' , the higher frequencies remain steady throughout the measurement window, and the lower frequencies experience a slow increase after 40 minutes. Frequency convergence is reached after 60 minutes for G' and around 90 minutes for G'' .

The large difference between the values of G' and G'' rapidly increases after approximately 40 minutes, whereby a divergence between these values progresses, denoting the progression of the electrode slurry gelation.

By comparing the results of the electrode slurry found in Chapter 4, it can be concluded that the divergence between G' and G'' is related to the relaxation time of the electrode slurry gel, i.e the progression of the electrode slurry gelation. The magnitude of G' and G'' , primarily the storage modulus, G' , relates to the strength of the network in the electrode slurry. A higher value of G' infers that more energy is required to breakup the network. It is the combination of these two factors, as well as the results exhibited in the phase angle and relaxation time data, that demonstrate the most effective acid additive.

The final property demonstrated in the storage and loss modulus data is the frequency convergence. Once full convergence is reached, this dictates that particle sedimentation is unable to occur and the gel network is sufficient to entrap particles.

For the electrode slurries that contain acetic acid, it is evident that both G' and G'' start at higher values than the reference electrode slurry.

G' starts between a value of 70 and 250 Pa for the lowest and highest frequencies,

respectively, and G'' starts between 20 and 200 Pa. Over the time range, this is very little frequency convergence, evidence of a low degree of dynamic arrest. Small convergence can be noted in G' , suggestive of slight structural development. Both G' and G'' increase over a time of 45 minutes, whereby a plateau is reached. Final values of G' and G'' are averaged to 1000 and 200 Pa, respectively. This final value of G' reached is significantly lower than that of the reference electrode slurry, suggesting a reduction in the degree of gelation. Similarly, the smaller magnitude of disparity between G' and G'' over the reference electrode slurry indicates that a much weaker and less developed gel network has formed. The disparity between G' and G'' seems to initiate after 40 minutes and increases slowly thereafter, indicating that the gelation network becomes physically evident after 40 minutes, albeit as a weaker gel.

From the results of the storage and loss modulus for the electrode slurries that contain maleic acid, Figure 6.5, it is evident that it shares similar behaviour with acetic acid. Values of G' and G'' start at approximately 100 and 30 Pa, respectively, slightly higher than the reference electrode slurry. These values increase over the time duration to approximately 6000 and 900 Pa for G' and G'' , respectively, with a decrease in the growth of G' and G'' occurring after 30 minutes. There is a convergence in G' after approximately 80 minutes, and a very slight convergence in G'' . Contrary to the reference electrode slurry and the electrode slurries that contain acetic acid, the divergence between G' and G'' begins at the earlier point of approximately 30 minutes. The final magnitude of the divergence between G' and G'' is less than that of the reference electrode slurry and greater than that of the electrode slurries that contain acetic acid. It can be concluded that the gel network becomes more evident at an earlier time but the final strength is weaker than the reference electrode slurry.

For the electrode slurries that contain oxalic acid, the behaviour of G' and G'' is very different from the other measured electrode slurries. A large divergence between G' and G'' is evident at the onset of measurements. G' exhibits a slow rate of increase until approximately 55 minutes from 1000 Pa to 3000 Pa. After 55 minutes, the rate of growth

in G' increases and the divergence between G' and G'' rapidly rises. G' finalises at value of approximately 10,000 Pa. G'' initiates at a value of 200 Pa and progresses with a very slight increase until the final measurement point of approximately 300 Pa. There is a slight dip in G'' after 55 minutes. Before 55 minutes, it can be suggested that the physical structure of the gel remains fairly consistent and constant, with large physical effects occurring thereafter.

Stearic acid-containing electrode slurries exhibit very different trends. A steep increase in both G' and G'' occurs from the onset of measurements. G' increases from a value of 150 Pa to 30,000 Pa over approximately 25 minutes with a region of slow logarithmic growth following. The final value of G' is approximately 400,000 Pa. G'' displays similar trends to G' , there is an increase from 60 Pa to 10,000 Pa over a 25 minute period with a slow growth to a value of 20,000 Pa occurring thereafter. There is a large degree of frequency convergence across the entire timescale with almost complete convergence occurring after approximately 25 minutes. After approximately 25 minutes, the difference between G' and G'' remains fairly constant. It can be inferred that, while the gel network does not develop much past 25 minutes, the initial formation creates a very strong gel with a very high apparent viscosity.

Electrode slurries containing succinic acid demonstrate trends that are similar to the reference electrode slurry. There is an initial slow increase in both G' and G'' until 50 minutes with an approximate plateau forming thereafter. G' increases from a value of 100 Pa to 2000 Pa after 50 minutes and then to a final value of 3000 Pa at the conclusion of measurements. G'' increases from a value of 30 Pa to 100 Pa after 50 minutes and then plateaus and remains at this value for the remainder of the measurements. These electrode slurries that contain succinic acid see a large divergence between G' and G'' initiating after approximately 30 minutes and finalised by approximately 70 minutes. After 70 minutes there appears to be very little increase in the structural development.

The variations in the storage and loss modulus could be explained by the hypothesised formation of different micelle structures, as outlined in Section 6.1 and

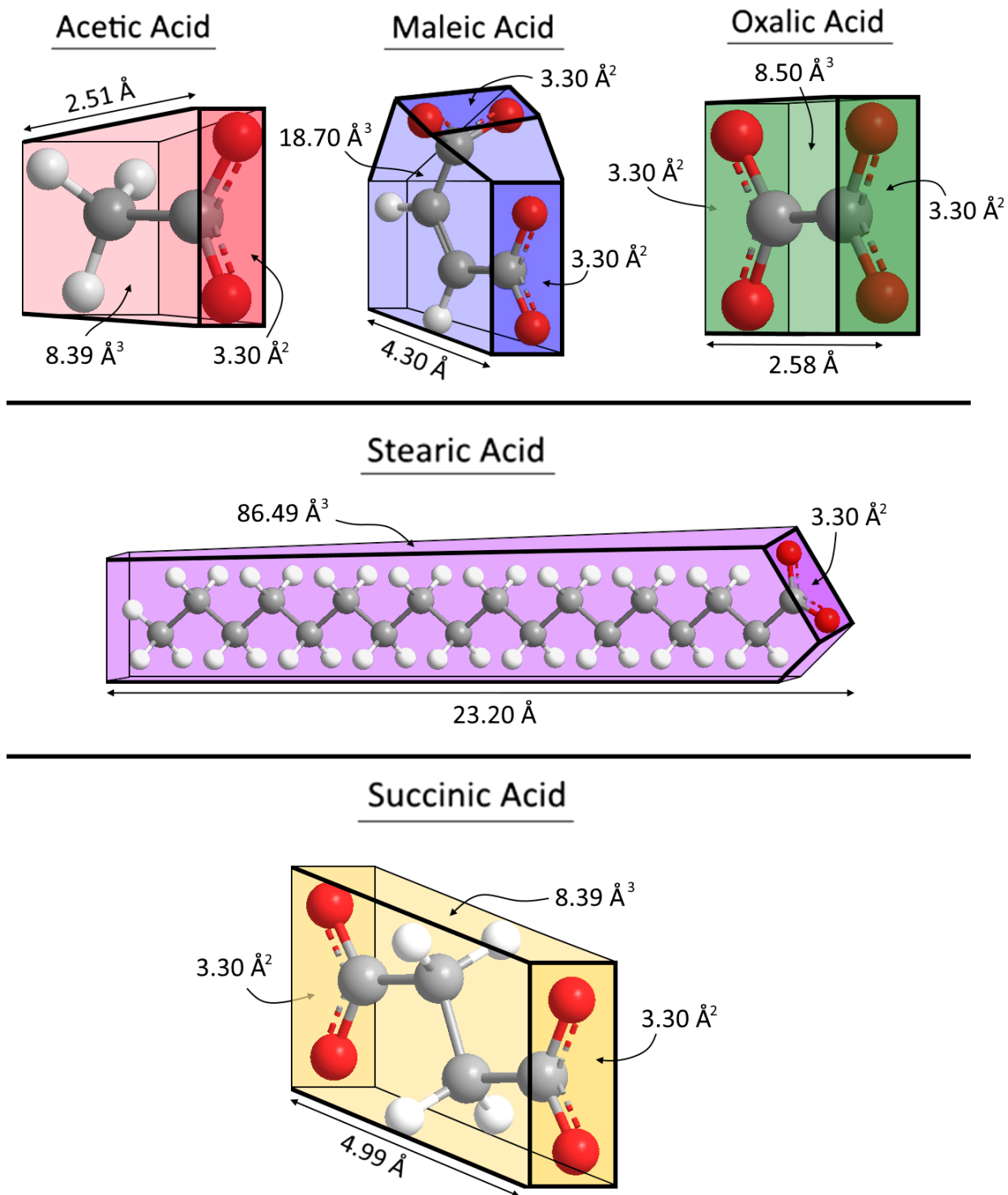


Figure 6.6: Approximated disassociated acid dimensions - dimensions were calculated using Chem3D, PerkinElmer.

Table 6.4: Approximated micelle critical packing parameters (from Figure 6.6) and predicted structures.

	Acetic Acid	Maleic Acid	Oxalic Acid	Stearic Acid	Succinic Acid
Approximate Volume, V (\AA^3)	8.39	18.70	8.50	86.49	19.63
Length, l_c (\AA)	2.51	4.30	2.58	23.20	4.99
Polar Area, a_o (\AA^2)	3.30	3.30	3.30	3.30	3.30
Critical Packing Parameter, $V/l_c a_o$	1.01	1.32	1.00	1.13	1.19
		0.66	0.50		0.60

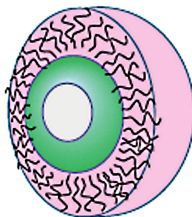
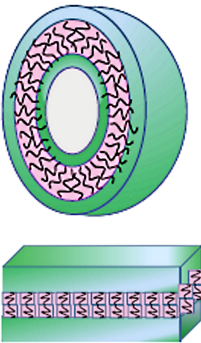
Acid Additive	Predicted Micelle Structure
Acetic acid, Maleic acid, Stearic acid	 <p>Inverse Micelle</p>
Oxalic acid, Succinic acid	 <p>Bilayer Vesicles, Lamellar Phases</p>

Figure 6.2. The micelle structures formed can be predicted using values of the critical packing parameter. A summary of these approximated values, along with the corresponding predicted structures can be observed in Table 6.4. As demonstrated in Figure 6.3, critical packing parameters between 0.50 and 1.00 would form bilayer vesicles, values of approximately 1.00 would form lamellar phases, and values above 1.00 would form inverse micelles.

For the electrode slurries containing acetic acid, which seems to be the "best" performing additive, rheologically, approximations of the dimensions of acetic acid (Figure 6.6) and a calculation of the critical packing parameter (Table 6.4) produces a value of 1.01, relating to inverse micelles. These inverse ionic micelles formed would end in a neutrally charged tail that surrounds active material particles (see Figures 6.2 and 6.3). [276] The neutrally charged tail is important as it can reduce the electric double layer and reduce colloidal jamming.

For electrode slurries containing stearic acid as an additive, calculations of the critical packing parameters, give a value of 1.13, suggesting that there would be inverse micelles formed (Table 6.4). However, it is suggested that the long chain length of stearic acid would create very large micelles that would likely exhibit entangling effects and jamming between each other, thereby increasing the elastic rheological properties.

Conversely, for the dicarboxylic acids, oxalic, maleic, and succinic, any ionic micelles formed would contain a charged tail, as shown in Figure 6.2. Therefore, either, the jamming effect of an electric double layer would still be present, or, due to both head-groups interacting, bilayer vesicles or lamellar phases [276] would form instead of the inverse micelles. These bilayer vesicles and lamellar phases (as shown in Table 6.4) would therefore provide little shielding to the active material, and hence still allow a gelation of the electrode slurry. The critical packing parameters come to a value of 0.50 and 0.60, for oxalic acid and succinic acid, respectively (providing that both head-groups are able to interact). However, it is likely that some inverse micelles would form due to only one head-group interacting and some stabilisation would occur.

For maleic acid, as it performs better than succinic acid in stabilising the electrode slurry, it is prudent to suggest that the unsaturated structure plays a key role in the formation of these micelles. With no rotation across the double bond structure, the steric hindrance could prevent the bilayer vesicles and lamellar phases forming and the micelles are forced to be inverse micelles, like acetic acid. In the calculations of the critical packing parameter (Table 6.4), this would be demonstrated by the value of 1.32, rather than 0.66.

6.4.1.2.2 Phase Angle

The phase angle between G' and G'' for the electrode slurries containing the acid additives can be seen in Figure 6.7. Observations of the phase angle are useful as they can demonstrate the point at which the storage modulus begins to dominate over the loss modulus, and elasticity dominates. A value of 0° describes an elastic like deformation of the electrode slurry. 90° demonstrates a completely fluid like response to deformation and 45° describes mixed behaviour.

From Figure 6.7, the reference electrode slurry, which has been included for comparative purposes, experiences a decline from a phase angle of 60° to an angle of 3° over approximately 60 minutes. After 60 minutes there is a frequency convergence and the phase angle plateaus at a value of 3° . This is demonstrative of a high degree of structural elasticity forming in the electrode slurry. [287] Furthermore, this point of frequency convergence suggests a retention of particles in the electrode slurry with sedimentation unlikely to occur, as would be expected for a physical gel network.

By comparison, both the electrode slurries containing acetic or maleic acid show very different structural development and final values of the phase angle. For the electrode slurries containing acetic acid, the phase angle begins at approximately 30° (depending on the frequency) and steadily decreases over a 60 minute period until the frequencies (apart from 10 Hz) converge at a phase angle of 15° . Similarly, the phase angle for electrode slurries containing maleic acid starts at approximately 30° (depending on the frequency)

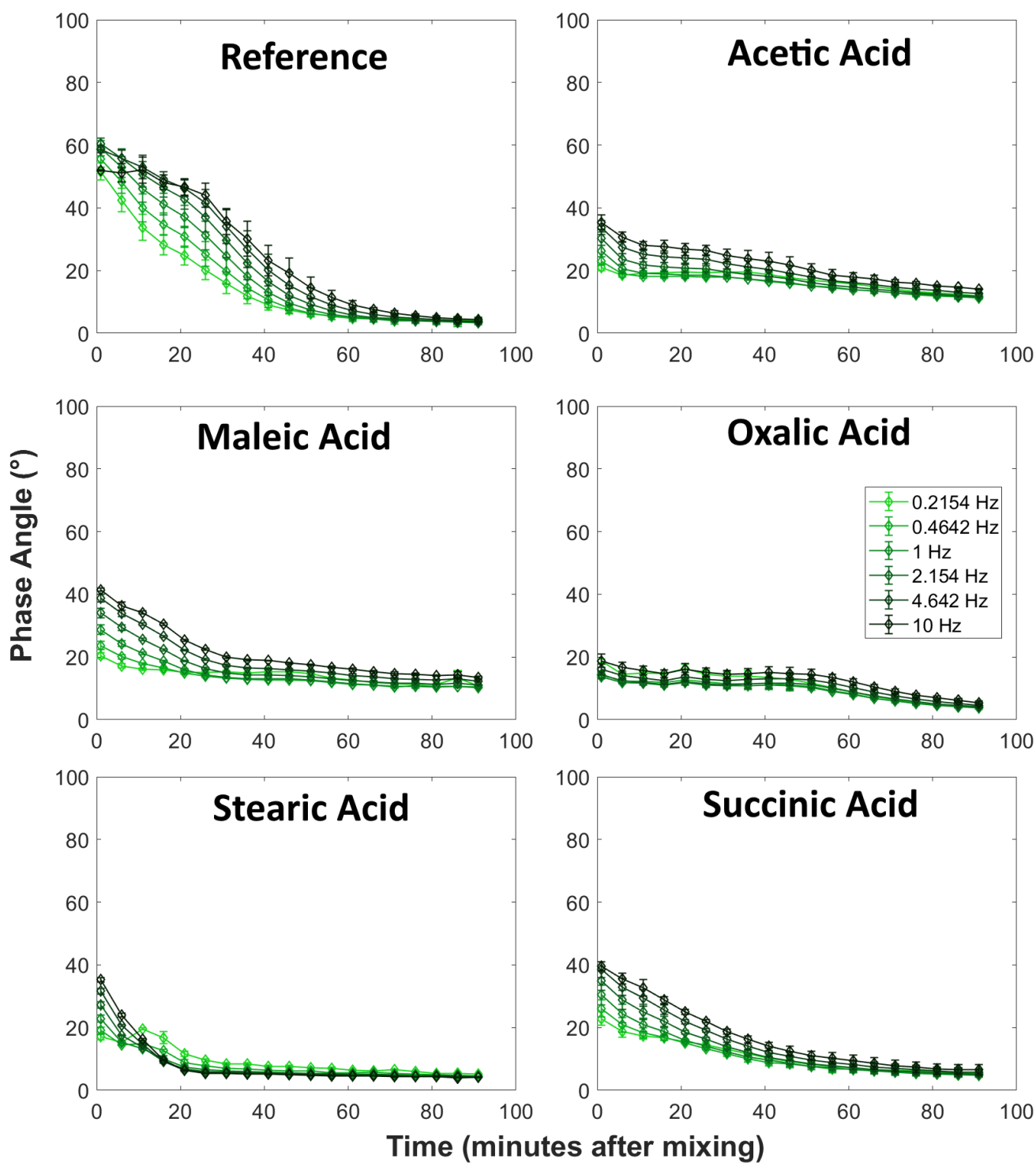


Figure 6.7: Phase Angle for the reference electrode slurry and all the electrode slurries containing 2.0 wt% of the acid additives.

and more rapidly declines to a value of 15° over 30 minutes.

This higher value of 15° , for both electrode slurries containing acetic acid or maleic acid, suggests that the gel formed is less elastic than the reference electrode slurry and has a more fluid response to deformation.

For the electrode slurries containing oxalic acid, the phase angle begins at an average value of 15° and remains constant for approximately 50 minutes. After 50 minutes, there is a steady decline to a value of approximately 5° where the lower frequencies converge. The value of 5° demonstrates a point where the gel network has developed sufficiently for the electrode slurry to be uncoatable. The initial value of 15° is more difficult to interpret. Physically, the electrode slurry appears completely fluid and flows under deformation. A suggestion is that the inclusion of the oxalic acid into the electrode slurry has altered the charge distribution causing an increase in the effect of particle confinement. For colloidal solutions, such as these electrode slurries, where the high solids content pushes the deformation behaviour towards elasticity [127], any change to the electric double layers can easily disrupt the flow and elasticity.

In the case of the electrode slurries that contain stearic acid, the phase angle starts at an average value of 30° and experiences a rapid decline over 20 minutes to the final plateaued value of approximately 5° . Frequency convergence is reached after approximately 60 minutes. This final value of 5° suggest the final gel form is similar in strength and structure to that of the reference electrode slurry.

The final acid additive examined, succinic acid, exhibits similar phase angle behaviour to those electrode slurries containing maleic acid, albeit with lower final values of phase angle. There is a gradual and steady decrease in the phase angle, coupled with a convergence of frequencies, to a final value of approximately 5° . Initial values of phase angle, similar to the other acid additives, are far lower than those of the reference electrode slurry, starting between 20° and 40° across the frequency range.

Table 6.5 demonstrates a summary of the oscillatory rheology data, and presents a comparison of the key values after 40 and 90 minutes.

Table 6.5: Summary of storage and loss values, phase angle values and the loss factor (G'/G'') after 40 minutes and 90 minutes.

	After 40 minutes				After 90 Minutes			
	G'	G''	Loss Factor	Phase Angle (°)	G'	G''	Loss Factor	Phase Angle (°)
Reference	218.3	50.1	4.4	16.4	2043.3	124.2	16.5	3.5
Acetic Acid	888.0	275.6	3.2	18.1	1735.7	363.3	4.8	11.8
Maleic Acid	845.7	214.8	3.9	14.2	3776.7	736.7	5.1	11.0
Oxalic Acid	2406.7	494.0	4.9	11.7	6620.0	464.7	14.2	4.1
Stearic Acid	86433.3	8516.7	10.1	5.6	330000.0	25233.3	13.1	4.4
Succinic Acid	1406.7	258.1	5.4	10.5	4820.0	405.5	11.9	5.1

Based on Table 6.5, it can be noted that after 40 minutes, the reference electrode slurries demonstrate the lowest rigidities, with electrode slurries containing acetic and maleic acid showing the next lowest rigidities. This can be observed in the values of G' and G'' . However, the most viscous electrode slurry, with the weakest gel strength is acetic acid. The reference electrode slurry, and electrode slurries containing maleic acid demonstrate the next lowest gel strengths. These strengths can be noted in the loss factor and phase angle columns.

After 90 minutes, it is clear, from Table 6.5, that electrode slurries containing acetic acid show the lowest gel rigidities and strengths. Furthermore, electrode slurries containing acetic acid, values of G' and G'' show only a two-fold increase between 40 and 90 minutes, whereas the reference electrode slurry increases ten-fold. Electrode slurries containing maleic acid demonstrate similar strengths to those containing acetic acid, however, the rigidities are far higher.

Based on these values in Table 6.5 and the data displayed in Figures 6.5 and 6.7, the milled additive with the best improvements to the electrode slurry is acetic acid.

6.4.1.2.3 Relaxation Time

It has been established in the literature of the glass jamming in repulsive systems that the presence of strong dynamic arresting suggests two distinct stress relaxation processes [287, 288]. These two stress relaxation processes can be found observed and explored through the use of Maxwell Model calculations, Figure 6.8.

The storage and loss moduli have been fitted to a 2 mode Maxwell Model, as explored in chapters 4 and 5. The relaxation times extracted from these modes can be found in Figure 6.8. The relaxation time, a ratio between the viscous and elastic elements, denotes the timescales of the material's response to deformation. Below the relaxation time the material will act elastically and above it, as a viscous material.

These two stress relaxations can be seen in Figure 6.8 via the primary and secondary relaxation times. Through the Maxwell Model, separate relaxation times occur through the use of multiple modes, but relate physically to different properties and timescales.

The secondary relaxation time denotes the behaviour of the electrode slurry over very short times scales. Below approximately 0.15, depending on the acid additive (see Figure 6.8), the secondary relaxation time signifies that the electrode slurries exhibit a strong elastic response, similar to that of a yield stress in a Herschel-Bulkley fluid. Yield stresses have been previously observed in electrode slurries [289, 290] and for high solids content fine-particles suspensions [291, 292] analogous to electrode slurries.

Above this secondary relaxation time, the strong elasticity of the electrode slurry partially relaxes, and the primary Maxwell mode elastic response dominates. It is only above the primary relaxation time that the electrode slurry will act fully viscous and fluid.

As demonstrated by Figure 6.8 and expanded in Chapter 4 the reference material follows a three stage gelation process and takes approximately 45 minutes for the final gelation plateau to be reached. It is clear from Figure 6.8 that for all of the acids, despite starting with higher relaxation times, exhibit lower primary relaxation times after 45 minutes. Furthermore, these primary relaxation times for the electrode slurries containing the acid additives are lower than the reference electrode slurry after 90 minutes.

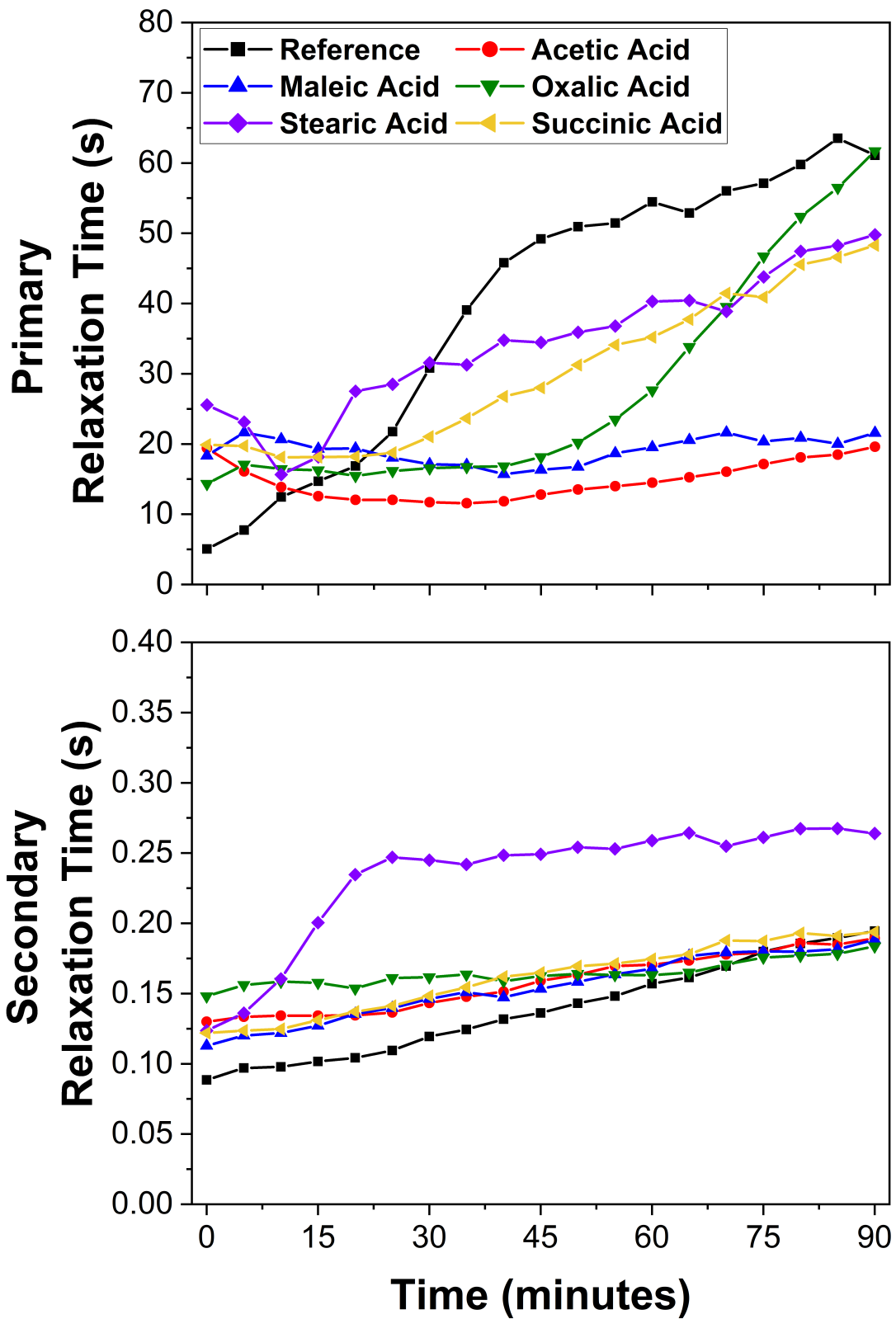


Figure 6.8: Maxwell Mode - Primary and Secondary Relaxation Times for the reference electrode slurry and all the electrode slurries containing 2.0 wt% of acid additives.

For the additives of acetic and maleic acid, the primary relaxation time has been greatly stabilised, with a near constant apparent relaxation time lasting the entire duration of measurements, demonstrating the greatest stabilisation of the acid additives.

Electrode slurries containing oxalic acid show a similar improvement to the stabilisation of the relaxation time over a 50 minute window. However, these electrode slurries exhibit a drastic increase in the relaxation time after 50 minutes and reach a final relaxation time that equals the reference electrode slurry.

For electrode slurries containing stearic acid and succinic acid, the primary relaxation time follows a steady increase over the entire time duration.

For all electrode slurries, the secondary relaxation times slowly increases over the time duration, with electrode slurries containing oxalic acid demonstrating the smallest increase. Electrode slurries containing stearic acid demonstrate a rapid increase over the first 20 minutes, however, this could be due to the fitting, as the primary relaxation times show a decrease over this time period.

It should be noted that these relaxation times purely denote the balance between the viscous and elastic behaviours of the electrode slurries. The final strengths and degrees of elasticity should be primarily observed in the storage and loss modulus, Figure 6.5.

6.4.2 Effect of the Stabilising Additives on the Electrodes

These electrode slurries containing the acid additives have been coated onto an aluminium current collector so measurements on the electrodes can be obtained. This has been performed using the method outlined in Chapter 3. It should be noted that, unless stated, these electrodes were coated immediately after mixing has been concluded, and will relate to the time zero measurements demonstrated in Section 6.4.1.

6.4.2.1 Physical Electrode Measurements

Electrode measurements have been split into physical measurements and electrochemical measurements. Physical measurements will cover the adhesion of the electrodes, and the

conductivities of the electrode.

6.4.2.1.1 Electrode Adhesion Measurements

The importance of the coating adhesion strength has been demonstrated in Chapter 2, and as such the effect of the acid additives on the adhesion strength has been measured.

Figure 6.9 shows the adhesion strengths for electrodes made from the reference electrode slurry and electrode slurries containing the acid additives. It is clear from observations of Figure 6.9 that the additives cause large changes to the adhesion between the electrode and the aluminium current collector. It can be noted that all additives, except oxalic acid, cause a decrease to the adhesion strength over the reference coating. Electrode coatings containing stearic acid demonstrate very poor adhesive strength at 7.9 Nm^{-1} . Those containing acetic acid and maleic acid exhibit similarly poor adhesive strengths at 29.1 Nm^{-1} and 15.7 m^{-1} , respectively. Succinic acid as an additive seems to marginally reduce the adhesion strength to 77.9 m^{-1} from the reference coating, 91.0 Nm^{-1} . Oxalic acid increases the adhesion strength up to 122 Nm^{-1} .

The reference electrode has a high adhesion strength due to two main reasons. Firstly, due to the cross-linking of the PVDF (immediately after mixing, the reference electrode slurry will contain some crosslinks and NaOH), the adhesion strength is increased. Analogous fluoroelastomers have been shown to have great adhesion to metal when cross-linked [199], and for many polymers, an increase to the molecular weight and crosslinking increases the adhesion strength [293]. Secondly, the etching and corrosion of NaOH onto the aluminium current collector, allowing the electrode to bind more strongly. The effect of this can be seen in Figure 6.10.

As discussed in Section 6.1, the increased adhesion strength of PAA over PVDF can be attributed to the carboxylic groups. For oxalic acid, and succinic acid, where the carboxylic groups on either end the hydrogen bonding effect over the carboxylic groups can will relate to an increased bonding strength. The higher adhesion strength of oxalic

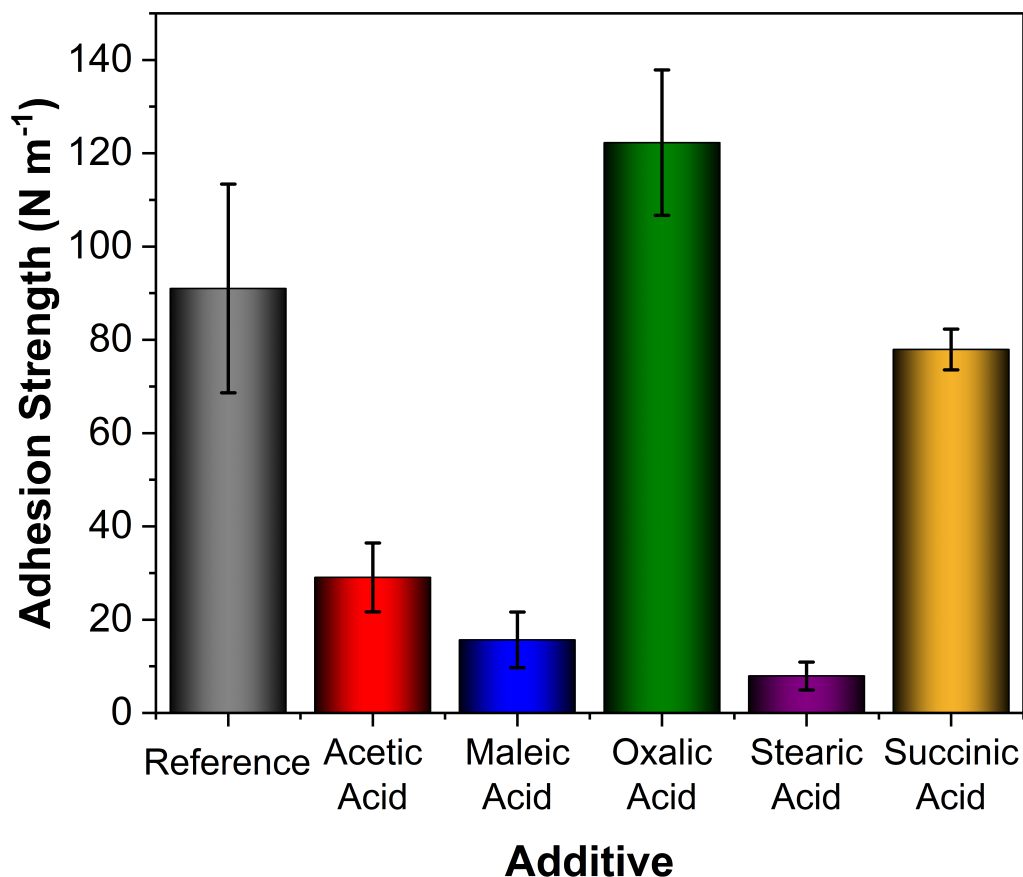


Figure 6.9: Adhesion strength for electrodes made from the reference electrode slurry and all the electrode slurries containing 2.0 wt% of the acid additives. Electrode slurries were coated immediately after mixing was completed.

acid comes from the lower molecular weight, resulting in a greater number of carboxylic groups, and the corrosion and etching effect introduced in Section 6.1.

For maleic acid, while it has two carboxylic groups, there is no rotation in the double bond and so this steric hindrance will mean it cannot give higher adhesion strengths than succinic acid (the acid additive with the same carbon backbone chain length). Instead, due to the presence of the acid, the degree of cross-linking has been reduced and the concentration of NaOH is reduced. These combined effects, ultimately, will give rise to a weaker adhesion strength than the reference electrodes.

For acetic acid, and stearic acid, where there is only a single carboxylic group, there will be no improvement to the adhesion strength. Instead, as with maleic acid, the present

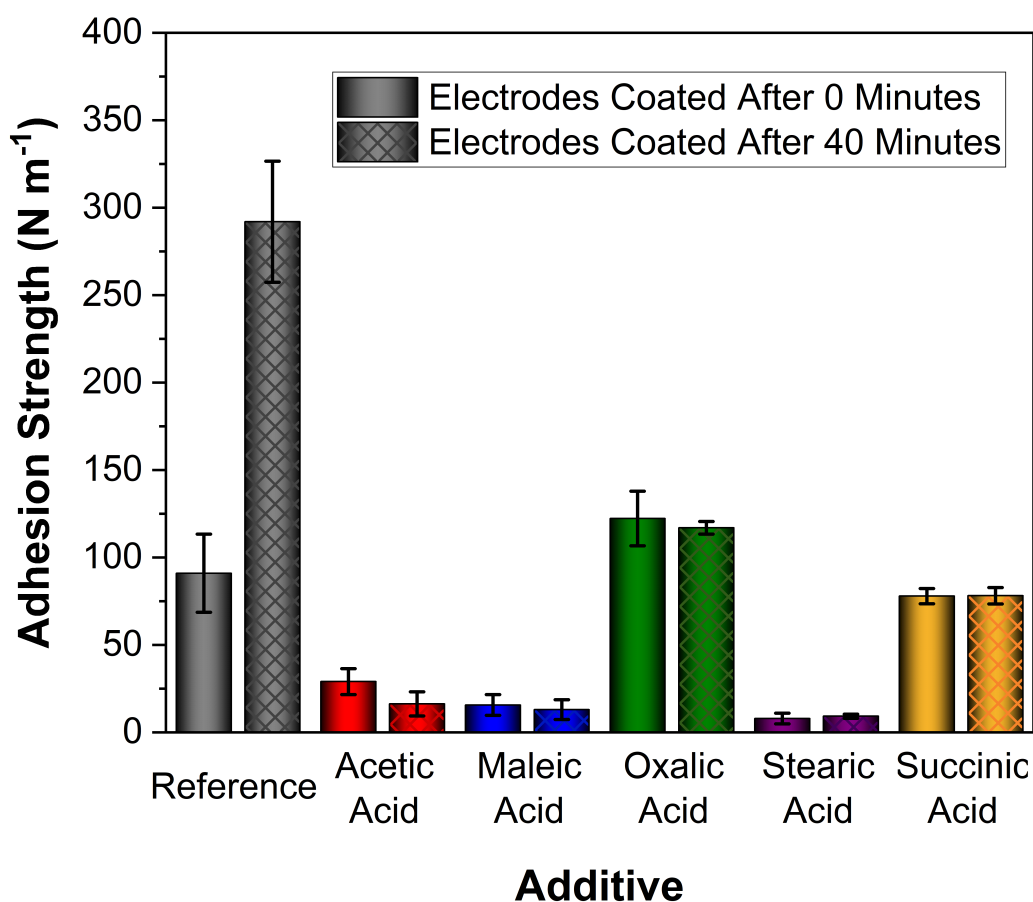


Figure 6.10: Comparison adhesion strength for electrodes made from the reference electrode slurry and all the electrode slurries containing 2.0 wt% of the acid additives. Bars show coatings made from electrode slurries coated immediately after, and 40 minutes after mixing was completed.

of the acid additive, will reduce the amount of cross-linking and concentration NaOH, producing a lower adhesion strength. Furthermore, stearic acid is a long chain fatty acid, and will likely form an oil barrier that can reduce the adhesion strength.

Figure 6.10 shows the adhesion strengths for sets of electrodes that were coated immediately after mixing and electrodes that were coated 40 minutes after mixing. It is evident from Figure 6.10 that by coating the electrode slurry 40 minutes after mixing there is a very large increase to the adhesion strength of the reference electrode. This is due to the increased quantities of cross-linking in the polymer chains, ensuring strong adhesion to the metal current collector, and through the increase concentration of

NaOH, etching and corroding the aluminium current collector. This large increase of the adhesion strength between coating immediately after mixing and 40 minutes after mixing is the expected result for these electrode slurries.

All the acid additives, apart from stearic acid and succinic acid, after 40 minutes cause a slight decrease to their electrode's adhesion strength. However, these very slight changes to the adhesion strength do fall within the margin of error between the adhesion strength of coating immediately after mixing and the coating 40 minutes after mixing. Therefore, it can be suggested that for the electrode slurries containing the acid additives, the lack of a large increase in the adhesion strength suggests that after 40 minutes all acid additives have reduced the cross-linking development in the electrode slurries.

6.4.2.1.2 Electrode Conductivity

Figure 6.11 shows the conductivity measurements for electrodes made from the electrode slurries containing 2.0 wt% of the acid additives. Electrodes made from the reference electrode slurry have been included for ease of comparison. It is important to note that these measurements are not the actual conductivities of the electrodes as these have not been measured using a non-conductive substrate. However, as all measurements were performed on aluminium current collector from the same reel it is thought that they can be used for comparative purposes.

It is clear from Figure 6.11, that only the electrodes containing oxalic acid and stearic acid as additives cause increases to the conductivity, at values of 273 and 229 Sm^{-1} , respectively. It is therefore suggested that the resistance of these electrodes will be lower, and higher cycling capacities can be realised. Electrodes containing oxalic acid have very large standard deviations associated with the average values. It is suggested that these large errors may arise from the oxalic acid corrosion of the aluminium substrate and, hence altering both the thickness of the aluminium and the contact between the aluminium and the electrode.

Electrodes containing succinic acid slightly lower the conductivity over reference

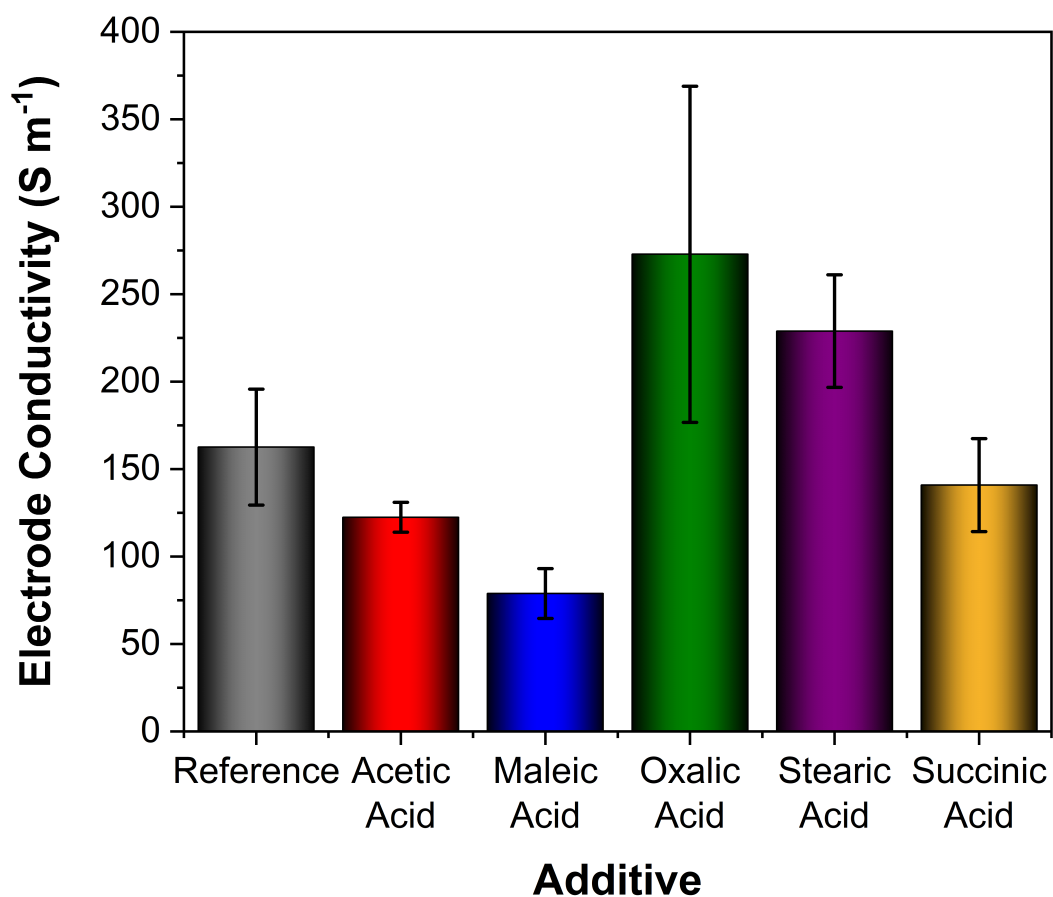


Figure 6.11: Comparison electrode conductivity for electrodes made from the reference electrode slurry and all the electrode slurries containing 2.0 wt% of the acid additives.

electrodes, with conductivity values of 141 and 163 $S m^{-1}$ for succinic acid-containing electrodes and reference electrodes, respectively.

The final electrode slurry additives, acetic acid (122 $S m^{-1}$) and maleic acid (78.8 $S m^{-1}$), cause significant reductions to the conductivity of the electrodes. These far lower conductivities will likely cause increased electrode resistances and poorer cycling performances.

6.4.3 Effect of the Stabilising Additives on the Electrochemical Performance

6.4.3.1 Electrochemistry Cycling Performance

Electrodes were made into half cells and cycled according to the cycling settings outlined in Chapter 3. The first cycle of each cell is a formation cycle at a current rate of 15mA g^{-1} , with subsequent cycles at a cycling rate of $C/10$ - a battery capacity determination was performed after the formation cycle.

These discharge capacities over the cycling of the electrodes can be found in Figure 6.12.

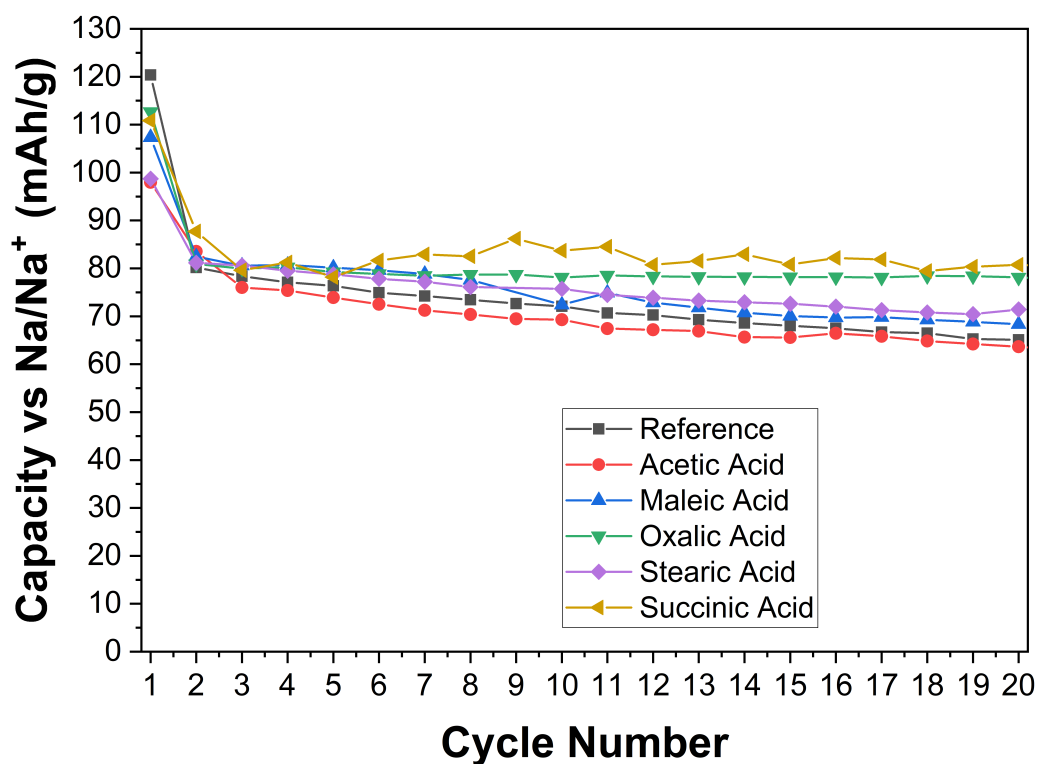


Figure 6.12: Cycling capacity vs cycle number for electrodes made from the reference electrode slurry and all the electrode slurries containing 2.0 wt% of the acid additives.

Based on the observed conductivities, demonstrated in Figure 6.11, it is clear that electrodes formed from electrode slurries containing acetic acid demonstrate the lowest

capacities, lower than the reference electrode. These electrodes have a first cycle capacity of 98.0 ± 9.1 mAh/g that falls to 83.5 ± 11.7 mAh/g after the second cycle and 62.9 ± 11.3 mAh/g after 20 cycles. Acetic acid-containing electrodes have similarly exhibited lower conductivity and adhesion strength than the reference electrodes, suggesting how valuable these properties are for electrode performance.

All other electrodes containing acid additives demonstrate higher capacities vs Na/Na⁺ than the reference electrodes. Maleic acid- and stearic acid-containing electrodes demonstrate capacities that are only marginally higher than the reference material. Maleic acid-containing electrodes have a first cycle capacity of 107.4 ± 1.2 mAh/g, which falls to 82.5 ± 4.0 mAh/g after the second cycle and 68.3 ± 2.7 mAh/g after 20 cycles. Maleic acid electrodes exhibit conductivities and adhesion strengths that are lower than acetic acid. Therefore, it can be suggested that the acid chemistries play a role in the electrochemical performance.

Stearic acid-containing electrodes, which also demonstrate low adhesion strengths, show similar performance to maleic acid. Electrodes have a first cycle capacity of 98.7 ± 2.5 mAh/g, which falls to 81.2 ± 2.7 mAh/g and 71.4 ± 1.1 mAh/g, after the second and 20th cycles, respectively.

The remaining electrodes, those containing succinic acid or oxalic acid, demonstrate the highest capacities. Succinic acid-containing electrodes demonstrate the highest capacities, however, the data fluctuates greatly and the standard deviations are high. Electrodes have a first cycle capacity of 110.8 ± 5.2 mAh/g, which falls to 87.7 ± 8.8 mAh/g and 80.4 ± 5.6 mAh/g, after the second and 20th cycles, respectively. Data values at the 3rd and 5th cycles show standard deviations of 18.9 and 22.1 mAh/g, respectively.

Electrodes containing oxalic acid, which show the largest conductivity and adhesion strength, demonstrate the most stable electrochemical cycling and the second highest capacities. Electrodes containing oxalic acid exhibit a first cycle capacity of 112.7 ± 0.3 mAh/g that falls to 80.9 ± 7.5 mAh/g after the second cycle and 77.8 ± 6.6 mAh/g after

20 cycles. This demonstrates a capacity retention of 96.1 % after the formation cycle, the first cycle.

Notably, the errors and standard deviations for these discharge capacities demonstrate an overlap between the average capacities. Additionally, it should be noted that electrodes containing succinic acid as an additive show the largest error values.

The poor electrochemical performances of the electrodes tested in this chapter can be suggested as a result of reactions of the active materials with air. Section 7.4.1.2.1 has established that, despite the inclusions of the acid additives, a full stabilisation of the electrode slurry has not been possible and reactions of the active materials with air still occurs. Furthermore, it is suggested that these reactions are able to occur during the coating and drying stages of electrode manufacture. As the NaNMST active material reacts with air, forming NaOH, demonstrated in Chapter 4, sodium is withdrawn from its structure, ultimately decreasing its capacity. Similarly, reactions of NaOH with the PVDF binder material forms resistive in-organics such as NaF.

6.4.3.2 Electrochemical Impedance Spectroscopy

To further investigate the electrochemical behaviour, electrochemical impedance spectroscopy, EIS, and equivalent circuit models were employed. EIS measurements can be seen in Figure 6.13. These measurements were performed on cells after the formation cycle and after 10 cycles. Measurements were taken at 50 % state of charge (SoC) to avoid large polarisation effects.

From Figure 6.13 it is evident that the impedance of these electrodes is different for each acid additive, both in the magnitude and shape of the impedance spectra. Immediately after formation, the reference electrode demonstrate a large initial semi circle, followed by a second smaller semi circle before the 45° line of the Warburg diffusion begins.

For the spectra after 10 cycles there appears to be only one semi circle feature. However, due to the frequency mapping of these measurements, it becomes clear that

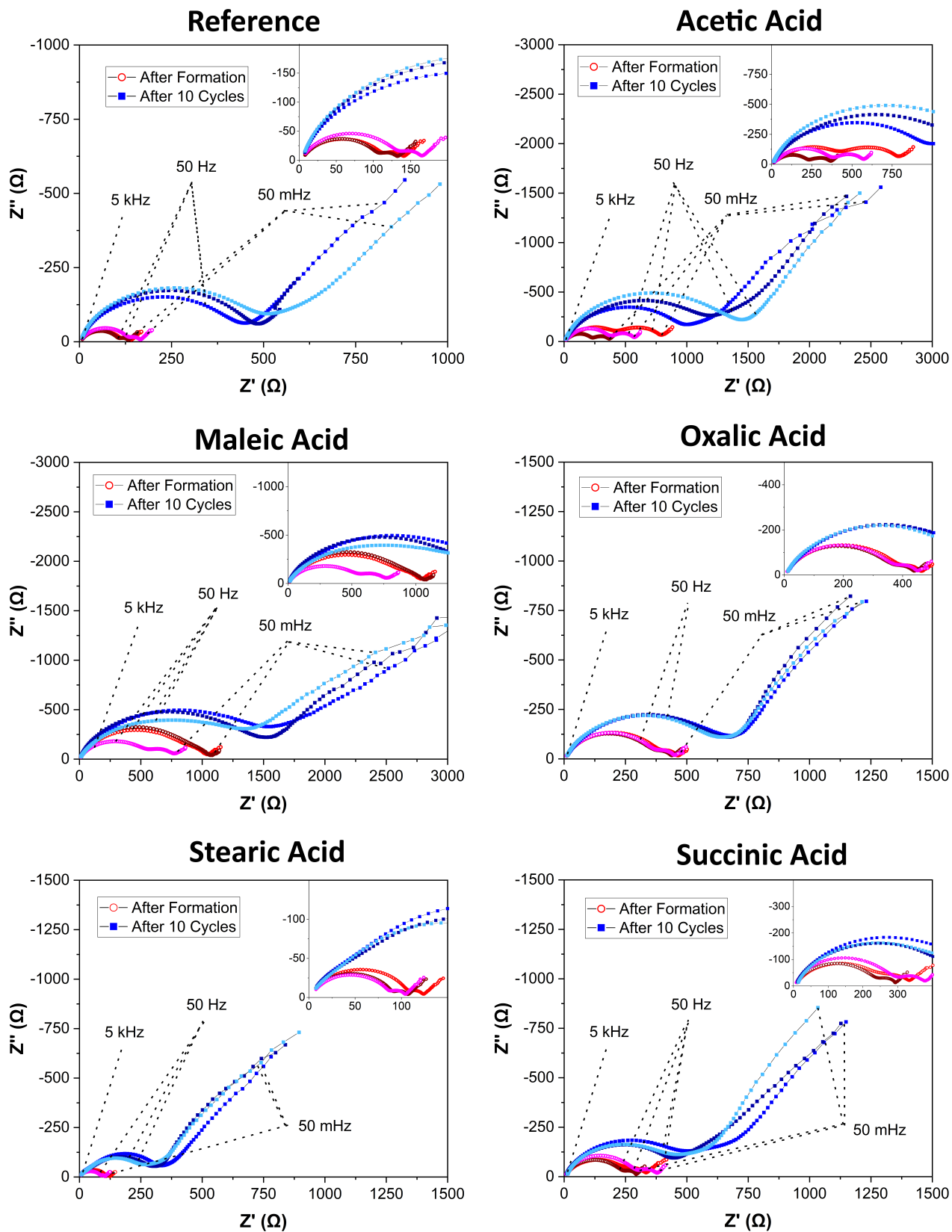


Figure 6.13: Electrochemical Impedance Spectroscopy for electrodes made from the reference electrode slurry and all the electrode slurries containing 2.0 wt% of the acid additives.

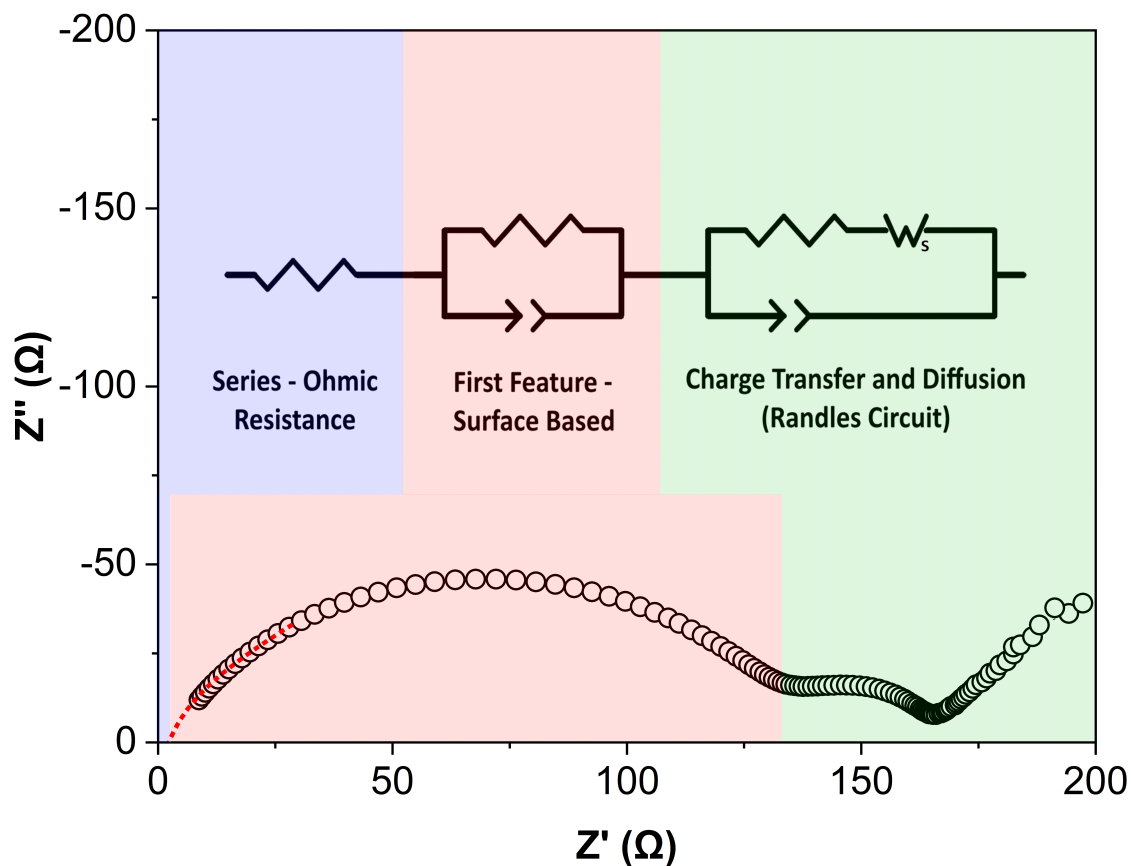


Figure 6.14: Equivalent circuit used for the electrochemical impedance spectroscopy.

there are two semi circle features that are overlapping. After formation, the measurement frequency for the midpoint between the two semi circle features is at 50 Hz. Similarly, for the measurements after 10 cycles, the frequency lies around the midpoint of the one visible semi circle.

The measurements at 50 Hz have been similarly annotated on the other, acid-containing electrodes in Figure 6.13. These two semi circles remains prevalent for all acid-containing electrodes. However, the distinction between these two features seems to have shifted to lower frequencies. It is possible that by shifting this midpoint to lower frequencies it suggests that the transfer of ions through this first semi circle feature, attributable to a CEI, takes longer than the reference electrode.

The attribution of these features has been performed in conjunction with the fitting of an equivalent circuit model, Figures 6.14, 6.15, and 6.16.

EIS measurements were fitted to a modified Randles circuit [294,295] as seen in Figure 6.14. Constant phase elements (CPE) have been used to replace the double-layer capacitor elements for the ease of fitting to the ellipsoidal semi-circles. As a note, the unmodified Randles circuit [41,294,296] does not contain the resistor in parallel with a constant phase element. However, as the taken impedance spectra (Figure 6.13) contains two distinct semi-circles, the extra resistor and CPE elements were included.

This equivalent circuit (Figure 6.14) contains a resistor that denotes the series, or bulk, resistance of the cell. This covers all linear resistances such as the separator resistance, the electrolyte resistance, and the current collector resistances [295,297].

The first semi-circle feature has been attributed to a thin cathodic film, or cathode electrolyte interphase (CEI), that can form after electrode cycling due to the decomposition of the electrolyte and reactions of the electrode with the electrolyte [295]. Discussed in Section 6.1, the electrochemical reduction of carboxylic acid groups has been shown to help stabilise and improve the SEI of silicon anodes [267,268]. This stabilisation (or lack of stabilisation) would, primarily, be exhibited in changes to this first semi-circle feature over cycling.

The second semi-circle feature has been attributed to the charge transfer resistance. The charge transfer is linked to the kinetics of the electrochemical reaction [295]. Larger values of this charge transfer resistance could suggest slower kinetics of the electrochemical reaction, which could result in lower capacities or less potential power for the cells. In the Randles circuit, the Warburg impedance is included into the circuit with the charge transfer elements as the diffusion will occur with the transfer into the material matrix.

From Figure 6.15, it is clear that the resistance due to the CEI layer changes greatly over the course of electrode cycling. The reference electrode, which has been included for comparison purposes, sees an increase in the CEI resistance from a value of $118.5 \pm 12.1 \Omega$ to a value of $340.3 \pm 97.4 \Omega$.

Electrodes containing acetic acid and maleic acid see a decrease in this CEI resistance after 10 cycles. The values of the CEI resistance decrease from $385.2 \pm 113.8 \Omega$ to $36.4 \pm$

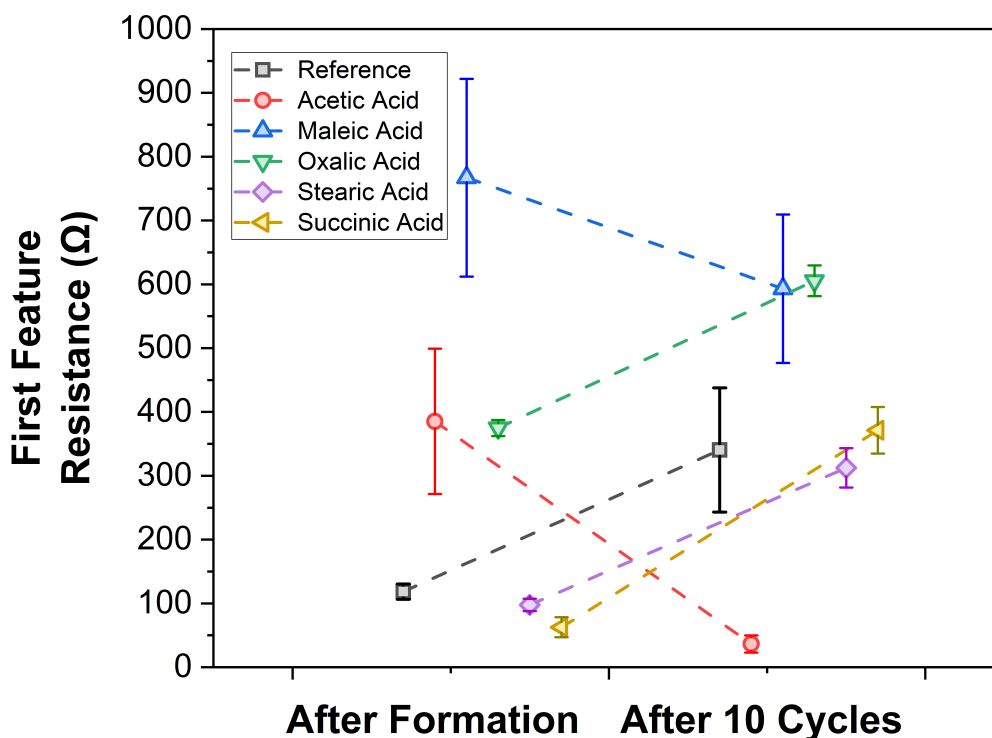


Figure 6.15: Cathode solid electrolyte interphase layer resistance fitted from the electrochemical impedance spectroscopy in figure 6.13 after the formation cycle and after 10 cycles.

13.5 Ω for acetic acid, and 767.1 \pm 155.0 Ω to 593.1 \pm 116.2 Ω for maleic acid-containing electrodes.

The remaining electrodes containing acid additives all follow the trend of the reference electrode, and the CEI resistance increases after 10 cycles. Electrodes containing oxalic acid see an increase in the CEI resistance from 374.8 \pm 12.5 Ω to 605.6 \pm 24.0 Ω . Those containing stearic acid increase from 97.7 \pm 9.6 Ω to 312.3 \pm 30.9 Ω . Electrodes containing succinic acid increase from 62.7 \pm 15.7 Ω to 371.3 \pm 36.4 Ω .

For the electrodes that see an increase in this CEI resistance, it is suggestive of two possibilities. Firstly, that the film has not fully developed after the formation cycle and, therefore, further develops and increases over subsequent cycles. Secondly, that these particular acid additives (oxalic, stearic, and succinic acid) do not stabilise in the same

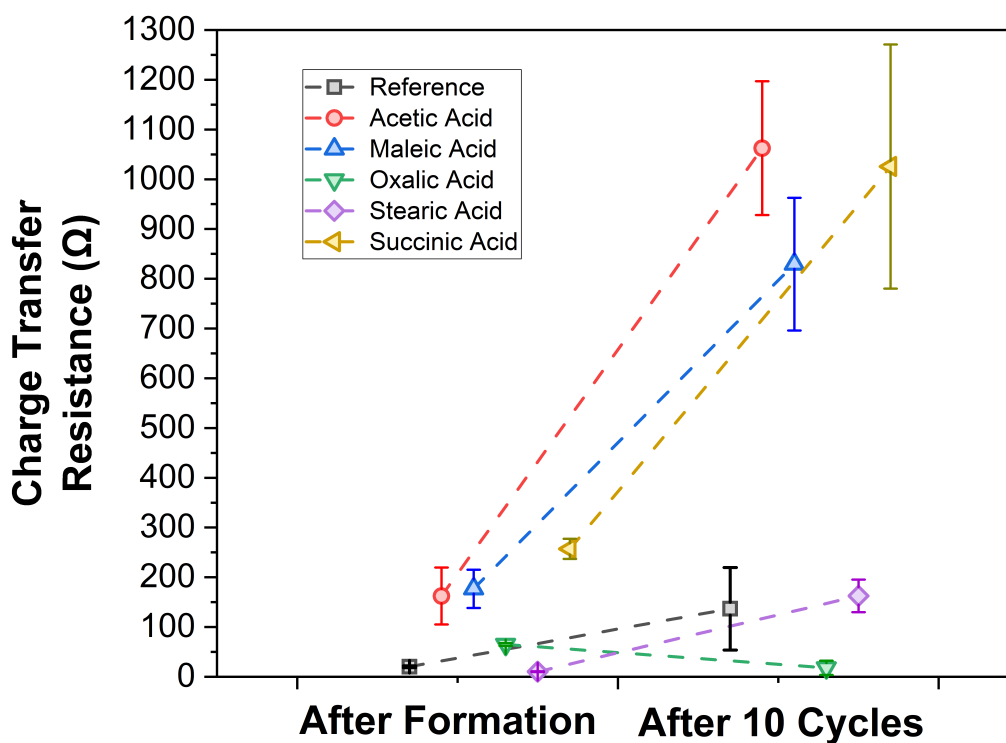


Figure 6.16: Charge transfer resistance fitted from the electrochemical impedance spectroscopy in figure 6.13 after the formation cycle and after 10 cycles.

manner as suggested by Nguyen *et al.*, 2017 [267,268] and explored in the Section 6.1. It was suggested by Nguyen *et al.*, 2017, that the electrochemical reduction of the carboxylic acid group in citric acid stabilises the active material (silicon) surface and suppresses further electrolyte reduction. [268] As these acids do not demonstrate a stabilised CEI, it can be suggested that, either, this surface stabilisation does not occur for these cathode active materials, or that particular acid additives do not electrochemically reduce to form carboxylates. The magnitude of the increase in this CEI resistance for these acid additive-containing electrodes is similar to the reference electrode, suggesting that this increase is due to the nominal increase of the material.

Similarly, for the electrodes containing acetic acid or maleic acid, where the resistance decreases, it could be suggested that this layer has been stabilised. The carboxylic groups have been electrochemically reduced to form carboxylates. Therefore, whether the acid

groups are reduced or not, could be a result of access. Where inverse micelles can form, the carboxylic acid groups can be reduced, For micelles structures, such as bilayer vesicles, or lamellar phases (see Figure 6.3), where the acid groups are surrounded by the active material, they are unable to be electrochemically reduced.

For the charge transfer resistance, the reference electrode increase from $20.4 \pm 1.8 \Omega$ to a value of $136.8 \pm 83.0 \Omega$. Electrodes containing stearic acid show a similar increase, from $10.4 \pm 0.7 \Omega$ to $163.6 \pm 32.6 \Omega$.

Electrodes containing acetic acid, maleic acid, and succinic acid, all demonstrate a drastic increase in the charge transfer resistance. The charge transfer resistance for acetic acid sees an increase from $162.3 \pm 57.2 \Omega$ to $1062.5 \pm 134.5 \Omega$. Electrodes containing maleic acid see an increase from $176.8 \pm 38.5 \Omega$ to $829.4 \pm 133.3 \Omega$. Lastly, succinic acid-containing electrodes see an increase in the charge transfer resistance from $257.0 \pm 20.3 \Omega$ to $1025.7 \pm 245.3 \Omega$.

Only electrodes containing oxalic acid exhibit a decrease in the charge transfer resistance after cycling. The resistance decreases from $65.0 \pm 2.8 \Omega$ to $17.9 \pm 14.3 \Omega$.

These changes in the charge transfer resistance are consistent with the electrochemical cycling data as shown in Figure 6.12. Electrodes where the charge transfer resistance has increased as the cells are cycled (reference electrodes, and electrodes containing acetic, maleic, succinic, or stearic acid), also experience a capacity loss. Only electrodes containing oxalic acid experience a decrease in the charge transfer resistance, which demonstrates a steady cycling capacity with little decline.

6.4.4 Summary

Table 6.6 shows a summary of the results collected during this chapter. In the case of summary of the FTIR analysis, where no quantified values have been extracted, additives have been ranked based on observed chemical changes to the $\nu(\text{OH}--\text{H}_2\text{O})$ peak, and the degree of changes to the $\nu(\text{C}=\text{O})$ peak (the inset of Figure 6.4) over a 20 minute period (based on objective 1). For these FTIR ratings, electrode slurries have been ranked

Table 6.6: Summary of effects to the electrode slurry and electrodes due to the acid additives.

	Electrode Slurry Characterisation									Electrode Characterisation		
	After 40 minutes				After 90 Minutes				FTIR (Ranked by observed changes)	Adhesion		Electrode Conductivity ($S\ m^{-1}$)
	G'	G''	Loss Factor	Phase Angle (°)	G'	G''	Loss Factor	Phase Angle (°)		After 0 minutes	After 40 minutes	
Reference	218.3	50.1	4.4	16.4	2043.3	124.2	16.5	3.5	5	91.0	292.0	163.0
Acetic Acid	888.0	275.6	3.2	18.1	1735.7	363.3	4.8	11.8	4	29.1	16.3	122.0
Maleic Acid	845.7	214.8	3.9	14.2	3776.7	736.7	5.1	11.0	2	15.7	13.0	78.8
Oxalic Acid	2406.7	494.0	4.9	11.7	6620.0	464.7	14.2	4.1	1	122.0	117.0	273.0
Stearic Acid	86433.3	8516.7	10.1	5.6	330000.0	25233.3	13.1	4.4	6	7.9	9.2	229.0
Succinic Acid	1406.7	258.1	5.4	10.5	4820.0	405.5	11.9	5.1	3	77.9	78.1	141.0

	Electrochemical Characterisation					
	Electrochemical Cycling		CEI Resistance		Charge Transfer Resistance	
	1st to 2nd Cycle Discharge Capacity Loss	20th Cycle Capacity	After Formation Cycle	After 10 Cycles	After Formation Cycle	After 10 Cycles
Reference	40.2	65.1	118.5	340.3	20.4	136.8
Acetic Acid	14.4	63.7	385.2	36.44	162.3	1062.5
Maleic Acid	24.9	68.3	767.1	593.1	176.8	829.4
Oxalic Acid	31.7	78.7	374.8	605.6	65.0	17.9
Stearic Acid	17.5	70.4	97.7	312.3	10.4	162.6
Succinic Acid	23.1	80.8	62.7	371.3	257.0	1025.7

between 1, demonstrating the least chemical changes, to 6 demonstrating the greatest chemical changes. This table should primarily be used as a point of comparison for these acid additives.

6.5 Conclusions

The research presented in this chapter sought to extend the processing window of sodium layered O₃ cathode slurries and investigate the stabilisation mechanism of these electrode slurries.

The first objective, achieving a stabilisation of the electrode slurry gelation past the 20 minute processing window of the reference electrode slurry was analysed both physically and chemically. Chemical analysis (Figure 6.4) of the electrode slurry gelation over a 20 minute processing window demonstrates favourable improvements with all additives, apart from stearic acid. These additives show improvement to the quantities of the OH stretching shoulder peak in this short window.

Over longer timescale, i.e. after the 360 minute testing window, additives of oxalic acid and maleic acid showed the smallest amount of shifting in the C=O peak. As the peak shifting is related to hydrogen bonding and water absorbed into the sample, these electrode slurries demonstrated a small amount of water formed between the reaction of acid and base. Hence, less base was formed on the surface of the active material. Similarly, electrode slurries containing these acid additives of maleic acid and oxalic acid show reduced quantities of OH stretching shoulder peak at approximately 3300 cm⁻¹. These chemical stabilisations seem to be most attributable to strength of the acid, as found in Table 6.2, with oxalic acid showing the lowest overall changes.

Physically, however, oxalic acid does not prove to be the best electrode slurry stabilising additive. Based on the oscillatory rheology measurements, in Figures 6.5, 6.7, and 6.8, over the entire 90 minute measurement window, additives of acetic acid and maleic acid, show the most stabilisation. Furthermore these two additives, show an

almost complete stabilisation of the electrode slurry relaxation time. This physical stabilisation of the electrode slurry seems to be associated with the shape of micelles formed, with acetic and maleic acid predicted to form inverse micelles.

In the observation of the electrode slurry measured rheological properties over time, the second objective, (Figure 6.5 and shown Table 6.6), it can be noted that for all electrode slurries despite the inclusion of the additives there is an increase in both G' and G'' , suggesting that none of the attempted acid additives have fully stabilised the gelation. This conclusion can be similarly observed in the chemical analysis of the electrode slurries, the FTIR results, Figure 6.4. As, despite inclusions of any of the acid additives, the electrode slurries still demonstrate chemical changes over time.

Based on the third objective, which examines if the processing window can be extended, the analysis of the relaxation time establishes that for electrode slurries containing acetic acid, maleic acid, and oxalic acid, this processing window can be increased to 45 minutes. Unfortunately, due to time constraints, additional analysis of electrodes, containing these additives and coated at various times after mixing, to further establish a new processing window, could not be completed.

The final objective, measuring the effect that these stabilising additives have on the properties of the electrodes can further establish the most effective additives. These can be clearly noted in Table 6.6. In the adhesion (Figures 6.9 and 6.10) and conductivity (Figure 6.11) properties of the electrodes it is most evident that oxalic acid proves to be the most effective additive. Electrodes formed from slurries containing oxalic acid cause an improvement to the adhesion strength to the aluminium current collector over the reference electrodes. Electrodes made from slurries containing maleic or acetic acid demonstrate very poor adhesion. This same effect can be noted in the electrode conductivity. Electrodes containing oxalic acid show improvements over the reference electrode slurry whereas those containing maleic acid or acetic acid show reductions.

In terms of the electrochemical performance, it is evident from Table 6.6 that electrodes containing oxalic acid and succinic acid show the greatest benefits to the long term cycling

stability, likely due to their high adhesion properties over the other additives. Electrodes containing oxalic acid similarly show favourable improvements to their charge transfer resistance during cycling.

Overall, it has been shown that some stabilisation can be achieved using acid additives of oxalic acid, maleic acid, and acetic acid. However, none of the examined acid additives fully stabilise the electrode slurry gelation, and sodium is still removed from the active material to form NaOH. For lab scale testing, the partial stabilisation of the electrode slurries is sufficient to enable electrodes to be produced within the stability window, furthering the research into these materials. For industry use, the stabilisation is not sufficient and there is still a loss of sodium from the active material, lowering the capacity of the electrodes. Hence, other methods of extending the stability window should be sought. One such method would be to use additives that contain sodium, such as sodium salts of these acid additives.

Chapter 7

Sacrificial Stabilising Additives for High Nickel Content Cathode Materials

7.1 Introduction

As established in Chapter 6, the gelation of the electrode slurries can be effectively stabilised through the use of organic acid additives. Additives of acetic or maleic acid have been shown to greatly improve the processing window of the cathode electrode slurries.

However, electrodes formed using these additives see significant capacity fade during cycling. Similarly, reactions of the active material, forming NaOH, cause losses of sodium that can considerably reduce the capacity of cells. As demonstrated in Chapter 6, while some additives improve this chemical stability, this loss of sodium persists regardless of the additive used.

Therefore reducing this sodium loss while maintaining the stabilisation of the slurry gelation becomes the next priority. A suggested method is the sacrificial coating of the active materials with sodium salts of acid additives, as shown in Figure 7.1. Furthermore,

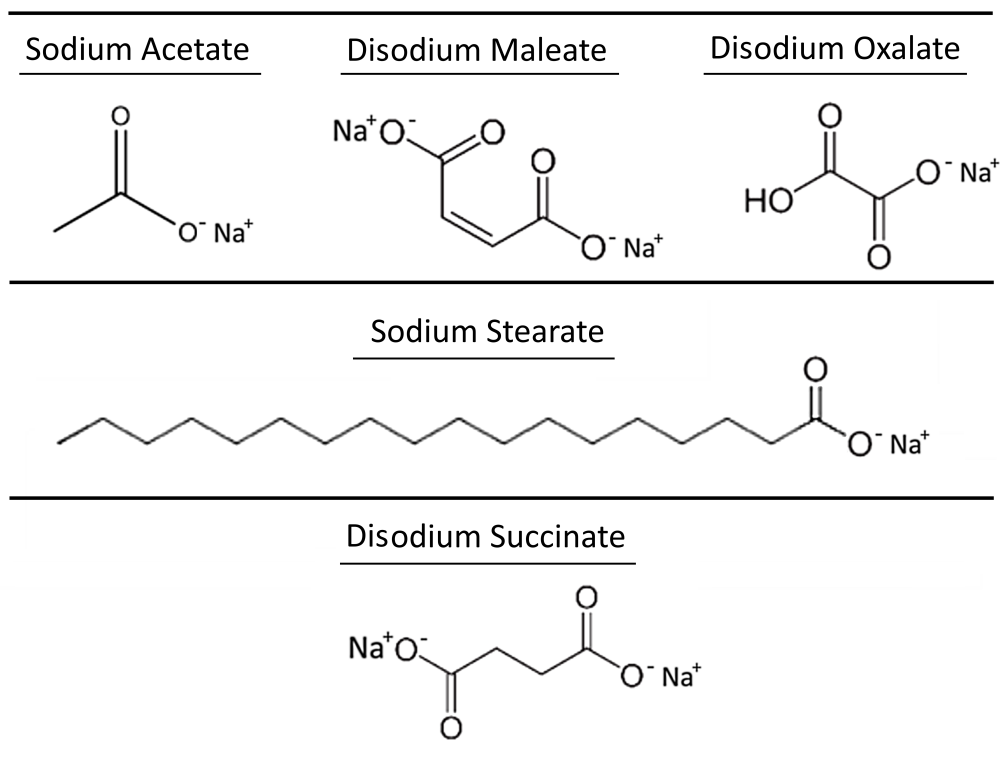


Figure 7.1: Acid additive chemical structures.

by utilising salts of the carboxylic acids from Chapter 6, it is hypothesised that the stabilisation of the electrode slurry gelation will be retained. The method of surface coating will be by ball milling together with the conductive additive.

The surface coating of the active materials has been utilised in both lithium and sodium-ion batteries [9, 298–304]. The function of these coatings can take several forms. Protective coatings, such as studied by Ahaliabadeh *et al.*, 2021, can reinforce the electrode structure and protect the active material from surface and degradation reactions. Ni'mah *et al.*, 2018, has demonstrated that the protective coating can additionally enhance the electron transport during cycling. [298, 305–307]

Sacrificial coatings are another potential method of active material surface coating. These coatings can preferentially react instead of the active material or can provide a source of sodium ions to compensate for those irreversibly consumed. [9, 300, 303, 304]

Furthermore, sodium oxalate has been used as a sacrificial additive and has been proven to significantly increase the capacity retention [303, 304]. These studies paired

sodium oxalate with P2-layered oxide materials [303] or anode materials [304] and focused on the improvements to the electrochemical performance. Therefore, the use of sacrificial coatings, utilising the sodium salts of the acid additives studied in Chapter 6 was chosen for this research. No studies have been found utilising the sodium salts of the other acid additives as sacrificial coatings.

Ball milling has been shown to be an effective method of coating the active material particles either with a protective or sacrificial coating [298–302], or with conductive compounds [308–314]. Furthermore, the use of ball milling can decrease the particle size and increase the active surface area. Similarly, modifications to the morphology and texture of the active materials can be adjusted by altering the milling parameters. [309–312, 315–317]

It was intended for these sodium salts to be sacrificially coated onto the active material through the use of ball milling. However, while the sodium salts were milled with the active material, no detailed study was made into whether coatings actually been achieved, henceforth these sacrificial coatings will be referred to as sacrificial additives.

7.2 Aims and Objectives

The main focus of the research presented in this chapter was the enhancement of the electrochemical performance of the Na-NMST active material through sacrificial additive using the sodium salts of the acids explored in Chapter 6. However, by using sodium salts of the previously tested acid additives, a reduction to the gelation of the electrode slurry and an improvement to the processing window of the electrode slurry is a secondary goal. The aims of this chapter are therefore to:

- Assess the stabilisation of the electrode slurry gelation,
- Observe how the measured rheological properties of the electrode slurry change in this time,

- Measure the effect these sacrificial additives have on the properties of the electrodes,
- Assess the improvement to the electrochemical performance of the active material.

7.3 Experimental Setup

Na-NMST ($\text{NaNi}_{1/2}\text{Mn}_{1/4}\text{Sn}_{1/8}\text{Ti}_{1/8}\text{O}_2$) was coated with the sacrificial additives of the acid salts using in a Retsch PM100 Planetary Ball Mill. The acid salts used were HPLC grade with a purity $\geq 99\%$: sodium acetate (Fisher Scientific), disodium maleate (MERCK), disodium oxalate (MERCK), sodium stearate (VWR), disodium succinate (MERCK). Quantities of acid salts were added to form a quantity in the electrode slurry solids of 2.0 wt%. One third of the total conductive carbon black (IMERYS, Super C65) was added to further coat the particles and to aid in the conductive properties of the electrode. The conductive carbon black and acid salt were added at the same time. 45g of 5 mm, and 15g of 10 mm zirconia balls were added to the 50 mL mill pot. The powders were milled at 300 rpm for 45 minutes, with a reversal of direction every 15 minutes.

Electrode slurries were formed using the standard method outlined in Chapter 3. The sacrificially coated Na-NMST was mixed with the remaining conductive carbon black, and an 8 wt% PVDF (polyvinylidene fluoride) (Solvey 5130) binder in NMP (n-methyl-2-pyrrolidone) solution. Quantities were measured to give a final ratio of the solids content of 87:2:6:5 by weight (Active Material:Sacrificial additive:Conductive Additive:Binder). The cathode ink was mixed in sealed pots in a Thinky ARE-250 Planetary Mixer, situated in a Munters dry room with a maximum dew point of -40°C . Materials were measured out under a recirculator hood (also situated in a dry room) or in an argon filled glove box.

There were three stages of mixing: initially the active material and the extra NMP, measured to give a final solids content of 40 wt%, followed by the addition of carbon black, and, finally, the PVDF solution. Each mixing stage lasted 5 minutes with a speed of 1300 rpm. For situations where additives were employed, they were mixed with the

NMP, prior to the start of this mixing route.

Dissolution tests were performed by mixing the sodium salts in NMP in the quantities expected in the electrode slurries. Approximately 2.7 g of NMP with 57.0 mg of the sodium salts were added to vials and mixed using a magnetic stirrer bar on a stirrer-plate set to 1500 rpm. The dissolution was checked and photographed after 15 minutes - to mimic the mixing time of the electrode slurries - and after 24 hours - to observe the extended dissolution properties.

All other analysis methods can be found detailed in Chapter 3.

7.4 Results and Discussion

The analysis of these sodium salt additives (Figure 7.1) will be explored in a similar manner as the acid additives of Chapter 6.

1. The effect these sodium salts have on the stability of the electrode slurries will be explored through the use of oscillatory rheology and the fitting of a Maxwell model. The analysis will be split between the measured storage and loss modulus and the phase angles from the oscillatory rheology, and the fitted relaxation times from the Maxwell models. Additional analysis will come from dissolution tests of the sodium salts in NMP.
2. The changes to the electrode properties will be analysed through the use adhesion measurements and conductivity measurements.
3. Finally, the effects of the sodium salts on the electrochemical properties will be measured using cycling analysis and electrochemical impedance spectroscopy evaluations.

7.4.1 Stabilisation of the Electrode Slurries

7.4.1.1 Dissolution of Milled Materials in NMP

The dissolution of the sacrificial sodium salts in NMP was characterised using a simple lab dissolution test. These dissolution tests of the sodium salts in NMP can be found in Figure 7.2. The images in Figure 7.2 show the dissolution after 15 minutes, however, after 24 hours the results were largely unchanged.

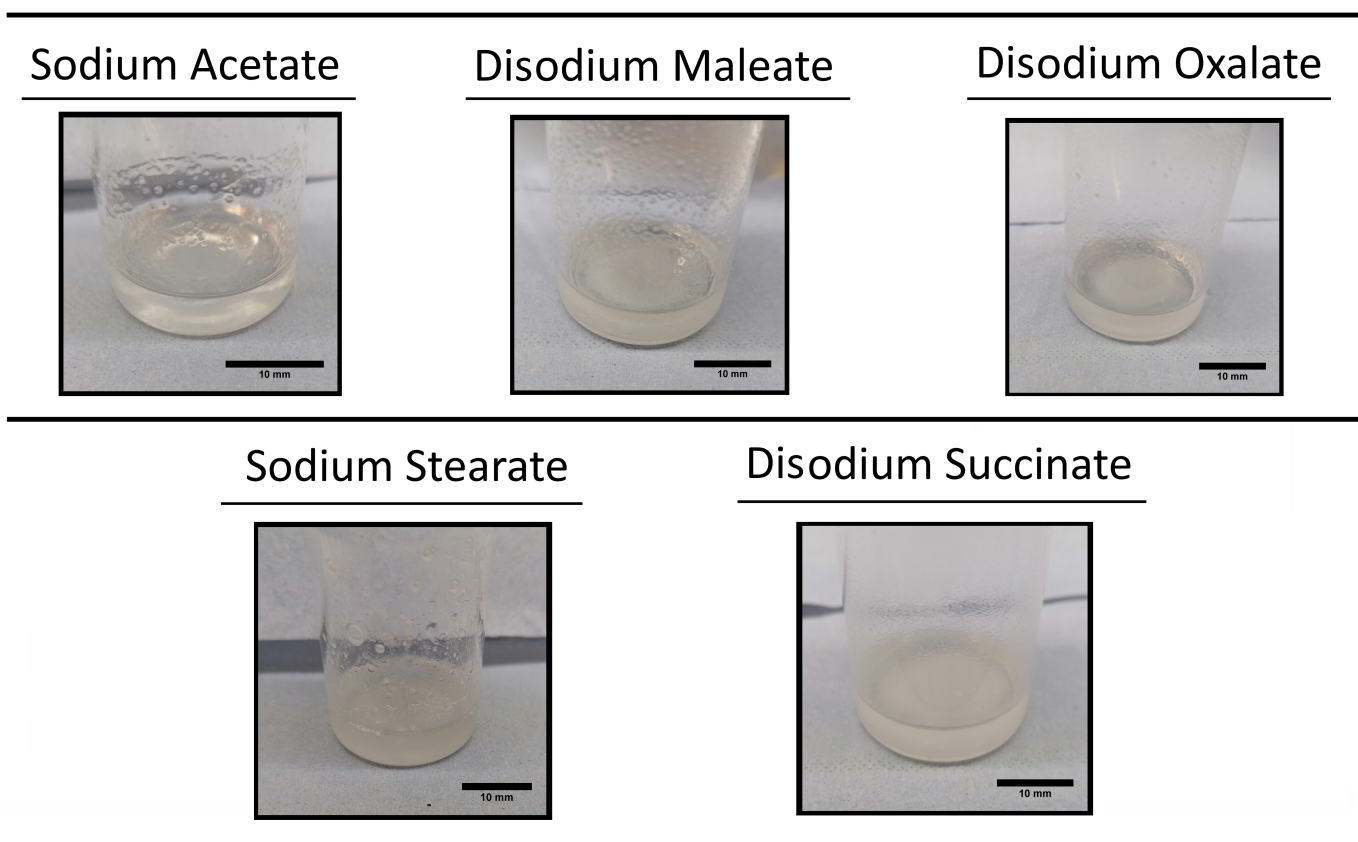


Figure 7.2: Dissolution of sodium acid salts in NMP.

From these images it can be noted that none of the sodium salts have full dissolution in NMP. There are clearly particulates on the sides of the vials, and in the solution of liquid. The reduction in the volume of visible particles does suggest partial dissolution.

This lack of full dissolution has the potential to cause problems in the stabilisation of the electrode slurries. The volume fraction of particles will remain high and so the possibility of colloidal jamming, as established in chapters 4 and 5, is increased.

However, the lack of immediate dissolution will prove to be beneficial to the protection of the active material. If the sacrificial additive were to immediately dissolve into solution then the protection of the active material would not exist as the electrode slurries are mixed.

7.4.1.2 Ex-situ Rheology studies of Electrode Slurries

Rheological analysis of the electrode slurries has been performed in the same manner as in chapters 4 and 6.

It is been established in Chapter 4, that the absolute values of G' and, to some extent, G'' relate to the rigidity of the gel. [227–229] This is a measure of the electrode slurry's inability to be deformed. The ratio between G' and G'' , and the phase angle, demonstrates the strength of the gel formed. [229] A summary of these values can be found after Section 7.4.1.2.2.

7.4.1.2.1 Storage and Loss Modulus

The storage and loss modulus changes for electrode slurries containing the acid additives can be found in Figure 7.3.

The storage and loss modulus for electrode slurries formed from the sacrificially coated active material can be found in Figure 7.2. It should be noted that the maximum frequency for these results is 4.642 Hz. Results were recorded for frequencies of 10 Hz and above, however, these data points were erroneous due to the dominance of inertia.

The storage and loss modulus for the reference electrode slurry has been included for comparative purposes. The analysis for the reference electrode slurry has been covered in chapters 4 and 6. For easy reference, the storage and loss moduli are initially very similar, with values between 10 Pa and 100 Pa across the frequencies. A divergence between G' and G'' begins after 40 minutes with final values of 2000 Pa and 100 Pa for G' and G'' , respectively.

For the electrode slurries containing the active material coated with sodium acetate,

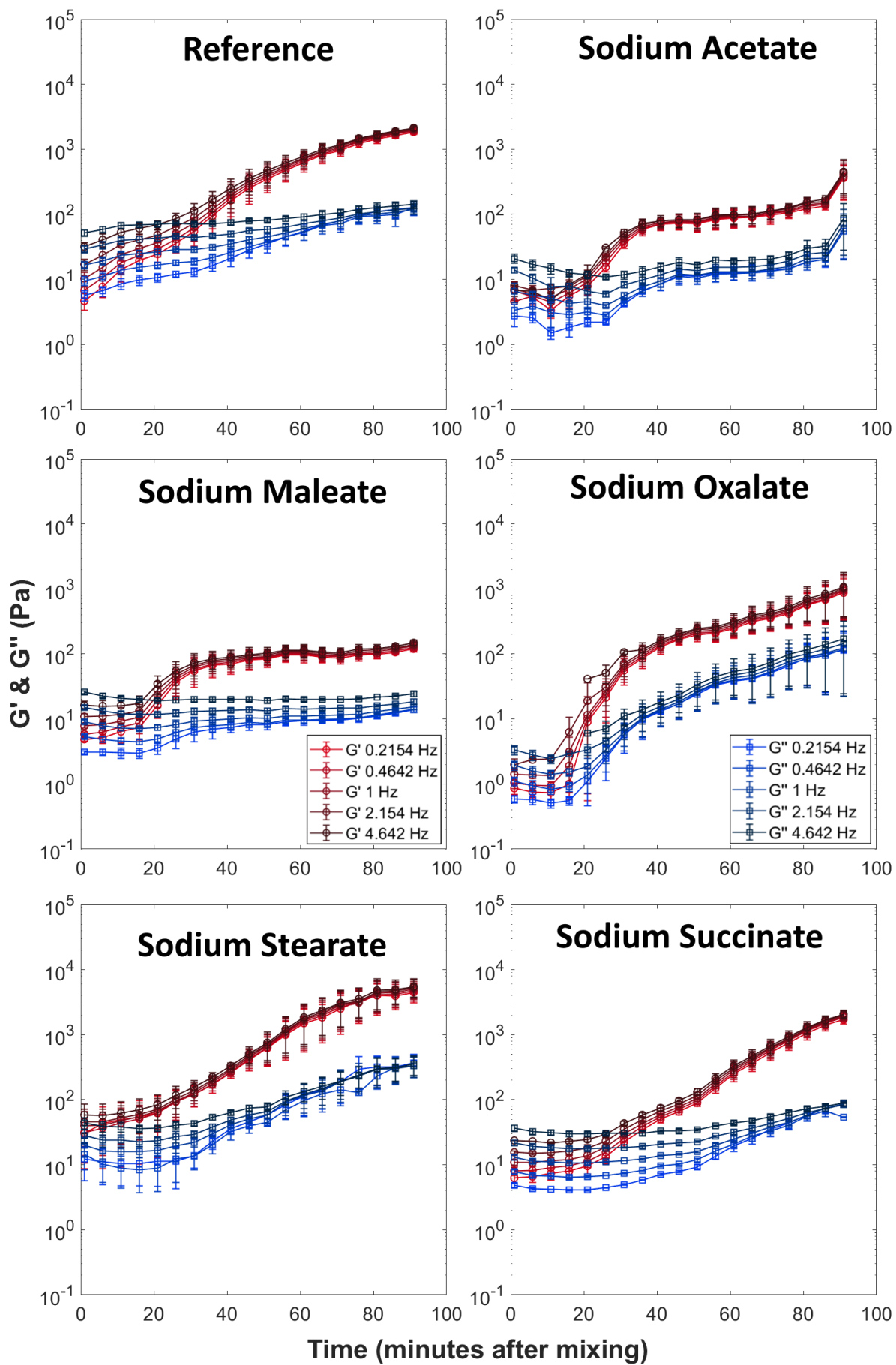


Figure 7.3: Storage and Loss Modulus for the reference electrode slurry and all the electrode slurries containing the active material milled with 2.0 wt% of the sodium salts.

values of G' start at approximately 10 Pa and increase to 100 Pa over a 40-minute period. After 40 minutes, there is a plateau in G' at 100 Pa for 50 minutes, until an increase at 90 minutes to a value of approximately 300 Pa. From the onset of the rheological measurements there is a tight grouping of G' values across all measured frequencies and then after 40 minutes there is almost complete convergence. G' becomes independent of frequency. This pattern of increases and plateaus follows the same 3 phase gelation, established for the reference electrode material in Chapter 4. However, in contrast to the reference electrode slurry the changes are more extreme.

The loss modulus begins with values between approximately 3 and 20 Pa, over the frequency range, and experiences an initial decrease, before returning to the initial values, albeit with a slight convergence of values. From 40 to 90 minutes, G'' plateaus, with values between 90 and 160 Pa, over the frequency range.

After 20 minutes, the electrode slurry begins to exhibit typical gel-like behaviour, where $G' > G''$, irrespective of frequency. [261–263] Similar to the previously tested electrode slurries in chapters 4 and 6, there is no discernible gel point where $G' = G''$, independent of frequency. [318] However, as $G' > G''$, and the pattern of G' is consistent with previously studied electrode slurries, it is clear that there is cross-linking and gel-like behaviour occurring. [319]

The values of G'' see a slight frequency convergence after 50 minutes, which then fully converges after 90 minutes. Pellet and Cloitre, 2016, explored the glass and jamming transitions in suspensions and established that for jammed suspensions, $G' > G''$ across the frequency range with G' being independent of frequency, and G'' dependent. [259] This finding was similarly observed by Franco *et al.*, 2021. [260]

Compared to the reference electrode slurry where G' only reaches a convergence after 70 minutes, G' converges after 40 minutes for those electrode slurries containing sodium acetate. As the sodium acetate material does not disassociate and dissolve in NMP, Figure 7.2, it can be suggested that after 40 minutes there is a strong jamming effect occurring due to the high particle concentration.

Therefore, despite the dominance of G' over G'' after 20 minutes depicting gel-like behaviour, there is a physical colloidal jamming effect that is manifesting itself as gel-like behaviour. Only after the values of G'' converge can it be established that chemical gelation has occurred and not colloidal jamming.

Sodium maleate-based electrode slurries demonstrate similar behaviour to those containing sodium acetate. Values of G' are initially between 3 and 15 Pa and increase over a 40-minute period to approximately 100 Pa. After this time, there is a frequency convergence and the value of G' plateaus at approximately 100 Pa.

The loss modulus, demonstrates behaviour similar to the reference electrode slurry. Values of G'' start at between approximately 4 and 30 Pa. There is a slight frequency convergence that initiates after approximately 20 minutes. However, the values of G'' never fully converge and G'' remains frequency dependent across the full measurement window. The final values are between approximately 10 and 20 Pa.

Similar to the sodium acetate-based electrode slurries, it can be inferred that there is colloidal jamming occurring after 20 minutes. The sodium maleate does not disassociate and dissolve in NMP, Figure 7.2 and G' becomes frequency independent while G'' remains frequency dependent. [259,260] An electrode slurry gel is, however, indeed forming, where $G' \gg G''$, [261–263] and G'' has a sufficient degree of frequency convergence. Furthermore, the pattern in G' and G'' is consistent with the gelation established in Chapter 4.

Sodium oxalate- and sodium stearate-based electrode slurries share similar behaviour. Over the first 15 to 20 minutes, the values of G' and G'' see a slight increase. At this point the elastic behaviour dominates ($G' > G''$) and G' becomes frequency independent while G'' remains frequency dependent, suggesting colloidal jamming. [259,260] After 40 minutes, the frequency dependence of G'' lessens for both sodium oxalate- and sodium stearate-based electrode slurries. At this point, it can be suggested that the jamming effects have been reduced, and the gel behaviour has become more prevalent. The final values of G' and G'' , 1000 Pa and 150 Pa, and 5300 Pa and 340 Pa, for sodium oxalate- and sodium stearate-based electrode slurries suggests that the inclusion of sodium stearate

form gels with a higher rigidity. [227–229] Compared to the other sacrificial additives, sodium stearate based electrode slurries show the highest final values of G' and G'' , denoting the highest gel rigidity.

Electrode slurries containing the sodium succinate coated active material exhibit behaviour that is very similar to the reference electrode slurry. The values of the storage and loss moduli initially begin at similar values, between approximately 8 and 50 Pa across the frequency range. A divergence between G' and G'' begins after 40 minutes, where $G' > G''$. Full frequency convergence occurs after 80 minutes for the storage modulus, and after approximately 80 minutes for the loss modulus. The final values of G' and G'' are approximately 2000 Pa and 100 Pa, respectively. Based on the similarities between the storage and loss behaviour for sodium succinate-based electrode slurries and the reference electrode slurries, it can be suggested that there is no colloidal jamming occurring, and that sodium succinate does not interfere in the gelation reaction. [259, 260] Furthermore, as G' and G'' become frequency independent at the same time, while $G' \gg G''$, the formation of a gel can be confirmed. [261–263]

7.4.1.2.2 Phase Angle

The phase angle can be examined to determine the degree of viscoelasticity of the electrode slurry. Values of 0° describe fully elastic behaviour, 90° demonstrates fully viscous behaviour, and 45° , equal contribution of both.

The changes to the phase angle over time for the reference electrode slurry and those containing the active material milled with the sacrificial salts can be found in Figure 7.4.

It is evident from Figure 7.4 that the behaviour of the electrode slurries containing the sacrificial salts is different from the reference electrode slurry.

At the start of the phase angle measurements, $t = 0$ minutes, for all sacrificial additives, the values of the phase angle are widely spread across the different frequencies. For the reference electrode slurry, the initial phase angle is frequency independent. As discussed in Section 7.4.1.2.1, the effects of colloidal jamming will appear in the oscillatory rheology as

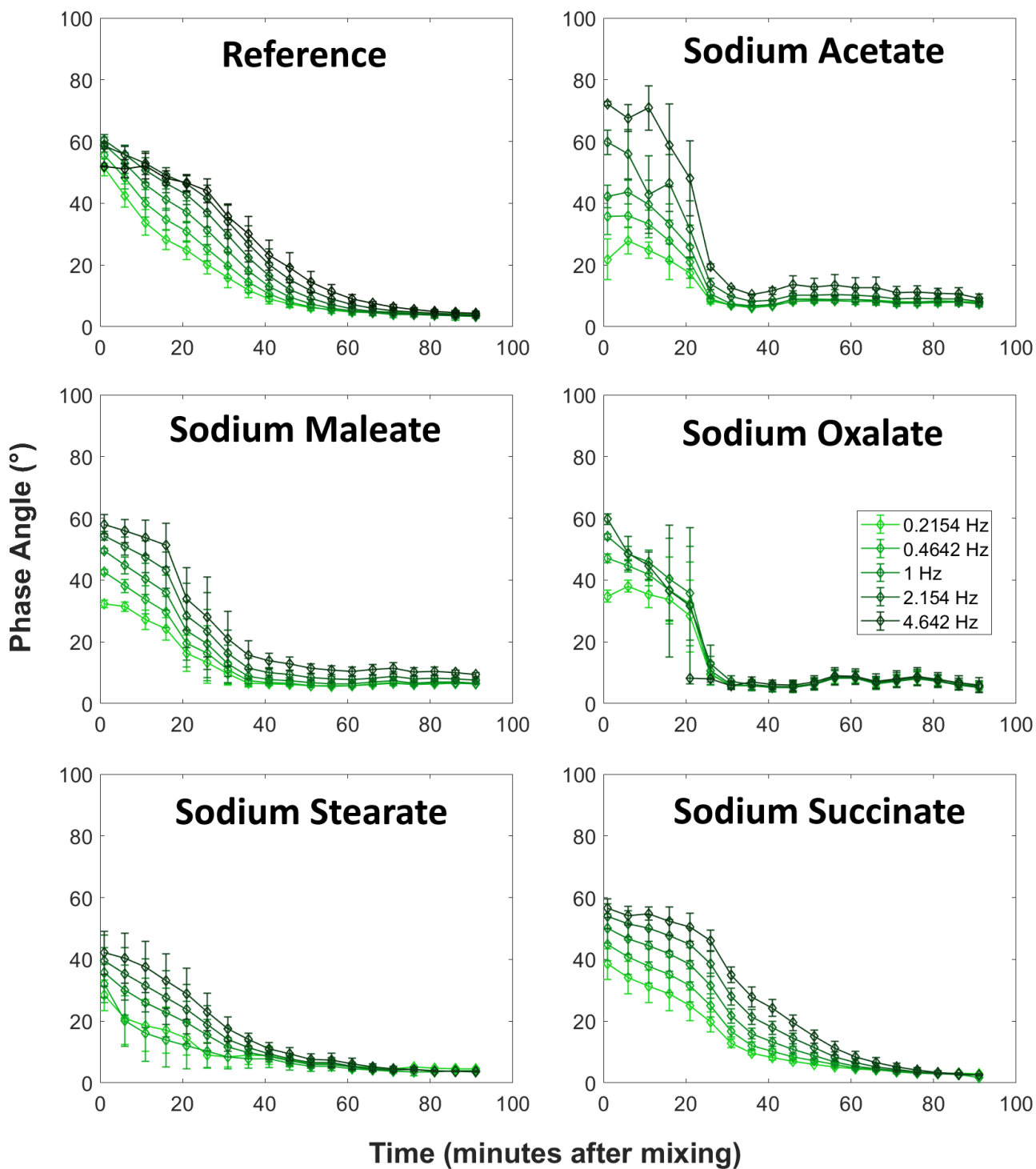


Figure 7.4: Phase angle changes for the reference electrode slurry and all the electrode slurries containing the active material milled with 2.0 wt% of the sodium salts.

a frequency independent G' and a frequency dependent G'' , and where $G' > G''$. [259,260]

Chu *et al.*, 2020, and Noirez *et al.*, 2012, have explored different jamming effects. [320, 321] Chu *et al.*, 2020, established that at high frequencies, a colloidal glass will exhibit more solid-like behaviour ($< 45^\circ$), and at the lower frequencies equal or viscous behaviour ($\geq 45^\circ$). [320]. Noirez *et al.*, 2012, ascertained that a low frequency shear elasticity ($< 45^\circ$) will arise from a compression and confinement effect. [321–323]

In these electrode slurries, it can be noted that the elastic behaviour exists, at least initially, for the low frequencies. For the higher frequencies, more viscous behaviour of the electrode slurries prevails. It can therefore be suggested that this elastic behaviour arises from a confinement and jamming effect of the discrete phase in the electrode slurry. [321–323] It could be suggested that this is a repulsive effect due to presence of these sacrificial additives. These confinements could similarly arise from the larger coated particles.

Initial phase angle values for sodium acetate-based electrode slurries range between 71° and 22° , demonstrating the largest spread of all electrode slurries, 49° .

Sodium maleate-, sodium oxalate-, and sodium succinate-based electrode slurries all demonstrate a spread of approximately 22° , between 60° and 38° . Finally, sodium stearate based electrode slurries show a phase angle range between 42° and 31° . This frequency dependence in the phase angle values demonstrate strong elastic behaviour of confined and jammed colloids. [321–323].

The decline of these confinement effects suggests that some dissolution or a breakup of the sacrificial additives is occurring.

For sodium acetate, the frequency dependence of the phase angle remains for approximately 25 minutes, after which the phase angle reduces to approximately 9° , denoting strong elastic behaviour. By this point, as the frequency dependence has decreased significantly and the colloidal jamming effects have been halted.

Sodium maleate based electrode slurries demonstrate similar behaviour. The frequency dependence predominately exists in the electrode slurry until 20 minutes. After 20 minutes, there is a slow frequency convergence until approximately 40 minutes,

whereby the phase angle reaches 10° . This phase angle further declines towards the end of oscillatory measurements to a value of approximately 8° .

For sodium oxalate, the frequencies rapidly converge after 20 minutes. However, the values between 15 and 25 minutes can be considered erroneous. Inertial effects are dominant in many of these repeats and the error values are very large. Therefore it is difficult to analyse the sodium oxalate based electrode slurry. These inertial effects would persist throughout repeats. It is suggested that the colloidal confinement and jamming effects caused inertial effects to hinder the rheological measurements. Following this erroneous data region, the confinement effects reduce (the phase angle become frequency independent) and elastic behaviour (a phase angle of approximately 6°) persists until 90 minutes.

Electrode slurries containing sodium stearate or sodium succinate exhibit a smoother transition between the initial spread of phase angles to the frequency convergence. This suggests a more gradual breaking of the discrete phase confinement effects. Electrode slurries containing sodium stearate demonstrate a phase angle frequency convergence after 40 minutes. At this point the phase angle plateaus at a value of approximately 9° .

As suggested in Section 7.4.1.2.1, sodium succinate electrode slurries demonstrate behaviour that is similar to the reference electrode slurry. The sacrificial additive has very little influence on the gelation of the electrode slurry. After 40 minutes, the phase angle averages to a value of 17.8° (16.4° for the reference electrode slurry). Full frequency convergence is reached after approximately 75 minutes, and the final value of the phase angle is 2.5° (3.5° for the reference electrode slurry). The main difference is the frequency dependence at 0 minutes, suggesting the same confinement effects introduced by the other sacrificial additives.

Table 7.1 demonstrates a summary of the oscillatory rheology data, and presents a comparison of the key values after 40 and 90 minutes.

Based on table 7.1, it can be noted that after 40 minutes, sodium acetate, sodium maleate, and sodium succinate based electrode slurries show the lowest rigidities. This

Table 7.1: Summary of storage and loss values, phase angle values and the loss factor (G'/G'') after 40 minutes and 90 minutes.

	After 40 minutes				After 90 Minutes			
	G'	G''	Loss Factor	Phase Angle (°)	G'	G''	Loss Factor	Phase Angle (°)
Reference	218.3	50.1	4.4	16.4	2043.3	124.2	16.5	3.5
Sodium Acetate	78.5	11.7	6.7	8.6	427.7	71.5	6.0	8.2
Sodium Maleate	84.3	13.5	6.2	10.0	140.3	18.6	7.5	7.6
Sodium Oxalate	153.3	15.7	9.7	5.5	1030.3	144.6	7.1	5.5
Sodium Stearate	304.2	48.4	6.3	9.5	5280.0	336.3	15.7	3.6
Sodium Succinate	66.7	20.9	3.2	17.8	2006.7	84.6	23.7	2.5

can be observed in the values of G' and G'' . However, at this time the most viscous electrode slurries and those with the weakest gel strength are the reference electrode slurry and the sodium succinate based electrode slurry. These strengths can be noted in the loss factor and phase angle columns.

After 90 minutes, the electrode slurries containing the active material milled with either sodium acetate or sodium maleate clearly show the lowest rigidities, with the lowest absolute values of both G' and G'' . Additionally these two electrode slurries, with sodium acetate or sodium maleate, show the weakest gel strengths and the most viscous slurries.

Based on these values in Table 7.1 and the data displayed in Figures 7.3 and 7.4, the milled additive with the best improvements to the electrode slurry is sodium maleate, with sodium acetate as a close second.

It is worth noting that sodium oxalate as a milled additive shows improvements over the reference electrode slurry after 90 minutes, however, its stabilising performance after 40 minutes is very poor compared to sodium acetate or sodium maleate, with a greater jamming effect.

Ultimately, in most cases (apart from sodium succinate) additions of the sacrificial additives has caused a confinement jamming effect for at least the first 20 minutes of electrode slurry processing. This means that coating at a low frequency, which loosely translates as a slow coating speed, will be very difficult. The particles in the electrode slurries will jam and the high elastic behaviour could render homogeneous coating impossible. As demonstrated in Figure 7.4, high frequencies causes the electrode slurries to exhibit more viscous behaviour. It is therefore suggested that the use of these sacrificial additives will require a change to the coating procedure to accommodate this viscous behaviour.

7.4.1.2.3 Relaxation Time

The changes to the relaxation time of the electrode slurries, fitted from the 2 mode Maxwell model, as covered in Chapter 5, can be found in Figure 7.5.

As established in Chapter 4, the reference material follows a three stage gelation process and takes approximately 45 minutes for the final gelation plateau to be reached.

Instead, when the sacrificial additives are used, this three stage gelation process is less detectable in the relaxation time. Electrode slurries containing sodium maleate demonstrate a pattern that could be interpreted as an accelerated three stage gelation process. However, the decline in relaxation time after 60 minutes suggests that a chemical gel had not been formed, and instead confinement jamming effects were dominant.

Furthermore, it can be observed in the primary relaxation time (Figure 7.5) that, for the first 40 minutes, all the sacrificial additives increase the primary relaxation time of the electrode slurry. As established, this increase in elastic properties is primarily a result of the confinement jamming in the electrode slurries.

Sodium acetate- and sodium oxalate-based electrode slurries demonstrate a reduction in the relaxation time after 40-45 minutes, after the effects of the confinement jamming appear to reduce.

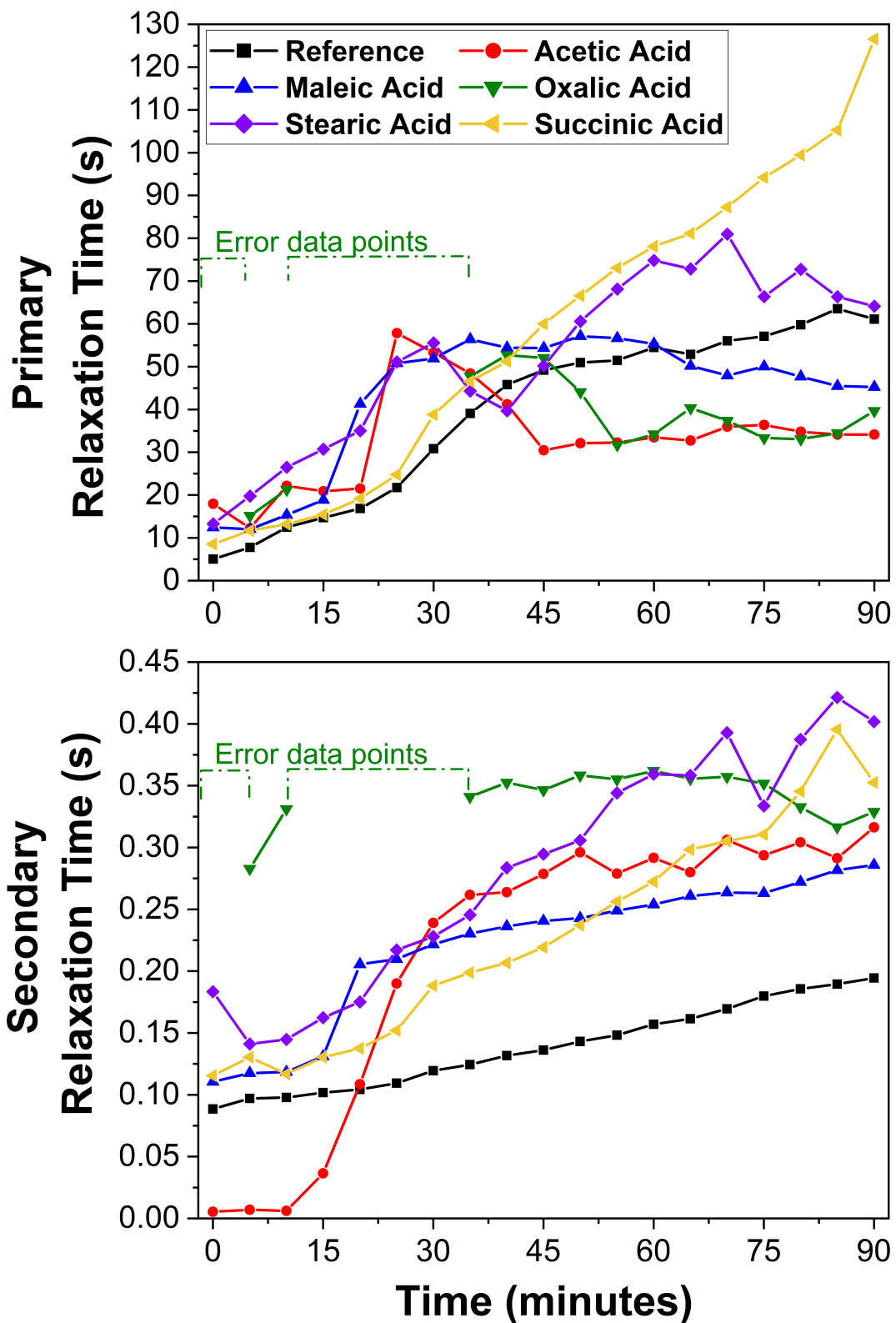


Figure 7.5: Maxwell Mode - Primary and Secondary Relaxation Times for the reference electrode slurry and all the electrode slurries containing the active material milled with 2.0 wt% of the sodium salts.

Electrodes containing sodium succinate, up to 45 minutes, follow a similar gelation pattern to the reference, further reinforcing the notion that the sodium succinate does not influence the electrode slurry gelation.

Finally, electrode slurries containing sodium stearate do demonstrate a distorted three stage gelation progress, although there is a slight dip at 40 minutes, the point at which the confinement jamming effects reduce for the other electrode slurries.

As alluded to in Chapter 6, the secondary relaxation time signifies that the electrode slurries exhibit a strong elastic response. [289–292] For the majority of measurements, electrode slurries containing the sacrificial additives demonstrate a higher secondary relaxation time than the reference slurry. This higher secondary relaxation time further suggests the notion of high volume fraction confinement jamming of solid particles - high solids content fine-particles suspensions have been shown to demonstrate yield stresses. [291, 292]

7.4.2 Effect on the Electrode Properties

7.4.2.1 Electrode Adhesion Strength

The importance of electrode adhesion has been highlighted in Chapter 2.

The adhesion strength of electrodes made from the reference electrode slurry and those containing the active material milled with the sacrificial additives can be observed in Figure 7.6.

The sacrificial additive of the active material particles can be seen to significantly decrease the adhesion strength when compared to the reference electrode. Sodium acetate-based electrodes have an adhesion strength of 24.5 Nm^{-1} , the lowest adhesion strength of all those additives tested. Sodium oxalate-based electrodes have the highest adhesion strength of 89.9 Nm^{-1} , marginally lower than the adhesion strength of the reference electrode, 91.0 Nm^{-1} . The next highest adhesion strengths belong to sodium stearate, with an adhesion strength of 73.6 Nm^{-1} , sodium maleate, 63.0 Nm^{-1} , and

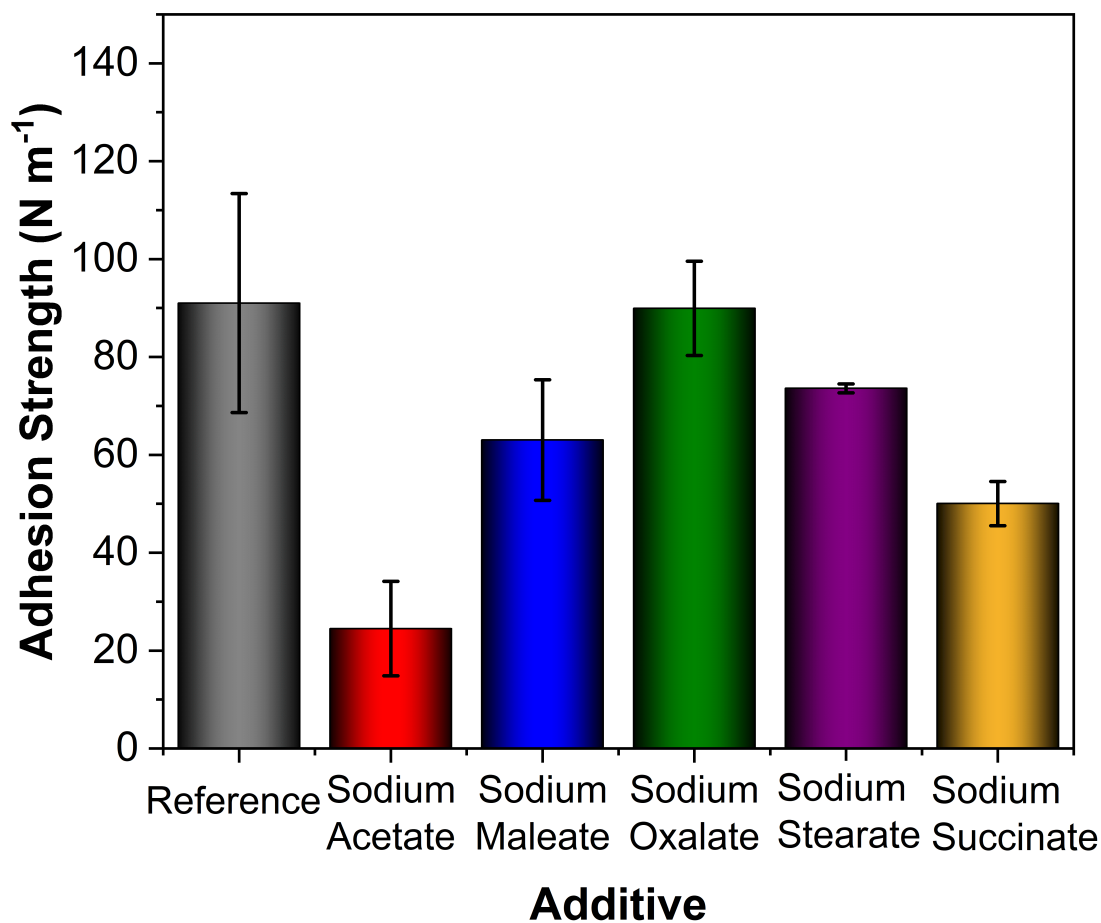


Figure 7.6: Adhesion strength for electrodes made from the reference electrode slurry and all the electrode slurries containing the active material milled with 2.0 wt% of the sodium salts. Electrode slurries were coated immediately after mixing was completed.

sodium succinate, 50.0 Nm⁻¹.

These reductions to the adhesion strength of the electrodes, as established in Chapter 2, could cause issues due to decreased mechanical strengths in the handling of electrodes during cell construction, and so extra care needs to be employed during this stage of manufacture. Additionally, reductions to the adhesion strength have the potential to decrease the long term cycling stability of these electrodes. Further analysis of this can be observed in the electrochemical behaviour of these cells.

As established in Chapter 6, the high adhesion strength of the reference electrode is due to the cross-linking of the PVDF binder, [199,293] and the etching and corrosion of

the NaOH on the aluminium current collector [273].

The reduction of the adhesion strength due to the sacrificial additive of the active material, therefore, suggests two inferences. These sacrificial additives have successfully reduced the quantities of NaOH formed. NaOH is normally formed through the surface reactions of the active material in air, as explored in Chapter 4. Secondly, it can be suggested that the cross-linking of PVDF chains has been similarly reduced, further corroborating the results determined by the oscillatory rheology, Section 7.4.1.2.

The adhesion strength of electrodes made from the reference electrode slurry and those containing the active material milled with the sacrificial additives coated after 40 minutes can be observed in Figure 7.7.

From Figure 7.7 it can be seen that by coating the reference electrode slurry 40 minutes after mixing, the adhesion strength increases to a value of 292.0 Nm^{-1} . Sacrificial active material additives of sodium acetate (35.5 Nm^{-1}) and sodium maleate (66.5 Nm^{-1}) see a relatively smaller increase in the adhesion strength by coating after 40 minutes.

All the remaining sacrificial additives see a decrease in the adhesion strength by coating 40 minutes after mixing. Sodium oxalate-based electrodes see a decrease to 64.5 Nm^{-1} , sodium stearate-based electrodes, 44.0 Nm^{-1} , and sodium succinate-based electrodes drop to 45.1 Nm^{-1} .

As established, the high adhesion strength in the reference electrodes coated 40 minutes after mixing is a result of the increased cross-linking in the PVDF binder, [199,293] and the etching and corrosion of the NaOH on the aluminium current collector [273]. The extra time of air exposure allows more NaOH to form and additional cross-links to form throughout the dissolved PVDF binder.

The slight changes to the adhesion strengths of electrodes containing the sacrificial additives further reinforces the notion of electrode slurry stabilisation. Furthermore, these slight changes suggests that consistent electrode properties can still be achieved throughout the 40 minute coating window.

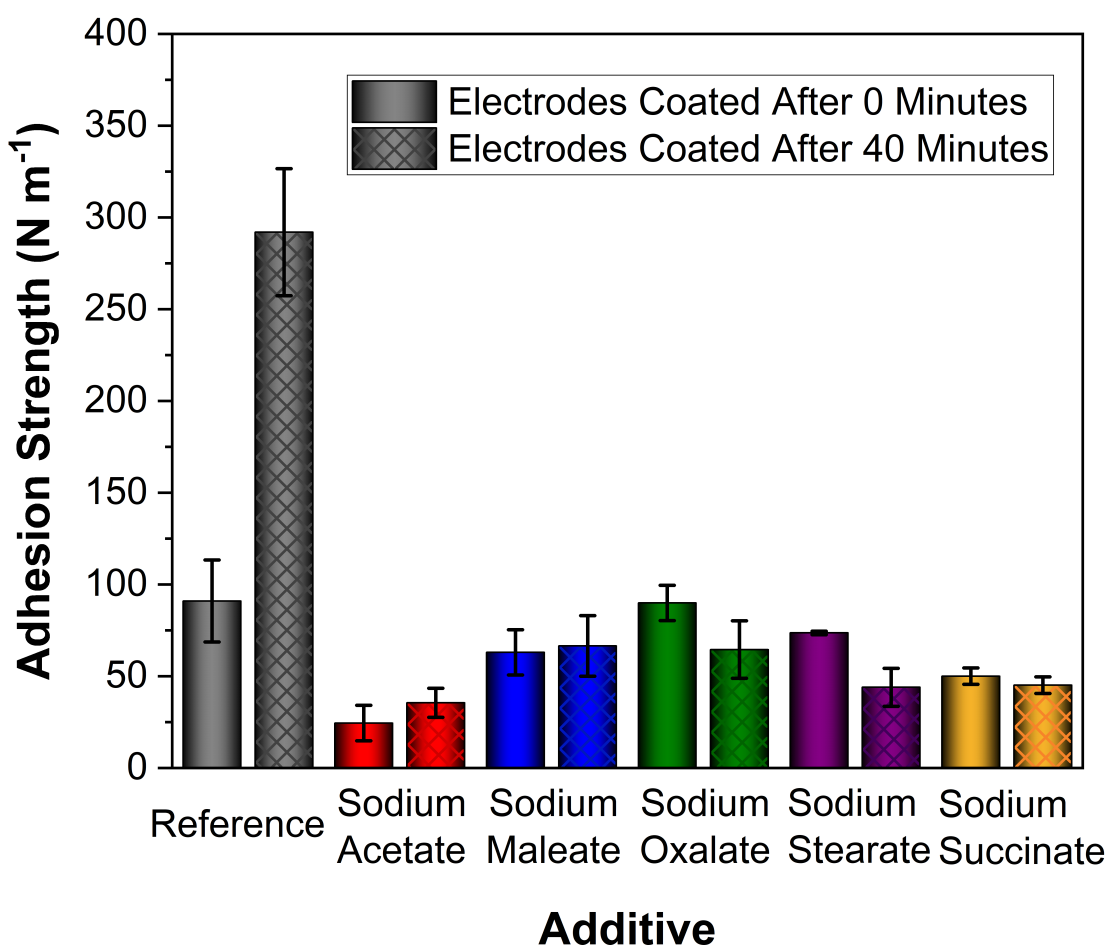


Figure 7.7: Comparison adhesion strength for electrodes made from the reference electrode slurry and all the electrode slurries containing the active material milled with 2.0 wt% of the sodium salts. Bars show coatings made from electrode slurries coated immediately after, and 40 minutes after mixing was completed.

7.4.2.2 Electrode Conductivity

To further characterise the electrode properties, conductivity measurements were performed. Figure 7.8 shows the conductivity measurements for electrodes made from the electrode slurries containing the active material milled with 2.0 wt% of the sodium salts. Electrodes made from the reference electrode slurry has been included from ease of comparison. As explored in Chapter 6, these electrode conductivities have been measured using an aluminium current collector.

Figure 7.8 shows that by milling the active material with the sodium salt additives

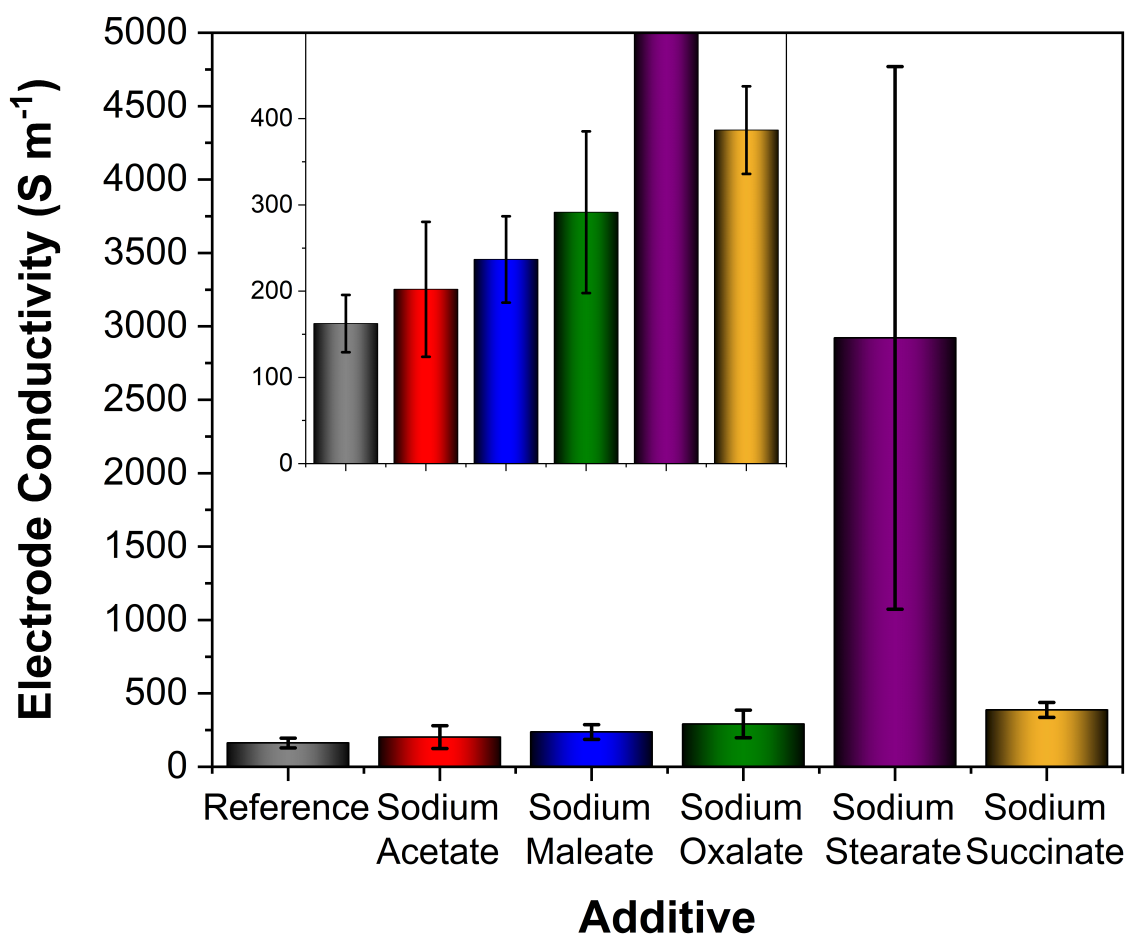


Figure 7.8: Comparison electrode conductivity for electrodes made from the reference electrode slurry and all the electrode slurries containing the active material milled with 2.0 wt% of the sodium salts. The inset graph shows conductivities between 0 and 400 S m^{-1} , for a clearer comparison between all electrodes, other than those containing sodium stearate.

increases the conductivity of the electrode. Additionally, this increase in conductivity occurs regardless of sodium salt used. The electrodes with the highest conductivity by far are those containing sodium stearate, with a conductivity of $2920 \pm 1850 \text{ S m}^{-1}$. Despite the high error in these measurements, these values still range from more than 4 times to more than 20 times the conductivity of the reference electrode, $163 \pm 33.2 \text{ S m}^{-1}$. It has been established that in ion-containing polymer systems, such as these electrodes, amorphous materials are required to give the highest ionic conductivities. [324, 325] Although this strictly applies for fully amorphous or fully

crystalline polymers, it can still be used to infer the structure of these electrodes. [324, 325] It can be suggested that the use of sodium stearate, with its long chain fatty acid group and flexible structure, disrupts the structured electrode formation and produces amorphous structures. However, as the importance of electrode homogeneity has been established in Chapter 2, these amorphous structures can produce numerous environments, making electrochemical testing difficult. Furthermore, these amorphous and unstructured electrodes could produce more inaccessible and blocked pores.

The other sodium salt additives, as stated, all demonstrate favourable improvements to the electrode conductivity over the reference electrode, which could be a result of two things. Firstly, the addition of these sacrificial additives themselves has increased the conductivity of the electrodes. Secondly, the sacrificial additives have influenced the structure of the electrodes, altering the conductive carbon black network or forming an amorphous structures. [324, 325]

Electrodes containing sodium acetate, sodium maleate, or sodium oxalate, all fall within the same threshold of conductivity (if the standard deviations and errors are taken into account), and it can be suggested that their electrode structures are fairly similar to one another. Sodium acetate based electrodes have a conductivity that is marginally greater than the reference electrode, $202 \pm 78.2 \text{ Sm}^{-1}$. Sodium maleate based electrodes have a conductivity of $237 \pm 50.1 \text{ Sm}^{-1}$. Sodium oxalate based electrodes have a conductivity of $292 \pm 93.8 \text{ Sm}^{-1}$.

Finally, electrodes containing sodium succinate have a conductivity of $387 \pm 50.1 \text{ Sm}^{-1}$. However, as the conductivity of these sodium succinate based electrodes is more comparable to those of sodium oxalate than sodium stearate, it prudent to suggest that the structure of electrodes containing sodium succinate is close to that of sodium oxalate.

7.4.3 Effect on the Electrochemical Performance

The reference electrodes and electrodes containing the milled active material with 2.0 wt% of the sodium salts have been electrochemically assessed in the same manner as in Chapter 6. The electrochemical performance of these electrodes will be explored, firstly via a standard cycling procedure, outlined in Chapter 3, and secondly through EIS measurements performed after the first cycle and after the tenth cycle.

7.4.3.1 Electrochemical Cycling Performance

A comparison of the cycling performance of the electrodes containing the sodium salt additives and the reference electrodes can be found in Figure 7.9.

From Figure 7.9, the benefit of the sacrificial additive is immediately obvious, especially in the reduction of the first to second cycle discharge capacity loss.

For comparison purposes, the reference electrodes have a first cycle discharge capacity (vs Na/Na⁺) of 120.4 ± 3.1 mAh/g which falls to 80.2 ± 4.0 mAh/g for the second cycle. This is a first cycle loss of 40.2 ± 7.1 mAh/g. By the 20th cycle the electrodes have a discharge capacity of 65.1 ± 3.3 mAh/g.

The best performing sacrificial additives are sodium succinate and sodium maleate, with sodium succinate performing marginally better than sodium maleate. Electrodes containing the sacrificial additive of sodium succinate have a first cycle discharge capacity of 123.3 ± 2.3 mAh/g, which falls to 121.5 ± 1.7 mAh/g for the second cycle, resulting in a loss of 1.8 ± 4.0 mAh/g between these cycles. By the 20th cycle the discharge capacity of the electrodes had fallen to 104.1 ± 2.9 mAh/g, a capacity retention of 84.4 %.

Sodium maleate-based electrodes has a similarly high first cycle discharge capacity of 122.4 ± 1.8 mAh/g, which falls to 120.1 ± 1.6 mAh/g. This loss of 2.3 ± 3.4 mAh/g is comparably to the sodium succinate-based electrodes. The final measured discharge capacity, for the 20th cycle is 100.5 ± 1.8 mAh/g. This is a capacity retention of 83.7 %.

For sodium maleate- and sodium succinate-based electrodes, despite having a

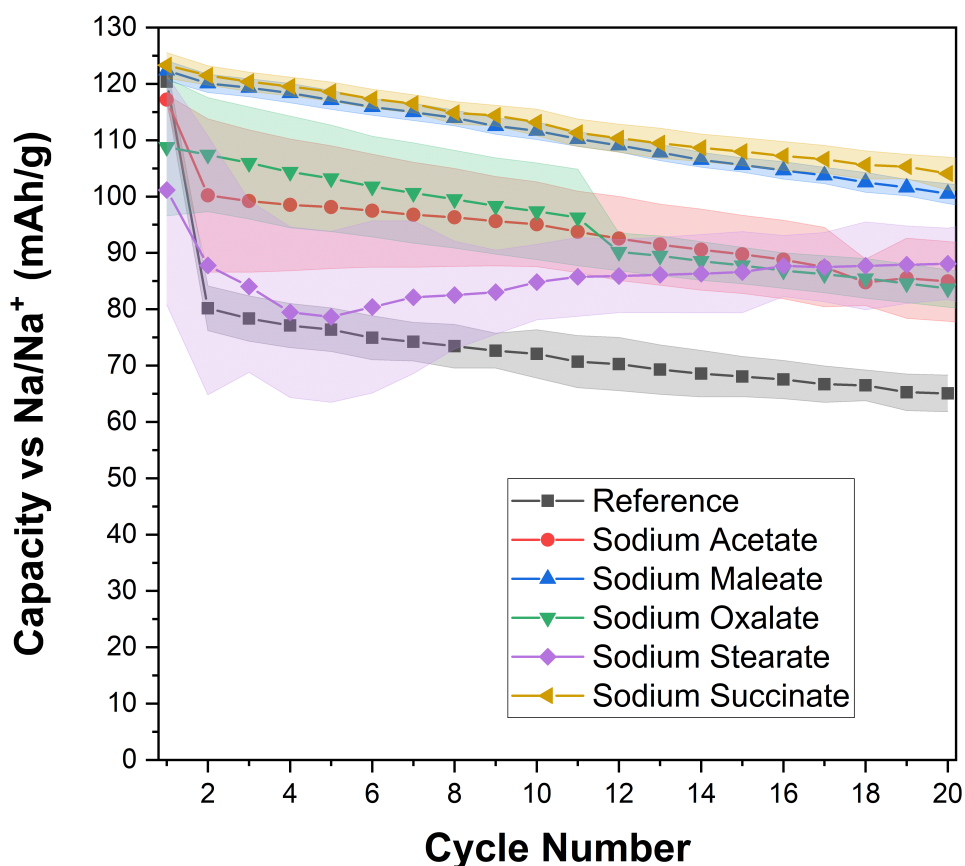


Figure 7.9: Cycling capacity vs cycle number for electrodes made from the reference electrode slurry and all the electrode slurries containing the active material milled with 2.0 wt% of the sodium salts. The shaded areas denote the standard deviations of the measurements.

formation discharge capacity that is similar to the reference electrode, the subsequent discharge capacity reductions are far less. It is clear that the reservoir of sodium ions provided by the sacrificial additives have enabled a greater capacity retention. It is likely that these sacrificial additives have preferentially reacted over the active material when forming the CEI layers.

Electrodes containing sodium stearate as the sacrificial additive exhibit a cycling performance that is only marginally better than the reference electrode, and is the worst of the sacrificial additives. The first cycle has a discharge capacity of 101.2 ± 20.4 mAh/g, which falls to 87.8 ± 23.0 mAh/g for the second cycle. This is a loss of 13.4 ± 43.4 mAh/g. By the 20th cycle the electrodes have a discharge capacity of 88.1 ± 6.3

mAh/g

Electrodes containing sodium acetate and sodium oxalate have similar performances, although sodium oxalate-based electrodes do demonstrate a lower discharge capacity loss between the formation and second cycles. The first cycle discharge capacity for sodium oxalate-based electrodes is 108.8 ± 12.2 mAh/g. This falls to 107.4 ± 10.1 mAh/g for the second cycle, resulting in a first cycle loss of 1.4 ± 22.3 mAh/g. By the 20th cycle the discharge capacity has fallen to 83.7 ± 3.3 mAh/g.

Sodium acetate-based electrodes have a first cycle discharge capacity of 117.2 ± 0.8 mAh/g, which falls to 100.2 ± 13.6 mAh/g, resulting in a loss of 17.0 ± 14.4 mAh/g. The final measured cycle, 20th, has a discharge capacity of 84.9 ± 7.1 mAh/g.

7.4.3.2 Electrochemical Impedance Spectroscopy

Electrochemical impedance spectroscopy, EIS measurements were taken after the formation cycle and after the tenth cycle, and can be found in Figure 7.10. Measurements were performed at 50 % SoC to avoid large polarisation effects. 50 % SoC was reached via charging from a state of discharge. Out of all the insertion sites, the most kinetically favourable will be filled, leaving 50 % of the least kinetically favourable sites empty.

As explored in Chapter 6, the reference electrode EIS after the formation cycle depicts two semi circles features followed by a 45° line, relating to the CEI impedance, the charge transfer impedance, and the Warburg diffusion. The midpoint of the two semi circles is taken at a frequency of 50 Hz. The reference EIS after the tenth cycle shows an elongated semi circle followed by a 45° line. The frequency mapping shows that the point taken at 50 Hz lays approximately two thirds along the elongated semi circle, suggesting that there is two features. The frequency mapping for the electrodes containing the sacrificial additive demonstrates two semi circle features obscured by a single ellipsoidal semi circle in the same way.

Further analysis on these electrodes, and the remaining sacrificial additives, has been

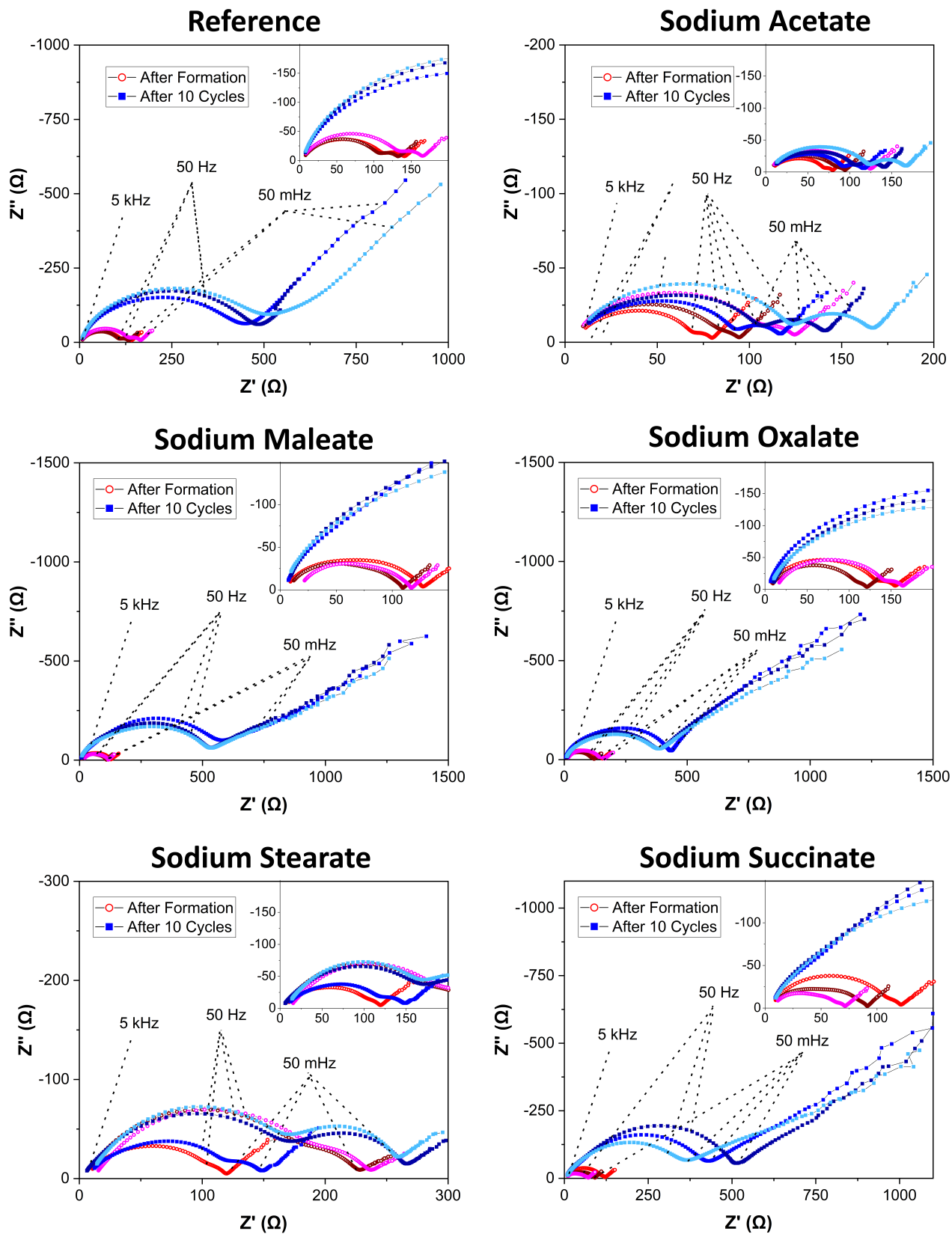


Figure 7.10: Electrochemical Impedance Spectroscopy for the reference electrodes and electrode containing the sacrificial additives. Performed after the formation (first cycle) and after the tenth cycle.

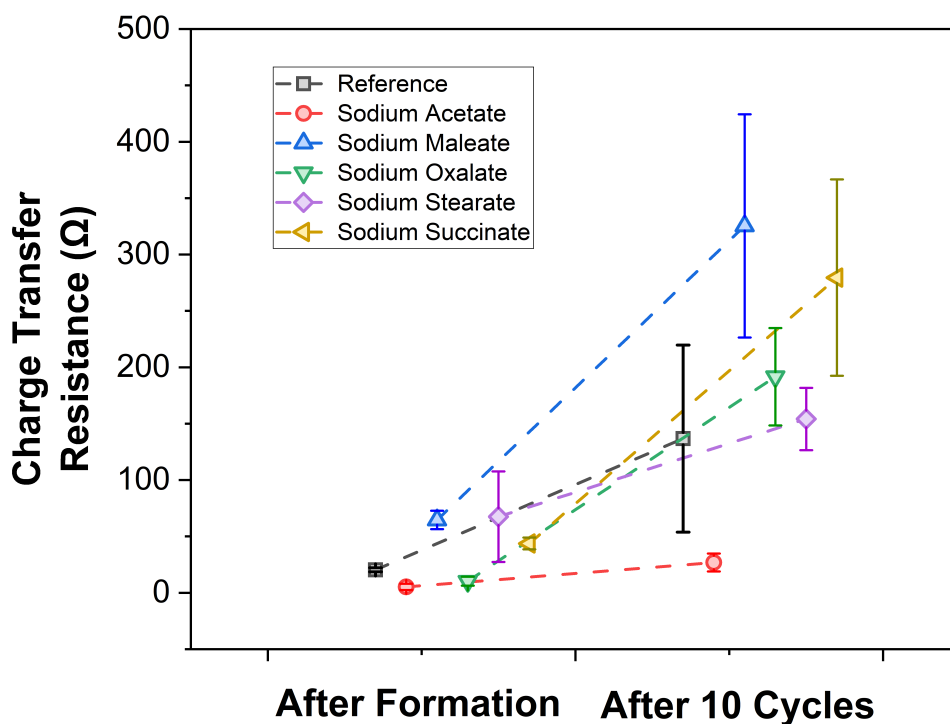
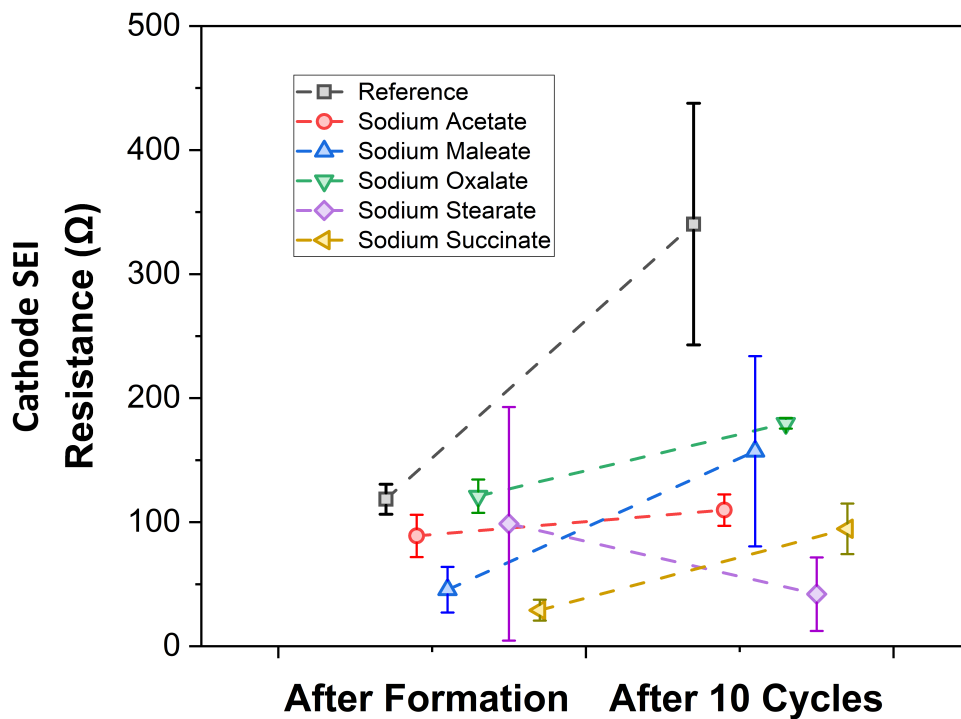


Figure 7.11: Cathode solid electrolyte interphase layer resistance and charge transfer resistance - fitted from the electrochemical impedance spectroscopy in Figure 7.10 after the formation cycle and after 10 cycles. Samples have been incremented along the x-axis for clearer distinction between them.

accomplished through the fitting of these EIS measurements to an equivalent circuit model. Fitted values to the CEI resistance and the charge transfer resistance can be found in Figure 7.11. For ease of comparison, the reference electrodes have a CEI resistance of $118.5 \pm 12.1 \Omega$ that increases to $340.3 \pm 97.4 \Omega$ over 10 cycles. The charge transfer resistance of the reference electrodes is $20.4 \pm 1.8 \Omega$ after formation, which increases to $136.8 \pm 83.0 \Omega$.

It can be noted that while the reference electrodes sees an almost two fold increase in the cathode solid electrolyte interface resistance after 10 cycles, those electrodes containing the sacrificial additives see only marginal increases, or decreases. Electrodes containing sodium stearate show one of the higher fitted CEI resistances of $98.7 \pm 94.1 \Omega$. Over the course of cycling, this SEI resistance decreases to a value of $42.0 \pm 29.6 \Omega$, suggesting that a thick SEI layer had initially formed with poor stability, and is then dissolved or destroyed during cycling. [295]

Furthermore, electrodes containing sodium stearate, shown to have the highest electrical conductivity in Figure 7.8, demonstrates the highest charge transfer resistance $67.6 \pm 40.2 \Omega$. As the high electrical conductivity should facilitate the transfer of charge throughout the electrode, [305] it can be suggested that the addition of sodium stearate creates an electrode structure that has poor kinetics when cycled.

The charge transfer resistance increases to a value of $154 \pm 27.7 \Omega$ after 10 cycles. Coupled with the large decreases in discharge capacity over cycling, it can be suggested that the most kinetically favourable insertion sites become inaccessible as cycling progresses. This could be a result of SEI growth causing a reduction in the pore network, blocking sites. [108] Hence the increase in the charge transfer resistance as the more kinetically unfavourable sites are filled at 50 % SoC.

The remaining electrodes (those containing sodium acetate, sodium maleate, sodium oxalate, and sodium succinate) all demonstrate increases to both the CEI resistance and the charge transfer resistance with cycling, as can be observed in Figure 7.11.

Electrodes containing sodium oxalate see an increase in the CEI resistance from 121.0

$\pm 13.5 \Omega$ to $180.0 \pm 4.3 \Omega$ over cycling. A rise in the CEI resistance indicates the cathode interface layer has not fully formed after the formation cycle, and requires additional cycling. The degree of change in this resistance is far less than that of the reference electrodes, which could imply that the carboxylic groups in the sacrificial additive have helped to form a more stable CEI (as suggested in Chapter 6). [267, 268] The formation of these stable CEI films could similarly be suggested for all the sacrificial additives (excluding sodium stearate).

Sodium oxalate based electrodes also demonstrate an increase to charge transfer resistance after cycling. After formation, the charge transfer resistance is $10.3 \pm 4.0 \omega$, which rises to $191.7 \pm 43.2 \omega$ after 10 cycles. These charge transfer resistances are within the same margin of error as the reference electrodes, hence it can be assumed that the sodium oxalate sacrificial additive has not influenced the electrode kinetics. This change to the charge transfer resistance is the nominal increase of the material when subjected to these cycling parameters.

Electrodes containing the sacrificial coatings of sodium maleate and sodium succinate exhibit greater growth in the charge transfer resistance than the reference electrodes. Sodium maleate based electrodes demonstrate a value of $64.6 \pm 8.2 \Omega$, which increases to $325.4 \pm 99.0 \Omega$. For sodium succinate based electrodes the charge transfer resistance starts at a value of $43.7 \pm 5.2 \Omega$, which rises to a value of $279.5 \pm 87.1 \Omega$ after 10 cycles. These electrodes containing sodium succinate and sodium maleate similarly see increases in the values of their CEI resistances - $29.0 \pm 8.4 \Omega$ to $94.7 \pm 20.4 \Omega$ for sodium succinate and $45.6 \pm 18.4 \Omega$ to $157.2 \pm 76.7 \Omega$ for sodium maleate. This growth in the CEI resistance and gradual decline in the capacity of these cycles, despite being the most promising in terms of electrochemical performances, suggests a gradual blocking of pores and insertion sites. [108] While these electrodes have demonstrated a lower decline between the first to second cycle discharge capacities (Figure 7.9) than the reference electrodes, their capacity decline between the 2nd cycle and the 10th cycle (the cycles between the EIS measurements) is marginally larger than the reference electrode, despite

the additional sodium reservoir. For sodium maleate there is a discharge capacity loss between the 2nd and 10th cycle of 8.4 ± 3.2 mAh/g. This is a value of 8.3 ± 4.1 mAh/g for sodium succinate, and 8.1 ± 8.2 mAh/g. The larger increase of charge transfer resistance suggests a greater reduction in the electrode transfer kinetics after the 10th cycle.

The final electrodes, those containing sodium acetate, out of all the additives, show the smallest deviations to both their CEI and charge transfer resistances after 10 cycles. After formation the CEI resistance is $88.9 \pm 17.1 \Omega$, which increases to $109.7 \pm 12.7 \Omega$ after 10 cycles. For the charge transfer resistance, this increases from $5.2 \pm 2.7 \Omega$ to $26.9 \pm 8.0 \Omega$ after 10 cycles. It can therefore be suggested that the carboxylic groups of sodium acetate in the sacrificial additive have aided in the formation a very stable CEI, [267,268]. Similarly, it can be suggested that the sacrificial additive has reduced the increase of the charge transfer resistance, and hence stabilised the electrode kinetics over 10 cycles.

7.4.4 Summary

Table 7.2 shows a summary of the results collected during this chapter. This table should primarily be used as a reference table for comparisons of the sacrificial additives.

7.5 Conclusions

This research presented in this chapter sought to investigate the effects that sodium salts, forming sacrificial additives, had upon the properties of the electrode slurry and subsequently manufactured electrodes. The sacrificial additives studied were sodium salts of the organic acids tested in Chapter 6. Coatings were intended to be achieved through the milling of the active materials with the sodium salts, however no evidence was found to verify the presence of a coating.

The first objective and second objectives, the assessment and observation of the stabilisation of the electrode slurry gelation, were accomplished through the use of dissolution tests, oscillatory rheology, and fitting to Maxwell models. It was established

Table 7.2: Summary of effects to the electrode slurry and electrodes due to the sacrificial additives.

	Electrode Slurry Characterisation								Electrode Characterisation		
	After 40 minutes				After 90 Minutes				Adhesion		Electrode Conductivity ($S\ m^{-1}$)
	G'	G''	Loss Factor	Phase Angle (°)	G'	G''	Loss Factor	Phase Angle (°)	After 0 minutes	After 40 minutes	
Reference	218.3	50.1	4.4	16.4	2043.3	124.2	16.5	3.5	91.0	292.0	163.0
Sodium Acetate	78.5	11.7	6.7	8.6	427.7	71.5	6.0	8.2	24.5	35.5	202.0
Sodium Maleate	84.3	13.5	6.2	10.0	140.3	18.6	7.5	7.6	63.0	66.5	237.0
Sodium Oxalate	153.3	15.7	9.7	5.5	1030.3	144.6	7.1	5.5	89.9	64.5	292.0
Sodium Stearate	304.2	48.4	6.3	9.5	5280.0	336.3	15.7	3.6	73.6	44.0	2920.0
Sodium Succinate	66.7	20.9	3.2	17.8	2006.7	84.6	23.7	2.5	50.0	45.1	387.0

	Electrochemical Characterisation					
	Electrochemical Cycling		CEI Resistance		Charge Transfer Resistance	
	1st to 2nd Cycle Discharge Capacity Loss	20th Cycle Capacity	After Formation Cycle	After 10 Cycles	After Formation Cycle	After 10 Cycles
Reference	40.2	65.1	118.5	340.3	20.4	136.8
Sodium Acetate	17.0	84.9	88.9	109.7	5.2	26.9
Sodium Maleate	2.3	100.5	45.6	157.2	64.6	325.4
Sodium Oxalate	1.4	83.7	121.0	180.0	10.3	191.7
Sodium Stearate	13.4	88.1	98.7	42.0	67.6	154.0
Sodium Succinate	1.8	104.1	29.0	94.7	43.7	279.5

that confinement jamming was a consistent issue for all electrode slurries containing sacrificial additives. These electrode slurries showed a fast frequency convergence in G' and a slower convergence in G'' and high secondary relaxation times. Out of the sacrificial additives, sodium maleate proved to be the most beneficial to the stabilisation of the electrode slurries as it retained low slurry rigidity and strengths over the course of oscillatory measurements. However, changes to the coater speed and stress applied are suggested to overcome the solid particle confinement for facile electrode manufacture.

The third objective, the measurement of the effect of the sacrificial additives on the properties of the electrodes, was achieved through the use of adhesion and conductivity measurements. The addition of the sacrificial additives proved to cause a marginal reduction in the adhesion strength of the electrode over the reference electrode, with only slight difference between the sodium salts. Similarly, only marginal differences in the electrode conductivity were established for the different sodium salts, with the exception of sodium stearate. For electrodes coated after 40 minutes, unlike the reference electrodes, there was very little change in the adhesion strength for those that contain the sacrificial additives, reinforcing the notion of gelation stabilisation.

The fourth and final objective of this research chapter, the assessment of the improvement to the electrochemical performance of the active material, was accomplished through the use of electrochemical cycling and EIS measurements. Of the different sacrificial additives, sodium maleate and sodium succinate proved to be the most beneficial to the electrochemical performance.

Ultimately, due to the electrochemical performance and the reductions to the electrode slurry gelation, facilitating electrode manufacture, sodium maleate is suggested as the most optimal of those sacrificial additives tested. However, further testing is required to optimise the quantity of sodium maleate whereby the electrochemical benefits are ensured and the confinement jamming is minimised.

Chapter 8

Conclusions and Future Work

Gelation leading to difficulties in coating PVDF and NMP electrode slurries is widespread and affects many materials, especially high nickel content layered O₃ sodium-ion cathode materials. A review of established literature before this PhD, demonstrated a significant lack of research into the specific gelation mechanism of high nickel content layered lithium ion cathode materials, and even less research into the mechanism of the similar sodium ion layered O₃ oxides. This PhD sought to investigate the gelation mechanism, partially through the development of a novel characterisation technique, and then to examine methods of stabilising this mechanism.

The first research objective, explored in Chapter 4, was the elucidation and examination of the specific gelation mechanism that occurs in sodium ion layered O₃ oxide electrode slurries, and was tackled through a material, electrode slurry, and electrode analysis approach. Through the formation of NaOH on the active material, the three-stage gelation process and presence of C=C in the electrode slurry, and presence of NaF on the uncycled electrodes, it has been established that a dehydrofluorination reaction of the PVDF, followed by a cross-linking causes a non-reversible chemical gelation of the slurry. Electrochemical testing in sodium-metal anode half-cells with coatings produced 0, 20, and 40 minutes after mixing showed limited initial capacity differences, however, after 50 cycles, an increased capacity

decline was observed for electrodes coated after 40 minutes of mixing. Due to the rheological characterisation of the electrode slurry and the electrochemical analysis, a maximum processing window of 20 minutes has been established for electrode slurries containing these materials and analogous materials.

As explored in the literature review, research into this mechanism would be highly beneficial to the industry (as stated by Seong *et al.*, 2020 [102]), not only for sodium ion layered O3 oxides but, due to the structural and material similarities, this research would also be beneficial to lithium ion high nickelate based cathodes. The identification and demonstration of the dehydrofluorination reaction due to the formation of hydroxides enables researchers and manufacturers to develop counter measures to these issues. These counter measures could be classified between a materials stabilisation, preventing or removing the formation of hydroxides, or through an electrode slurry stabilisation. As these problems have been highlighted for both sodium ion electrode slurries and lithium ion electrode slurries, this PhD presents a highly beneficial study to a large range of analogous materials.

The identification of the three-stage gelation process, and the recognition of a maximum processing window was made possible through the development of the novel oscillatory rheological characterisation method. The second objective of this research, examined in Chapter 5, was the development of a non-destructive, non-interfering analysis technique to assess the gelation and structure of rechargeable battery electrode slurries. The development of this method explored trial characterisation techniques of both rotational and oscillatory rheology methods, before the final method of multiple rapid frequency sweeps and Maxwell mode fitting was established.

Many of the analysis benefits of this method follow as a direct result of the range of data that can be quantified in rapid increments over a nominal characterisation window. The use of rapid scans enables the characterisation of processes that occur in an electrode slurry over timescales of as little as 5 minutes. Although, depending on the frequency range required by researchers this minimum timescale can be reduced. Furthermore, as

this technique scans across different frequencies, the analysis of multiple electrode slurry jamming mechanisms can be made, many of these have been observed across this PhD. As a demonstration, using this method, confinement jamming has been characterised in Chapter 7, a retention of particles in the electrode slurry (no sedimentation occurring) was demonstrated in Chapter 6, and the gelling of electrode slurries was monitored and analysed throughout.

Chapters 6 and 7 have utilised the findings of Chapters 4 and 5 to explore ways of stabilising the electrode slurry gelation. Chapter 6 had the objective of investigating the prevention or reduction of this gelation mechanism. The stabilisation of the electrode slurry gelation mechanism was approached through the addition of organic acids to the electrode slurry. Additives of acetic and maleic acid were demonstrated to be the most effective. These additives showed very little change in the relaxation time over the entire characterisation window of 90 minutes, although the increases to the rigidities of the electrode slurry gels demonstrated that a full stabilisation had not been reached. It is likely that the shape of the micelles formed greatly affects the stabilisation performance. Through an approximation of the micelle critical packing parameters, acetic acid (1.01) and maleic acid (1.32) are predicted to produce inverse micelles due to C_{PP} values greater than 1. However, electrodes formed with these additives had poor electrochemical performance, likely due to reactions of the active materials with air, removing sodium and forming resistive inorganics. Therefore, replacing these additives with ones that can preferentially react over the NaNMST active material is suggested, hence the motivation for Chapter 7.

Chapter 7 aimed to explore the improvement to the electrochemical performance of the active material, while maintaining the stability of electrode slurry. Sodium salts of the acids tested in Chapter 6 were intended to be sacrificially coated onto the active materials. Continuing the trend of Chapter 6, sacrificial additives of sodium maleate and sodium acetate demonstrated the greatest stabilisation to the electrode slurry gelation. Sodium maleate was overall the most beneficial additive as it

additionally showed significant improvements to the electrochemical performance of these cells.

Ultimately, the most substantial contributions from this work are: the identification of the electrode slurry gelation mechanism (Chapter 4), the development of the method used to characterise and analyse these electrode slurries (Chapter 5), and the identification of the additive sodium maleate (Chapter 7), due to its combined improvements to the electrode slurry stabilisation and electrochemical performance. From an industry standpoint, the findings in these first two contributions (Chapters 4 and 5) are extremely useful and can be utilised in many ways. The other main contribution, however, is less relevant to industry use, as sodium maleate does not fully stabilise the electrode slurry gelation, and, therefore, would not be sufficient for large scale manufacturing. At a lab scale, however, the research benefits of the stabilisation studies of Chapters 6 and 7, along with the findings in Chapters 4 and 5, should be evident, and these partially stabilising additives will unquestionably enable research and exploration into electrode materials that are more air sensitive and would otherwise be unfeasible.

8.1 Future Work

However, there have been some issues and limitations in this PhD. For all the sacrificial coatings explored in Chapter 7, despite demonstrating stabilisations to the electrode slurry, additions of these materials have introduced a new electrode slurry processing problem, confinement jamming. This confinement jamming, explored in Chapter 2, is a physical gel effect whereby the movement of particles is prevented due to the confinement of surrounding particles. It has been theorised that a reduction to the quantity of sacrificial coating (2.0 wt% was tested) could reduce the jamming effects of these additives. Therefore, a future optimisation between the electrode slurry stabilisation and the electrochemical performance, and the confinement jamming effects

is recommended, with an optimal quantity, x , expected to be $0.0 \text{ wt}\% < x < 2.0 \text{ wt}\%$.

Another limitation was introduced due to the loss of samples and the time restrictions created by the COVID-19 pandemic. Across the additives tested in Chapters 6 and 7, the electrochemical testing of electrodes coated 20 and 40 minutes after mixing would be of particular interest and would further aid in the conclusive identification of the optimal additive. Furthermore, all the electrochemical testing was performed in half-cell configurations, where there is an excess of sodium ions present. Electrochemical testing in full cells, where the sodium quantities are limited, would allow a further differentiation between additives, especially in situations where sodium is extracted from the active material. These areas create valuable future work in this area.

Ultimately, this work has developed methods to understand the origins of the instability of high nickel content sodium cathode materials, and has developed rheological tools to study the time dependency and stability of the slurries for coating electrodes. Different methods to stabilise the electrode slurries have been proposed using organic acids or their sodium salts, and the effect upon the electrochemical properties discussed. These methods and tools, although developed for sodium ion will, no doubt, be relevant for other battery types, such as lithium-ion, and will serve as a valuable resource for any future research pertaining to electrode slurry manufacture and processing.

Appendix A

FTIR Peak Fitting Procedure

FTIR peak fitting was performed using the Fityk software. A linear baseline and Voigt curved profile were used to fit under the C=O peaks.

The choice between the fitting profiles falls between Gaussian, Lorentzian, Gaussian-Lorentzian (G-L), and Voigt. The Gaussian profile works well for solid samples, powders, gels or resins. The Lorentzian profile works best for gases, but can also fit liquids in many cases. The best functions for liquids are the combined G-L function or the Voigt profile. The Voigt profile is similar to the G-L, where it is comprised of Gaussian profiles and Lorentzian profiles. However, in the Voigt profile the line width, Δx , of the Gaussian and Lorentzian components are able to be independently varied. Ultimately the Voigt profile was chosen, to enable the flexibility between the gel fitting of Gaussian, and the liquid fitting of Lorentzian (required for the electrode slurries, which transform from a liquid to a gel). [326, 327]

Several different baseline were investigated for this fitting procedure, including: two types of linear baselines (one consisting of two points and one with extra points, forming edges), a cubic spline, a convex hull, and no baseline at all.

Fitting the FTIR data without a baseline, as demonstrated in Figure A.1 was considered unsatisfactory as the resultant fit, regardless of the number of peaks, produced a prioritised peak with an unfeasible FWHM for this region of IR, Figure A.1.

Furthermore, due to peaks on either side of the target region, more notably on the lower frequency side – several peaks lie at 1500 cm^{-1} , this has caused the data to appear increased on one side, hence the need for a baseline.

A curved baseline – cubic spline (expand) - Figure A.2 - initially appeared as the most appropriate, as at the extremities of the region, where data was not expected, the data seemed to adhere well to this structure of baseline. However, there was a strong risk that this cubic spline baseline was fitting potential peaks, or hiding peaks, especially at approximately 1725 cm^{-1} , whereby there is evidence of a small peak, as can be seen in figure A.2.

An alternative method of baseline fitting would be to use a convex hull, Figure A.3, able to be simply fit based on the extremities of the region, and as such, enabled the removal of human bias, however, this method of baseline fitting shares similarities with the curved baseline, and, hence, has the risk of hiding or obscuring peaks. Hence, it proved sensible to examine linear baselines as well.

Using a linear baseline, with extra points to fit better to the edge cases, as seen in Figure A.4, allows sensible peaks to be fitted in the targeted area. However, similar to using a cubic spline, it proved difficult to remove bias when fitting a baseline to this data.

Ultimately it was decided to use a straight linear baseline, consisting of two points, at 1750 cm^{-1} and 1550 cm^{-1} , as can be seen in Figure A.5.

Four Voigt peaks were then fitted using the Fityk software, as this number of peaks gave the fitting with the lowest error, without necessary repeated wavenumbers or unfeasible full-width-half-maximums (FWHMs).

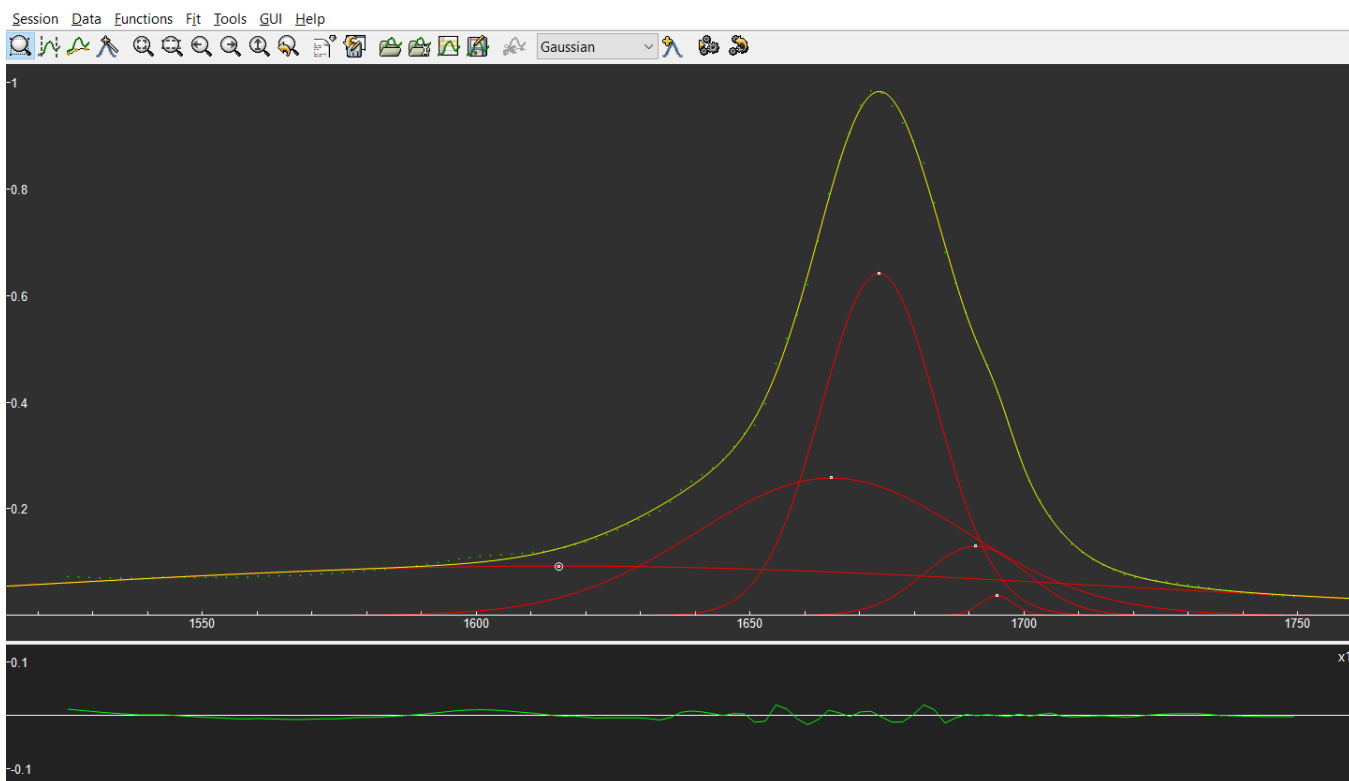


Figure A.1: FTIR Peak Fitting with No Baseline

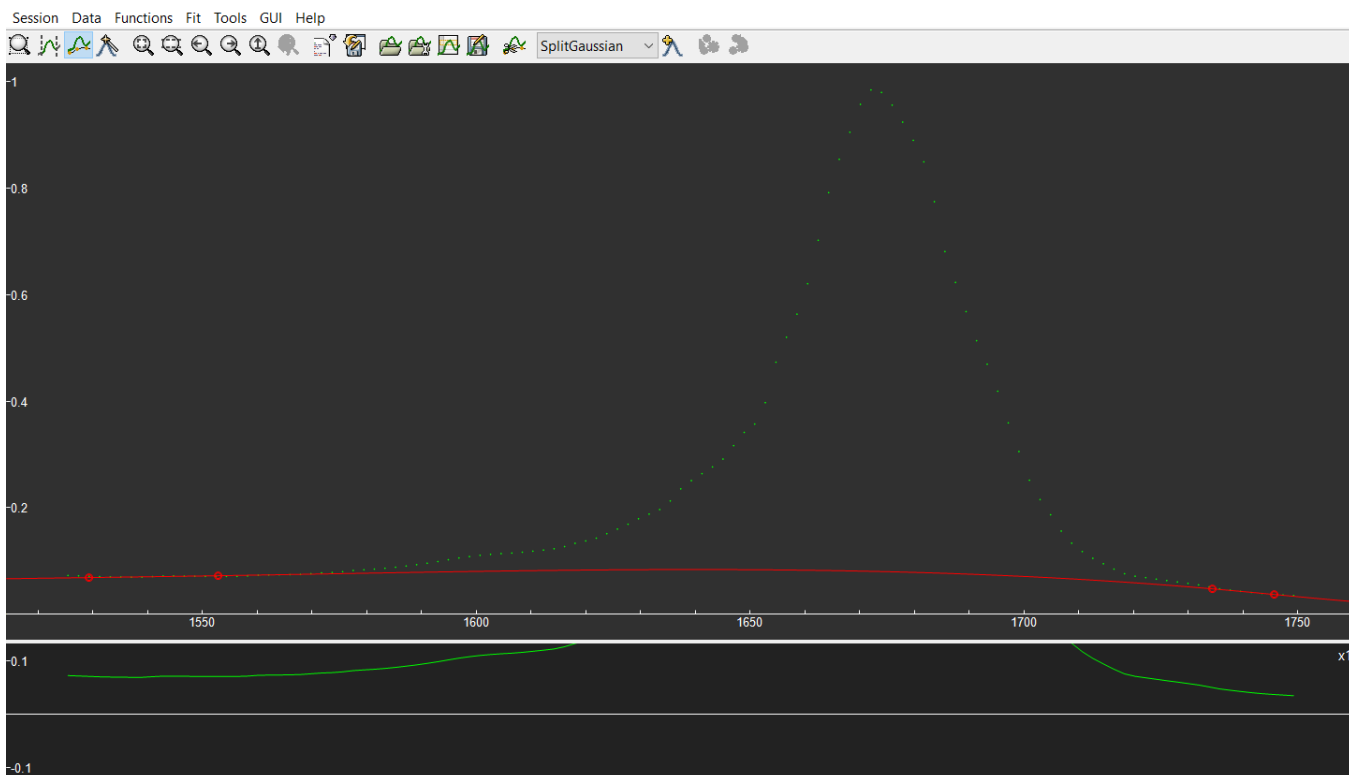


Figure A.2: FTIR Peak Fitting - Cubic Spline Baseline

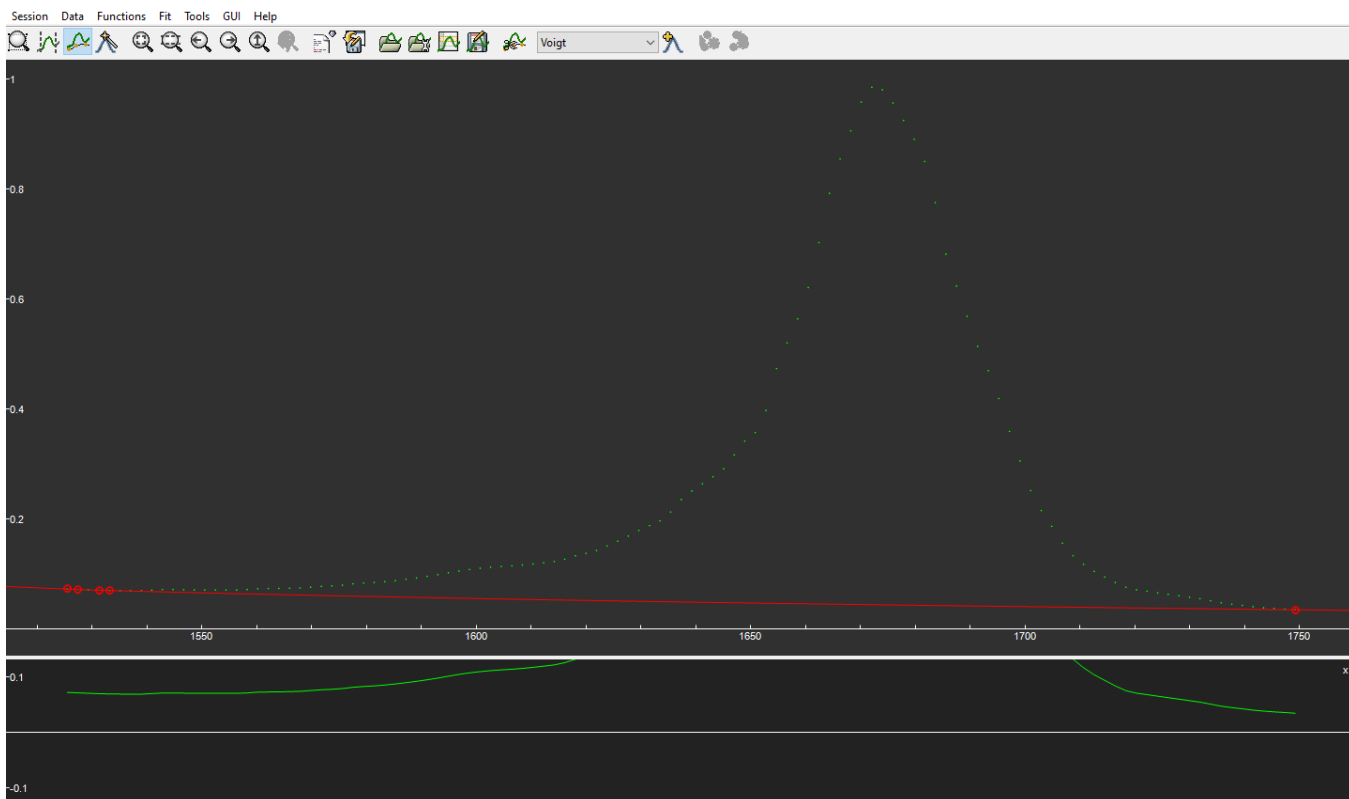


Figure A.3: FTIR Peak Fitting - Convex Hull Baseline



Figure A.4: FTIR Peak Fitting - Linear Baseline with additional edge points

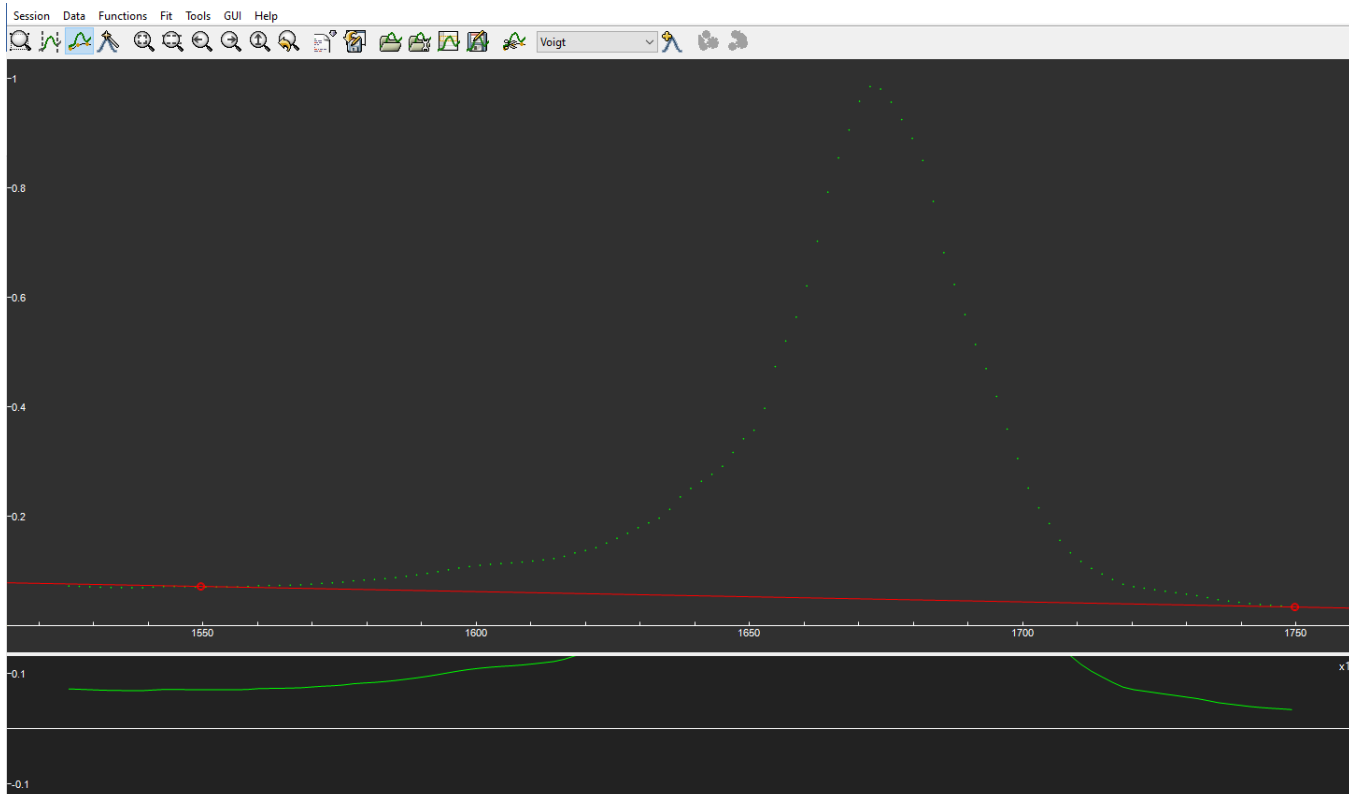


Figure A.5: FTIR Peak Fitting - Straight, Linear Baseline

Appendix B

Rotational Rheology

B.1 Shear ramp with rest intervals

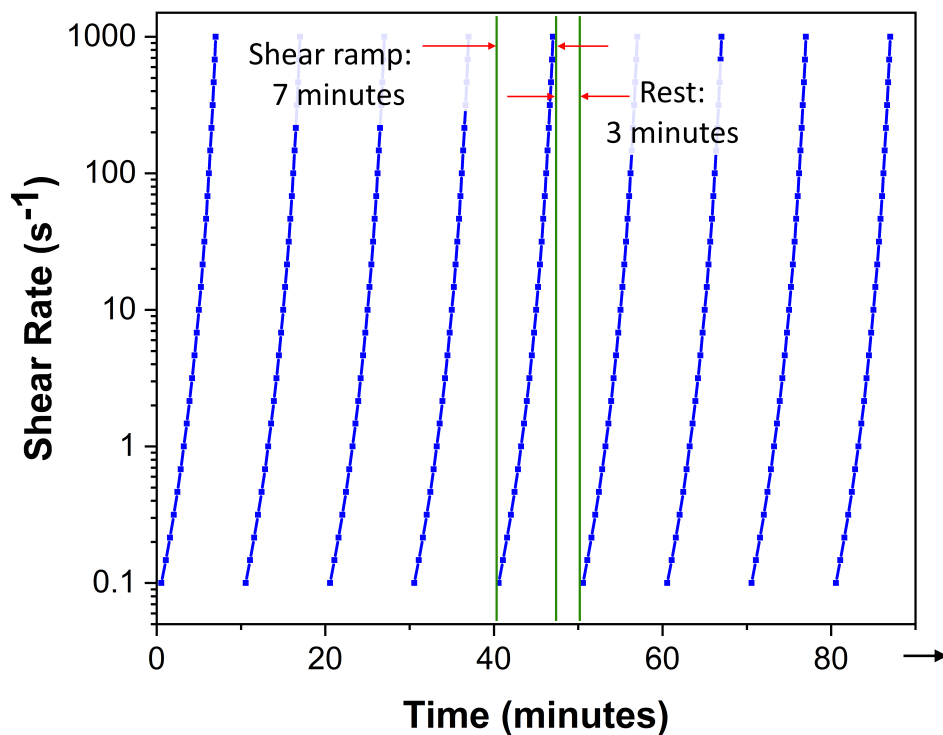


Figure B.1: Shear ramp with rest intervals.

B.2 Constant shear rate with shear ramps

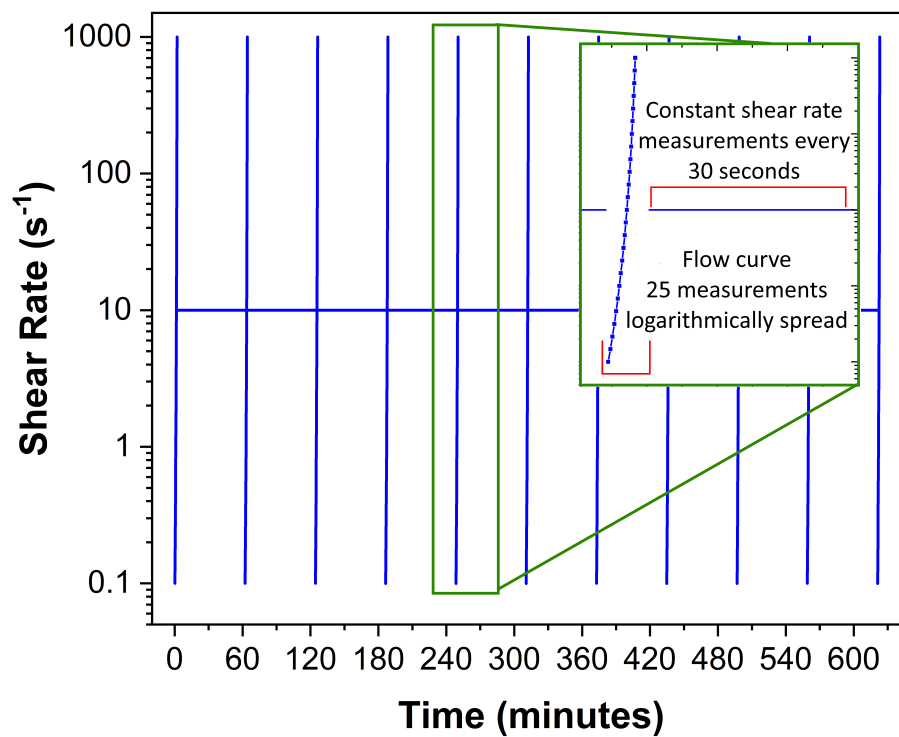


Figure B.2: Constant shear rate with shear ramps.

References

- [1] Q. Li, J. Chen, L. Fan, X. Kong, and Y. Lu, “Progress in electrolytes for rechargeable Li-based batteries and beyond,” *Green Energy & Environment*, vol. 1, no. 1, pp. 18–42, 2016.
- [2] Y. Wang, R. Chen, T. Chen, H. Lv, G. Zhu, L. Ma, C. Wang, Z. Jin, and J. Liu, “Emerging non-lithium ion batteries,” *Energy Storage Materials*, vol. 4, pp. 103–129, 2016.
- [3] Q. Wang, C. Zhao, Y. Lu, Y. Li, Y. Zheng, Y. Qi, X. Rong, L. Jiang, X. Qi, Y. Shao, D. Pan, B. Li, Y. S. Hu, and L. Chen, “Advanced Nanostructured Anode Materials for Sodium-Ion Batteries,” *Small*, vol. 13, no. 42, pp. 1–32, 2017.
- [4] S. Mariyappan, Q. Wang, and J. M. Tarascon, “Will sodium layered oxides ever be competitive for sodium ion battery applications?,” *Journal of the Electrochemical Society*, vol. 165, no. 16, pp. A3714–A3722, 2018.
- [5] M. I. Jamesh and A. Prakash, “Advancement of technology towards developing Na-ion batteries,” *Journal of Power Sources*, vol. 378, no. October 2017, pp. 268–300, 2018.
- [6] J. Darga, J. Lamb, and A. Manthiram, “Industrialization of Layered Oxide Cathodes for Lithium-Ion and Sodium-Ion Batteries: A Comparative Perspective,” *Energy Technology*, vol. 8, no. 12, p. 2000723, 2020.
- [7] M. S. Whittingham, “Lithium batteries and cathode materials,” *Chemical Reviews*, vol. 104, no. 10, pp. 4271–4301, 2004.
- [8] E. Irisarri, A. Ponrouch, and M. R. Palacin, “Review—Hard Carbon Negative Electrode Materials for Sodium-Ion Batteries,” *Journal of The Electrochemical Society*, vol. 162, no. 14, pp. A2476–A2482, 2015.
- [9] N. Tapia-Ruiz, A. R. Armstrong, H. Alptekin, M. A. Amores, H. Au, J. Barker, R. Boston, W. R. Brant, J. M. Brittain, Y. Chen, M. Chhowalla, Y.-s. Choi, S. I. R. Costa, M. C. Ribadeneyra, S. A. M. Dickson, E. I. Eweka, J. D. Forero-saboya, C. P. Grey, Z. Li, S. F. L. Mertens, R. Mogensen, L. Monconduit, D. M. C. Ould, R. G. Palgrave, P. Poizot, A. Ponrouch, S. Renault, E. M. Reynolds, A. Rudola, R. Sayers, D. O. Scanlon, S. Sen, V. R. Seymour, B. Silv, G. S. Stone, C. I. Thomas, M.-m. Titirici, J. Tong, T. J. Wood, D. S. Wright, and R. Younesi, “2021 roadmap for sodium-ion batteries,” *Journal of Physics: Energy*, vol. 3, p. 031503, 2021.

- [10] Y. Zheng, Y. Wang, Y. Lu, Y. S. Hu, and J. Li, "A high-performance sodium-ion battery enhanced by macadamia shell derived hard carbon anode," *Nano Energy*, vol. 39, no. June, pp. 489–498, 2017.
- [11] B. Scrosati and J. Garche, "Lithium batteries: Status, prospects and future," *Journal of Power Sources*, vol. 195, no. 9, pp. 2419–2430, 2010.
- [12] M. A. Munoz-Marquez, D. Saurel, J. L. Gomez-Camer, M. Casas-Cabanas, E. Castillo-Martinez, and T. Rojo, "Na-Ion Batteries for Large Scale Applications: A Review on Anode Materials and Solid Electrolyte Interphase Formation," *Advanced Energy Materials*, vol. 7, no. 20, pp. 1–31, 2017.
- [13] Y. Liang, W.-H. Lai, Z. Miao, and S.-L. Chou, "Nanocomposite Materials for the Sodium-Ion Battery: A Review," *Small*, vol. 14, no. 5, p. 1702514, 2017.
- [14] S. Roberts and E. Kendrick, "The re-emergence of sodium ion batteries: Testing, processing, and manufacturability," *Nanotechnology, Science and Applications*, vol. 11, pp. 23–33, 2018.
- [15] H. Wang, M. Gu, J. Jiang, C. Lai, and X. Ai, "An O3-type $\text{NaNi}_{0.5}\text{Mn}_{0.3}\text{Ti}_{0.2}\text{O}_2$ compound as new cathode material for room-temperature sodium-ion batteries," *Journal of Power Sources*, vol. 327, pp. 653–657, 2016.
- [16] I. Wolfram Research, "Mathematica - Version 13.0.0," [Online] <https://www.wolfram.com/mathematica> [Accessed: 01-06-2022], 2022.
- [17] Z. Dai, U. Mani, H. T. Tan, and Q. Yan, "Advanced Cathode Materials for Sodium-Ion Batteries: What Determines Our Choices?," *Small Methods*, vol. 1, no. 5, p. 1700098, 2017.
- [18] A. Rudola, A. J. Rennie, R. Heap, S. S. Meysami, A. Lowbridge, F. Mazzali, R. Sayers, C. J. Wright, and J. Barker, "Commercialisation of high energy density sodium-ion batteries: Faradion's journey and outlook," *Journal of Materials Chemistry A*, vol. 9, no. 13, pp. 8279–8302, 2021.
- [19] C. Vaalma, D. Buchholz, M. Weil, and S. Passerini, "A cost and resource analysis of sodium-ion batteries," *Nature Reviews Materials*, vol. 3, no. 1, p. 18013, 2018.
- [20] M. J. Aragón, P. Lavela, G. Ortiz, R. Alcántara, and J. L. Tirado, "Nanometric $\text{P}_2\text{-Na}_{2/3}\text{Fe}_{1/3}\text{Mn}_{2/3}\text{O}_2$ with controlled morphology as cathode for sodium-ion batteries," *Journal of Alloys and Compounds*, vol. 724, pp. 465–473, 2017.
- [21] A. Abouimrane, W. Weng, H. Eltayeb, Y. Cui, J. Niklas, O. Poluektov, and K. Amine, "Sodium insertion in carboxylate based materials and their application in 3.6 V full sodium cells," *Energy & Environmental Science*, vol. 5, no. 11, p. 9632, 2012.
- [22] I. Hasa, S. Passerini, and J. Hassoun, "A rechargeable sodium-ion battery using a nanostructured Sb-C anode and P2-type layered $\text{Na}_{0.6}\text{Ni}_{0.22}\text{Fe}_{0.11}\text{Mn}_{0.66}\text{O}_2$ cathode," *RSC Advances*, vol. 5, no. 60, pp. 48928–48934, 2015.

- [23] M. Kouthaman, K. Kannan, P. Arjunan, T. Meenatchi, R. Subadevi, and M. Sivakumar, "Novel layered O₃-NaFe_{0.45}Co_{0.45}Ti_{0.10}O₂ cathode material for sodium batteries," *Materials Letters*, vol. 276, p. 128181, 2020.
- [24] I. Moez, D. Susanto, G. Ali, H. G. Jung, H. D. Lim, and K. Y. Chung, "Effect of the interfacial protective layer on the NaFe_{0.5}Ni_{0.5}O₂ cathode for rechargeable sodium-ion batteries," *Journal of Materials Chemistry A*, vol. 8, no. 28, pp. 13964–13970, 2020.
- [25] S. Demirel, E. Oz, E. Altin, S. Altin, A. Bayri, P. Kaya, S. Turan, and S. Avci, "Growth mechanism and magnetic and electrochemical properties of Na_{0.44}MnO₂ nanorods as cathode material for Na-ion batteries," *Materials Characterization*, vol. 105, pp. 104–112, 2015.
- [26] Z. Jian, L. Zhao, H. Pan, Y. S. Hu, H. Li, W. Chen, and L. Chen, "Carbon coated Na₃V₂(PO₄)₃ as novel electrode material for sodium ion batteries," *Electrochemistry Communications*, vol. 14, no. 1, pp. 86–89, 2012.
- [27] W. Tang, R. Liang, D. Li, Q. Yu, J. Hu, B. Cao, and C. Fan, "Highly Stable and High Rate-Performance Na-Ion Batteries Using Polyanionic Anthraquinone as the Organic Cathode," *ChemSusChem*, vol. 12, no. 10, pp. 2181–2185, 2019.
- [28] Y. Liu, G. Wei, M. Ma, and Y. Qiao, "Role of Acid in Tailoring Prussian Blue as Cathode for High-Performance Sodium-Ion Battery," *Chemistry - A European Journal*, vol. 23, no. 63, pp. 15991–15996, 2017.
- [29] H. Ye, Y. Wang, F. Zhao, W. Huang, N. Han, J. Zhou, M. Zeng, and Y. Li, "Iron-based sodium-ion full batteries," *Journal of Materials Chemistry A*, vol. 4, no. 5, pp. 1754–1761, 2016.
- [30] Q. Wang, S. Chu, and S. Guo, "Progress on multiphase layered transition metal oxide cathodes of sodium ion batteries," *Chinese Chemical Letters*, vol. 31, no. 9, pp. 2167–2176, 2020.
- [31] E. Kendrick, R. Gruar, M. Nishijima, H. Mizuhata, T. Otani, I. Asako, and Y. Mimura, "Tin Containing Compounds," *WO 2015177568 A1*, pp. 1–89, 2015.
- [32] M. H. Han, E. Gonzalo, G. Singh, and T. Rojo, "A comprehensive review of sodium layered oxides: powerful cathodes for Na-ion batteries," *Energy & Environmental Science*, vol. 8, no. 1, pp. 81–102, 2015.
- [33] J. Xu, E. Hu, D. Nordlund, A. Mehta, S. N. Ehrlich, X.-q. Yang, and W. Tong, "Understanding the Degradation Mechanism of Lithium Nickel Oxide Cathodes for Li-Ion Batteries," *ACS Applied Materials & Interfaces*, vol. 8, pp. 31677–31683, 2016.
- [34] J.-Y. Hwang, S.-T. Myung, J. U. Choi, C. S. Yoon, H. Yashiro, and Y.-K. Sun, "Resolving the degradation pathways of the O₃-type layered oxide cathode surface through the nano-scale aluminum oxide coating for high-energy density sodium-ion batteries," *Journal of Materials Chemistry A*, vol. 5, no. 45, pp. 23671–23680, 2017.

- [35] J.-Y. Hwang, S.-T. Myung, J. U. Choi, C. S. Yoon, H. Yashiro, and Y.-K. Sun, "Resolving the degradation pathways on O3-type layered oxides cathode surface through the nano-scale aluminum oxide coating for high-energy density sodium-ion batteries," *J. Mater. Chem. A*, vol. 5, pp. 23671–23680, 2017.
- [36] M. Biso, R. Colombo, M.-J. Uddin, M. Stanga, and S.-J. Cho, "A Rheological Behavior of Various Polyvinylidene Difluoride Binders for High Capacity LiNi_{0.6}Mn_{0.2}Co_{0.2}O₂," *Engineering*, vol. 47, pp. 21–25, 2007.
- [37] J. E. Marshall, A. Zhenova, S. Roberts, T. Petchey, P. Zhu, C. E. Dancer, C. R. McElroy, E. Kendrick, and V. Goodship, "On the solubility and stability of polyvinylidene fluoride," *Polymers*, vol. 13, no. 9, pp. 1–31, 2021.
- [38] S. Roberts, L. Chen, B. Kishore, C. E. Dancer, M. J. Simmons, and E. Kendrick, "Mechanism of gelation in high nickel content cathode slurries for sodium-ion batteries," *Journal of Colloid and Interface Science*, vol. 627, pp. 427–437, 2022.
- [39] K. Kubota, M. Dahbi, T. Hosaka, S. Kumakura, and S. Komaba, "Towards K-Ion and Na-Ion Batteries as - "Beyond Li-Ion"," *The Chemical Record*, vol. 18, no. 4, pp. 459–479, 2018.
- [40] P. Atkins and J. de Paula, *Physical Chemistry for the Life Sciences*. New York: W. H. Freeman and Company, 2006.
- [41] X. Yang and A. L. Rogach, "Electrochemical Techniques in Battery Research: A Tutorial for Nonelectrochemists," *Advanced Energy Materials*, vol. 9, no. 25, pp. 1–10, 2019.
- [42] W. M. Haynes, *CRC Handbook of Chemistry and Physics*. CRC Handbook of Chemistry and Physics, Boca Raton, Florida, United States: CRC Press, 92nd ed., 2011.
- [43] E. Gabriel, D. Hou, E. Lee, and H. Xiong, "Multiphase layered transition metal oxide positive electrodes for sodium ion batteries," *Energy Science & Engineering*, vol. 10, no. 5, pp. 1–34, 2022.
- [44] K. M. Abraham, "How Comparable Are Sodium-Ion Batteries to Lithium-Ion Counterparts?," *ACS Energy Letters*, vol. 5, no. 11, pp. 3544–3547, 2020.
- [45] L. Liu, J. Zhu, and L. Zheng, "An Effective Method for Estimating State of Charge of Lithium-Ion Batteries Based on an Electrochemical Model and Nernst Equation," *IEEE Access*, vol. 8, pp. 211738–211749, 2020.
- [46] M. S. Dresselhaus and G. Dresselhaus, "Intercalation compounds of graphite," *Advances in Physics*, vol. 30, no. 2, pp. 139–326, 1981.
- [47] H. Moon, R. Tatara, T. Mandai, K. Ueno, K. Yoshida, N. Tachikawa, T. Yasuda, K. Dokko, and M. Watanabe, "Mechanism of Li ion desolvation at the interface of graphite electrode and glyme-li salt solvate ionic liquids," *Journal of Physical Chemistry C*, vol. 118, no. 35, pp. 20246–20256, 2014.

- [48] M. S. Whittingham, "Chemistry of intercalation compounds: Metal guests in chalcogenide hosts," *Progress in Solid State Chemistry*, vol. 12, no. 1, pp. 41–99, 1978.
- [49] T. Jacobsen, K. West, and S. Atlung, "Electrostatic Interactions During Intercalation of Li in Li_xTiS_2 ," *Electrochimica Acta*, vol. 27, no. 8, pp. 1007–1011, 1982.
- [50] M. Hahn, H. Buqa, P. W. Ruch, D. Goers, M. E. Spahr, J. Ufheil, P. Novak, and R. Kotz, "A Dilatometric Study of Lithium Intercalation into Powder-Type Graphite Electrodes," *Electrochemical and Solid-State Letters*, vol. 11, no. 9, p. A151, 2008.
- [51] S. Takeuchi, S. Yano, T. Fukutsuka, K. Miyazaki, and T. Abe, "Electrochemical Intercalation/De-Intercalation of Lithium Ions at Graphite Negative Electrode in TMP-Based Electrolyte Solution," *Journal of the Electrochemical Society*, vol. 159, no. 12, pp. A2089–A2091, 2012.
- [52] S. Takeuchi, R. Kokumai, S. Nagata, T. Fukutsuka, K. Miyazaki, and T. Abe, "Effect of the Addition of Bivalent Ions on Electrochemical Lithium-Ion Intercalation at Graphite Electrodes," *Journal of The Electrochemical Society*, vol. 163, no. 8, pp. A1693–A1696, 2016.
- [53] B. Jache, J. O. Binder, T. Abe, and P. Adelhelm, "A comparative study on the impact of different glymes and their derivatives as electrolyte solvents for graphite co-intercalation electrodes in lithium-ion and sodium-ion batteries," *Phys. Chem. Chem. Phys.*, vol. 18, no. 21, pp. 14299–14316, 2016.
- [54] H.-Y. Song, T. Fukutsuka, K. Miyazaki, and T. Abe, "Suppression of Co-Intercalation Reaction of Propylene Carbonate and Lithium Ion into Graphite Negative Electrode by Addition of Diglyme," *Journal of The Electrochemical Society*, vol. 163, no. 7, pp. A1265–A1269, 2016.
- [55] C. Marino, M. El Kazzi, E. J. Berg, M. He, and C. Villevieille, "Interface and Safety Properties of Phosphorus-Based Negative Electrodes in Li-Ion Batteries," *Chemistry of Materials*, vol. 29, no. 17, pp. 7151–7158, 2017.
- [56] G. Zhao, L. Zhang, C. Li, H. Huang, X. Sun, and K. Sun, "A practical Li ion battery anode material with high gravimetric/volumetric capacities based on $\text{T-Nb}_2\text{O}_5$ /graphite composite," *Chemical Engineering Journal*, vol. 328, pp. 844–852, 2017.
- [57] W. Wang, S. Wang, H. Jiao, P. Zhan, and S. Jiao, "A sodium ion intercalation material: A comparative study of amorphous and crystalline FePO_4 ," *Physical Chemistry Chemical Physics*, vol. 17, no. 6, pp. 4551–4557, 2015.
- [58] Y. K. Sun, "Direction for Commercialization of O3-Type Layered Cathodes for Sodium-Ion Batteries," *ACS Energy Letters*, vol. 5, no. 4, pp. 1278–1280, 2020.

- [59] K. Morimoto, T. Kusumoto, K. Nishioka, K. Kamiya, Y. Mukoyama, and S. Nakanishi, "Dynamic Changes in Charge Transfer Resistances during Cycling of Aprotic Li-O₂Batteries," *ACS Applied Materials and Interfaces*, vol. 12, no. 38, pp. 42803–42810, 2020.
- [60] B. Anothumakkool, N. Dupré, P. Moreau, D. Guyomard, T. Brousse, and J. Gaubicher, "Peculiar Li-storage mechanism at graphene edges in turbostratic carbon black and their application in high energy Li-ion capacitor," *Journal of Power Sources*, vol. 378, no. January, pp. 628–635, 2018.
- [61] M. Z. Bazant, "Theory of chemical kinetics and charge transfer based on nonequilibrium thermodynamics," *Accounts of Chemical Research*, vol. 46, no. 5, pp. 1144–1160, 2013.
- [62] I. V. Thorat, D. E. Stephenson, N. A. Zacharias, K. Zaghbi, J. N. Harb, and D. R. Wheeler, "Quantifying tortuosity in porous Li-ion battery materials," *Journal of Power Sources*, vol. 188, no. 2, pp. 592–600, 2009.
- [63] F. Torabi and P. Ahmadi, "Chapter 2 - Fundamentals of batteries," in *Simulation of Battery Systems* (F. Torabi and P. Ahmadi, eds.), pp. 55–81, Academic Press, 2020.
- [64] J.-Y. Hwang, S.-T. Myung, and Y.-K. Sun, "Sodium-ion batteries: present and future," *Chemical Society Reviews*, vol. 46, no. 12, pp. 3529–3614, 2017.
- [65] J. W. Fergus, "Recent developments in cathode materials for lithium ion batteries," *Journal of Power Sources*, vol. 195, no. 4, pp. 939–954, 2010.
- [66] L. Bao, L. Li, G. Xu, J. Wang, R. Zhao, G. Shen, G. Han, and S. Zhou, "Olivine LiFePO₄ nanocrystallites embedded in carbon-coating matrix for high power Li-ion batteries," *Electrochimica Acta*, vol. 222, pp. 685–692, 2016.
- [67] P. Axmann, C. Stinner, M. Wohlfahrt-Mehrens, A. Mauger, F. Gendron, and C. M. Julien, "Nonstoichiometric LiFePO₄: Defects and related properties," *Chemistry of Materials*, vol. 21, no. 8, pp. 1636–1644, 2009.
- [68] J. Chen, M. J. Vacchio, S. Wang, N. Chernova, P. Y. Zavalij, and M. S. Whittingham, "The hydrothermal synthesis and characterization of olivines and related compounds for electrochemical applications," *Solid State Ionics*, vol. 178, no. 31-32, pp. 1676–1693, 2008.
- [69] J. Maier and R. Amin, "Defect Chemistry of LiFePO₄," *Journal of The Electrochemical Society*, vol. 155, no. 4, p. A339, 2008.
- [70] R. M. Gao, Z. J. Zheng, P. F. Wang, C. Y. Wang, H. Ye, and F. F. Cao, "Recent advances and prospects of layered transition metal oxide cathodes for sodium-ion batteries," *Energy Storage Materials*, vol. 30, no. May, pp. 9–26, 2020.
- [71] J. K. Kim, Y. J. Lim, H. Kim, G. B. Cho, and Y. Kim, "A hybrid solid electrolyte for flexible solid-state sodium batteries," *Energy and Environmental Science*, vol. 8, no. 12, pp. 3589–3596, 2015.

- [72] A. M. Skundin, T. L. Kulova, and A. B. Yaroslavtsev, “Sodium-Ion Batteries (a Review),” *Russian Journal of Electrochemistry*, vol. 54, no. 2, pp. 113–152, 2018.
- [73] M. Pasta, C. D. Wessells, N. Liu, J. Nelson, M. T. McDowell, R. A. Huggins, M. F. Toney, and Y. Cui, “Full open-framework batteries for stationary energy storage,” *Nature Communications*, vol. 5, pp. 1–9, 2014.
- [74] J. Zhang, D. Zhang, F. Niu, X. Li, C. Wang, and J. Yang, “FeFe(CN)₆Nanocubes as a Bipolar Electrode Material in Aqueous Symmetric Sodium-Ion Batteries,” *ChemPlusChem*, vol. 82, no. 9, pp. 1170–1173, 2017.
- [75] C. Wang, Y. Fang, Y. Xu, L. Liang, M. Zhou, H. Zhao, and Y. Lei, “Manipulation of Disodium Rhodizonate: Factors for Fast-Charge and Fast-Discharge Sodium-Ion Batteries with Long-Term Cyclability,” *Advanced Functional Materials*, vol. 26, no. 11, pp. 1777–1786, 2016.
- [76] M. Y. Wang, J. Z. Guo, Z. W. Wang, Z. Y. Gu, X. J. Nie, X. Yang, and X. L. Wu, “Isostructural and Multivalent Anion Substitution toward Improved Phosphate Cathode Materials for Sodium-Ion Batteries,” *Small*, vol. 16, no. 16, pp. 1–10, 2020.
- [77] H. He, D. Sun, Y. Tang, H. Wang, and M. Shao, “Understanding and improving the initial Coulombic efficiency of high-capacity anode materials for practical sodium ion batteries,” *Energy Storage Materials*, vol. 23, no. March, pp. 233–251, 2019.
- [78] J. Y. Hwang, S. T. Myung, and Y. K. Sun, “Sodium-ion batteries: Present and future,” *Chemical Society Reviews*, vol. 46, no. 12, pp. 3529–3614, 2017.
- [79] Y. Lyu, Y. Liu, Z. E. Yu, N. Su, Y. Liu, W. Li, Q. Li, B. Guo, and B. Liu, “Recent advances in high energy-density cathode materials for sodium-ion batteries,” *Sustainable Materials and Technologies*, vol. 21, 2019.
- [80] H. Chen, Z. Wu, Y. Zhong, T. Chen, X. Liu, J. Qu, W. Xiang, J. Li, X. Chen, X. Guo, and B. Zhong, “Boosting the reactivity of Ni²⁺/Ni³⁺ redox couple via fluorine doping of high performance Na_{0.6}Mn_{0.95}Ni_{0.05}O_{2-x}F_x cathode,” *Electrochimica Acta*, vol. 308, pp. 64–73, 2019.
- [81] K. Kubota, N. Yabuuchi, H. Yoshida, M. Dahbi, and S. Komaba, “Layered oxides as positive electrode materials for Na-ion batteries,” *MRS Bulletin*, vol. 39, no. 5, pp. 416–422, 2014.
- [82] K. Kubota, S. Kumakura, Y. Yoda, K. Kuroki, and S. Komaba, “Electrochemistry and Solid-State Chemistry of NaMeO₂ (Me = 3d Transition Metals),” *Advanced Energy Materials*, vol. 8, p. 1703415, 2018.
- [83] S. Guo, Y. Sun, J. Yi, K. Zhu, P. Liu, Y. Zhu, G.-z. Zhu, M. Chen, M. Ishida, and H. Zhou, “Understanding sodium-ion diffusion in layered P2 and P3 oxides via experiments and first-principles calculations: a bridge between crystal structure and electrochemical performance,” *NPG Asia Materials*, vol. 48, no. 8, pp. 829–834, 2016.

- [84] J. Martinez De Ilarduya, L. Otaegui, J. M. López del Amo, M. Armand, and G. Singh, “NaN₃ addition, a strategy to overcome the problem of sodium deficiency in P2-Na_{0.67}[Fe_{0.5}Mn_{0.5}]O₂ cathode for sodium-ion battery,” *Journal of Power Sources*, vol. 337, pp. 197–203, 2017.
- [85] L. Wu, D. Buchholz, C. Vaalma, G. A. Giffin, and S. Passerini, “Apple-Biowaste-Derived Hard Carbon as a Powerful Anode Material for Na-Ion Batteries,” *ChemElectroChem*, vol. 3, no. 2, pp. 292–298, 2016.
- [86] C. Zhao, Z. Yao, Q. Wang, H. Li, J. Wang, M. Liu, S. Ganapathy, Y. Lu, J. Cabana, B. Li, X. Bai, A. Aspuru-Guzik, M. Wagemaker, L. Chen, and Y. S. Hu, “Revealing High Na-Content P2-Type Layered Oxides as Advanced Sodium-Ion Cathodes,” *Journal of the American Chemical Society*, vol. 142, no. 12, pp. 5742–5750, 2020.
- [87] Q. Wang, S. Mariyappan, G. Rouse, A. V. Morozov, B. Porcheron, R. Dedryvère, J. Wu, W. Yang, L. Zhang, M. Chakir, M. Avdeev, M. Deschamps, Y. S. Yu, J. Cabana, M. L. Doublet, A. M. Abakumov, and J. M. Tarascon, “Unlocking anionic redox activity in O3-type sodium 3d layered oxides via Li substitution,” *Nature Materials*, vol. 20, pp. 353–361, 2021.
- [88] D. Zhou, J. Wang, X. Liu, X. He, F. Sun, V. Murzin, G. Schumacher, X. Yao, M. Winter, and J. Li, “Operando X-ray absorption spectroscopy investigations on Na_xNi_{1/3}Fe_{1/3}Mn_{1/3}O₂ positive electrode materials for sodium and sodium ion batteries,” *Journal of Power Sources*, vol. 473, no. May, p. 228557, 2020.
- [89] L. Mu, S. Xu, Y. Li, Y.-S. Hu, H. Li, L. Chen, and X. Huang, “Prototype Sodium-Ion Batteries Using an Air-Stable and Co Ni-Free O3-Layered Metal Oxide.pdf,” *Advanced Materials*, vol. 27, pp. 6928–6933, 2015.
- [90] K. Kubota and S. Komaba, “Review—Practical Issues and Future Perspective for Na-Ion Batteries,” *Journal of The Electrochemical Society*, vol. 162, no. 14, pp. A2538–A2550, 2015.
- [91] P. K. Nayak, L. Yang, W. Brehm, and P. Adelhelm, “From Lithium-Ion to Sodium-Ion Batteries: Advantages, Challenges, and Surprises,” *Angewandte Chemie - International Edition*, vol. 57, no. 1, pp. 102–120, 2018.
- [92] E. De La Llave, V. Borgel, K. J. Park, J. Y. Hwang, Y. K. Sun, P. Hartmann, F. F. Chesneau, and D. Aurbach, “Comparison between Na-Ion and Li-Ion Cells: Understanding the Critical Role of the Cathodes Stability and the Anodes Pretreatment on the Cells Behavior,” *ACS Applied Materials and Interfaces*, vol. 8, no. 3, pp. 1867–1875, 2016.
- [93] R. Jung, R. Morasch, P. Karayaylali, K. Phillips, F. Maglia, C. Stinner, Y. Shao-Horn, and H. A. Gasteiger, “Effect of Ambient Storage on the Degradation of Ni-Rich Positive Electrode Materials (NMC811) for Li-Ion Batteries,” *Journal of The Electrochemical Society*, vol. 165, no. 2, pp. A132–A141, 2018.

- [94] Z. Chen, J. Wang, J. Huang, T. Fu, G. Sun, S. Lai, R. Zhou, K. Li, and J. Zhao, “The high-temperature and high-humidity storage behaviors and electrochemical degradation mechanism of LiNi_{0.6}Co_{0.2}Mn_{0.2}O₂ cathode material for lithium ion batteries,” *Journal of Power Sources*, vol. 363, pp. 168–176, 2017.
- [95] I. A. Shkrob, J. A. Gilbert, P. J. Phillips, R. Klie, R. T. Haasch, J. Bareño, and D. P. Abraham, “Chemical Weathering of Layered Ni-Rich Oxide Electrode Materials: Evidence for Cation Exchange,” *Journal of The Electrochemical Society*, vol. 164, no. 7, pp. A1489–A1498, 2017.
- [96] Y. Su, L. Li, G. Chen, L. Chen, N. Li, Y. Lu, L. Bao, S. Chen, and F. Wu, “Strategies of Removing Residual Lithium Compounds on the Surface of Ni-Rich Cathode Materials†,” *Chinese Journal of Chemistry*, vol. 39, no. 1, pp. 189–198, 2021.
- [97] L. Zou, Y. He, Z. Liu, H. Jia, J. Zhu, J. Zheng, G. Wang, X. Li, J. Xiao, J. Liu, J. G. Zhang, G. Chen, and C. Wang, “Unlocking the passivation nature of the cathode–air interfacial reactions in lithium ion batteries,” *Nature Communications*, vol. 11, no. 1, 2020.
- [98] C. Busà, M. Belekoukia, and M. J. Lovridge, “The effects of ambient storage conditions on the structural and electrochemical properties of NMC-811 cathodes for Li-ion batteries,” *Electrochimica Acta*, vol. 366, 2021.
- [99] W. Li, X. Liu, Q. Xie, Y. You, M. Chi, and A. Manthiram, “Long-Term Cyclability of NCM-811 at High Voltages in Lithium-Ion Batteries: An In-Depth Diagnostic Study,” *Chemistry of Materials*, vol. 32, no. 18, pp. 7796–7804, 2020.
- [100] J. M. Paulsen, H.-k. Park, and Y. H. Kwon, “Process of making cathode material containing Ni-based lithium transition metal oxide,” 2013.
- [101] P. Teichert, G. G. Eshetu, H. Jahnke, and E. Figgemeier, “Degradation and aging routes of ni-rich cathode based li-ion batteries,” *Batteries*, vol. 6, no. 1, pp. 1–26, 2020.
- [102] W. M. Seong, Y. Kim, and A. Manthiram, “Impact of residual lithium on the adoption of high-nickel layered oxide cathodes for lithium-ion batteries,” *Chemistry of Materials*, vol. 32, no. 22, pp. 9479–9489, 2020.
- [103] N. N. Loginova, L. Y. Madorskaya, and N. K. Podlesskaya, “Relations between the thermal stability of partially fluorinated polymers and their structure,” *Polymer Science U.S.S.R.*, vol. 25, no. 12, pp. 2995–3000, 1983.
- [104] A. Kraytsberg and Y. Ein-Eli, “Conveying Advanced Li-ion Battery Materials into Practice The Impact of Electrode Slurry Preparation Skills,” *Advanced Energy Materials*, vol. 6, no. 21, p. 1600655, 2016.
- [105] P. B. Balbuena, “Electrolyte materials - Issues and challenges,” *AIP Conference Proceedings*, vol. 1597, no. 2014, pp. 82–97, 2014.

- [106] C. Daniel, D. Mohanty, J. Li, and D. L. Wood, “Cathode materials review,” *AIP Conference Proceedings*, vol. 1597, no. 2014, pp. 26–43, 2014.
- [107] J. Zhang, D. Sun, Z. Tang, C. Xie, J. Yang, J. Tang, X. Zhou, Y. Tang, and H. Wang, “Scalable slurry-coating induced integrated 3D lithiophilic architecture for stable lithium metal anodes,” *Journal of Power Sources*, vol. 485, no. September 2020, p. 229334, 2021.
- [108] D. Ledwoch, L. Komsiyiska, E. M. Hammer, K. Smith, P. R. Shearing, D. J. Brett, and E. Kendrick, “Determining the electrochemical transport parameters of sodium-ions in hard carbon composite electrodes,” *Electrochimica Acta*, vol. 401, 2022.
- [109] T. Takamura, M. Saito, A. Shimokawa, C. Nakahara, K. Sekine, S. Maeno, and N. Kibayashi, “Charge/discharge efficiency improvement by the incorporation of conductive carbons in the carbon anode of Li-ion batteries,” *Journal of Power Sources*, vol. 90, no. 1, pp. 45–51, 2000.
- [110] H. Bockholt, M. Indrikova, A. Netz, F. Golks, and A. Kwade, “The interaction of consecutive process steps in the manufacturing of lithium-ion battery electrodes with regard to structural and electrochemical properties,” *Journal of Power Sources*, vol. 325, pp. 140–151, 2016.
- [111] Z. Liu and P. P. Mukherjee, “Microstructure Evolution in Lithium-Ion Battery Electrode Processing,” *Journal of the Electrochemical Society*, vol. 161, no. 8, pp. E3248–E3258, 2014.
- [112] L. Qiu, Z. Shao, D. Wang, F. Wang, W. Wang, and J. Wang, “Novel polymer Li-ion binder carboxymethyl cellulose derivative enhanced electrochemical performance for Li-ion batteries,” *Carbohydrate Polymers*, vol. 112, pp. 532–538, 2014.
- [113] L. Yin, Y. Wang, C. Han, Y. M. Kang, X. Ma, H. Xie, and M. Wu, “Self-assembly of disordered hard carbon/graphene hybrid for sodium-ion batteries,” *Journal of Power Sources*, vol. 305, pp. 156–160, 2016.
- [114] H.-C. Chen, J. Patra, S.-W. Lee, C.-J. Tseng, T.-Y. Wu, M.-H. Lin, and J.-K. Chang, “Electrochemical Na⁺ storage properties of SnO₂/graphene anodes in carbonate-based and ionic liquid electrolytes,” *J. Mater. Chem. A*, vol. 5, no. 26, pp. 13776–13784, 2017.
- [115] J. He, H. Zhong, J. Wang, and L. Zhang, “Investigation on xanthan gum as novel water soluble binder for LiFePO₄ cathode in lithium-ion batteries,” *Journal of Alloys and Compounds*, vol. 714, pp. 409–418, 2017.
- [116] M. Winter and R. J. Brodd, “What are batteries, fuel cells, and supercapacitors?,” *Chemical Reviews*, vol. 104, no. 10, pp. 4245–4269, 2004.
- [117] D. E. Stephenson, B. C. Walker, C. B. Skelton, E. P. Gorzkowski, D. J. Rowenhorst, and D. R. Wheeler, “Modeling 3D Microstructure and Ion Transport in Porous Li-Ion Battery Electrodes,” *Journal of The Electrochemical Society*, vol. 158, no. 7, p. A781, 2011.

- [118] S. Sampath, “Organic materials as Electrodes for Li-ion Batteries,” tech. rep., Indian Institute of Science, Bangalore, India, 2015.
- [119] S. Chae, N. Kim, J. Ma, J. Cho, and M. Ko, “One-to-One Comparison of Graphite-Blended Negative Electrodes Using Silicon Nanolayer-Embedded Graphite versus Commercial Benchmarking Materials for High-Energy Lithium-Ion Batteries,” *Advanced Energy Materials*, vol. 7, no. 15, pp. 1–9, 2017.
- [120] S. Qiu, L. Xiao, M. L. Sushko, K. S. Han, Y. Shao, M. Yan, X. Liang, L. Mai, J. Feng, Y. Cao, X. Ai, H. Yang, and J. Liu, “Manipulating Adsorption–Insertion Mechanisms in Nanostructured Carbon Materials for High-Efficiency Sodium Ion Storage,” *Advanced Energy Materials*, vol. 7, no. 17, pp. 1–11, 2017.
- [121] G. A. Williamson, V. W. Hu, T. B. Yoo, M. Affandy, C. Opie, E. K. Paradis, and V. C. Holmberg, “Temperature-Dependent Electrochemical Characteristics of Antimony Nanocrystal Alloying Electrodes for Na-Ion Batteries,” *ACS Applied Energy Materials*, vol. 2, no. 9, pp. 6741–6750, 2019.
- [122] A. Wang, S. Kadam, H. Li, S. Shi, and Y. Qi, “Review on modeling of the anode solid electrolyte interphase (SEI) for lithium-ion batteries,” *npj Computational Materials*, vol. 4, no. 1, 2018.
- [123] V. Sivasankaran, C. Marino, M. Chamas, P. Soudan, D. Guyomard, J. C. Jumas, P. E. Lippens, L. Monconduit, and B. Lestriez, “Improvement of intermetallics electrochemical behavior by playing with the composite electrode formulation,” *Journal of Materials Chemistry*, vol. 21, no. 13, p. 5076, 2011.
- [124] J. Fondard, E. Irisarri, C. Courrèges, M. R. Palacin, A. Ponrouch, and R. Dedryvère, “SEI Composition on Hard Carbon in Na-Ion Batteries After Long Cycling: Influence of Salts (NaPF₆, NaTFSI) and Additives (FEC, DMCF),” *Journal of The Electrochemical Society*, vol. 167, no. 7, p. 070526, 2020.
- [125] M. K. Gulbinska, ed., *Lithium-ion Battery Materials and Engineering*. London: Springer-Verlag, 1 ed., 2014.
- [126] K. R. Crompton and B. J. Landi, “Opportunities for near zero volt storage of lithium ion batteries,” *Energy Environ. Sci.*, vol. 9, no. 7, pp. 2219–2239, 2016.
- [127] C. D. Reynolds, P. R. Slater, S. D. Hare, M. J. Simmons, and E. Kendrick, “A review of metrology in lithium-ion electrode coating processes,” *Materials and Design*, vol. 209, p. 109971, 2021.
- [128] S. Jaiser, J. Kumberg, J. Klaver, J. L. Urai, W. Schabel, J. Schmatz, and P. Scharfer, “Microstructure formation of lithium-ion battery electrodes during drying – An ex-situ study using cryogenic broad ion beam slope-cutting and scanning electron microscopy (Cryo-BIB-SEM),” *Journal of Power Sources*, vol. 345, pp. 97–107, 2017.
- [129] H. Sun, A. E. Del Rio Castillo, S. Monaco, A. Capasso, A. Ansaldo, M. Prato, D. A. Dinh, V. Pellegrini, B. Scrosati, L. Manna, and F. Bonaccorso, “Binder-free graphene as an advanced anode for lithium batteries,” *Journal of Materials Chemistry A*, vol. 4, no. 18, pp. 6886–6895, 2016.

- [130] W. Haselrieder, B. Westphal, H. Bockholt, A. Diener, S. Höft, and A. Kwade, “Measuring the coating adhesion strength of electrodes for lithium-ion batteries,” *International Journal of Adhesion and Adhesives*, vol. 60, pp. 1–8, 2015.
- [131] F. W. Billmeyer, *Textbook of Polymer Science, 3rd Edition*. Wiley, 1984.
- [132] Adeyinka Aina, Andrew Morris, Manish Gupta, Nashiru Billa, Neesha Madhvani, Ritika Sharma, Stephen Doughty, Vivek Shah, and Yamina Boukari, “Dissolution behavior of poly vinyl alcohol in water and its effect on the physical morphologies of PLGA scaffolds,” *Pharmaceutical and Biosciences Journal*, no. March 2016, pp. 01–06, 2014.
- [133] P. J. Flory, “Thermodynamics of high polymer solutions,” *The Journal of Chemical Physics*, vol. 10, no. 1, pp. 51–61, 1942.
- [134] M. L. Huggins, “Theory of Solutions of High Polymers,” *Journal of the American Chemical Society*, vol. 64, no. 7, pp. 1712–1719, 1942.
- [135] C. M. Hansen, *Hansen Solubility Parameters - A User’s Handbook*, vol. 1. CRC Press, 2nd ed., 2007.
- [136] A. F. M. Barton, *CRC Handbook of Solubility Parameters and Other Cohesion Parameters, 2nd Edition*. CRC Press, 1991.
- [137] C. S. Brazel and S. L. Rosen, *Fundamental Principles of Polymeric Materials, 3rd Edition*. Wiley, 2012.
- [138] W. Bauer and D. Nötzel, “Rheological properties and stability of NMP based cathode slurries for lithium ion batteries,” *Ceramics International*, vol. 40, no. 3, pp. 4591–4598, 2014.
- [139] B. Bitsch, J. Dittmann, M. Schmitt, P. Scharfer, W. Schabel, and N. Willenbacher, “A novel slurry concept for the fabrication of lithium-ion battery electrodes with beneficial properties,” *Journal of Power Sources*, vol. 265, pp. 81–90, 2014.
- [140] H. Kang, C. Lim, T. Li, Y. Fu, B. Yan, N. Houston, V. De Andrade, F. De Carlo, and L. Zhu, “Geometric and Electrochemical Characteristics of $\text{LiNi}_{1/3}\text{Mn}_{1/3}\text{Co}_{1/3}\text{O}_2$ Electrode with Different Calendering Conditions,” *Electrochimica Acta*, vol. 232, pp. 431–438, 2017.
- [141] C. Meyer, H. Bockholt, W. Haselrieder, and A. Kwade, “Characterization of the calendering process for compaction of electrodes for lithium-ion batteries,” *Journal of Materials Processing Technology*, vol. 249, no. May, pp. 172–178, 2017.
- [142] S. H. Kim, K. H. Choi, S. J. Cho, S. Choi, S. Park, and S. Y. Lee, “Printable Solid-State Lithium-Ion Batteries: A New Route toward Shape-Conformable Power Sources with Aesthetic Versatility for Flexible Electronics,” *Nano Letters*, vol. 15, no. 8, pp. 5168–5177, 2015.
- [143] I. Y. Wang, M. Zhang, and U. Sacken, “Additives for improving cycle life of non-aqueous rechargeable lithium batteries,” *US006045948A*, 2000.

- [144] V. G. Pol, E. Lee, D. Zhou, F. Dogan, J. M. Calderon-Moreno, and C. S. Johnson, "Spherical Carbon as a New High-Rate Anode for Sodium-ion Batteries," *Electrochimica Acta*, vol. 127, pp. 61–67, 2014.
- [145] M. Lao, Y. Zhang, W. Luo, Q. Yan, W. Sun, and S. X. Dou, "Alloy-Based Anode Materials toward Advanced Sodium-Ion Batteries," *Advanced Materials*, vol. 1700622, pp. 1–23, 2017.
- [146] H. Mao and J. Reimers, "Use of B2O3 Additive in Non-Aqueous Rechargeable Lithium Batteries," *US005964902A*, 1999.
- [147] M. Dahbi, M. Fukunishi, T. Horiba, N. Yabuuchi, S. Yasuno, and S. Komaba, "High performance red phosphorus electrode in ionic liquid-based electrolyte for Na-ion batteries," *Journal of Power Sources*, vol. 363, pp. 404–412, 2017.
- [148] W. Zhang, M. Dahbi, and S. Komaba, "Polymer binder: a key component in negative electrodes for high-energy Na-ion batteries," *Current Opinion in Chemical Engineering*, vol. 13, pp. 36–44, 2016.
- [149] S. J. R. Prabakar, J. Jeong, and M. Pyo, "Nanoporous hard carbon anodes for improved electrochemical performance in sodium ion batteries," *Electrochimica Acta*, vol. 161, pp. 23–31, 2015.
- [150] R. Chen, Y. Wu, and X. Y. Kong, "Monodisperse porous LiFePO₄/C microspheres derived by microwave-assisted hydrothermal process combined with carbothermal reduction for high power lithium-ion batteries," *Journal of Power Sources*, vol. 258, pp. 246–252, 2014.
- [151] M. E. Spahr, D. Goers, A. Leone, S. Stallone, and E. Grivei, "Development of carbon conductive additives for advanced lithium ion batteries," *Journal of Power Sources*, vol. 196, no. 7, pp. 3404–3413, 2011.
- [152] H. Zheng, R. Yang, G. Liu, X. Song, and V. S. Battaglia, "Cooperation between active material, polymeric binder and conductive carbon additive in lithium ion battery cathode," *Journal of Physical Chemistry C*, vol. 116, no. 7, pp. 4875–4882, 2012.
- [153] M. Wang, D. Dang, A. Meyer, R. Arsenault, and Y.-T. Cheng, "Effects of the Mixing Sequence on Making Lithium Ion Battery Electrodes," *Journal of The Electrochemical Society*, vol. 167, no. 10, p. 100518, 2020.
- [154] B. G. Westphal, N. Mainusch, C. Meyer, W. Haselrieder, M. Indrikova, P. Titscher, H. Bockholt, W. Viöl, and A. Kwade, "Influence of high intensive dry mixing and calendaring on relative electrode resistivity determined via an advanced two point approach," *Journal of Energy Storage*, vol. 11, pp. 76–85, 2017.
- [155] M. A. Sawhney, M. Wahid, S. Mukherjee, R. Griffin, A. Roberts, S. Ogale, and J. Baker, "Process–Structure–Formulation Interactions for enhanced sodium Ion Battery Development: A Review," *ChemPhysChem*, vol. 202100860, 2022.

- [156] D. Liu, L.-C. Chen, T.-J. Liu, T. Fan, E.-Y. Tsou, and C. Tiu, “An Effective Mixing for Lithium Ion Battery Slurries,” *Advances in Chemical Engineering and Science*, vol. 04, no. 04, pp. 515–528, 2014.
- [157] P. N. Pusey and W. v. Meegen, “Phase behaviour of concentrated suspensions of nearly colloidal spheres,” *Nature*, vol. 320, pp. 340–342, 1986.
- [158] P. N. Pusey and W. Van Meegen, “Observation of a glass transition in suspensions of spherical colloidal particles,” *Physical Review Letters*, vol. 59, no. 18, pp. 2083–2086, 1987.
- [159] W. C. K. Poon, S. M. Ilett, and P. N. Pusey, “Phase Behaviour of Colloid-Polymer Mixtures (*).,” *International Conference on Scaling Concepts and Complex Fluids*, vol. 16, no. 8, pp. 1127–1139, 1994.
- [160] T. Van De Laar, R. Hügler, K. Schroeën, and J. Sprakel, “Discontinuous nature of the repulsive-to-attractive colloidal glass transition,” *Scientific Reports*, vol. 6, no. February, pp. 4–10, 2016.
- [161] A. P. Philipse, “Colloidal sedimentation (and filtration),” *Current Opinion in Colloid & Interface Science*, vol. 2, no. 2, pp. 200–206, 1997.
- [162] J. P. Pascault and R. J. Williams, *Overview of thermosets: Present and future*. Elsevier Ltd, 2 ed., 2018.
- [163] B. Bbosa, E. DelleCase, M. Volk, and E. Ozbayoglu, “Development of a mixer-viscometer for studying rheological behavior of settling and non-settling slurries,” *Journal of Petroleum Exploration and Production Technology*, vol. 7, no. 2, pp. 511–520, 2017.
- [164] K. M. Kim, W. S. Jeon, I. J. Chung, and S. H. Chang, “Effect of mixing sequences on the electrode characteristics of lithium-ion rechargeable batteries,” *Journal of Power Sources*, vol. 83, no. 1-2, pp. 108–113, 1999.
- [165] M. Schmitt, M. Baunach, L. Wengeler, K. Peters, P. Junges, P. Scharfer, and W. Schabel, “Slot-die processing of lithium-ion battery electrodes-Coating window characterization,” *Chemical Engineering and Processing: Process Intensification*, vol. 68, pp. 32–37, 2013.
- [166] G. W. Lee, J. H. Ryu, W. Han, K. H. Ahn, and S. M. Oh, “Effect of slurry preparation process on electrochemical performances of LiCoO₂ composite electrode,” *Journal of Power Sources*, vol. 195, no. 18, pp. 6049–6054, 2010.
- [167] S. Lanceros-méndez and C. M. Costa, “The Influence of Slurry Rheology on Lithium-ion Electrode Processing,” in *Printed Batteries: Materials, Technologies and Applications, First Edition.*, pp. 63–79, John Wiley & Sons Ltd, 2018.
- [168] J. Mewis and N. J. Wagner, “Thixotropy,” *Advances in Colloid and Interface Science*, vol. 147-148, no. C, pp. 214–227, 2009.

- [169] H. A. Barnes, *A Handbook of Elementary Rheology*. Aberystwyth, Wales: The University of Wales, Institute of Non-Newtonian Fluid Mechanics, 2000.
- [170] M. Meyers and K. Chawla, *Mechanical Behavior of Materials*. Cambridge: Cambridge University Press, 1st ed., 2008.
- [171] H. S. Ji, W. G. Ahn, I. Kwon, J. Nam, and H. W. Jung, “Operability coating window of dual-layer slot coating process using viscocapillary model,” *Chemical Engineering Science*, vol. 143, pp. 122–129, 2016.
- [172] K. B. Hatzell, M. B. Dixit, S. A. Berlinger, and A. Z. Weber, “Understanding inks for porous-electrode formation,” *Journal of Materials Chemistry A*, vol. 5, no. 39, pp. 1–7, 2017.
- [173] Y. J. Nam, D. Y. Oh, S. H. Jung, and Y. S. Jung, “Toward practical all-solid-state lithium-ion batteries with high energy density and safety: Comparative study for electrodes fabricated by dry- and slurry-mixing processes,” *Journal of Power Sources*, vol. 375, no. September 2017, pp. 93–101, 2018.
- [174] M. M. Forouzan, C. W. Chao, D. Bustamante, B. A. Mazzeo, and D. R. Wheeler, “Experiment and simulation of the fabrication process of lithium-ion battery cathodes for determining microstructure and mechanical properties,” *Journal of Power Sources*, vol. 312, pp. 172–183, 2016.
- [175] O. Fromm, A. Heckmann, U. C. Rodehorst, J. Frerichs, D. Becker, M. Winter, and T. Placke, “Carbons from biomass precursors as anode materials for lithium ion batteries: New insights into carbonization and graphitization behavior and into their correlation to electrochemical performance,” *Carbon*, vol. 128, pp. 147–163, 2017.
- [176] R. Wang, L. Feng, W. Yang, Y. Zhang, Y. Zhang, W. Bai, B. Liu, W. Zhang, Y. Chuan, Z. Zheng, and H. Guan, “Effect of Different Binders on the Electrochemical Performance of Metal Oxide Anode for Lithium-Ion Batteries,” *Nanoscale Research Letters*, vol. 12, pp. 1–11, 2017.
- [177] J. Zhi and L.-Z. Zhang, “Durable superhydrophobic surfaces made by intensely connecting a bipolar top layer to the substrate with a middle connecting layer,” *Scientific Reports*, vol. 7, no. 1, p. 9946, 2017.
- [178] K. Fu, Y. Wang, C. Yan, Y. Yao, Y. Chen, J. Dai, S. Lacey, Y. Wang, J. Wan, T. Li, Z. Wang, Y. Xu, and L. Hu, “Graphene Oxide-Based Electrode Inks for 3D-Printed Lithium-Ion Batteries,” *Advanced Materials*, vol. 28, no. 13, pp. 2587–2594, 2016.
- [179] Y. Liu, B. Yang, X. Dong, Y. Wang, and Y. Xia, “A Simple Prelithiation Strategy To Build a High-Rate and Long-Life Lithium-Ion Battery with Improved Low-Temperature Performance,” *Angewandte Chemie International Edition*, pp. 16833–16837, 2017.
- [180] Y. Masaki, A. Kozawa, and R. J. Brodd, *Lithium-Ion Batteries*. Springer, 1st ed., 2013.

- [181] N. Susarla, S. Ahmed, and D. W. Dees, “Modeling and analysis of solvent removal during Li-ion battery electrode drying,” *Journal of Power Sources*, vol. 378, no. August 2017, pp. 660–670, 2018.
- [182] P. Rupnowski, M. Ulsh, B. Sopori, B. G. Green, D. L. Wood, J. Li, and Y. Sheng, “In-line monitoring of Li-ion battery electrode porosity and areal loading using active thermal scanning - modeling and initial experiment,” *Journal of Power Sources*, vol. 375, pp. 138–148, 2018.
- [183] S. Komaba, N. Yabuuchi, T. Ozeki, Z. J. Han, K. Shimomura, H. Yui, Y. Katayama, and T. Miura, “Comparative study of sodium polyacrylate and poly(vinylidene fluoride) as binders for high capacity si-graphite composite negative electrodes in Li-ion batteries,” *Journal of Physical Chemistry C*, vol. 116, no. 1, pp. 1380–1389, 2012.
- [184] Y. C. Lu, C. Ma, J. Alvarado, N. Dimov, Y. S. Meng, and S. Okada, “Improved electrochemical performance of tin-sulfide anodes for sodium-ion batteries,” *J. Mater. Chem. A*, vol. 3, no. 33, pp. 16971–16977, 2015.
- [185] N. Raske, R. W. Hewson, N. Kapur, G. N. D. Boer, N. Raske, R. W. Hewson, N. Kapur, and G. N. D. Boer, “A predictive model for discrete cell gravure roll coating A predictive model for discrete cell gravure roll coating,” *Physics of Fluids*, vol. 062101, pp. 0–13, 2017.
- [186] H. Zheng, L. Tan, G. Liu, X. Song, and V. S. Battaglia, “Calendering effects on the physical and electrochemical properties of Li[Ni_{1/3}Mn_{1/3}Co_{1/3}]O₂cathode,” *Journal of Power Sources*, vol. 208, pp. 52–57, 2012.
- [187] J.-k. Park, *Principles and applications of lithium secondary batteries*. Weinheim, Germany: Wiley-VCH Verlag & Co. KGaA, 1 ed., 2012.
- [188] M. Gockeln, S. Pokhrel, F. Meierhofer, J. Glenneberg, M. Schowalter, A. Rosenauer, U. Fritsching, M. Busse, L. Mädler, and R. Kun, “Fabrication and performance of Li₄Ti₅O₁₂/C Li-ion battery electrodes using combined double flame spray pyrolysis and pressure-based lamination technique,” *Journal of Power Sources*, vol. 374, no. October 2017, pp. 97–106, 2018.
- [189] S. Haj Ibrahim, M. Neumann, F. Klingner, V. Schmidt, and T. Wejrzanowski, “Analysis of the 3D microstructure of tape-cast open-porous materials via a combination of experiments and modeling,” *Materials and Design*, vol. 133, pp. 216–223, 2017.
- [190] F. Huttner, W. Haselrieder, and A. Kwade, “The Influence of Different Post-Drying Procedures on Remaining Water Content and Physical and Electrochemical Properties of Lithium-Ion Batteries,” *Energy Technology*, vol. 8, no. 2, pp. 1–11, 2020.
- [191] S. Jaiser, M. Müller, M. Baunach, W. Bauer, P. Scharfer, and W. Schabel, “Investigation of film solidification and binder migration during drying of Li-Ion battery anodes,” *Journal of Power Sources*, vol. 318, pp. 210–219, 2016.

- [192] Y. H. Chen, C. W. Wang, X. Zhang, and A. M. Sastry, “Porous cathode optimization for lithium cells: Ionic and electronic conductivity, capacity, and selection of materials,” *Journal of Power Sources*, vol. 195, no. 9, pp. 2851–2862, 2010.
- [193] H. Zheng, G. Liu, X. Song, P. Ridgway, S. Xun, and V. S. Battaglia, “Cathode Performance as a Function of Inactive Material and Void Fractions,” *Journal of The Electrochemical Society*, vol. 157, no. 10, p. A1060, 2010.
- [194] W. Haselrieder, S. Ivanov, D. K. Christen, H. Bockholt, and A. Kwade, “Impact of the Calendering Process on the Interfacial Structure and the Related Electrochemical Performance of Secondary Lithium-Ion Batteries,” *ECS Transactions*, vol. 50, no. 26, pp. 59–70, 2013.
- [195] H. Zheng, G. Liu, X. Song, P. Ridgway, and V. Battaglia, “Optimization of Ratio and Amount of CMC/SBR Binder for a Graphite Anode,” *ECS Meeting Abstracts*, vol. 218th ECS, no. 4, p. 200, 2010.
- [196] X. H. Wu, Q. P. Feng, M. Wang, and G. W. Huang, “Spherical Al-substituted alpha-nickel hydroxide with high tapping density applied in Ni-MH battery,” *Journal of Power Sources*, vol. 329, pp. 170–178, 2016.
- [197] Y. S. Zhang, J. J. Bailey, Y. Sun, A. M. Boyce, W. Dawson, C. D. Reynolds, Z. Zhang, X. Lu, P. Grant, E. Kendrick, P. R. Shearing, and D. J. Brett, “Applications of advanced metrology for understanding the effects of drying temperature in the lithium-ion battery electrode manufacturing process,” *Journal of Materials Chemistry A*, pp. 10593–10603, 2022.
- [198] Solvay, “Solef 5130 PVDF - Technical Data Sheet,” tech. rep., Solvay, 2014.
- [199] A. Taguet, B. Ameduri, and B. Boutevin, “Crosslinking of vinylidene fluoride-containing fluoropolymers,” *Advances in Polymer Science*, vol. 184, no. July, pp. 127–211, 2005.
- [200] P. Bei, H. Liu, H. Yao, A. Hu, Y. Sun, and L. Guo, “Preparation and characterization of PVDF/CaCO₃ composite membranes etched by hydrochloric acid,” *Environmental Science and Pollution Research*, vol. 26, p. 33607–33620, 2019.
- [201] Y. H. Teow, A. A. Latif, J. K. Lim, H. P. Ngang, L. Y. Susan, and B. S. Ooi, “Hydroxyl functionalized PVDF-TiO₂ ultrafiltration membrane and its antifouling properties,” *Journal of Applied Polymer Science*, vol. 132, no. 21, pp. 1–11, 2015.
- [202] R. Jung, R. Morasch, P. Karayaylali, K. Phillips, F. Maglia, C. Stinner, Y. Shao-horn, and H. A. Gasteiger, “Effect of Ambient Storage on the Degradation of Ni-Rich Positive Electrode Materials (NMC811) for Li-Ion Batteries,” *Journal of The Electrochemical Society*, vol. 165, no. 2, pp. 132–141, 2018.
- [203] J. Wootthikanokkhan and P. Changsuwan, “Dehydrofluorination of PVDF and Proton Conductivity of the Modified PVDF/Sulfonated SEBS Blend Membranes,” *Journal of Metals, Materials and Minerals*, vol. 18, no. 2, pp. 57–62, 2008.

- [204] H. Kise, H. Ogata, and M. Nakata, "Chemical dehydrofluorination and electrical conductivity of poly(vinylidene fluoride) films," *Die Angewandte Makromolekulare Chemie*, vol. 168, no. 1, pp. 205–216, 1989.
- [205] M. F. Rabuni, N. M. Nik Sulaiman, M. K. Aroua, and N. A. Hashim, "Effects of alkaline environments at mild conditions on the stability of PVDF membrane: An experimental study," *Industrial and Engineering Chemistry Research*, vol. 52, no. 45, pp. 15874–15882, 2013.
- [206] L. Xiao, D. M. Davenport, L. Ormsbee, and D. Bhattacharyya, "Polymerization and Functionalization of Membrane Pores for Water Related Applications," *Ind. Eng. Chem. Res.*, vol. 54, pp. 4174–4182, 2015.
- [207] G. J. Ross, J. F. Watts, M. P. Hill, and P. Morrissey, "Surface modification of poly(vinylidene fluoride) by alkaline treatment: 1. The degradation mechanism," *Polymer*, vol. 41, no. 5, pp. 1685–1696, 2000.
- [208] A. García-Abuín, D. Gómez-Díaz, and J. M. Navaza, "Density, speed of sound, viscosity, refractive index, and excess volume of n -methyl-2-pyrrolidone (NMP) + water + ethanol from T = (293.15 to 323.15) K," *Journal of Chemical and Engineering Data*, vol. 56, no. 4, pp. 646–651, 2011.
- [209] Y. J. Ou, X. M. Wang, C. L. Li, Y. L. Zhu, and X. L. Li, "The Effects of Alkali and Temperature on the Hydrolysis Rate of N-methylpyrrolidone," *IOP Conference Series: Earth and Environmental Science*, vol. 100, p. 012036, 2017.
- [210] A. Jouyban, M. A. Fakhree, and A. Shayanfar, "Review of pharmaceutical applications of N-methyl-2-pyrrolidone," *Journal of Pharmacy and Pharmaceutical Sciences*, vol. 13, no. 4, pp. 524–535, 2010.
- [211] D. A. Wells, H. F. Thomas, and G. A. Digenis, "Mutagenicity and Cytotoxicity of N-Methyl-2- pyrrolidone and 4- (Methylamino) butanoic Acid in the Salmonella / Microsome Assay," *Journal of Applied Toxicology*, vol. 8, no. 2, pp. 135–139, 1988.
- [212] L. Poulain, A. Monod, and H. Wortham, "Development of a new on-line mass spectrometer to study the reactivity of soluble organic compounds in the aqueous phase under tropospheric conditions: Application to OH-oxidation of N-methylpyrrolidone," *Journal of Photochemistry and Photobiology A: Chemistry*, vol. 187, no. 1, pp. 10–23, 2007.
- [213] T. Uno and M. Yamamoto, "Color reaction of amines and the colorimetric determination of aromatic secondary amines with quinonedichlorodiimide," *Bunseki Kagaku*, vol. 17, no. 3, pp. 306–310, 1968.
- [214] H. C. Yau, M. K. Bayazit, J. H. G. Steinke, and M. S. P. Shaffer, "Sonochemical degradation of N-methylpyrrolidone and its influence on single walled carbon nanotube dispersion," *Chem. Commun.*, vol. 51, pp. 16621–16624, 2015.
- [215] S. Kim and S. J. Park, "Effect of acid/base treatment to carbon blacks on preparation of carbon-supported platinum nanoclusters," *Electrochimica Acta*, vol. 52, no. 9, pp. 3013–3021, 2007.

- [216] R. K. Gautam and A. Verma, “Chapter 3.4 - Electrocatalyst Materials for Oxygen Reduction Reaction in Microbial Fuel Cell,” in *Microbial Electrochemical Technology* (S. V. Mohan, S. Varjani, and A. Pandey, eds.), Biomass, Biofuels and Biochemicals, pp. 451–483, Elsevier, 2019.
- [217] M. Taibi, S. Ammar, N. Jouini, F. Fiévet, P. Molinié, and M. Drillon, “Layered nickel hydroxide salts: Synthesis, characterization and magnetic behaviour in relation to the basal spacing,” *Journal of Materials Chemistry*, vol. 12, no. 11, pp. 3238–3244, 2002.
- [218] F. Rolle and M. Segal, “Use of FTIR spectroscopy for the measurement of CO₂ carbon stable isotope ratios,” in *19th International Congress of Metrology*, vol. 05002, pp. 1–6, 2019.
- [219] S. Campbell and K. M. Poduska, “Incorporating far-infrared data into carbonate mineral analyses,” *Minerals*, vol. 10, no. 7, pp. 1–11, 2020.
- [220] H. Zhang, H. Ming, W. Zhang, G. Cao, and Y. Yang, “Coupled Carbonization Strategy toward Advanced Hard Carbon for High-Energy Sodium-Ion Battery,” *ACS Applied Materials and Interfaces*, vol. 9, no. 28, pp. 23766–23774, 2017.
- [221] P. J. Linstrom, W. G. Mallard, and Eds., *NIST Chemistry WebBook, NIST Standard Reference Database Number 69*. Gaithersburg MD: National Institute of Standards and Technology, 20899 ed., 2017.
- [222] J. W. Sons and I. SpectraBase, “SpectraBase,” <https://spectrabase.com/about> [Online] Accessed: 2022-02-15, 2022.
- [223] J. Park, K. Shin, and C. Lee, “Improvement of cross-machine directional thickness deviation for uniform pressure-sensitive adhesive layer in roll-to-roll slot-die coating process,” *International Journal of Precision Engineering and Manufacturing*, vol. 16, no. 5, pp. 937–943, 2015.
- [224] Z. Qiao, Z. Wang, C. Zhang, S. Yuan, Y. Zhu, and J. Wang, “PVAm-PIP/PS composite membrane with high performance for CO₂/N₂ separation,” *AIChE Journal*, vol. 59, no. 4, pp. 215–228, 2012.
- [225] J. Wang and Q. Mao, “Methodology Based on the PVT Behavior of Polymer for Injection Molding,” *Advances in Polymer Technology*, vol. 32, no. 2013, pp. 474–485, 2012.
- [226] W. C. K. Poon, “Colloidal Glasses,” *MRS Bulletin*, no. February, pp. 96–99, 2004.
- [227] H. Wildmoser, J. Scheiwiller, and E. J. Windhab, “Impact of disperse microstructure on rheology and quality aspects of ice cream,” *Lebensm.-Wiss. u.-Technol.*, vol. 37, pp. 881–891, 2004.
- [228] G. Peters, O. Wendler, D. Böhringer, A. O. Gostian, S. K. Müller, H. Canziani, N. Hesse, M. Semmler, D. A. Berry, S. Kniesburges, W. Peukert, and M. Döllinger,

- “Human laryngeal mucus from the vocal folds: Rheological characterization by particle tracking microrheology and oscillatory shear rheology,” *Applied Sciences (Switzerland)*, vol. 11, no. 7, pp. 1–15, 2021.
- [229] N. H. Ahmad, J. Ahmed, D. M. Hashim, Y. A. Manap, and S. Mustafa, “Oscillatory and steady shear rheology of gellan/dextran blends,” *Journal of Food Science and Technology*, vol. 52, no. 5, pp. 2902–2909, 2015.
- [230] C. Yan and D. Pochan, J., “Rheological properties of peptide-based hydrogels for biomedical and other applications,” *Chem. Soc. Rev.*, vol. 39, no. 9, pp. 3528–3540, 2010.
- [231] F. Chambon and H. H. Winter, “Linear Viscoelasticity at the Gel Point of a Crosslinking PDMS with Imbalanced Stoichiometry,” *Journal of Rheology*, vol. 31, no. 8, pp. 683–697, 1987.
- [232] H. H. Winter, “Can the gel point of a cross-linking polymer be detected by the $G' - G''$ crossover?,” *Polymer Engineering & Science*, vol. 27, no. 22, pp. 1698–1702, 1987.
- [233] V. A. H. Boudara, D. J. Read, and J. Ramírez, “ reptate rheology software: Toolkit for the analysis of theories and experiments ,” *Journal of Rheology*, vol. 64, no. 3, pp. 709–722, 2020.
- [234] T. Venerová and M. Pekař, “Rheological properties of gels formed by physical interactions between hyaluronan and cationic surfactants,” *Carbohydrate Polymers*, vol. 170, pp. 176–181, 2017.
- [235] H. Bai, X. Wang, Y. Zhou, and L. Zhang, “Preparation and characterization of poly(vinylidene fluoride) composite membranes blended with nano-crystalline cellulose,” *Progress in Natural Science: Materials International*, vol. 22, no. 3, pp. 250–257, 2012.
- [236] D. Li and M. Liao, “Dehydrofluorination mechanism, structure and thermal stability of pure fluoroelastomer (poly(VDF-ter-HFP-ter-TFE) terpolymer) in alkaline environment,” *Journal of Fluorine Chemistry*, vol. 201, no. August, pp. 55–67, 2017.
- [237] H. Kise and H. Ogata, “Phase Transfer Catalysis in Dehydrofluorination of Poly(Vinylidene Fluoride) By Aqueous Sodium Hydroxide Solutions.,” *Journal of Polymer Science. Part A-1, Polymer chemistry*, vol. 21, no. 12, pp. 3443–3451, 1983.
- [238] D. M. Brewis, I. Mathieson, I. Sutherland, R. A. Cayless, and R. H. Dahm, “Pretreatment of poly(vinyl fluoride) and poly(vinylidene fluoride) with potassium hydroxide,” *International Journal of Adhesion and Adhesives*, vol. 16, no. 2, pp. 87–95, 1996.
- [239] W. Haselrieder, S. Ivanov, H. Y. Tran, S. Theil, L. Froböse, B. Westphal, M. Wohlfahrt-Mehrens, and A. Kwade, “Influence of formulation method and related processes on structural, electrical and electrochemical properties of

- LMS/NCA-blend electrodes,” *Progress in Solid State Chemistry*, vol. 42, no. 4, pp. 157–174, 2014.
- [240] A. Etiemble, N. Besnard, J. Adrien, P. Tran-Van, L. Gautier, B. Lestriez, and E. Maire, “Quality control tool of electrode coating for lithium-ion batteries based on X-ray radiography,” *Journal of Power Sources*, vol. 298, pp. 285–291, 2015.
- [241] M. Smith, R. E. García, and Q. C. Horn, “The Effect of Microstructure on the Galvanostatic Discharge of Graphite Anode Electrodes in LiCoO₂-Based Rocking-Chair Rechargeable Batteries,” *Journal of The Electrochemical Society*, vol. 156, no. 11, p. A896, 2009.
- [242] K. Y. Cho, Y. I. Kwon, J. R. Youn, and Y. S. Song, “Evaluation of slurry characteristics for rechargeable lithium-ion batteries,” *Materials Research Bulletin*, vol. 48, no. 8, pp. 2922–2925, 2013.
- [243] S. Lim, S. Kim, K. Hyun, and S. Jong, “The effect of binders on the rheological properties and the microstructure formation of lithium-ion battery anode slurries,” *Journal of Power Sources*, vol. 299, pp. 221–230, 2015.
- [244] W. Porcher, B. Lestriez, S. Jouanneau, and D. Guyomard, “Design of Aqueous Processed Thick LiFePO₄ Composite Electrodes for High-Energy Lithium Battery,” *Journal of The Electrochemical Society*, vol. 156, no. 3, pp. 133–144, 2009.
- [245] K. Woo, D. Jang, Y. Kim, and J. Moon, “Relationship between printability and rheological behavior of ink-jet conductive inks,” *Ceramics International*, vol. 39, no. 6, pp. 7015–7021, 2013.
- [246] J. H. Hung, J. H. Mangalara, and D. S. Simmons, “Heterogeneous Rouse Model Predicts Polymer Chain Translational Normal Mode Decoupling,” *Macromolecules*, vol. 51, no. 8, pp. 2887–2898, 2018.
- [247] B. S. Khatri and T. C. McLeish, “Rouse model with internal friction: A coarse grained framework for single biopolymer dynamics,” *Macromolecules*, vol. 40, no. 18, pp. 6770–6777, 2007.
- [248] C. Svaneborg, H. A. Karimi-Varzaneh, N. Hojdis, F. Fleck, and R. Everaers, “Kremer-Grest models for universal properties of specific common polymer species,” *arXiv*, vol. 1606.05008, no. July, 2016.
- [249] K. Kremer, “Computer simulations for macromolecular science,” *Macromolecular Chemistry and Physics*, vol. 204, no. 2, pp. 257–264, 2003.
- [250] Q. Xu, B. Engquist, M. Solaimanian, and K. Yan, “A new nonlinear viscoelastic model and mathematical solution of solids for improving prediction accuracy,” *Scientific Reports*, vol. 10, no. 1, pp. 1–11, 2020.
- [251] H. Tang, D. Wang, and Z. Duan, “New Maxwell Creep Model Based on Fractional and Elastic-Plastic Elements,” *Advances in Civil Engineering*, vol. 2020, no. ID9170706, 2020.

- [252] M. R. Symonds and A. Moussalli, “A brief guide to model selection, multimodel inference and model averaging in behavioural ecology using Akaike’s information criterion,” *Behavioral Ecology and Sociobiology*, vol. 65, no. 1, pp. 13–21, 2011.
- [253] K. P. Burnham and D. R. Anderson, “Multimodel inference: Understanding AIC and BIC in model selection,” *Sociological Methods and Research*, vol. 33, no. 2, pp. 261–304, 2004.
- [254] K. P. Burnham, D. R. Anderson, and K. P. Huyvaert, “AIC model selection and multimodel inference in behavioral ecology: Some background, observations, and comparisons,” *Behavioral Ecology and Sociobiology*, vol. 65, no. 1, pp. 23–35, 2011.
- [255] S. H. Sung, S. Kim, J. H. Park, J. D. Park, and K. H. Ahn, “Role of PVDF in Rheology and Microstructure of NCM Cathode Slurries for Lithium-Ion Battery,” *Materials*, vol. 13, pp. 4544–4555, 2020.
- [256] M. N. Al-shroofy, *Understanding and Improving Manufacturing Processes for Making Lithium-Ion Battery Electrodes*. PhD thesis, University of Kentucky, 2017.
- [257] B. Cabane, K. Wong, P. Lindner, and F. Lafuma, “Shear induced gelation of colloidal dispersions,” *Journal of Rheology*, vol. 41, no. 3, pp. 531–547, 1997.
- [258] D. Dörr, U. Kuhn, and V. Altstädt, “Rheological study of gelation and crosslinking in chemical modified polyamide 12 using a multiwave technique,” *Polymers*, vol. 12, no. 4, pp. 7–9, 2020.
- [259] C. Pellet and M. Cloitre, “The glass and jamming transitions of soft polyelectrolyte microgel suspensions,” *Soft Matter*, vol. 12, no. 16, pp. 3710–3720, 2016.
- [260] S. Franco, E. Buratti, V. Nigro, E. Zaccarelli, B. Ruzicka, and R. Angelini, “Glass and jamming rheology in soft particles made of pnipam and polyacrylic acid,” *International Journal of Molecular Sciences*, vol. 22, no. 8, 2021.
- [261] A. Kowalczyk, B. Hochstein, P. Stähle, and N. Willenbacher, “Characterization of complex fluids at very low frequency: Experimental verification of the strain rate-frequency superposition (SRFS) method,” *Applied Rheology*, vol. 20, no. 5, pp. 1–12, 2010.
- [262] C. Ibănescu, M. Danu, A. Nanu, M. Lungu, and B. C. Simionescu, “Stability of disperse systems estimated using rheological oscillatory shear tests,” *Revue Roumaine de Chimie*, vol. 55, no. 11-12, pp. 933–940, 2010.
- [263] M. Sun, H. Sun, Y. Wang, M. Sánchez-Soto, and D. A. Schiraldi, “The relation between the rheological properties of gels and the mechanical properties of their corresponding aerogels,” *Gels*, vol. 4, no. 2, pp. 2–11, 2018.
- [264] J. H. Lee, U. Paik, V. A. Hackley, and Y. M. Choi, “Effect of poly(acrylic acid) on adhesion strength and electrochemical performance of natural graphite negative electrode for lithium-ion batteries,” *Journal of Power Sources*, vol. 161, no. 1, pp. 612–616, 2006.

- [265] S.-L. Chou, Y. Pan, J.-Z. Wang, H.-K. Liu, and S.-X. Dou, “Small things make a big difference: binder effects on the performance of Li and Na batteries,” *Phys. Chem. Chem. Phys.*, vol. 16, no. 38, pp. 20347–20359, 2014.
- [266] D.-H. Cho, C.-H. Jo, W. Cho, Y.-J. Kim, H. Yashiro, Y.-K. Sun, and S.-T. Myung, “Effect of Residual Lithium Compounds on Layer Ni-Rich Li[Ni 0.7 Mn 0.3]O 2 ,” *Journal of The Electrochemical Society*, vol. 161, no. 6, pp. A920–A926, 2014.
- [267] C. C. Nguyen, T. Yoon, D. M. Seo, P. Guduru, and B. L. Lucht, “Systematic Investigation of Binders for Silicon Anodes: Interactions of Binder with Silicon Particles and Electrolytes and Effects of Binders on Solid Electrolyte Interphase Formation,” *ACS Applied Materials and Interfaces*, vol. 8, no. 19, pp. 12211–12220, 2016.
- [268] C. C. Nguyen, D. M. Seo, K. W. Chandrasiri, and B. L. Lucht, “Improved Cycling Performance of a Si Nanoparticle Anode Utilizing Citric Acid as a Surface-Modifying Agent,” *Langmuir*, vol. 33, no. 37, pp. 9254–9261, 2017.
- [269] J. F. J. Dippy, S. R. C. Hughes, and A. Rozanski, “The Dissociation Constants of Some Symmetrically Disubstituted Succinic Acids,” *Journal of the Chemical Society*, no. 0, pp. 2492–2498, 1959.
- [270] H. Brown, E. E. Braude, and F. E. Nachod, *Determination of Organic Structures by Physical Methods*. New York: Academic Press, 1st ed., 1955.
- [271] R. Aveyard, B. Binks, N. Carr, and A. Cross, “Stability of insoluble monolayers and ionisation of Langmuir-Blodgett multilayers of octadecanoic acid,” *Thin Solid Films*, vol. 188, pp. 361–373, 1990.
- [272] M. Singh and A. Gupta, “Corrosion characteristics of some aluminium alloys in oxalic acid,” *Indian Journal of Chemical Technology*, vol. 3, no. 1, pp. 32–36, 1996.
- [273] S. D. Cramer and B. S. Covino, *ASM Handbook, Volume 13A: Corrosion: Fundamentals, Testing, and Protection*. ASM Handbook Series, ASM International, 2003.
- [274] J. Halambek, M. C. Bubalo, I. R. Redovnikovic, and K. Berkovic, “Corrosion behaviour of aluminium and AA5754 alloy in 1% acetic acid solution in presence of laurel oil,” *International Journal of Electrochemical Science*, vol. 9, no. 10, pp. 5496–5506, 2014.
- [275] D. Pavlov, “Chapter 15 - Lead–Carbon Electrodes,” in *Lead-Acid Batteries: Science and Technology*, pp. 621–662, Amsterdam: Elsevier, 2nd ed., 2017.
- [276] D. Lombardo, M. A. Kiselev, S. Magazù, and P. Calandra, “Amphiphiles self-assembly: Basic concepts and future perspectives of supramolecular approaches,” *Advances in Condensed Matter Physics*, vol. 2015, p. 151683, 2015.
- [277] K. D. Danov, P. A. Kralchevsky, S. D. Stoyanov, J. L. Cook, and I. P. Stott, “Analytical modeling of micelle growth. 3. Electrostatic free energy of ionic wormlike

- micelles – Effects of activity coefficients and spatially confined electric double layers,” *Journal of Colloid and Interface Science*, vol. 581, pp. 262–275, 2021.
- [278] O. G. Us’yarov, “The electrical double layer of micelles in ionic surfactant solutions in the presence of a background electrolyte: 1. Diluted micellar solutions of sodium dodecyl sulfate,” *Colloid Journal*, vol. 69, no. 1, pp. 95–102, 2007.
- [279] D. C. Poland and H. A. Scheraga, “Hydrophobic bonding and micelle stability; the influence of ionic head groups,” *Journal of Colloid And Interface Science*, vol. 21, no. 3, pp. 273–283, 1966.
- [280] P. E. Linstrom and W. E. Mallard, *NIST Chemistry WebBook, NIST Standard Reference Database Number 69*,. Gaithersburg MD: National Institute of Standards and Technology, 20899 ed., 2022.
- [281] M. T. Colomer, “Straightforward synthesis of Ti-doped YSZ gels by chemical modification of the precursors alkoxides,” *Journal of Sol-Gel Science and Technology*, vol. 67, no. 1, pp. 135–144, 2013.
- [282] M. F. Atitar, H. Belhadj, R. Dillert, and D. W. Bahnem, “The Relevance of ATR-FTIR Spectroscopy in Semiconductor Photocatalysis,” in *Emerging Pollutants in the Environment - Current and Further Implications*, IntechOpen, 1st ed., 2015.
- [283] S. D. Brooks, R. M. Garland, M. E. Wise, A. J. Prenni, M. Cushing, E. Hewitt, and M. A. Tolbert, “Phase changes in internally mixed maleic acid/ammonium sulfate aerosols,” *Journal of Geophysical Research: Atmospheres*, vol. 108, no. 15, pp. 1–10, 2003.
- [284] C. Muthuselvi, A. Arunkumar, and G. Rajaperumal, “Growth and Characterization of Oxalic Acid Doped with Tryptophan Crystal for Antimicrobial Activity,” *Der Chemica Sinica*, vol. 7, no. 4, pp. 55–62, 2017.
- [285] A. Seyed Yagoubi, F. Shahidi, M. Mohebbi, M. Varidi, and S. Golmohammadzadeh, “The effect of different lipids on physicochemical characteristics and stability of phycocyanin - loaded solid lipid nanoparticles,” *Iranian Journal of Food Science and Technology*, vol. 14, no. 67, pp. 83–93, 2017.
- [286] A. Delphin, B. Kavitha, G. Madhurambal, and M. Dhamodaran, “Growth and characterisation of L-Tryptophan Succinate Dihydrate,” *International Journal of Research and Analytical Reviews*, vol. 5, no. 3, pp. 777–783, 2018.
- [287] G. Yuan, H. Cheng, and C. C. Han, “The glass formation of a repulsive system with also a short range attractive potential: A re-interpretation of the free volume theory,” *Polymer*, vol. 131, pp. 272–286, 2017.
- [288] K. Binder and W. Kob, *Glassy Materials and Disordered Solids: An Introduction to Their Statistical Mechanics*. World Scientific, 2011.
- [289] Y. I. Kwon, J. D. Kim, and Y. S. Song, “Agitation Effect on the Rheological Behavior of Lithium-Ion Battery Slurries,” *Journal of Electronic Materials*, vol. 44, no. 1, pp. 475–481, 2015.

- [290] W. B. Hawley and J. Li, “Beneficial rheological properties of lithium-ion battery cathode slurries from elevated mixing and coating temperatures,” *Journal of Energy Storage*, vol. 26, no. October, p. 100994, 2019.
- [291] I. Rosalina and M. Bhattacharya, “Flow curves, stress relaxation and creep measurements of starch gels,” *Journal of Texture Studies*, vol. 32, no. 4, pp. 247–269, 2001.
- [292] A. S. Baumgarten and K. Kamrin, “Modeling stress relaxation in dense, fine-particle suspensions,” *Journal of Rheology*, vol. 64, no. 2, pp. 367–377, 2020.
- [293] J. H. Lee, T. H. Lee, K. S. Shim, J. W. Park, H. J. Kim, Y. Kim, and S. Jung, “Molecular weight and crosslinking on the adhesion performance and flexibility of acrylic PSAs,” *Journal of Adhesion Science and Technology*, vol. 30, no. 21, pp. 2316–2328, 2016.
- [294] Q. Wang, X. Zhu, Y. Liu, Y. Fang, X. Zhou, and J. Bao, “Rice husk-derived hard carbons as high-performance anode materials for sodium-ion batteries,” *Carbon*, vol. 127, pp. 658–666, 2018.
- [295] W. Choi, H. C. Shin, J. M. Kim, J. Y. Choi, and W. S. Yoon, “Modeling and applications of electrochemical impedance spectroscopy (EIS) for lithium-ion batteries,” *Journal of Electrochemical Science and Technology*, vol. 11, no. 1, pp. 1–13, 2020.
- [296] Z. Song, X. Han, Y. Deng, N. Zhao, W. Hu, and C. Zhong, “Clarifying the Controversial Catalytic Performance of $\text{Co}(\text{OH})_2$ and Co_3O_4 for Oxygen Reduction/Evolution Reactions toward Efficient Zn-Air Batteries,” *ACS Applied Materials and Interfaces*, vol. 9, no. 27, pp. 22694–22703, 2017.
- [297] M. D. Levi and D. Aurbach, “Simultaneous measurements and modeling of the electrochemical impedance and the cyclic voltammetric characteristics of graphite electrodes doped with lithium,” *Journal of Physical Chemistry B*, vol. 101, no. 23, pp. 4630–4640, 1997.
- [298] Z. Ahaliabadeh, V. Miikkulainen, M. Mäntymäki, S. Mousavihashemi, J. Lahtinen, Y. Lide, H. Jiang, K. Mizohata, T. Kankaanpää, and T. Kallio, “Understanding the Stabilizing Effects of Nanoscale Metal Oxide and Li-Metal Oxide Coatings on Lithium-Ion Battery Positive Electrode Materials,” *ACS Applied Materials and Interfaces*, vol. 13, no. 36, pp. 42773–42790, 2021.
- [299] S. Kim, J. K. Noh, M. Aykol, Z. Lu, H. Kim, W. Choi, C. Kim, K. Y. Chung, C. Wolverton, and B. W. Cho, “Layered-Layered-Spinel Cathode Materials Prepared by a High-Energy Ball-Milling Process for Lithium-ion Batteries,” *ACS Applied Materials and Interfaces*, vol. 8, no. 1, pp. 363–370, 2016.
- [300] T. A. Yersak and J. R. Salvador, “Protective Sacrificial Coating to Enhance Stability of Battery Materials,” *US20200395630*, 2019.

- [301] Z. Zhao, X. Cai, X. Yu, H. Wang, Q. Li, and Y. Fang, “Zinc-assisted mechanochemical coating of a reduced graphene oxide thin layer on silicon microparticles to achieve efficient lithium-ion battery anodes,” *Sustainable Energy and Fuels*, vol. 3, no. 5, pp. 1258–1268, 2019.
- [302] A. Shevtsov, H. Han, A. Morozov, J. C. Carozza, A. A. Savina, I. Shakhova, N. R. Khasanova, E. V. Antipov, E. V. Dikarev, and A. M. Abakumov, “Protective spinel coating for $\text{Li}_{1.17}\text{Ni}_{0.17}\text{Mn}_{0.50}\text{Co}_{0.17}\text{O}_2$ cathode for Li-ion batteries through single-source precursor approach,” *Nanomaterials*, vol. 10, no. 9, pp. 1–16, 2020.
- [303] Y. B. Niu, Y. J. Guo, Y. X. Yin, S. Y. Zhang, T. Wang, P. Wang, S. Xin, and Y. G. Guo, “High-Efficiency Cathode Sodium Compensation for Sodium-Ion Batteries,” *Advanced Materials*, vol. 32, no. 33, pp. 1–7, 2020.
- [304] Z. Song, G. Zhang, X. Deng, K. Zou, X. Xiao, R. Momen, A. Massoudi, W. Deng, J. Hu, H. Hou, G. Zou, and X. Ji, “Ultra-Low-Dose Pre-Metallation Strategy Served for Commercial Metal-Ion Capacitors,” *Nano-Micro Letters*, vol. 14, no. 1, 2022.
- [305] Y. L. Ni’Mah, J. H. Cheng, M. Y. Cheng, W. N. Su, and B. J. Hwang, “Improvement of cycling performance of $\text{Na}_{2/3}\text{Co}_{2/3}\text{Mn}_{1/3}\text{O}_2$ cathode by PEDOT/PSS surface coating for na ion batteries,” *Indonesian Journal of Chemistry*, vol. 18, no. 1, pp. 127–136, 2018.
- [306] Q. Liu, Z. Hu, C. Zou, H. Jin, S. Wang, and L. Li, “Structural engineering of electrode materials to boost high-performance sodium-ion batteries,” *Cell Reports Physical Science*, vol. 2, no. 9, p. 100551, 2021.
- [307] J. H. Jo, J. U. Choi, A. Konarov, H. Yashiro, S. Yuan, L. Shi, Y.-K. Sun, and S.-T. Myung, “Sodium-Ion Batteries Building Effective Layered Cathode Materials with Long-Term Cycling,” *Advanced Functional Materials*, vol. 28, no. 14, p. 1705968, 2018.
- [308] J. Chen, “Recent progress in advanced materials for lithium ion batteries,” *Materials*, vol. 6, no. 1, pp. 156–183, 2013.
- [309] F. Salver-Disma, J. M. Tarascon, C. Clinard, and J. N. Rouzaud, “Transmission electron microscopy studies on carbon materials prepared by mechanical milling,” *Carbon*, vol. 37, no. 12, pp. 1941–1959, 1999.
- [310] F. Salver-Disma, A. Du Pasquier, J. M. Tarascon, J. C. Lassègues, and J. N. Rouzaud, “Physical characterization of carbonaceous materials prepared by mechanical grinding,” *Journal of Power Sources*, vol. 81-82, pp. 291–295, 1999.
- [311] F. Disma, L. Aymard, L. Dupont, and J. Tarascon, “Effect of Mechanical Grinding on the Lithium Intercalation Process in Graphites and Soft Carbons,” *Journal of The Electrochemical Society*, vol. 143, no. 12, pp. 3959–3972, 1996.
- [312] J. M. Tarascon, M. Morcrette, J. Saint, L. Aymard, and R. Janot, “On the benefits of ball milling within the field of rechargeable Li-based batteries,” *Comptes Rendus Chimie*, vol. 8, no. 1, pp. 17–26, 2005.

- [313] S. Li, S. Wen, H. Ding, L. Yang, D. Zhao, N. Zhang, H. Dong, S. Wang, J. Zhang, and J. Wang, "Improve the Electrochemical Performance of Na₂Ti₃O₇ Nanorod through Pitch Coating," *ACS Sustainable Chemistry & Engineering*, 2022.
- [314] S. Mukherjee, S. B. Mujib, D. Soares, and G. Singh, "Electrode materials for high-performance sodium-ion batteries," *Materials*, vol. 12, no. 12, 2019.
- [315] M. Morcrette, C. Wurm, and C. Masquelier, "On the way to the optimization of Li₃Fe₂(PO₄)₃ positive electrode materials," *Solid State Sciences*, vol. 4, no. 2, pp. 239–246, 2002.
- [316] L. Beaulieu, D. Larcher, R. A. Dunlap, and J. R. Dahn, "Nanocomposites in the Sn-Mn-C system produced by mechanical alloying," *Journal of Alloys and Compounds*, vol. 297, no. 1-2, pp. 122–128, 2000.
- [317] D. Larcher, L. Y. Beaulieu, D. D. MacNeil, and J. R. Dahn, "In Situ X-Ray Study of the Electrochemical Reaction of Li with crystalline intermetallic - Cu₆Sn₅," *Journal of The Electrochemical Society*, vol. 147, no. 5, p. 1658, 2000.
- [318] K. H. Tran-Ba, D. J. Lee, J. Zhu, K. Paeng, and L. J. Kaufman, "Confocal Rheology Probes the Structure and Mechanics of Collagen through the Sol-Gel Transition," *Biophysical Journal*, vol. 113, no. 8, pp. 1882–1892, 2017.
- [319] D. Dörr, U. Kuhn, and V. Altstädt, "Rheological study of gelation and crosslinking in chemical modified polyamide 12 using a multiwave technique," *Polymers*, vol. 12, no. 4, pp. 7–9, 2020.
- [320] G. Chu, G. Vasilyev, D. Qu, S. Deng, L. Bai, O. J. Rojas, and E. Zussman, "Structural Arrest and Phase Transition in Glassy Nanocellulose Colloids," *Langmuir*, vol. 36, no. 4, pp. 979–985, 2020.
- [321] L. Noirez and P. Baroni, "Identification of a low-frequency elastic behaviour in liquid water," *Journal of Physics Condensed Matter*, vol. 24, no. 37, 2012.
- [322] A. Zaccone and K. Trachenko, "Explaining the low-frequency shear elasticity of confined liquids," *Proceedings of the National Academy of Sciences of the United States of America*, vol. 117, no. 33, pp. 19353–19655, 2020.
- [323] R. Biehl and T. Palberg, "Modes of motion in a confined colloidal suspension under shear," *Europhysics Letters*, vol. 66, no. 2, pp. 291–295, 2004.
- [324] J. Owen, "21 - Ionic Conductivity," in *Comprehensive Polymer Science and Supplements* (G. Allen and J. C. Bevington, eds.), pp. 669–686, Amsterdam: Pergamon, 1989.
- [325] M. Echeverri, C. Hamad, and T. Kyu, "Highly conductive, completely amorphous polymer electrolyte membranes fabricated through photo-polymerization of poly(ethylene glycol diacrylate) in mixtures of solid plasticizer and lithium salt," *Solid State Ionics*, vol. 254, pp. 92–100, 2014.

- [326] M. Bradley, “Curve Fitting in Raman and IR Spectroscopy : Basic Theory of Line Shapes and Applications,” *Thermo Fisher Scientific Application Note*, p. AN50733, 2007.
- [327] A. Sadat and I. J. Joye, “Peak fitting applied to fourier transform infrared and raman spectroscopic analysis of proteins,” *Applied Sciences (Switzerland)*, vol. 10, no. 17, 2020.